STRUCTURE AND REACTIVITY OF ENDOHEDRAL (METALLO)FULLERENES

Marc Garcia Borràs

Dipòsit legal: Gi. 1385-2015
http://hdl.handle.net/10803/302920

Universitat de Girona

Doctoral Thesis:

Structure and Reactivity of Endohedral (Metallo)Fullerenes

Marc Garcia Borràs

2015

Doctoral Programme in Experimental Sciences and Sustainability

Supervised by:
Prof. Miquel Solà Puig
Dr. Josep Maria Luis Luis

Tutor:
Prof. Miquel Solà Puig

This manuscript has been presented to opt for the doctoral degree from the University of Girona

Universitat de Girona

Prof. Dr. Miquel Solà i Puig and Dr. Josep Maria Luis Luis, of Universitat de Girona,

WE DECLARE:

That the thesis entitled "Structure and Reactivity of Endohedral (Metallo) Fullerenes", presented to obtain a doctoral degree, has been completed under our supervision and meets the requirements to opt for an International Doctorate.

For all intents and purposes, we hereby sign this document.

Signature

Prof. Dr. Miquel Solà Puig Dr. Josep Maria Luis Luis

Girona, 5th May 2015

als avis,

a los abuelos,

a la mama, al papa, a l'Ivan.

Acknowledgments

Una Tesi és com anar a córrer amb la bici el Terra de Remences o la Puertos de la Ribagorza. Comences fort, amb ganes de tot. Tens forces i energia per anar avançant, potser més ràpid del que tocaria. Els primers ports de muntanya són fàcils de superar, t'has entrenat, i desbordes vitalitat per arreu. Però és quan arriben els grans ports, quan ja portes kilòmetres a sobre, que les cames comencen a tremolar i arriben les primeres *rampes*. Intentes seguir pedalant igual de fort, però les cames no responen. El cap comença a dir-te que "no", i sembla que no hi ha manera de continuar movent aquells plats i pinyons amb unes forces que ja no hi són. Tot i que ja sabies que seria dur, comences a pensar que això és massa. És aleshores quan mires al teu costat i hi veus a tot un equip esperan-te, empenyen-te i portan-te muntanya amunt. No estàs sol, i quan les coses van mal dades ells sempre hi seran. El camí és llarg i dur. Però la satisfacció de creuar la meta acompanyat de tots els qui sempre heu estat al meu costat no es pot descriure. Gràcies!

Per a realitzar aquesta Tesi he estat finançat amb una beca predoctoral del "Ministerio de Educación, Cultura y Deporte" per a la "Formación de Profesorado Universitario" (FPU) AP2010-2517.

En primer lloc, m'agradaria començar agraint als meus directors de Tesi, en Josep Maria i en Miquel, primer per captar-me per a la causa durant els "Casals d'Estiu IQC" organitzats per en Josep Maria, seguidament per oferir-me la possibilitat de fer el Treball Experimental i gaudir d'una beca de col·laboració del Ministerio durant l'últim curs de carrera, i finalment per animar-me i engrescar-me a començar l'aventura del Doctorat. Vosaltres sabeu tant bé com jo que els inicis no van ser fàcils, i mai podré agraïr-vos suficient tot el que vareu fer per mi quan vau buscar contractes de sota les pedres perquè pogués

tenir un petit sou fins que els senyors del Ministerio van decidir donar-me la beca predoctoral. Moltes gràcies Miquel per apostar i creure en mi durant tots aquests anys, per tota l'ajuda que m'has ofert i la teva predisposició i ganes de treballar que sempre ens encomanes a tots. Espero haver-te tornat tota aquesta confiança en forma de feina i treball. Amb en Josep Maria vam començar a treballar plegats a l'estiu del 2008 (farà 7 anys ja... uff!) i després de patir una mica, de passar-nos-ho molt bé, i d'aprendre moltíssim pel camí, hem arribat fins aquí. Moltíssimes gràcies per tot el que has fet, fas, i estic segur que faràs per mi. Gràcies per ensenyar-me a ser pràctic i a com afrontar els diferents problemes tant a nivell científic com a nivell personal. Moltes gràcies als dos per ensenyar-me tot el que sé, i per apostar per mi.

A la Sílvia, una amiga, també li vull agraïr molt especialment tot el seu suport. Quan vaig acabar la carrera, just marxaveu amb en Narcís a la cerca del vostre somni americà. Però això no va impedir que sempre que ho necessités em donéssis un cop de mà amb el que fós, i que fins a dia d'avui hàgim format l'increïble M&S team! Les hores asseguts al despatx colze a colze solucionant mil problemes, les hores caminant per Disney World, Universal's, i els inmensos Outlets de les costes Est i Oest... Quants moments i històries!! També et vull donar les gràcies per ensenyar-me de tot i més, per la teva paciència (sé que sóc un pesat), i per donar-me la possibilitat de poder seguir treballant junts en aquest prometedor futur que començarà ara.

A l'Eloy, company de despatx, de pis a *can Precarios* des dels seus inicis, de patiments amb la bici, i de mil històries. A l'Eduard, per totes les converses, sopars, partits del barça, i confidències que hem compartit. Et vaig acompanyar a Brusel·les una vegada, i hi tornarem amic! I juntament amb en Pedro, us vull agraïr tota l'ajuda que sempre m'heu ofert quan l'he necessitat referent als vostres ESI-3D i APOST-3D. De debò, ningú es pot imaginar què seria de l'IQC sense tota la vostra feina. Em sento un afortunat, perquè a part de poder dir que he estat company vostre i que he pogut aprendre d'uns científics excepcionals, puc dir que us tinc com a amics. Moltíssimes gràcies per tot nois!

A en Ferran, company de mil aventures, i totes les que encara vindràn! Ara que tenim una nova incorporació, l'Adrià, que ens acompanyarà també en el nostre camí per mantenir l'ordre i l'equilibri a l'Univers IQCCer... amb l'inestimable ajuda de la Vero, quan no ens la *segrestin* des de la sucursal que l'IQC ha muntat a Donosti! ;)

De l'IQCC no em voldria oblidar de la Carme, la mama de tots, que s'ha preocupat de que mengés bé durant tots aquests anys, i en Dani, el *guardian de las*

estrellas que aconsegueix que el Beta (casi) mai mori encara que li quedi només un mes de contracte.. per cert, un mes infinit! I per molts anys!! Moltes gràcies a en Quim per controlar tot i més, i mantenir-nos al dia de tot!! Agraïr també a tota la tropa de sèniors amb els que hem compartit grup durant tots aquests anys, i dels que he après molt també: en Lluís, l'Alexander, la Sílvia S., en Miquel Duran, en Sergei, i en Marcel. Especialment, moltes gràcies Marcel per totes les hores que m'has dedicat per solucionar problemes i dubtes! Als post-docs presents i passats, des de'n Primo (nits mítiques per Platea....), l'efímera Alatriste (que també va passar per can Precarios), en petit gran Quansong Li, en Carles (sort que tu ens "cuidaves" a en Primo!), en Miquel Torrent i la nova església de la Asexualitat, i als banyolins Jordi i Albert. A tots els estudiants amb els que hem compartit moltes estones al despatx de becaris del Parc i també al ja mític 177 de la Facultat: l'Eugene (el nostre nedador a la triatló per equips), en Majid (merengue, merengue!), la Laia, en Sergi (Pikachu), la Cristina Butchosa (encara que em piquis i em maltractis), en Mauricio (company de Canpre també!!, i vividor follador), l'Abril, i en Ouissam. I als ex-IQC, que tot i no haver coincidit a l'IQC, ja ens ho hem fet venir bé per trobar-nos de tant en tant i muntar sopars i partidets de furgol. Merci per tots aquests moments fora del despatx Pata, i infinites gràcies Juanma per tota l'ajuda amb la Marie Curie i les beques de postdoc!! Algo rascarem.. jejeje!

Durant el periode de doctorat, he treballat i col·laborat amb molta gent, però vull agraïr especialment a en Heribert, en David, i a en Ken el seu tracte i ajuda durant les estades que he fet a Atenens, París, i Los Angeles. Thank you David for your help with the ElVibRot code!! Thank you so much Heribert for all your help during the ammonia projects and during my visit to Athens and its chaotic administrative stuff!!! I would like to thank you Ken for giving me the opportunity to visit your group for three months during my Thesis and to giving me the opportunity to come back soon. Thank you all!! Finally, let me thank Prof. Kirtman for all his help, support, and fantastic work on the NLOP projects along all these years. I have learned a lot from you Prof. Kirtman. Thank you!

No puedo olvidarme de mi familia *americana*, Pablo, Gloria, Edurne y Blanca. Gracias por acojerme con los brazos abiertos, cuidar de mi, y hacerme sentir como en casa en todo momento. Nunca podré olvidar esos tres meses en Los Angeles, las cenas en el Marica, los Happy Hours en el Sepis, los atracones en el In-N-out, el Halloween en West Hollywood... Bueno, esto último sí que lo olvidaré.. jajaja!! Pablo y Gloria, infinitas gracias por alojarme en vuestra casa durante unos días y por como me tratasteis. Sois increíbles chicos!!!! Musho Betis!!!! :)

Tornant cap a casa, vull agraïr a en Xavi i a en Miquel C. que m'hagin permès seguir treballant i col·laborant amb la Cris en els projectes de les nano-càpsules (conegudes també com cris-càpsules). Des del 2008 que vam començar a treballar-hi, fins a veure tot el que la Cristina ha construït... em fa sentir especialment orgullós de tenir-te com a companya i amiga Cris! Ets una crack Cristinita!! Són ja molts anys, moltes aventures... i les que vindràn!

I bueno.... Arriba el moment d'agraïr infinitament la paciència que heu tingut amb mi nois: a la Mai, en Dani, l'Alex, en Vito, l'Eva, l'Arturo, en Kelvyn... La colla de Santa Cristina, on passi el que passi sempre ens tindrem els uns als altres. Vosaltres heu vist que això ha estat llarg i difícil, però ja ho tenim!! Per tots els cafès, sopars, barbacoes, petanques... En definitiva, per tots els moments junts. Gràcies per fer que tots aquests moments plegats siguin únics. Mai us podré agraïr lo feliç que em feu, amics!!! Us desitjo lo millor a tots perquè us ho mereixeu tot. Sou genials família!!! Vull agraïr-te a tu també Alba tota la paciència i males cares que has hagut d'aguantar sobretot en aquesta part final de la Tesi. M'has animat i arrencat un somriure sempre que ho he necessitat i quan més al límit he estat. Gràcies per voler compartir els bons i no tant bons moments amb mi. Cacahuet, pio!! No vull oblidar-me tampoc de'n David M.. Encara que no ens poguem veure tant com ens agradaria, sé que quan et necessiti et tindré ben aprop, i saps que tu també em tindràs a mi al costat. A tota la colla del *Lado Oscuro*, que encara que passi el temps, ens poguem seguir trobant per recordar les grans gestes dels dies d'institut!! Gràcies a tots per creure en mi i animar-me durant tot aquest temps!!

Ja per últim, vull donar-vos les gràcies Mama i Papa. Gràcies per fer de l'Ivan i de mi el que som a dia d'avui. Gràcies per l'educació que ens heu donat, pels valors i cultura de l'esforç que ens heu inculcat. Vosaltres més que ningú heu patit aquesta Tesi tant o potser més que jo. L'Ivan i jo només volem que us sentiu orgullos de nosaltres, us estimem molt. Ivan, gràcies per confiar en mi i donar-me suport durant tot aquest llarg camí... i felicitats per tot el que estas aconseguint. Ets increïble... Passaran els anys, però sé que sempre us tindré amb mi. Gràcies per fer-me sentir estimat família!! Gràcies iaia Paquita i gràcies avi Joan, que encara que no ho puguis veure, sé que estas molt orgullós. Y gracias iaia Antonia y avi Lluís, por confiar tanto en mí, espero que os podais sentir muy orgullosos todos! Us estimo molt avis, i aquesta tesi us la dedico a vosaltres. No em vull oblidar dels meus tios preferits!! Gràcies tio David. M'has ensenyat a creure en les possibilitats d'un mateix i a lluitar a contracorrent. Ens has demostrat a tots que amb ganes, il·lusió i esforç, un pot convertir els seus somnis en realitat. Gràcies tia Marissa, tia Montse, i tio

Francesc, perquè sempre hi sou i sé que sempre hi sereu per cuidar de mi.

Aquesta Tesi posa punt i final a una de les etapes més maques de la meva vida. Sé que mai podré oblidar tots aquests anys que he compartit amb tots vosaltres, però això no para. Tanquem un capítol per obrir-ne un altre de nou. El que m'ofereix el futur és una mica incert degut als temps que ens han tocat viure, però puc dir que no tinc cap mena de por ni angoixa perquè sé que seguireu tots vosaltres al meu costat i mai estaré sol. Gràcies a tots per fer-me sentir únic, espero que estigueu orgullosos de mi.

Marc

Full list of Publications

This Thesis is presented as a compendium of publications.

Published articles included in this Thesis:

1. Garcia-Borràs, M.; Osuna, S.; Luis, J.M.; Swart, M.; Solà, M., "The Exohedral Diels-Alder Reactivity of the Titanium Carbide Endohedral Metallofullerene $Ti_2C_2@D_{3h}$-C_{78}: Comparison with D_{3h}-C_{78} and $M_3N@D_{3h}$-C_{78} (M=Sc and Y) Reactivity", *Chem. Eur. J.*, **2012**, 18, 7141-7154. (Impact factor: 5.831, position 21/152 in chemistry, multidisciplinary, 1^{st} quartile)

2. Garcia-Borràs, M.; Romero-Rivera, A., Osuna, S.; Luis, J.M.; Swart, M.; Solà, M., "The Frozen Cage Model: A Computationally Low-Cost Tool for Predicting the Exohedral Regioselectivity of Cycloaddition Reactions Involving Endohedral Metallofullerenes", *J. Chem. Theory Comput.*, **2012**, 8, 1671-1683. (Impact factor: 5.389, position 3/34 in physics, atomic, molecular & chemical, 1^{st} quartile)

3. Garcia-Borràs, M.; Osuna, S.; Luis, J.M.; Swart, M.; Solà, M., "A Complete Guide on the Influence of Metal Clusters in the Diels-Alder Regioselectivity of I_h-C_{80} Endohedral Metallofullerenes", *Chem. Eur. J.*, **2013**, 19, 14931-14940. (Impact factor: 5.696, position 22/148 in chemistry, multidisciplinary, 1^{st} quartile)

4. Garcia-Borràs, M.; Luis, J.M.; Swart, M.; Solà, M., "Diels-Alder and Retro-Diels-Alder Cycloadditions of (1,2,3,4,5-Pentamethyl)cyclopentadiene to $La@C_{2v}$-C_{82}: Regioselectivity and Product Stability", *Chem. Eur. J.*, 2013, 19, 4468-4479. Corrigendum: *Chem. Eur. J.*, **2013**, 19, 9739-9739. (Impact factor: 5.696, position 22/148 in chemistry, multidisciplinary, 1^{st} quartile)

5. Aroua, S.;† Garcia-Borràs, M.;† Osuna, S.; Yamakoshi, Y., "Essential factors for controlling the equilibrium in reversible rearrangement of $M_3N@I_h$-C_{80} fulleropyrrolidines: exohedral functional groups versus endohedral metal clusters", *Chem. Eur. J.*, **2014**, 20, 14032-14039. (†: The authors have equally contributed to the work) (Impact factor: 5.696, position 22/148 in chemistry, multidisciplinary, 1^{st} quartile)

6. Maroto, E.E.; Mateos, J.; Garcia-Borràs, M.; Osuna, S.; Filippone, S.; Herranz, M. A.; Murata, Y.; Solà, M.; Martín, N., "Enantiospecific cis-trans Isomerization in Chiral Fulleropyrrolidines: H-Bonding assistance in the carbanion stabilization in $H_2O@C_{60}$", *J. Am. Chem. Soc.*, **2015**, 137, 1190-1197. (Impact factor: 11.444, position 10/148 in chemistry, multidisciplinary, 1^{st} quartile)

7. Aroua, S.; Garcia-Borràs, M.; Bölter, M. F.; Osuna, S.; Yamakoshi, Y., "Endohedral Metal-induced Regioselective Formation of Bis-Prato Adduct of $Y_3N@I_h$-C_{80} and $Gd_3N@I_h$-C_{80}", *J. Am. Chem. Soc.*, **2015**, 137, 58-61. (Impact factor: 11.444, position 10/148 in chemistry, multidisciplinary, 1^{st} quartile)

8. Garcia-Borràs, M.; Osuna, S.; Swart, M.; Luis, J.M.; Solà, M., "Electrochemical control of the regioselectivity in the exohedral functionalization of C_{60}: the role of aromaticity", *Chem. Commun.*, **2013**, 49, 1220-1222. (Impact factor: 6.718, position 20/148 in chemistry, multidisciplinary, 1^{st} quartile)

9. Garcia-Borràs, M.; Osuna, S.; Swart, M.; Luis, J.M.; Solà, M., "Maximum Aromaticity as a Guiding Principle for the Most Suitable Hosting Cages in Endohedral Metallofullerenes", *Angew. Chem. Int. Ed.*, **2013**, 52, 9275-9278. Back Cover: *Angew. Chem. Int. Ed.*, **2013**, 52, 9332-9332. (Impact factor: 11.336, position 11/148 in chemistry, multidisciplinary, 1^{st} quartile)

10. Garcia-Borràs, M.; Osuna, S.; Swart, M.; Luis, J.M.; Echegoyen, L., Solà, M., "Aromaticity as the driving force for the stability of non-IPR endohedral metallofullerene Bingel-Hirsch adducts", *Chem. Commun.*, **2013**, 49, 8767-8769. (Impact factor: 6.718, position 20/148 in chemistry, multidisciplinary, 1^{st} quartile)

11. Garcia-Borràs, M.; Osuna, S.; Luis, J.M.; Swart, M.; Solà, M., "The role of aromaticity in determining the molecular structure and reactivity of (endohedral metallo)fullerenes", *Chem. Soc. Rev.*, **2014**, 43, 5089-5105.

(Impact factor: 30.425, position 2/148 in chemistry, multidisciplinary, 1^{st} quartile)

Articles in preparation included in this Thesis:

12. Garcia-Borràs, M.; Osuna, S.; Luis, J.M.; Solà, M., "Understanding the relative abundances of TNT-based endohedral metallofullerenes from aromaticity measures", *in preparation*, **2015**.

13. Garcia-Borràs, M.; Cerón, M.; Osuna, S.; Izquierdo-Barroso, M.; Luis, J.M.; Echegoyen, L., Solà, M., "The regioselectivity of Bingel-Hirsch cycloadditions on IPR endohedral metallofullerenes predicted from simple aromaticity measures. The $Sc_3N@D_{3h}$-C_{78} and $Sc_3N@D_{5h}$-C_{80} as model systems", *in preparation*, **2015**.

Other published articles not included in this Thesis:

14. Garcia-Borràs, M.; Solà, M.; Luis, J.M.; Kirtman, B., "Electronic and Vibrational Nonlinear Optical Properties of Five Representative Electrides", *J. Chem. Theory Comput.*, **2012**, 8, 2688-2697. (Impact factor: 5.389, position 3/34 in physics, atomic, molecular & chemical, 1^{st} quartile)

15. Garcia-Borràs, M.; Solà, M.; Lauvergnat, D.; Luis, J.M.; Kirtman, B., "A Full Dimensionality Approach to Evaluate the Nonlinear Optical Properties of Molecules with Large Amplitude Anharmonic Tunneling Motions", *J. Chem. Theory Comput.*, **2013**, 9, 520-532. (Impact factor: 5.310, position 3/33 in physics, atomic, molecular & chemical, 1^{st} quartile)

16. García-Simón, C.; Garcia-Borràs, M.; Gómez, L.; Garcia-Bosch, I.; Osuna, S.; Swart, M.; Luis, J.M.; Rovira, C.; Almeida, M.; Imaz, I.; Maspoch, D.; Costas, M.; Ribas, X., "Self-Assembled Tetragonal Prismatic Molecular Cage Highly Selective for Anionic Guests", *Chem. Eur. J.*, **2013**, 19, 1445-1456. (Impact factor: 5.696, position 22/148 in chemistry, multidisciplinary, 1^{st} quartile)

17. Reis, H.; Luis, J.M.; Garcia-Borràs, M.; Kirtman, B., "Computation of Nonlinear Optical Properties of Molecules with Large Amplitude Anharmonic Motions. III. Arbitrary Double-Well Potentials", *J. Chem. Theory Comput.*, **2014**, 10, 236-242. (Impact factor: 5.310, position 3/33 in physics, atomic, molecular & chemical, 1^{st} quartile)

18. García-Simón, C.; Garcia-Borràs, M.; Gómez, L.; Parella, T.; Osuna, S.; Juanhuix, J.; Imaz, I.; Maspoch, D.; Costas, M.; Ribas, X., "Sponge-like molecular cage for purification of fullerenes", *Nat. Commun.*, **2014**, 5, 5557. (Impact factor: 10.742, position 3/55 in chemistry, multidisciplinary, 1^{st} quartile)

19. Postils, V.; Garcia-Borràs, M.; Solà, M.; Luis, J.M.; Matito, E., "On the existence and characterization of molecular electrides", *Chem. Commun.*, **2015**, 51, 4865-4868. (Impact factor: 6.718, position 20/148 in chemistry, multidisciplinary, 1^{st} quartile)

Outreach publications:

20. Swart, M.; Osuna, S.; Garcia-Borràs, M.; Luis, J.M.; Solà, M., "Regioselectividad en fullerenos, una visión computacional", *An. Quím.*, **2013**, 109, 11-19.

21. Garcia-Borràs, M.; Osuna, S.; Solà, M., "La versatilidad de los fullerenos", *Investigación y Ciencia*, **2014**, 449, 10-12.

Book chapters:

22. Garcia-Borràs, M.; Osuna, S.; Swart, M.; Luis, J.M.; Solà, M., "Understanding the Exohedral Functionalization of Endohedral Metallofullerenes", Book chapter in "Exotic Properties of Carbon Nanomatter: Advances in Physics and Chemistry", Carbon Materials Series, M.V. Putz and O. Ori (Editors). *Springer Verlag*, Berlin, **2015**, Vol. 8, pp. 67-99. ISBN: 978-94-017-9566-1, DOI: 10.1007/978-94-017-9567-8_4.

List of Abbreviations

Abbreviation	Description
o-DCB	ortho-dichlorobenzene
5MRs	Five membered rings
6MRs	Six membered rings
a.m.u.	Atomic mass units
ALA	Additive local aromaticity
APP	Adjacent pentagon pair
ASE	Aromatic stabilization energies
BH	Bingel-Hirsch
BHJ	Bulk heterojunction
CNT	Carbon nanotube
COSMO	Conductor-like screening model
DA	Diels-Alder
DBU	1,8-diazabicyclo[5.4.0]undec-7-ene
DFT	Density functional theory
EFs	Endohedral fullerenes
EMFs	Endohedral metallofullerenes
FCM	Frozen cage model
FMO	Frontier molecular orbital
GGA	Generalized gradient appriximation
HOMA	Harmonic model oscillator of aromaticity
HOMO	Highest occupied molecular orbital
HSE	Homodesmotic stabilization energies
IPR	Isolated Pentagon Rule
IPSI	Inverse pentagon separation index
IUPAC	International Union of Pure and Applied Chemsitry
KS	Kohn-Sham
LDA	Local density approximation
LT	Linear transit

Abbreviation	**Description**
LUMO	Lowest unoccupied molecular orbital
MARC	Maximum aromaticity criterion
MCI	Multicentre index
MO	Molecular orbital
MRI	Magnetic resonance imaging
NICS	Nucleus-independent chemical shifts
NLOP	Nonlinear optical properties
PAC	Predictive aromaticity criteria
PAPR	Pentagon adjacency penalty rule
PCM	Polarizable continuum model
PDI	Para-delocalization index
PES	Potential energy surface
QTAIM	Quantum theory of atoms in molecules
SCRF	Self consistent reaction field
SP	Single point energy calculations
TNT	Trimetallic nitride template
TS	Transition state
ZORA	Zeroth-order regular approximation

List of Figures

List of Tables

Contents

Summary of the Thesis

It all started in 1985, when Kroto, Smalley and Curl discovered by serendipity a new carbon allotrope. They synthesized for the first time the C_{60} molecule, and named it as "Buckminsterfullerene", because of the similarity between its structure and the famous geodesic dome designed by the architect Richard Buckminster Fuller. Later on, the acronym "fullerene" was adopted to include related structures of this new family of carbon-based compounds. An interesting type of fullerenes are the so-called endohedral (metallo)fullerenes, which are fullerenes containing atoms, small molecules or metallic clusters inside. A huge interest in this new class of molecules has been awakened mainly due to their potential applications in many different fields, for example in (bio)medicine as a magnetic resonance imaging contrast agents, or in photovoltaics as a new and more efficient dye sensitized solar cells. To that end, it is essential to know and understand their chemical structure and reactivity to ensure their use for (bio)medical purposes and to modify their properties to develop new fullerene-based technology devices or biomaterials. In this thesis the chemical structure and reactivity of endohedral (metallo)fullerenes is studied in detail using state-of-the-art computational tools.

The thesis is divided into seven chapters that contain eleven related publications, and two additional publications that are in preparation. The first chapter corresponds to an introductory part. The molecular and electronic structure of fullerene compounds is reviewed, and different synthetic methods to obtain endohedral (metallo)fullerenes are described. The chemical functionalization of these compounds by means of cycloaddition reactions is also illustrated. We also report a brief overview of the computational methods, tools, and strategies that we have applied in the studies included in this thesis. Chapter 2 summarizes the objectives of the Thesis.

In chapter 3 the computational exploration of the Diels-Alder cycloaddition reaction involving endohedral metallofullerenes (EMFs) is presented. There are four different projects included in this chapter but they are all intrinsically related. First, we study the Diels-Alder reactivity of $Ti_2C_2@C_{78}$ endohedral

metallofullerene, and compare it with the reactivity of pristine C_{78}, $Sc_3N@C_{78}$, and $Y_3N@C_{78}$ previously studied in our group. Then, we use all the collected data related to the Diels-Alder addition on these systems to propose a new computational strategy to systematically study the regioselectivity of these reactions. As a result, we apply this new methodology to thoroughly examine the exohedral reactivity of the endohedral metallofullerene family based on I_h-C_{80} fullerene structure, which are those most abundant. Finally, we apply our acquired knowledge on the EMFs Diels-Alder reactivity to unravel the different regioselectivity and stability of two different $La@C_{82}$ Diels-Alder products.

Chapter 4 is devoted to the study of 1,3-dipolar additions (the Prato reaction) on endohedral (metallo)fullerenes, and the different factors that control the product stabilities and the thermal isomerization process experimentally observed. There are three related projects included as a consequence of different collaborations with two experimental groups, the group of Prof. Nazario Martín at Universidad Complutense de Madrid and the group of Dr. Yoko Yamakoshi at the ETH in Zürich. In collaboration with the group of Prof. Martín we study the enantiospecific formation of chiral C_{60}, C_{70}, and H_2OC_{60} fulleropyrrolidines and analyze the role played by the encapsulated water molecule on the isomerization process. In collaboration with the group of Dr. Yamakoshi we focus on the Prato additions on trimetallic nitride template EMFs, analyzing the role of the encapsulated metallic cluster and the exohedral group on the product stabilities and the isomerization rates.

Chapter 5 includes a set of five projects where, for the first time, we systematically study the role of aromaticity on the endohedral metallofullerene stability and reactivity. In the first project, we show that when negative charge is added to a fullerene structure, the aromaticity of pentagonal and hexagonal rings that form the fullerene cage are differently affected. This has a direct effect on their chemical reactivity and structure. The next two projects are devoted to demonstrate that there exist an intrinsic relationship between endohedral metallofullerenes stabilities and their aromaticities. Indeed, experimentally formed EMFs correspond to those which are the most aromatic ones. Finally, in the last two projects we use the aromaticity concept as an indicator for understanding and predicting the regioselectivity of the Bingel-Hirsch functionalization of endohedral metallofullerenes.

Finally, chapter 6 includes the discussion about the previously described results, and in chapter 7 the main conclusions drawn from this thesis are summarized.

Resum de la Tesi

Tot va començar el 1985, quan Kroto, Curl i Smalley van descobrir per casualitat una nova forma al·lotròpica del carboni. Acabaven de sintetitzar per primera vegada la molècula C_{60}, i la van anomenar "Buckminsterful·lerè" degut a la similitud entre la seva estructura i la famosa cúpula geodèsica dissenyada per l'arquitecte Richard Buckminster Fuller. Més tard, l'acrònim "ful·lerè" es va adoptar per a referir-se a totes les estructures d'aquesta nova família de compostos basats en el carboni. Un tipus de ful·lerens molt interessants són els anomenats (metalo)ful·lerens endohèdrics, que són aquells ful·lerens que contenen àtoms, molècules petites o agregats metàl·lics encapusulats al seu interior. Des del seu descobriment s'ha despertat un enorme interès en aquesta nova classe de molècules degut a les seves potencials aplicacions en camps molt diferents, com per exemple, en el camp de la (bio)medicina per al seu ús com a agents de contrast en imatge per ressonància magnètica, o en el camp de l'energia fotovoltaica per a la fabricació de noves cèl·lules solars més eficients. Per aquesta raó, és imprescindible conèixer i entendre la seva estructura i reactivitat química per tal de garantir el seu ús amb finalitats (bio)mèdiques i per modificar les seves propietats per desenvolupar nous dispositius o (bio)materials basats en ful·lerens. En aquesta tesi, l'estructura química i la reactivitat dels (metalo)ful·lerens endohèdrics s'estudien en detall utilitzant les eines de la química computacional.

La tesi es divideix en set capítols que contenen onze publicacions relacionades, i dues publicacions addicionals que estan en preparació. El primer capítol correspon a una part introductòria. Es descriu l'estructura molecular i electrònica dels (metalo)ful·lerens endohèdrics, així com diferents mètodes per a la seva síntesi. La funcionalització d'aquests compostos mitjançant reaccions de cicloaddició també s'il·lustra. Finalment, es proporciona també una breu descripció dels mètodes de càlcul, eines i estratègies que hem aplicat en els estudis inclosos en aquesta tesi. El capítol 2 recull els objectius de la Tesi.

En el capítol 3 es presenta l'estudi computacional de la reacció de cicloaddició de Diels-Alder en metaloful·lerens endohèdrics (MFE). S'han inclòs quatre

projectes diferents en aquest capítol, tots ells intrínsecament relacionats. En primer lloc, estudiem la reactivitat enfront de la reacció de Diels-Alder del compost MFE $Ti_2C_2@C_{78}$, i la comparem amb la reactivitat dels sistemes C_{78}, $Sc_3N@C_{78}$, i $Y_3N@C_{78}$ estudiats prèviament en el nostre grup de recerca. Tot seguit, utilitzem totes les dades recollides en relació amb l'addició de Diels-Alder en aquests sistemes per proposar una nova estratègia computacional per estudiar sistemáticament la regioselectivitat d'aquestes reaccions. Com a resultat, apliquem aquesta nova metodologia per examinar a fons la reactivitat exohèdrica de la família de metaloful·lerens endohèdrics basats en l'estructura del ful·lerè I_h-C_{80}, ja que són els més abundants. Finalment, apliquem els coneixements adquirits sobre la reactivitat Diels-Alder dels MFEs per explicar la diferent regioselectivitat i estabilitat de dos productes Diels-Alder diferents obtinguts sobre el compost $La@C_{82}$.

El capítol 4 es dedica a l'estudi de les addicions 1,3-dipolars (reacció de Prato) sobre metaloful·lerens endohèdrics, i els diferents factors que controlen les estabilitats dels productes així com el procés d'isomerització tèrmica observada experimentalment. S'han inclós tres projectes fruït de diferents col·laboracions amb dos grups experimentals, el grup del Prof. Nazario Martín a la Universitat Complutense de Madrid i el grup de la Dr. Yoko Yamakoshi a l'ETH de Zürich. En col·laboració amb el grup del Prof. Martín, estudiem la formació enantioespecífica de ful·leropirrolidines quirals basades en C_{60}, C_{70}, i $H_2O@C_{60}$, on també analitzem el paper exercit per la molècula d'aigua encapsulada en el procés d'isomerització. En col·laboració amb el grup de la Dr. Yamakoshi ens centrem en estudiar les addicions Prato sobre MFEs que conténen nitrurs trimetàl·lics, analitzant el paper de l'agrupació metàl·lica encapsulada i els substituents exohèdrics sobre les estabilitats dels productes i les velocitats d'isomerització.

El capítol 5 inclou un conjunt de cinc projectes en què, per primera vegada, s'estudia sistemàticament el paper de l'aromaticitat en l'estabilitat i la reactivitat dels metaloful·lerens endohèdrics. En el primer projecte, es mostra que quan s'afegeix càrrega negativa a una estructura ful·lerènica, l'aromaticitat dels anells pentagonals i hexagonals que formen l'estructura de carboni es veuen afectats de manera diferent. Això té un efecte directe sobre la seva reactivitat i estructura. Els següents dos projectes es dediquen a demostrar que hi ha una relació intrínseca entre l'estabilitat dels metaloful·lerens endohèdrics i la seva aromaticitat. De fet, es demostra que els MFEs experimentalment formats corresponen a aquells que són els més aromàtics. Finalment, en els dos últims projectes s'utilitza el concepte de l'aromaticitat com a indicador per entendre i predir la regioselectivitat de l'addició Bingel-Hirsch sobre els metaloful·lerens

endohèdrics.

Per acabar, el capítol 6 inclou la discussió sobre els resultats descrits anteriorment, i en el capítol 7 es resumeixen les principals conclusions d'aquesta tesi.

Resumen de la Tesis

Todo comenzó en 1985, cuando Kroto, Curl y Smalley descubrieron por casualidad una nueva forma alotrópica de carbono. Acababan de sintetizar por primera vez la molécula C_{60}, y la llamaron "buckminsterfullereno" debido a la similitud entre su estructura y la famosa cúpula geodésica diseñada por el arquitecto Richard Buckminster Fuller. Más tarde, se adoptó el acrónimo "fullereno" para englobar todas las estructuras de esta nueva familia de compuestos formadas por átomos de carbono. Un tipo de fulerenos muy interesantes son los llamados (metalo)fullerenos endohedicos, que son aquellos fullerenos que contienen átomos, moléculas pequeñas o clústeres metálicos encapsulados en su interior. Des de su descubrimiento, se ha despertado un enorme interés en esta nueva clase de moléculas debido a sus potenciales aplicaciones en muchos campos diferentes, por ejemplo, en (bio)medicina para ser usados como agentes de contraste en imagen por resonancia magnética, o en el campo de la energía fotovoltaica, para la fabricación de nuevas y más eficiente celdas solares. Por esta razón, es imprescindible conocer y comprender su estructura y reactividad química para garantizar su uso con fines (bio)médicos y para modificar sus propiedades para desarrollar nuevos dispositivos o (bio)materiales basados en fullerenos. En esta tesis, la estructura química y la reactividad de los (metalo)fullerenos endohédricos son estudiadas en detalle utilizando las herramientas de la química computacional.

La tesis se divide en siete capítulos que contienen once publicaciones relacionadas, y dos publicaciones adicionales que están en preparación. El primer capítulo corresponde a una parte introductoria. Se describe la estructura molecular y electrónica de los compuestos fullerénicos, así como diferentes métodos utilizados para su síntesis. La funcionalización de estos compuestos mediante reacciones de cicloadición también se ilustra. Finalmente, se proporciona una breve descripción de los métodos de cálculo, herramientas y estrategias computacionales que hemos aplicado en los estudios incluidos en esta tesis. El capítulo 2 engloba los objectivos de la Tesis.

En el capítulo 3 se presenta el estudio computacional de la reacción de cicload-

ición de Diels-Alder en metalofullerenos endohédricos (MFEs). Se han incluido cuatro proyectos diferentes en este capítulo, todos ellos intrínsecamente relacionados. En primer lugar, se estudia la reactividad de Diels-Alder del compuesto $Ti_2C_2@C_{78}$, y lo comparamos con la reactividad de los sistemas C_{78}, $Sc_3N@C_{78}$, y $Y_3N@C_{78}$, previamente estudiados en nuestro grupo de investigación. A continuación, utilizamos todos los datos obtenidos en relación a la adición de Diels-Alder en estos sistemas para proponer una nueva estrategia computacional para estudiar sistemáticamente la regioselectividad de estas reacciones. Como resultado, aplicamos esta nueva metodología para examinar a fondo la reactividad exohedral de la familia de metalofullerenos endohédricos basados en la estructura de fullereno I_h-C_{80}, ya que son los más abundantes. Por último, aplicamos los conocimientos adquiridos sobre la reactividad Diels-Alder de los MFEs para desentrañar la diferente regioselectividad y estabilidad de dos productos Diels-Alder del compuesto $La@C_{82}$.

El capítulo 4 se dedica al estudio de las adiciones 1,3-dipolares (reacción de Prato) sobre (metalo)fullerenos endohédricos, y los diferentes factores que controlan las estabilidades de los productos obtenidos y el proceso de isomerización térmica observada experimentalmente. Se incluyen tres proyectos producto de diferentes colaboraciones con dos grupos experimentales, el grupo del Prof. Nazario Martín en la Universidad Complutense de Madrid y el grupo de la Dr. Yoko Yamakoshi en el ETH de Zürich. En colaboración con el grupo del Prof. Martín, estudiamos la formación enantioespecífica de fulleropirrolidinas quirales basadas en C_{60}, C_{70}, i $H_2O@C_{60}$, donde también analizamos el papel desempeñado por la molécula de agua encapsulada en el proceso de isomerización. En colaboración con el grupo de la Dr. Yamakoshi nos centramos en estudiar las adiciones Prato en MFEs que contienen nitruros trimetálicos, analizando el papel de la agrupación metálica encapsulada y los sustituyentes exohedricos en las estabilidades de los productos y las velocidades de isomerización.

El capítulo 5 incluye un conjunto de cinco proyectos en los que, por primera vez, se estudia sistemáticamente el papel de la aromaticidad en la estabilidad y reactividad de los metalofullerenos endohédricos. En el primer proyecto, se muestra que cuando se añade carga negativa a una estructura fullerénica, la aromaticidad de los anillos pentagonales y hexagonales que forman la estructura de carbono se ve afectada de manera diferente. Esto tiene un efecto directo sobre su reactividad y estructura. Los siguientes dos proyectos se dedican a demostrar que existe una relación intrínseca entre las estabilidades de los MFEs y su aromaticidad. De hecho, se demuestra que los MFEs experimentalmente formados corresponden a aquellos que son los más aromáticos.

Por último, en los dos últimos proyectos se utiliza el concepto de aromaticidad como indicador para entender y predecir la regioselectividad de la funcionalización Bingel-Hirsch de metalofullerenos endohédricos.

Finalmente, el capítulo 6 incluye la discusión acerca de los resultados descritos anteriormente, y en el capítulo 7 se resumen las principales conclusiones de esta tesis.

Chapter 1

Introduction

Fullerenes

1.1 A brief introduction to fullerenes

Fullerenes are molecules composed by an even number of tricoordinated carbon atoms and located at vertices of polyhedra with typically pentagonal and hexagonal faces forming a hollow sphere. They are represented by the formula C_n, where n is the number of carbon atoms. As opposed to graphite and graphene that are exclusively formed by hexagonal rings, fullerene present pentagonal rings which makes them curved. Fullerenes, graphene and graphite are carbon allotropes, like diamond and carbon nanotubes (CNT). The main difference between the different allotropes of carbon is the hybridization of carbon atoms. For example, in diamond, carbon atoms have a sp^3 hybridization and tetrahedral coordination, but in graphite carbon atoms have a sp^2 hybridization and a trigonal planar coordination. Nevertheless, fullerenes and carbon nanotubes present an intermediate situation. Although their carbon atoms have sp^2 hybridization, the curvature of the structure does not allow a trigonal planar geometry, inducing an intrinsic pyramidalization of the carbons.

The buckminsterfullerene, C_{60}, is the most common and studied fullerene structure, and takes its name from the famous geodesic dome designed by the architect Richard Buckminster Fuller, which has similar geometric shape.

The buckminsterfullerene was the first fullerene structure discovered and the acronym "fullerene" was adopted to include related structures of this new family of carbon based compounds.

1.2 The beginnings: Discovering the C_{60}

In 1985 Kroto, Smalley, Curl and co-workers[1] were trying to understand the mechanism of formation of long-chain carbon molecules in interstellar space and circumstellar shells, vaporizing graphite by laser (Nd:YAG) irradiation. Nevertheless, under these conditions they observed an unexpected 720 mass peak detected by a time-of-flight mass spectroscopy. That peak corresponded to a C_{60} compound. They also observed clusters up to 190 carbon atoms, and noted that for clusters of more than 40 atoms only those containing an even number of carbon atoms were detected.

In order to satisfy all sp^2 valences, they proposed a spheroidal structure, also inspired by Buckminster Fuller's studies, which has icosahedral symmetry for the C_{60} cluster. They also noticed that the inner cavity of C_{60} (about 7 Å of diameter) was able to hold a variety of atoms, proposing the possibility of encapsulating atoms or small molecules inside these new structures.

Depending on the vaporization conditions, the abundance distribution of formed clusters changes, but C_{60} was always the most abundant species. The second carbon cluster in these distributions was C_{70}, but far from C_{60} values. They concluded that these two structures are the major constituent of circumstellar shells with high carbon content.

The possibility of having carbon clusters with hollow inner cavities was, however, proposed before the Kroto, Smalley, Curl discovery in 1985. Two decades earlier, in 1966 Jones[2] discussed the possibility of synthetize closed graphite sheets. His initial suggestion was that the graphite seet could be folded on itself. Later on, he also proposed the possibility of including pentagon rings to provide the necessary *defects* to allow the closure of the structure.[3] Notwithstanding, the first suggestion about the possible existence of spherical C_{60} molecule was reported by Osawa in 1970.[4] Even more, the stability of this hypotethical C_{60} molecule was discussed in terms of its electronic structure by Bochvar and Gal'pern[5] who performed Hückel calculations to prove that C_{60} would be a closed shell molecule with a very large HOMO-LUMO gap, which is a signature of chemical stability. However, none of these studies reported any experimental evidence and were only suppositions and conjectures.

In 1996, Kroto, Smalley and Curl were awarded the Nobel Prize in Chemistry for "*their discovery of fullerenes*".

1.2.1 Characterization of C_{60} structure

Since the publication of Kroto, Smalley and Curl discovery, many structural studies of buckminsterfullerene have been carried out, as well as different investigations about properties, stability, aromaticity and reactivity.

In 1990, Krätschmer *et al.*[6] developed a methodology to get macroscopic quantities of buckminsterfullerene using pure graphitic carbon soot produced by evaporating graphite electrodes in an atmosphere of about 100 torr of helium. The resulting product was dispersed in benzene to get a solution that exhibited a red-wine color. Then, the liquid was separated from the soot and dried, leaving a residue of dark brown to black crystals.

Different experiments were carried out to analyze the structure of the synthetized material. They reported a mass spectra that showed a strong peak at 720 a.m.u., electron and X-ray diffraction experiments and absortion spectra of the crystalline material. All these analysis showed evidences of the abundant presence of C_{60}.

Practically at the same time, Taylor *et al.*[7] reported the extraction and chromatographic separation of C_{60} and C_{70}, and their characterization by mass spectra. Moreover, ^{13}C-NMR measurements were carried out, showing unequivocally that all the carbons were equivalent in the case of C_{60} supporting the spherical buckminsterfullerene structure.

1.3 Fullerene structure

Fullerene structures are polyhedrons where atoms are situated in vertices, bonds in edges and rings in faces. Taking into account the Euler Theorem, the relationship between vertices (v), edges (e) and faces (f) is:

$$v + f = e + 2 \tag{1.1}$$

And the restriction of three σ-bonds per carbon atom, relates the number of vertices (v) and the number of edges (e) as gives the equation 1.2.

$$2e = 3v \tag{1.2}$$

If f_m is defined as the number of m-sided faces (rings), then the following relationship is accomplished:

$$2e = \sum_m m f_m \tag{1.3}$$

Considering a fullerene C_n, the number of vertices (*i.e.* atoms) is equal to n, and by the relation from equation 1.2 we can obtain the number of edges:

$$e = 3n/2 \tag{1.4}$$

And using the Euler Theorem given by equation 1.1, the number of faces is given by equation 1.5.

$$f = n/2 + 2 \tag{1.5}$$

Moreover, the number of pentagonal and hexagonal faces can be derived. The number of faces can also be expressed as given in equation 1.6:

$$f = \sum_m f_m \tag{1.6}$$

And making use of the expression given by equation 1.5, we can obtain equation 1.7:

$$\sum_m f_m = n/2 + 2 \tag{1.7}$$

If only fullerenes with pentagonal (f_5) and hexagonal (f_6) rings are considered, we can expand equation 1.7 into equation 1.8.

$$f_5 + f_6 = n/2 + 2 \tag{1.8}$$

And considering equations 1.3 and 1.4, with the restriction of having only pentagonal and hexagonal rings, equation 1.9 can be written.

$$5f_5 + 6f_6 = 3n \tag{1.9}$$

Then a linear system that includes equations 1.8 and 1.9 is obtained, whose solutions are:

$$f_5 = 12, f_6 = n/2 - 10 \tag{1.10}$$

That means, classical C_n fullerenes containing only five and six membered rings (5MRs and 6MRs, respectively) must have 12 pentagonal rings and $n/2 - 10$ hexagonal rings.[8]

Based on this theorem, the smallest possible fullerene is C_{20}, which has $20/2 - 10 = 0$ hexagonal rings. When the number of hexagonal rings increases, a wide range of fullerenes can be generated, and different isomers can be obtained. When the number of carbon atoms grows up, the number of possible isomers also increases but much faster. For example, for C_{20} there exists only 1 isomer that satisfies Euler's Theorem. For C_{60}, 1812 different isomers can be generated when one considers enantiomers as equivalent, and 3532 isomers when enantiomers are considered as non-equivalent (see Table 1.1).

Table 1.1: Enumeration of some C_n fullerene isomers generated by the spiral algorithm in the range $n = 20$ to 100 containing only pentagonal and hexagonal faces that can be obtained. In brackets, the isomer count when enantiomers are regarded as non-equivalent.

n	Isomers		n	Isomers	
20	1	(1)	64	3465	(4670)
24	1	(1)	66	4478	(8825)
28	2	(3)	68	6332	(12501)
30	3	(3)	70	8149	(16091)
34	6	(9)	74	14246	(28232)
38	17	(30)	78	24109	(47868)
40	40	(66)	80	31924	(63416)
44	89	(162)	82	39718	(79023)
48	199	(374)	86	63761	(126973)
50	271	(507)	88	81738	(162793)
54	580	(1113)	90	99918	(199128)
58	1205	(2344)	96	191839	(382627)
60	1812	(3532)	100	285913	(570602)

Because of the large number of structures that can be generated for a given fullerene C_n, an easy and efficient nomenclature system is required. The IUPAC method of naming fullerenes is too lengthy and complicated for a general use, and the most common and widely used way to name the different fullerene isomers is the one based on the spiral algorithm and the symmetry of the carbon cage.

The spiral algorithm is a general method, proposed by Fowler and Manolopoulos, to generate all possible isomeric structures for a given fullerene C_n, containing pentagonal and hexagonal rings.[9] Following this nomenclature, C_{60} is known as $I_h(1812)$-C_{60}.

1.3.1 The IPR rule

The formation of closed cages, as opposite to planar graphite, has associated a steric strain. In some cases, the strain energy is greater than the energy related to the formation of the cage. It is usually said that the more stable structure the less curvature. The reason for that is twofold. First, the strain induced on the σ-skeleton is reduced because of the deviation from the ideal planar trigonal sp^2 geometry; and second, less curved structures maximize the parallel overlap between adjacent π-orbitals by enhancing the π-electron delocalization, which contributes to the overall molecule stabilization. Introducing pentagonal rings in an hexagonal network intrinsically induces curvature to the molecule because of geometrical restrictions (see figure 1.1).

In 1987, Harry Kroto proposed the Isolated Pentagon Rule (IPR)[10] as a simple criterion to relate the stability of fullerene isomeric carbon cages and the disposition of their 12 pentagonal rings when different isomers are compared. The IPR rule states that most stable fullerene isomers are those where the 12 pentagons are isolated on the fullerene surface, *i.e.* when pentagonal rings are only surrounded by five hexagonal rings as represented in figure 1.1.

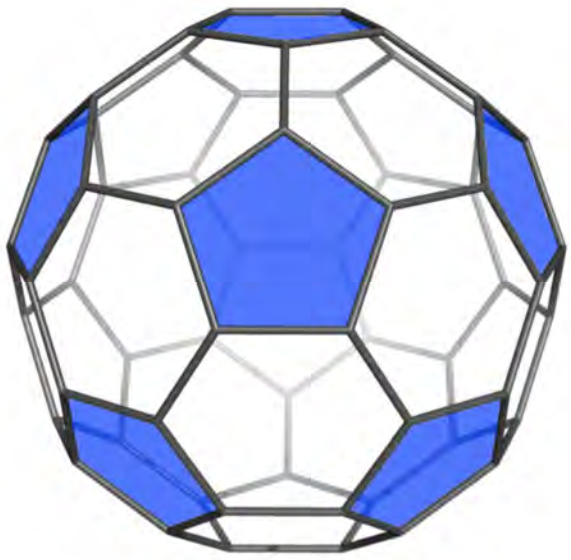

Figure 1.1: Isolated pentagons on buckminsterfullerene structure

When two pentagonal rings occupy adjacent positions on a spherical fullerene structure, a high steric tension is produced because of the geometrical restric-

tions, in addition to the destabilizing effect on the π structure of the molecule. According to the Hückel $4n + 2$ rule, π-electron stabilization is greatest for six-membered rings (6MRs), somewhat less for sizes 5 and 7, and dramatically less for sizes 4 and 8. Smaller rings (3 atoms) are unstable because of the σ-strain. In the case of having fused five-membered rings (5MRs), an eight-carbon cycle around the periphery of these pentalene units is formed, and it has a destabilizing effect on the π-electron structure.[8] Thus, the IPR rule indicates that the final stability of fullerenes is given by an equilibrium between the steric tension and π electronic structure.

It has been demonstrated that, for a given fullerene C_n, the larger the number of adjacent pentagon pairs (APPs), the less stable the fullerene. The energy rises linearly with the number of pentagon adjacencies. This property is called the pentagon adjacency penalty rule (PAPR), and the energetic cost of a pentagon adjacency was found to be about $17 - 36$ kcal·mol^{-1} per pentagon fusion.[11–13]

The IPR rule significantly reduces the total number of isomers to be considered for a given fullerene C_n. As shown in figure 1.2, for C_{60} and C_{70} there only exists one isomer that satisfies the IPR rule. Although the number of IPR isomers increases when the fullerene size goes up, it is much lower than the total number of non-IPR structures that can be generated. Therefore, the IPR rule was found to be an easy and rational way to justify the abundancies experimentally detected for C_{60} and C_{70} fullerenes, which are the smallest fullerenes that fulfill the IPR rule (no possible IPR isomers can be generated for C_{62}-C_{68} fullerenes). Nevertheless, as it will be shown later, the IPR rule is not always fulfilled.

1.3.2 C-C bonds in fullerenes

Because of the nature of fullerene structure, formed by pentagonal and hexagonal rings, different C-C bond types can be found. [6,6] bonds are those situated between 2 hexagonal rings, and [5,6] between an hexagonal and a pentagonal ring. For non-IPR isomers, there also exist [5,5] bonds, which are situated between two pentagonal rings in a pentalene motif. Moreover, for each bond type different environments can be found, allowing their classification into different subtypes. For the [6,6] bonds, there exist the pyracylenic or type A bonds, type B bonds, and pyrenic or type C bonds, as shown in figure 1.3.

Type A corresponds to a [6,6] C-C bond situated between two pentagonal rings and two hexagonal rings which confer high curvature to the pyracylene

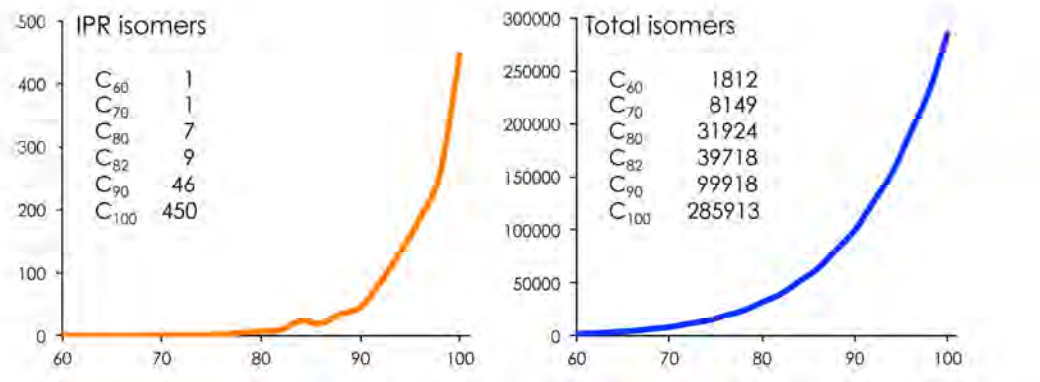

Figure 1.2: Number of C_n fullerene isomers and IPR isomers generated by the spiral algorithm in the range n=60-100, considering enantiomers as equivalent.

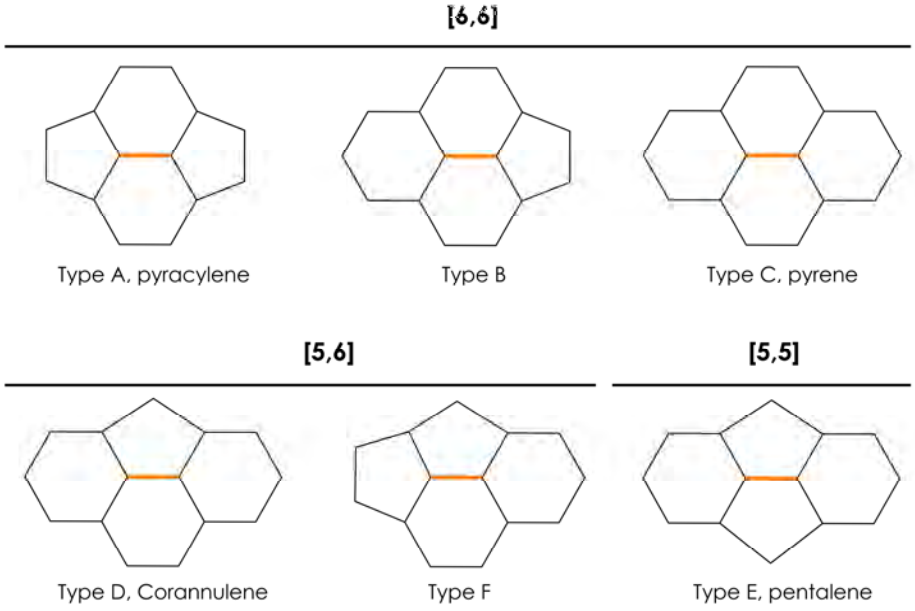

Figure 1.3: Representation of the different bond types that might be found in a fullerene structure.

motif. They are usually the shortest bonds on fullerene structures, and have strong double bond character. Type B bonds are the ones placed between three hexagonal rings and a pentagon. And type C, which are those completely surrounded by hexagonal rings being the more planar region of the fullerene structure.

[5,6] bonds can also be classified in two different subtypes: corannulene or type D, and type F bonds. Type F bonds can only be found in non-IPR fullerene structures. Finally, [5,5] bond types are typically classified as pentalene or type E bonds. Although it is possible to have different enviroments for [5,5] bonds, for example, when having three-fused pentagons, they have not been considered as a usual fullerene bonds. As type F, type E (pentalene) bonds have two pentagons abutted, and can only be found in structures that do not obey the IPR rule.

1.3.3 Electronic structure of fullerenes

The electronic structure of C_{60} results in a HOMO orbital that has bonding π interactions in the [6,6] bonds, and antibonding π interactions in the [5,6] ones. Thus, due to the shape of this HOMO orbital, [6,6] bond distances are shortened and [5,6] bonds are elongated. This fact produces a C-C bond distance alternation that does not allow a fully delocalization of the π electron between different bonds, and thus going against its aromatic character. The LUMO and LUMO+1 represent an inverse situation, so populating these orbitals causes an increase of the [6,6] bond distance, and a decrease of the [5,6], which in principle should favor the aromatic character of the molecule because all different types for C-C bond would have similar bond distances. These particularities can be extended to all fullerene compounds family.

1.3.4 Aromaticity in fullerenes

The possibility of C_{60} being a superaromatic molecule was originally proposed because of the presence of hexagonal rings in its structure.[1,14] The later was based on the large number of possible Kekulé structures that can be depicted for buckminsterfullerene.[14] Thus, the aromatic character of fullerenes, and C_{60} in particular, has been controversial since their discovery. As mentioned earlier, fullerenes present C-C bond length alternation, which is a clear difference from the prototypical aromatic molecule benzene, indicating a non-homogeneus π delocalization. Moreover, the curvature and pyramidalization of fullerene carbon atoms due to the strain, and the large variety of chemical transformations

of fullerenes go against their aromatic character.[15] However, magnetic and NMR properties indicate that fullerenes cyclic delocalization of π-electrons is the one as expected for aromatic molecules.[16–18] Consequently, it is now accepted that pristine fullerenes have ambiguous aromatic character, showing only a modest degree of aromaticity,[19–21] with some properties that are typical of aromatic compounds and others that are not, as it will be discussed in chapter 7.6.

Aromaticity is not an observable, and this precludes an unambiguous quantitative definition.[22] As a consequence, many different indirect measures have been proposed based on the different characteristics of aromaticity. There exist structural-, magnetic-, energetic-, electronic- and reactivity-based measures of aromaticity.

From the experimental point of view, aromaticity of fullerenes has been assessed using magnetic measures by determining the chemical shifts of encapsulated atoms and molecules such are ^{3}He,[23–26] ^{129}Xe,[27,28] and $^{1}H_2$,[29,30] by measuring ^{1}H-NMR of different substituents attached to the fullerene structure,[31] or by measuring magnetic susceptibilities.[32–34]

There exist different computational strategies and indicators that have been applied to measure the aromaticity of fullerenes. Magnetic-based descriptors of aromaticity such as the nucleus-independent chemical shifts (NICS),[35,36] ^{3}He and ^{129}Xe chemical shifts,[37–40] ring currents,[16,41–43] and magnetic susceptibilities[32,33,44,45] have been employed to assess the local and global aromaticity of fullerenes. For this purpose, the harmonic model oscillator of aromaticity (HOMA), which is a structural-based descriptor, has been also calculated.[39,46,47] Indices such as the aromatic stabilization energies (ASE),[39] homodesmotic stabilization energies (HSE),[48] and topological resonance energies (TRE)[49,50] based on energetic grounds have been also used for evaluating the global aromaticity of fullerenes. Finally, indicators based on electronic delocalization properties like multicentre index (MCI),[51] the para-delocalization index (PDI)[47,52,53] and the aromatic fluctuation index (FLU)[53] have been also computed to quantify the local aromaticity in fullerenes.

Aromaticity of fullerenes can be analyzed in terms of global and spherical aromaticity, considering the entire structure, or local aromaticity and homoaromaticity, when isolated rings that form the fullerene or fullerene derivative structures are considered. In the following subsections the spherical aromaticity and local aromaticity when applied on fullerenes are introduced.

Spherical aromaticity

Hückel's rule[54–57] of aromaticity indicates that a cyclic conjugated planar molecule of D_{nh} symmetry with $n = 4N + 2$ π-electrons is aromatic whereas antiaromatic when having $4N$ π-electrons. The aromaticity of these $4N + 2$ species is achieved when a closed-shell electronic structure is fulfilled. This situation provides extra energetic stability, similar to the situation found in noble gas elements.

The Baird rule[58–60] represents an extension of the Hückel rule for open-shell systems. According to Baird's rule the lowest-lying triplet state in the $4N$ π-annulenes with D_{nh} symmetry with $n = 4N$ is aromatic, and antiaromatic when it has $4N + 2$ π electrons. The extra stability of the $4N$ π electron Baird species is due to the half-filled degenerate highest-occupied with same spin electrons molecular orbitals.

In 2000, Hirsch and co-workers[61] proposed a rule for predicting the aromaticity of spherical systems, known as the $2(N + 1)^2$ rule. They considered that the π-electron system of an spherical system, such are fullerenes, can be approximated by a spherical electron gas surrounding the surface of an ideal sphere. The wave functions of this electron gas are characterized by the angular momentum quantum number l ($l = 0, 1, 2, 3...$), equivalent to the atomic orbitals scenario, and being each energy level $2l + 1$ times degenerated. As a consequence, all π shells are totally filled when there are $2(N + 1)^2$ electrons. Therefore, following this rule, spherical species with $2(N + 1)^2$ π-electrons are aromatic in an analogous way to $4N + 2$ π-annulenes.

According to Hirsch's rule, icosahedral C_{20}^{2+}, C_{60}^{10+} or C_{80}^{8+} are aromatic. This prediction was later confirmed by using NICS and MCI indicators of aromaticity.[62,63] In addition, the spherical aromaticity of the C_{60}^{10+} cation and the practical non-aromaticity of C_{60} was proved by the explicit study of the magnetically induced sphere currents by Johansson *et al.*.[64] Nevertheless, Schleyer, Hirsch, and co-workers[65] demonstrated that the $2(N + 1)^2$ rule breaks down when the energies of subshells with different angular quantum numbers intercalated. This happens for relatively large values of N. For example, they found that C_{60}^{12-} is not magnetically aromatic, as opposite to the $2(N + 1)^2$ rule prediction.

In 2011, following the same philosophy that Baird used to extend the Hückel rule to open-shell systems, Poater and Solà[51] extended the Hirsch rule to spherical open-shell systems. They proposed that, spherical compounds with

a half-filled last energy level, that is, those having $2N^2+2N+1$ electrons and spin $(N+1/2)$, should be aromatic. They showed that, for example, C_{60}^{19+} $(S=9/2)$ or C_{60}^{1-} $(S=11/2)$ are aromatic. Nevertheless, it is important to mention that, neither the $S=9/2$ electronic state for C_{60}^{19+} nor the $S=11/2$ for C_{60}^{1-} are their electronic ground states.

Local aromaticity

The local aromatic character of fullerenes can be quantified by analyzing the aromaticity of their hexagonal and pentagonal rings.

The local aromaticity of fullerenes has been computationally assessed by using different measures, such are the structural HOMA index,[46] the magnetic NICS measure,[21,47,66–68] or electronic PDI, MCI or FLU indexes.[47,51] All of them pointed out that for fullerenes in general, 6MRs present relatively weak aromaticity than that of benzene, and 5MRs have nonaromatic or slightly antiaromatic character, thus being 6MRs more aromatic than 5MRs.

This result is in line with strong paramagnetic currents associated with the pentagonal rings and the relatively weak diamagnetic currents of the hexagonal rings found in neutral, empty, and nonfunctionalized fullerenes.[16,17,41,42] Partial cancellation of these diamagnetic and paramagnetic currents results in vanishingly small magnetic susceptibilities.[33,34]

Interestingly, Van Lier and co-workers noted that the local aromatic character of a given 6MR in fullerenes and nanotubes increases the farther away the 5MRs are from this 6MR.[68]

Homoaromaticity

Homoaromaticity was first introduced by Prof. Saul Winstein (UCLA),[69] when he was studing the *tris-homocyclopropenyl* cation. He suggested that although the continuous π congugation in a ring is disrupted by the presence of a single sp^3 hybridized carbon atom, this discontinuity is bridged by the p-orbital overlap, as shown in figure 1.4b, to keep a continuous delocalization of π electrons that confers an extra stability to the system.

In some cases, addition to a certain C-C bond of a fullerene led to the breaking of the attacked C-C bond and the formation of adducts called fulleroids, with an open bond on the surface of the cage.[70] Sometimes, these open-cage fulleroids can be more stable than their closed bond counterparts (see figure 1.4).[70–72] They are considered π-homoaromatic species[72–74] and in these

adducts the 60 π-electron systems remain more or less intact, because all carbon atoms keep their sp^2 hybridization (see figure 1.4). Confirmation of this homo-conjugation comes from the similarity of the endohedral chemical shifts and UV spectra to that of the parent fullerenes,[75–77] significant π overlap values in Hückel MO theory[70] and from computational NICS and PDI values.[78]

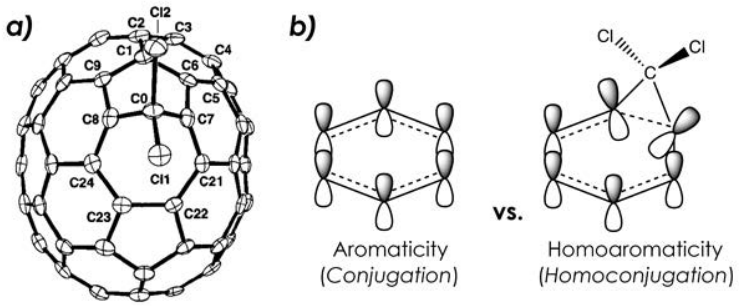

Figure 1.4: a) X-ray of the $C_{71}Cl_2$ fulleroid structure (reprinted with permission from ref.[70]) b) schematic representation of aromaticity vs homoaromaticity (from ref.[74]).

1.4 Endohedral fullerenes

When Kroto, Smalley, Curl and co-workers reported the discovery of the buckminsterfullerene in 1985, they already hypothesized about the fact that the diameter of this molecule was large enough to hold a variety of atoms inside the carbon cage.[1] The term *endohedral* has been adopted as a general specification to denote fullerenes encapsulating atoms, ions, or small molecules. This term comes from the Greek words *endon* (within) and *hedra* (face of a geometrical figure), and was introduced in 1991 independently by Cioslowski,[79] and Schwarz and Krätschmer.[80]

The first proof of the existence of this type of endohedral fullerenes was presented by Heath *et al.*[81] the same year of the discovery of the C_{60}. They found evidences of the formation of a stable $C_{60}La$ molecule, where the lanthanum atom was trapped inside the C_{60} cage, thus having the first synthesized endohedral metallofullerene (EMF) $La@C_{60}$.

Fullerenes can encapsulate a large variety of compounds (see figure 1.5), from atoms (such noble gases,[82] or reactive species such nitrogen[83–85] or phosphorus[86] atoms), ions (Li^+,[87] for example), metallic clusters (such is Sc_3N[88]) and

small molecules (such H_2,[89] N_2,[90] or H_2O[91]). But endohedral *metallo*fullerenes are those which have attracted much more attention (see next section).

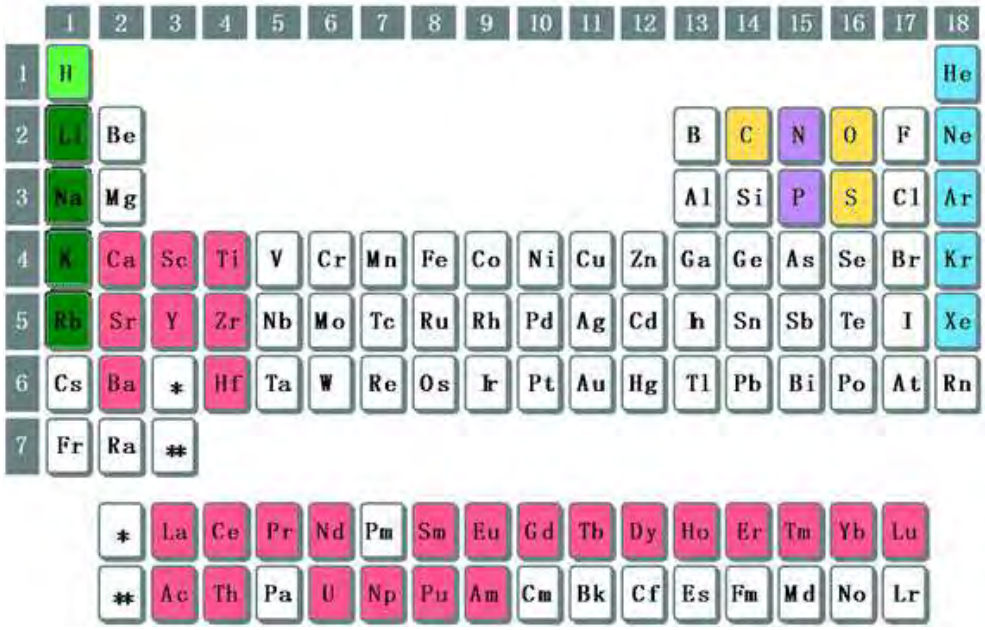

Figure 1.5: Periodic table showing elements that can be encapsulated inside fullerenes forming identificable endofullerenes (from ref.[92]).

To describe encapsulated species inside a fullerene, a special symbolism and nomenclature was introduced by Smalley and co-workers.[93] The symbol @ is used to indicate that the atoms listed to the left are somehow inside the cage, and the fullerene skeleton appears to the right of the @ symbol.

Since the discovery of the macroscopic production of fullerenes in 1990,[6] many metals and metallic clusters were encapsulated inside, however, the yields of the synthesized EMFs were rather low, on the order of 1% of the empty fullerenes. But the knowledge acquired during the last 15 years on the production of endohedral fullerenes and EMFs has enabled the development of new, more efficient techniques to synthesize these fascinating compounds (see section 1.4.2).

1.4.1 Classification of endohedral fullerenes

Endohedral fullerenes can be classified into two principal groups: (*i*) endohedral metallofullerenes (EMFs), those containing isolated metalic ions or metallic clusters; and (*ii*) nonmetallic endohedral fullerenes, which only contains

nonmetallic atoms or molecules.

In turn, EMFs can be divided into several classes:[94,95] (*a*) the so-called classical EMFs of the type $M@C_n$ and $M_2@C_n$; (*b*) trimetallic nitride templates (TNT) EMFs ($M_3N@C_n$); (*c*) metallic carbide EMFs ($M_2C_2@C_n$, $M_3C_2@C_n$, $M_4C_2@C_n$, $M_3CH@C_n$, and $M_3CN@C_n$); (*d*) metallic oxide EMFs ($M_4O_2@C_n$ and $M_4O_3@C_n$); and (*e*) metallic sulfide ($M_2S@C_n$) (see figure 1.6).

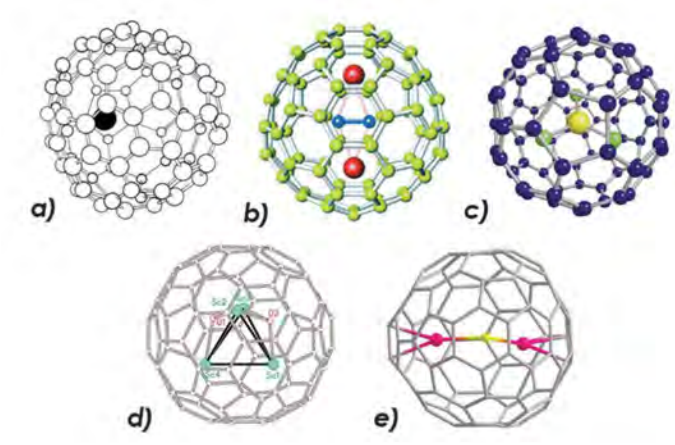

Figure 1.6: Examples of different EMFs: (a) classical ($La@C_{82}$), (b) metallic carbide ($Sc_2C_2@C_{84}$), (c) TNT ($Sc_3N@C_{80}$), (d) metallic oxide (Sc_4-(μ_3-O)$_2@I_h$-C_{80}), (e) metallic sulfide ($Sc_2S@C_{3v}(8)$-C_{82}) (from ref.[74])

1.4.2 Synthesis and characterization

Only days after the discovery of C_{60}, Kroto and co-workers synthesized the first endohedral metallofullerenes, $La@C_{60}$ and $La_2@C_{60}$, by vaporization of graphite rods impregnated with $LaCl_2$.[81] The mass spectrum of the resultant sample showed two peaks corresponding to the mentioned EMFs. Further work by Smalley and co-workers using a modified vaporization strategy allowed them to synthesize $La@C_{70}$, $La@C_{74}$, and $La@C_{82}$,[93] being the later the most abundant classical EMF. However, the large-scale production of EMFs was not achieved until 1990 when Krätschmer *et al.*[6] developed a method to successfully synthesize macroscopic quantities of C_{60} by resistive heating of graphite rods in a helium atmosphere.

Although there exist many methods for the production of EMFs, the most common one for the production of EMFs nowadays is the modified arc-discharged

Krätschmer-Huffman reactor, represented in figure 1.7. Using this strategy, graphite rods are packed with the desired metal oxide, or a combination of metal oxides to get mixed EMFs, and then the packed rods are annealed over several hours before finally being burned in the presence of He or Ar.[94,96–99]

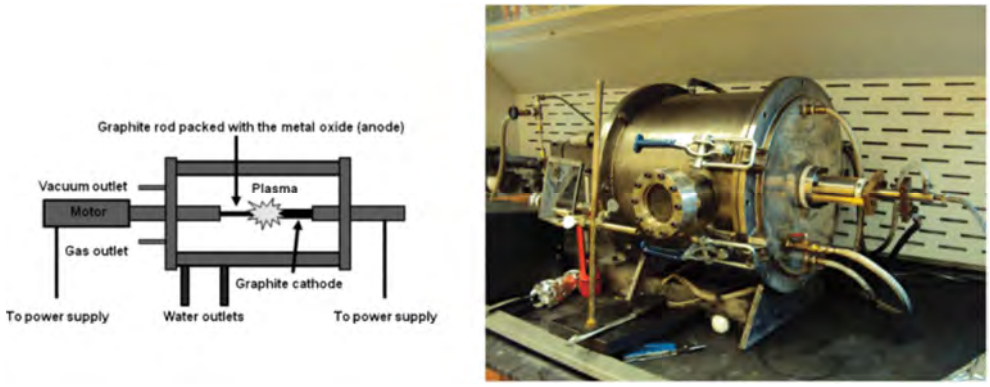

Figure 1.7: Left: Schematic representation of an arc-discharge reactor for the production of endohedral metallofullerenes (from ref.[94]). Right: Krätschmer-Huffman electric arc reactor from Echegoyen's Lab (taken from ref.[95])

For synthesizing trimetallic nitride templates, a nitrogen source is added. In 1999, Stevenson and Dorn[88] prepared the first TNT EMF, $Sc_3N@C_{80}$, by packing the graphite rods with Sc_2O_3 and using N_2 as the nitrogen source. This particular strategy is commonly known as the *trimetallic nitride template* method. Few years later, the TNT method was improved by Dunsch and co-workers, who developed the *reactive gas atmosphere* method.[100] In this method, the rods are packed as in the TNT method but ammonia gas is used as a source of nitrogen. Under this conditions, EMFs were produced as the dominant products in the soot extracts, and only a very low yield of empty fullerenes and non-EMFs were obtained. This was the first synthesis proposed where EMFs were preferentially produced as the major products.

Endohedral metallofullerenes containing a metal oxide cluster (Sc_2O, Sc_4O_2, Sc_4O_3),[101–103] and a metal sulfide cluster (Sc_2S, Ti_2S),[104–106] can all be synthesized by introducing the corresponding heterogeneous additives into the arc-discharged Krätschmer-Huffman reactor. For the formation of carbide metallofullerenes, it is not necessary to introduce any hetero element into the reactor chamber.[92]

The characterization of endohedral metallofullerenes has been hindered since

early 1990s by two principal causes. First, the low yields obtained when a new EMF is synthesized, and the non-efficient separation techniques to provide isomerically pure EMF samples. Second, the use of standard structural characterization tools has serious limitations due to the special properties of EMFs.[107]

EMF characterization by single-crystal X-ray diffraction was severely hampered by the low availability of EMFs single crystals, but also because of the rotational disorder of the fullerene molecule in their crystals. As an alternative to this technique, Shinohara and co-workers introduced the structural analysis of EMFs based on the powder X-ray diffraction data obtained with synchrotron irradiation combined with Rietveld/MEM analysis.[108,109] Nevertheless, this method is not as reliable as single-crystal X-ray. More recently, two different strategies have been developed to solve the problems with the single-crystal X-ray diffraction studies on EMFs. On one hand, the group of Balch proposed a method to hinder the rotation of fullerene molecules by the use of cocrystalyzing agents such as Ni- or Co-octaethylporphyrines.[110] Using this technique, a large amount of EMF structures have been elucidated.[95] On the other hand, chemical derivatization can prevent the rotation of EMF molecules in the crystals. Akasaka and co-workers have extensively used this strategy to determine by single-crystal X-ray diffaction many EMF structures analyzing their derivatives.[111]

Another common structural tool in the fullerene chemistry is the ^{13}C-NMR spectroscopy. Because of the low natural abundance of ^{13}C isotope, ^{13}C-NMR spectroscopy requires significant amounts of EMF sample, sometimes not available, to perform the measure. In addition to that, this method can only provide the symmetry of the carbon cage, remaining the structure ambiguous when several isomers of the same symmetry are possible. Due to the paramagnetic nature of some lanthanide encapsulated atoms in EMFs, which limits ^{13}C-NMR applicability, the use of bulk electrolysis of solutions of these paramagnetic EMFs, which yields their diamagnetic forms (usually monoanions) is required to perform the corresponding ^{13}C-NMR spectroscopic studies.[112]

Absortion spectra of EMFs in the visible and near-IR range are usually dominated by the π-π^* excitations of the carbon cage, being highly structure sensitive. As the case of vibrational spectroscopy, UV-vis-NIR absortion spectroscopy has been used in the structural elucidation of EMFs since it had been recognized that the spectra of EMFs with the same carbon cages and the metal atoms in the same valence state are very similar.[113] Thus, it is possible to use vibrational or absortion spectra to confirm or discard an isomeric structure of

a new synthesized EMF by comparison with the spectra of isostructural EMFs, whose structures containing other metals or clusters are already described in the literature and which are unequivocally determined by other methods.

It is worth mentioning that the elucidation of molecular structure of EMFs implies the determination of the carbon cage, but also the position of the metal or metallic cluster with respect to the carbon cage. Notwithstanding, the position of the metal atoms usually remains unclear even when a crystal structure of the EMF is avaliable, because many metal positions with close energies are possible and the interconversion between them present low barriers. Consequently, the molecular structure of EMF is determined if at least its carbon cage size and isomer is identified. As described later, the mobility and position of the inner metal atoms have a large impact on the reactivity of EMFs.

A good example of the inherent complexity of determining the correct structures of endohedral fullerenes is the special case of $Sc_3C_2@C_{80}$ metallic carbide. Sc_3C_{82} metallofullerene was synthesized by arc discharge of Sc-impregnated graphite rods in 1992.[114,115] Initially, electron paramagnetic resonance, theoretical studies and synchrotron X-ray powder diffraction studies suggested that a C_{82} cage was encapsulating three Sc ions. However, single-crystal X-ray structures of a chemically functionalized fullerene[116] and, high-resolution powder X-ray diffraction studies[117] revealed the presence of a Sc_3C_2 unit inside a I_h-C_{80} cage. Complementary DFT calculations showed that two $Sc_3C_2@I_h$-C_{80} isomers computed are 30.2 and 30.9 more stable than the initially postulated $Sc_3@C_{82}$ structure.[116]

Synthesis of nonmetal endohedral fullerenes: alternative methods

Because of the extreme conditions needed for the synthesis of endohedral fullerenes using arc-discharge and related methods, there exists a low selectivity in these hard-to-control strategies to obtain the desired EMF. Therefore, other approaches to obtain endohedral fullerenes from previously existing free fullerenes have been proposed.

One of the most interesting and versatile methods proposed up today, is the so-called *molecular surgery*. This synthetic strategy, initially proposed by Rubin in the late 1990s,[118] consists on three step procedure, as shown in figure 1.8. First, a *incision* of the fullerene to generate an opening on its surface is performed. Then, atom(s) or small molecule(s) are introduced through the new opening inside the fullerene. And finally, the fullerene surface is *sutured*

to recover the pristine carbon structure.

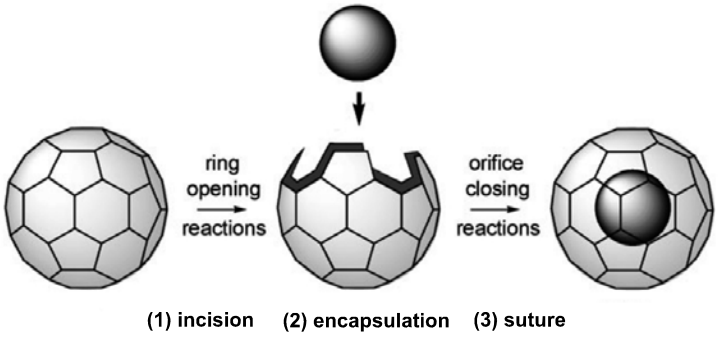

Figure 1.8: The fullerene molecular surgery approach (adapted from ref.[119])

Although *molecular surgery* represented a very challenging task during its initial stages, actually, *surgery of fullerenes*[29] is used to produce noble gases endohedral fullerenes,[120] and also fullerenes encapsulating small molecules that are not accessible by conventional methods, for example $H_2@C_{60}$[89] or $H_2O@C_{60}$.[91]

In 2003, Komatsu and co-workers were able to synthesize an open-cage C_{60} fullerene derivative having 13-membered ring orifice, which was able to incorporate a hydrogen molecule inside the hollow cavity under high pressures.[121] Few years later, they reported a four-step organic *suture* that completely closes the orifice of the open-cage fullerene to obtain $H_2@C_{60}$,[89,122] and $H_2@C_{70}$ and $(H_2)_2@C_{70}$ endohedral fullerenes.[123] Following the same strategy, they developed a new synthetic methodology to close the fullerene open-cage encapsulating a water molecule inside.[91,124] In this case, the structure of $H_2O@C_{60}$ was determined by single-crystal X-ray analysis. They have also encapsulated other small molecules inside open-cage C_{60}, such are ammonia[125] or carbon monoxide,[126] although the *suture* of these cages has not yet been possible.

1.4.3 Endohedral metallofullerenes structure: Breaking the IPR rule

Encapsulation of metal clusters in endohedral metallofullerenes takes place in cages that in most cases are far from being the most stable isomer in the corresponding hollow fullerenes. For example, the encapsulation of Sc_3N inside C_{80} takes place to form $Sc_3N@I_h(7)$-C_{80} isomer, the third most abundant fullerene after C_{60} and C_{70}.[88] The $Sc_3N@D_{5h}(6)$-C_{80} isomer is also experimentally

formed, but it is much less abundant.[127] Nevertheless, $I_h(7)$-C_{80} and $D_{5h}(6)$-C_{80} IPR isomers are the two less stable structures among the seven IPR isomers of empty C_{80} (see figure 1.9).[128] Indeed, the formation of $Sc_3N@I_h(7)$-C_{80} isomer was unexpected due to the fact that neither Sc_3N cluster nor $I_h(7)$-C_{80} isomer had been prepared individually. However, together they form an extremely stable compound, with a very special electronic structure.

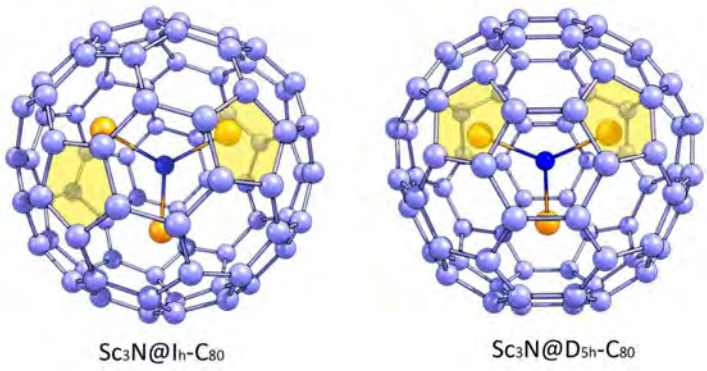

Figure 1.9: Structure of $Sc_3N@I_h(7)$-C_{80} and $Sc_3N@D_{5h}(6)$-C_{80} EMFs (from ref.[129])

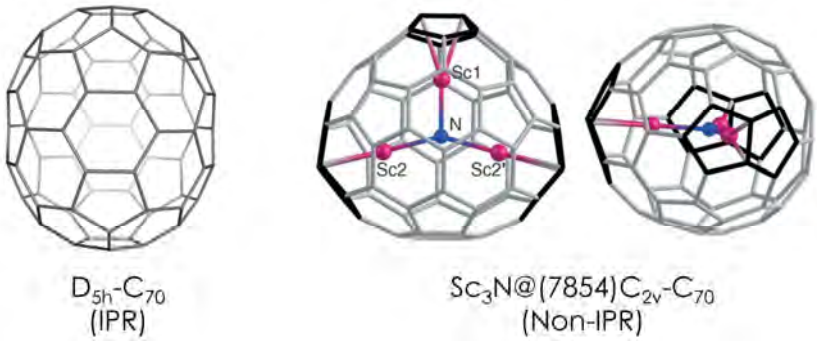

Figure 1.10: Structure of IPR pristine C_{70} fullerene and non-IPR $Sc_3N@C_{2v}(7854)$-C_{70} EMF (adapted from ref.[130]).

Usually, the encapsulation of metallic clusters to form EMFs takes place in a fullerene cage that does not fulfill the IPR rule, *i.e.* a non-IPR isomer. For example, for empty C_{70} fullerene only the IPR isomer is experimentally

formed. Nevertheless, when a Sc_3N cluster is encapsulated, the resulting endohedral metallofullerene is based on the non-IPR $C_{2v}(7854)$-C_{70} isomer cage.[130] Up to date, there have been synthesized many EMFs, whose structure is based on non-IPR isomers, such are $Sc_3N@D_3(6140)$-C_{68}, the smallest TNT synthesized,[131,132] $La_2@D_2(10611)$-C_{72},,[133,134] or $Gd_3N@C_s(39663)$-C_{82}[135] and $M_3N@C_s(51365)$-C_{82} $(M = Gd, Tm, Tb)$[136,137] whose structures are very similar and closely related. Therefore, the isolated pentagon rule cannot be applied in the case of EMFs as a general rule to rationalize and understand their stability, and additional rationalizations are needed.

1.4.4 Electronic structure of endohedral metallofullerenes: ionic model and orbital rule

The stabilization of a particular isomeric structure when EMFs are formed, is mainly attributed to the electronic interaction between the metallic cluster and the fullerene carbon structure. In 2002, the group of Prof. Poblet showed that there is a formal transfer of six electrons from the Sc_3N cluster to the $I_h(7)$-C_{80} and $D_{3h}(5)$-C_{78} fullerene cages when the TNT unit is encapsulated.[138]
They observed that in pristine $I_h(7)$-C_{80} and $D_{3h}(5)$-C_{78} cages there are π unocuppied orbitals lower in energy than the three highest occupied molecular orbitals (HOMOs) of the trimetallic unit. Thus, when the EMF is formed and the orbital mixing takes place, LUMO unoccupied orbitals of the fullerene structure can accommodate the six electrons that come from the TNT HOMO orbitals, as shown in figure 1.11. As a consequence, they concluded that formally six electrons are transferred from the nitride unit to the fullerene and the electronic structure of these EMFs can be described using an ionic model, and represented as $[Sc_3N]^{6+}@[I_h(7)\text{-}C_{80}]^{6-}$ and $[Sc_3N]^{6+}@[D_{3h}(5)\text{-}C_{78}]^{6-}$, respectively. Experimental proofs of this interaction were provided by EPR studies[139] and X-ray absortion spectroscopy,[140] which conclusively determined that there is indeed an electron transfer from the cluster to the EMF cage.

Poblet and co-workers demonstrated that the ability of a given fullerene isomer cage for encapsulating TNT moieties is based on the electronic structure of the free fullerene structure.[141] Sc_3N, and TNT-based EMFs in general, may be formally described by the ionic model as $[Sc_3N]^{6+}@[C_{80}]^{6-}$, in which 6 electrons are formally transferred from the three highest occupied TNT orbitals to three low-lying unoccupied cage orbitals. The stabilization afforded by the transfer of these electrons correlates with the fact that neither the trimetallic nitride clusters nor the encapsulating fullerene isomers can be isolated as neutral species by themselves. The resulting endohedral complex has a relatively

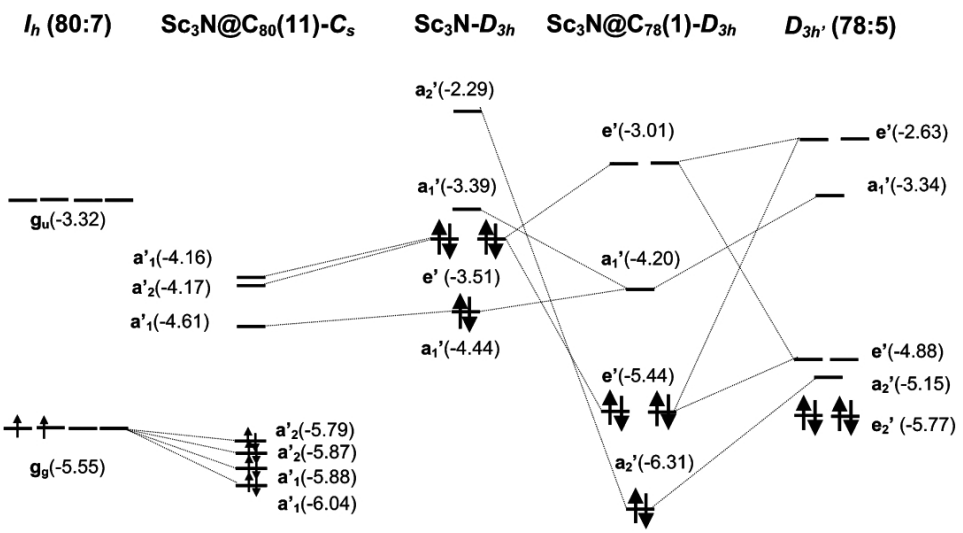

Figure 1.11: Orbital interaction diagram (energies in eV) for $Sc_3N@D_{3h}(5)$-C_{78} and $Sc_3N@I_h(7)$-C_{80}. Only the most important orbitals that participate in the bonding have been drawn (from ref.[138])

large HOMO-LUMO gap, which is an indication of its stability. This was the case of $Sc_3N@C_n$ $(n = 68, 78, 80)$ complexes studied. They showed that the final HOMO-LUMO gap of these TNT-based EMFs can be estimated from the (LUMO+3)-(LUMO+4) gap found in the free cages, which corresponds to the hypothetical anion when six additional electrons are added to the free cage C_n^{6-}.[141] Thus, as shown in figure 1.12, only those fullerene IPR isomers that exhibit (LUMO+3)-(LUMO+4) gaps larger than 1 eV would be able to encapsulate TNT metallic clusters. C_{60} is excluded because its inner cavity is too small to encapsulate a four atom moiety. Furthemore, non-IPR $D_3(6140)$-C_{68} isomer was predicted to obey the (LUMO+3)-(LUMO+4) orbital rule, and it was predicted that no other IPR fullerene cages between C_{60} and C_{84} would be suitable for encapsulating a TNT cluster.

Experiments support the orbital rule too.[142] The good correlations found between the measured electrochemical gaps for several EMFs and the orbital gaps calculated for the corresponding free carbon cages, provided direct experimental evidences to the six electron transfer in TNT-based EMFs.[142]

A few years later, Popov and Dunsch[143] showed that there exists a direct correlation between the stability of nitride clusterfullerenes and the stability of the empty 6-fold negatively charged fullerene isomers for $M_3N@C_n$ $(n = 68 - 98)$.

As a consequence, this study provided the proof of the usefulness of the ionic model for the study of endohedral metallofullerene stabilities: one can use the empty cage anions to reproduce the stability of entire EMFs.

The ionic model was also applied to understand the stability of metallic carbide (M_2C_2 where $M = Sc, Y$) EMFs, and all those EMFs in which the inner cluster formally transfers four electrons to the carbon structure. Poblet and co-workers[144] showed that empty cages with a large (LUMO-3)-(LUMO-2) gap are those more suitable for encapsulating the M_2C_2 moiety because of the stabilization obtained by the formal transfer of four electrons from the cluster to the LUMO-1 and LUMO-2 of the carbon cage. Thus, a carbide-containing endohedral fullerene can be seen as $[M_2C_2]^{4+}@[C_n]^{4-}$, where the C_2 unit is considered as an acetylide ion, C_2^{2-}. But not all metallic carbides transfer four electrons. In Ti_2C_2 cluster, each titanium atom transfers one extra electron to the carbon cage than scandium atoms, that is a total of six electrons for the entire Ti_2C_2 moiety. In this case, the (LUMO-4)-(LUMO-3) gap instead of the (LUMO-3)-(LUMO-2) one should be considered.

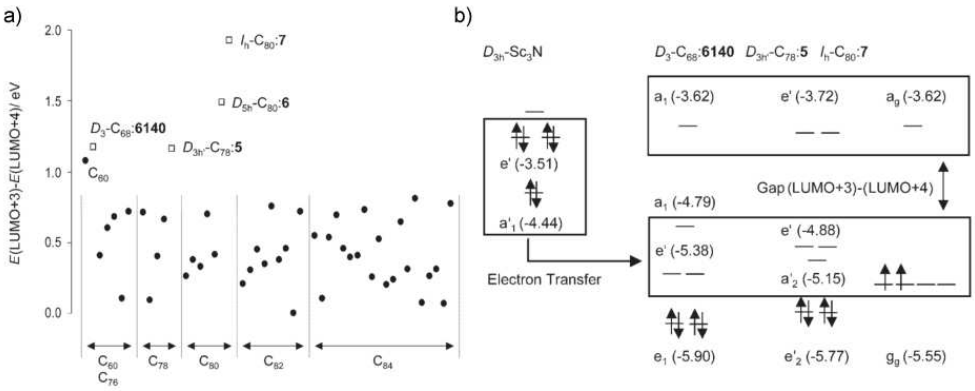

Figure 1.12: a) The (LUMO+3)-(LUMO+4) gap for all IPR isomers from C_{60} to C_{84} and also the non-IPR $D_3(6140)$-C_{68}. Only isomers with the gap larger than 1 eV have been capable of encapsulating TNT units; b) Representation of the ionic bond between the trimetallic nitride template (TNT) and the fullerene cages $D_3(6140)$-C_{68}, $D_{3h}(5)$-C_{78}, and $I_h(7)$-C_{80}. There is a formal transfer of six electrons from the three highest occupied orbitals of the TNT unit to the three lowest unoccupied orbitals of the fullerene cages. Consequently, the $M_3N@C_n$ ($n = 68$, 78, and 80) complexes are described as $Sc_3N^{6+}@C_n^{6-}$ with a relatively large HOMO-LUMO gap nearly equal to the (LUMO+3)-(LUMO+4) found in the free cages (adapted from ref.[141]).

Therefore, the orbital rule, in combination with the ionic model, give a simple but accurate description of the electronic structure of endohedral metallofullerenes.

1.4.5 The importance of pentagon distribution

As mentioned earlier, the IPR rule is no longer fulfilled for EMFs. Instead, several studies have pointed to pentagonal rings and their distribution along the fullerene structure to be a key factor on the final stability of endohedral metallofullerenes.

In a study of the relative stabilities of different non-IPR isomers of positively and negatively charged C_{60} and C_{70} fullerenes, Zettergren *et al.*[13] established that non-IPR isomers having a uniform and well-separated distribution of adjacent pentagon pairs (APPs), in negatively charged, and pyrene motifs formed by four adjacent hexagonal rings, positively charged, can be more stable than IPR isomers. The negative charge is mainly accumulated on APPs in the anionic case, and the positive charge is concentrated on pyrenes in the cations. Therefore, they considered that those isomers minimizing the Coulomb repulsion between the charges of equal sign are those more stable.

The maximum pentagon separation rule

In 2010, Rodríguez-Fortea *et al.*, using anionic empty fullerene cages as models for EMFs systems, showed that the stability of a particular fullerene anionic isomer is related to the separation among pentagons, which can be measured with the inverse pentagon separation index (IPSI) computed by:[95,145]

$$IPSI = \sum_{i=1}^{12} \sum_{j>i}^{12} 1/R_{ij} \tag{1.11}$$

where R_{ij} is the Euclidean distance between the centroids of pentagon i and j.

The largest pyramidalization of the atoms participating in [5,6] carbon-carbon bonds induces a higher concentration of the negative charge on the pentagons. The $IPSI$ value is defined as the sum of the inverse Euclidean distance between the centroids of all possible pairs of pentagons. Consequently, isomers with largest separation among pentagons (smallest $IPSI$ values) should reduce the Coulombic repulsion and become more stable.[95,145] For example, the stability of the 35 IPR hexaanions of C_{88} fullerene, computed at the AM1 level

of theory, correlates with isomers $IPSI$ values, as presented in figure 1.13. This revealed that there exists a correlation between the separation among the pentagons and the stability of the isomers. In addition, they also found that most stable isomers are those where the negative charge centred on pentagonal rings is maximized. The IPR C_{88} isomer 35, which is the IPR isomer with a lowest IPSI value and the largest concentration of negative charge on the pentagons, has been identified by X-ray crystallography as the cage that encapsulates Tb_3N and Gd_3N.[146] Therefore, the negatively charged fullerene isomers possessing favorable disposition of pentagons, *i.e.* lowest IPSI values, not only minimizes the steric strain and the Coulomb repulsion, but also maximizes the negative charge centred on pentagonal rings. All these factors stabilize the negatively charged fullerene structures, which are a model representation for endohedral metallofullerenes.

The maximum pentagon separation rule is less likely to be obeyed when the charge transferred from the metal to the cage is small or when the cage size is large. It is worth mentioning that using the maximum pentagon separation rule and the $IPSI$ index, one cannot directly compare the relative stability of isomers with different number of APPs. Therefore, it cannot be explained why the IPR rule is no longer fulfilled when EMFs are formed.

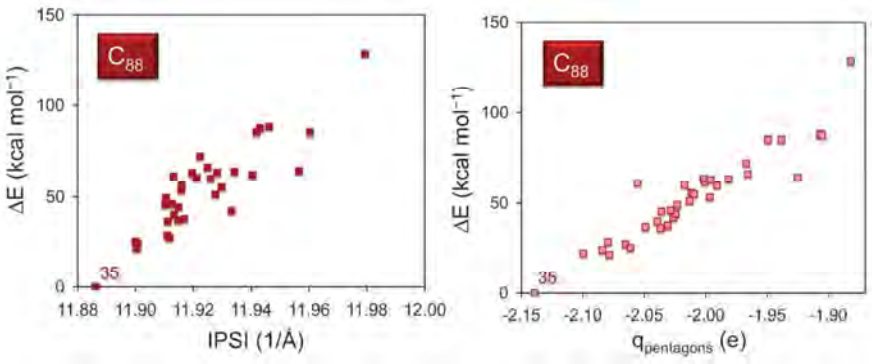

Figure 1.13: Representation of: (a) the relative stability of the 35 IPR isomers of C_{88} in their hexaanion form with respect to the Inverse Pentagon Separation Index (IPSI); and (b) charge localized on the pentagons. The most stable IPR isomer 35 encapsulating the Tb_3N and Gd_3N guests has been characterized by X-ray crystallography (adapted from ref.[95]).

1.5 Potential applications

Fullerenes and endohedral metallofullerenes are promising materials with a large number of interesting potential applications related to material sciences, photovoltaics or biomedicine, among many others. In the following lines, a few of these potential applications are described

The low toxicity of fullerene and endohedral metallofullerene derivatives makes fullerene-based drugs potentially feasible for medical applications.[147,148] In recent years, a great concern has arisen about fullerene toxicological effects.[149] For example, the inhibitory effect on bacterial growth due to the presence of fullerene nanoparticles was reported,[150] and mortality of *D. magna*, a planktonic crustaceans, has been described in presence of fullerene nanoparticles obtained by tetrahydrofuran (THF) dispersion in water, being a concentration-dependent effect.[151] Experiments on human dermal fibroblast, human liver carciroma cell (HepG2), and neuronal human astrocytes performed with pristine C_{60}, as nanoparticles, demonstrate toxicity at high concentrations due to lipid peroxidation, while mitochondrial activity is unaffected.[152] Nevertheless, the different toxicity observed and revealed in many studies could be associated to the different methodologies in the preparation of fullerene nanoparticles.[149] The negative effect has been imputed to the presence of THF into the preparation.[153] As a consequence, it is not surprising to find discordant results in the literature. There is still a lot of work to be done in further studies and analyses to discover, rationalize, and explain the activities and the behaviors of fullerenes in cells, animals, and human beings.[149]

In the case of EMFs, the internal metal or metallic cluster is effectively isolated from its surrounding enviroment, giving the EMF a distinct advantage of high stability and low toxicity over the metal chelate complexes commonly used in radio-medicine and diagnostic radiology.[107]

Biomedical applications of fullerenes and EMFs cover a wide range of possibilities. For example, gadolinium-based EMFs can be effectively used as a magnetic resonance imaging (MRI) contrast agents,[107,154] because Gd^{3+} ($S = 7/2$) ions have large paramagnetic character which enhance the relaxation rate of water protons. Lutetium-based EMFs have been applied as X-ray contrast agents because the large cross section of Lu atoms, which can provide directly comparable images with minimum exposure to the patient.[107,155]

Other potential application of EMFs in biomedicine is in the field of nuclear medicine with radiotracers and radiopharmaceuticals. Because of their resis-

tance to metabolism and kinetic stability, EMFs represent a unique alternative to chelating compounds since radioisotopes, such ^{140}La or ^{166}Ho, can be isolated from the biological enviroment without the possibility of release of any amount of these toxic radioactive metal ions.[156,157] In addition, the antitumoral activity of different $[Gd@C_{82}(OH)_{22}]_n$ nanoparticles has been extensively evaluated.[158]

In the photovoltaics field, fullerene and EMFs are proposed to be used as an acceptors in the polymeric solar cells, which consist in a conjugated electron-donating polymer and an electron-accepting fullerene.[159] Because of the low-cost production, printable, portable and flexible renewable energy source, these polymeric solar cells represent and extremely promising energetic alternative. Large efforts on the development of more efficient architectures have been done. The most efficient architecture up to date is the bulk heterojunction (BHJ) structure comprising a network of a conjugated polymer donor such as poly(3-hexylthiophene-2,5-diyl) and a soluble fullerene acceptor system which is typically [6,6]-phenyl-C_{61}-butyric acid methyl ester (PCBM) as the photoactive layer.[159,160]

The use of scandium or yttrium TNT-based EMFs compared C_{60} in conjugate ionic pair architectures, such is C_{60}-ferrocene, was predicted to be more promising since the TNT-based conjugate ionic pair state is significantly more stablized than in its C_{60} analogous structure; thus its application in organic photovoltaic solar cells as a covalent donor-acceptor dyad would be more efficient.[161]

Fullerenes and EMFs own a large variety of very special properties. Even more, by changing the encapsulated metal cluster, one can finely tune these properties, such are the HOMO-LUMO gaps, their paramagnetism or their nonlinear optical properties (NLOP). As a consequence, the features and possibilities that fullerenes and EMFs can offer to the society are still far to be revealed and a lot of work has still to be addressed, to explore all the capabilities of these fascinating compounds.

Exohedral Reactivity of Fullerene Compounds

1.6 The need of exohedral functionalization of fullerenes

In the previous chapter, the fascinating potential applications of fullerenes and endohedral metallofullerenes have been described. Most of them, are related with the use of fullerene or EMF derivatives for biomedical purposes as biomaterials. To that end, it is essential to prepare compounds with well-defined structures and scaffolds in order to ensure safety in the clinical use. The latter includes the enantiospecific preparation of well-defined enantiomers and diastereroisomers, as it is widely known the importance of using the correct enantiomer because their different bioactivity.[162] Chiral organofullerenes are used for instance in human immunodeficiency virus (HIV) protease inhibition where stereochemical configuration plays a crucial role,[163] also as helicity inducers in polymers,[164] or in peptide synthesis.[165] In addition to that, it is crucial to improve fullerene and EMF solubility in polar solvents, such is water, among other important biological solvents by functionalizing them. Improving the fullerene solubility is one of the most important obstacles to be overcome for the potential use of fullerenes in biologically relevant applications such as magnetic resonance imaging contrast agents.[107,154]

The use of pure enantiospecific metallofullerene derivatives in materials and electronics fields has been recently shown as a very powerful and promising new strategy, for example, to be used as charge-storage memory devices.[166]

The chemical functionalization of fullerene compounds is of utmost importance for the development of fullerene-based technology devices or biomaterials. In this thesis, we focus our attention on the reactivity of endohedral (metallo)fullerenes towards different relevant organic reactions in order to improve out current knowledge of these processes. Therefore, the most important

studies about the chemical functionalization of endohedral (metallo)fullerenes are summarized in the next sections.

1.7 Cycloaddition reactions on endohedral fullerenes

The chemical reactivity of fullerenes is typical of that of an electron deficient olefin, mostly determined by their π system. In EMFs, this π system is modified by the charge transfer from the inner metal clusters to the fullerene cage. The inhomogeneous distribution of this excess of electron density on the fullerene structure has an influence on the addition pattern and the physicochemical properties of the EMFs derivatives. The question of the regioselectivity of the chemical derivatization, due to the multiple addition sites avaliable on a fullerene cage, is one of the most challenging aspects in fullerene chemistry.[107] A large number of experimental studies on the chemical functionalization of empty fullerenes such as C_{60} and C_{70} have been already reported.[15]

Functionalization of fullerenes and endofullerenes is mainly achieved through cycloaddition reactions (see figure 1.14), being the Diels-Alder (DA) , the 1,3-dipolar or Prato, and the Bingel-Hirsch (BH) reactions, the most widely studied processes.[94,107]

Cycloadditions are included in the pericyclic major class of reactions and involve tro reactive species, one identified as an electrophilic and the other as a nucleophilic compounds. These are usually rearrangement reactions, wherein the transition state of the molecule has a cyclic geometry, and the reaction progresses in a concerted fashion.

All endohedral metallofullerene functionalizations through Diels-Alder, Prato and Bingel cycloaddition reactions studied so far are reported in table 1.2. And the major success and achievements for each of these cycloaddition reactions on EMFs are summarized in the next subsections.

1.7.1 Diels-Alder and 1,3-dipolar cycloaddition reactions on endohedral metallofullerenes

The most famous and representative cycloaddition reaction is the Diels-Alder (DA), which takes place between a conjugated *diene* and an olefin called

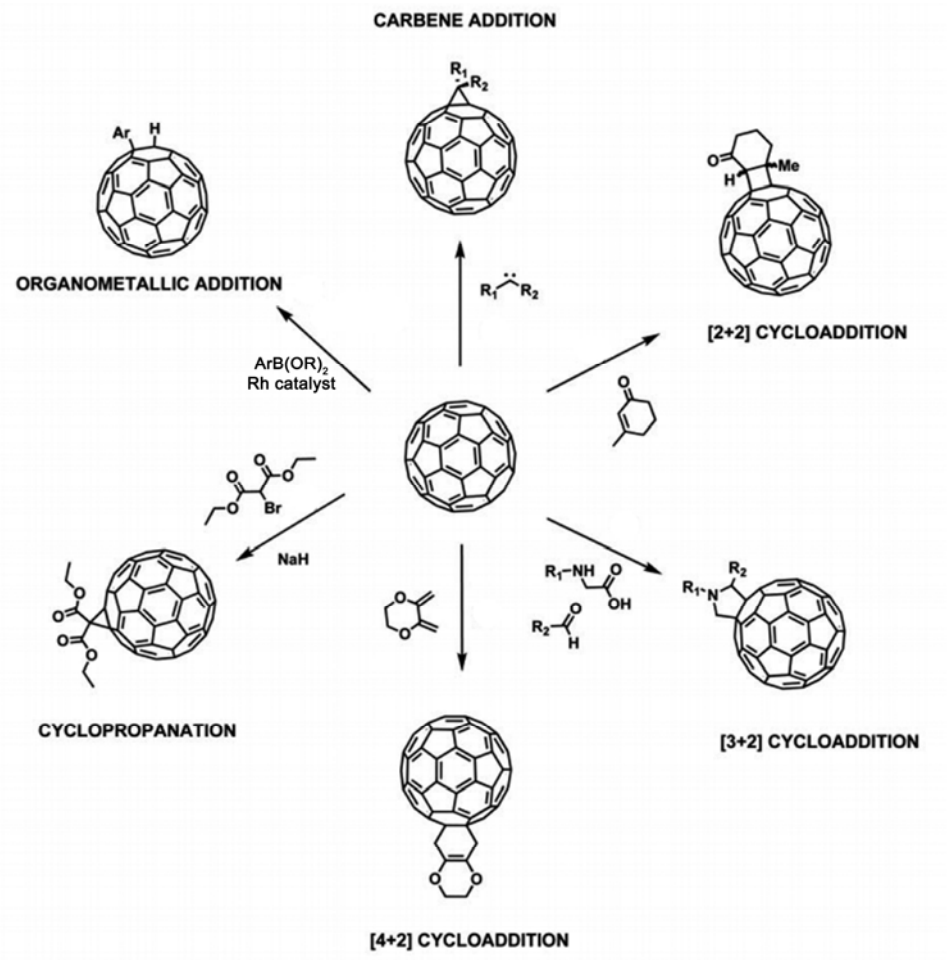

Figure 1.14: Schematic representation of principal well-stablished fullerene funtionalization methods: Carbene $[1+2]$ cycloaddition, $[2+2]$ thermal cycloaddition, $[3+2]$ 1,3-dipolar or Prato reaction, $[4+2]$ Diels-Alder cycloaddition, Bingel-Hirsch $[2+1]$ nucleophilic cyclopropanation, and organometallic addition (adapted from ref.[167])

Table 1.2: Most important chemical additions utilized to functionalize endohedral metallofullerenes (adapted from ref.[107]). When more than one isomer exists, isomeric structure of the major isomers is omitted (i.e., $I_h(7)$ for $M_3N@C_{80}$ and $M_2@C_{80}$, $C_{2v}(9)$ for $M@C_{82}$).

[3+2] 1,3 dipolar additions of azomethine ylides (Prato reaction):

$Y@C_{82}$,[168] $La@C_{72}(C_6H_3Cl_2)$,[169] $La@C_{82}$,[170–172] $La_2@C_{80}$,[172–176] $Ce_2@C_{80}$,[174] $Gd@C_{82}$,[168,177] $Sc_2C_2@C_{82}$-$C_s(6)$,[178] $Sc_2C_2@C_{82}$-$C_{2v}(9)$,[179] $Sc_3C_2@C_{80}$,[180,181] $Sc_3N@C_{78}$,[182] $Sc_3N@C_{80}$,[161,183–193] $Sc_3N@C_{80}$-$D_{5h}(6)$,[194] $Y_3N@C_{80}$,[186,192,193,195–198] $Y_xSc_{3-x}N@C_{80}$,[183] $GdSc_2N@C_{80}$,[199] $Gd_xSc_{3-x}N@C_{80}$,[185] $Gd_3N@C_{80}$,[192,193,198] $Er_3N@C_{80}$,[189,196,200] $Lu_3N@C_{80}$[192,193,201]

[1+2] Nucleophilic carbanion additions (Bingel-Hirsch reaction):

$La@C_{82}$,[202] $Sc_3N@C_{68}$,[203] $Sc_3N@C_{80}$,[204] $Sc_3N@C_{80}(CF_3)_{14}$,[205] $Y_3N@C_{80}$,[186,197,206] $Gd_3N@C_{80}$,[207] $Gd_3N@C_{84}$,[207] $Er_3N@C_{80}$,[196] $Lu_3N@C80$,[204] $Gd@C_{60}$,[208] $Sc_3N@C_{78}$[209]

[4+2] Diels-Alder reactions:

$La@C_{82}$,[210,211] $La@C_{82}$(Ad),[210] $Sc_3N@C_{80}$,[194,212] $Sc_3N@C_{80}$-$D_{5h}(6)$,[194] $Gd_3N@C_{80}$,[213] $Lu_3N@C_{80}$,[194] $Lu_3N@C80$-$D_{5h}(6)$[194]

dienophile, to form a new 6-membered ring (see figure 1.15). This reaction was described by Otto Diels and Kurt Alder in 1928,[214] and in 1950 they were awarded the Nobel Prize in Chemistry because of this work.

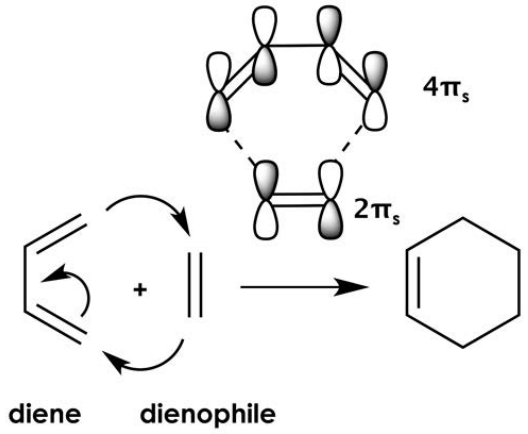

Figure 1.15: General mechanism of the Diels-Alder [4+2] cycloaddition between 1,3-*cis*-butadiene and ethylene.

The Diels-Alder reaction takes place in a single concerted step. DA mechanism can be described as a rotation of the electrons round a six-membered ring (as represented in figure 1.15), whose transition state has six delocalized electrons giving aromatic character to this transition structure. Finally, two π bonds disappear and two new σ and one π bonds are formed with four electrons moving smoothly out of the π system into the σ orbitals.

In the framework of the Woodward-Hoffmann description, the Diels-Alder reaction is often described as a $[4\pi_s+2\pi_s]$ reaction. In this notation, numbers followed by π denote the number of π electrons implied, so in this case, there are 4 π electrons from diene and 2 π electrons from dienophile implied in the reaction. The suffix '*s*' means *suprafacial*. *Suprafacial* is a topological concept that, together with '*a*' *antarafacial*, describes the relationship between two simultaneous chemical bond making and/or bond breaking processes in a reaction center. When both changes occur at the same face, the *suprafacial* interaction is produced. For the application of orbital symmetry to pericyclic reactions, K. Fukui and R. Hoffmann won the Nobel Prize in 1981 (R.B. Woodward died in 1979).

A second important example of cycloaddition reactions is the so-called 1,3-dipolar reaction. Although this type of reaction was initially described by

Smith in 1937,[215] it was not until 1961 when it was produced for the first time.[216] This cycloaddition involves a 1,3-dipole species and a dipolarophile which can range from alkenes, alkynes to fullerenes (see figure 1.16). 1,3-dipoles have four π electrons and different resonance structures, which can involve different zwitterionic structures, presenting positive and negative charge in a 1,3 relationship.There exist many different 1,3-dipoles, although the more repsentative are: nitrous oxides (N_2O), azides (N_3), imines (CR_2NR) or ylides ($CR_2N(R)CR_2$) (see figure 1.16).

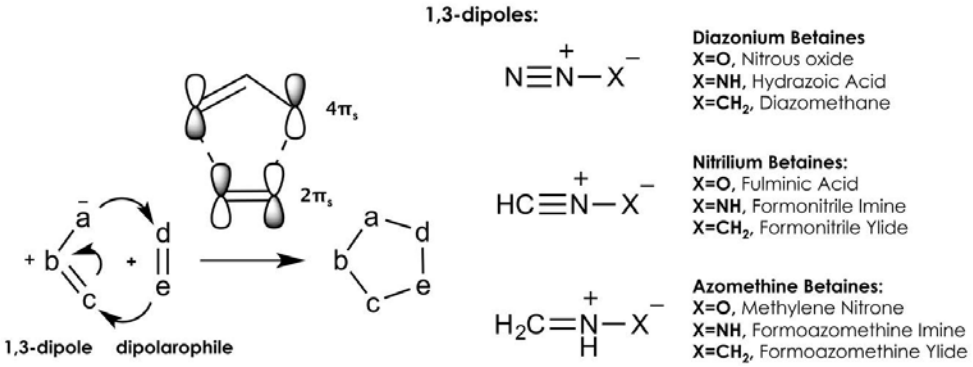

Figure 1.16: General mechanism of the 1,3-dipolar [4+2] cycloaddition, and different 1,3-dipoles.

It is important to notice here that, although previously we have classified 1,3-dipolar additions as [3 + 2] pericyclic reactions (see figure 1.14 or table 1.2), these reactions have to be formally described as a $[4\pi_s+2\pi_s]$ cycloadditions because there are four π electrons from the dipole and two π electrons from the dipolarophile involved. Nevertheless, the IUPAC recomendation is to use "[3 + 2]" label because of the number of atoms involved instead. But as it does not describe the correct picture of the reaction, and because 1,3-dipolar reactions and Diels-Alder reactions have extremelly similar behaviours, in this thesis the $[4\pi_s+2\pi_s]$ nomenclature for both 1,3-dipolar and Diels-Alder reactions will be used.

From the Diels-Alder reaction and the 1,3-dipolar cycloaddition, different stereospecific products can be obtained depending on the reaction conditions and the isomeric characteristics of the reactants. If the dienophile is unsymmetrical, there exist two possible stereochemical orientations with respect to the diene. When the reference substituent on the dienophile is oriented toward the π system of the diene the orientation is called *endo*, whereas it is named

exo when the substituent is situated away from the π system.The formation of one stereoisomer can be predicted and rationalized in terms of the Frontier Molecular Orbital (FMO) theory, described in the next chapter.

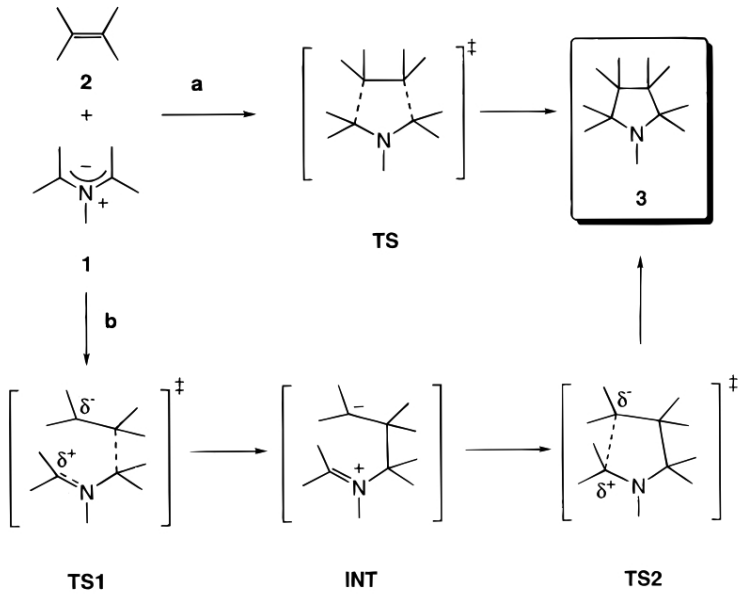

Figure 1.17: Schematic representation of the concerted *supra-supra* 1,3-dipolar mechanism proposed by Huisgen (path a);[217,218] and the 1,3-dipolar stepwise mechanism, where zwitterionic structures are the reaction intermediates, proposed few years later by Huisgen (path b).[219,220] (adapted from ref.[221])

Because of the great versatility of Diels-Alder and 1,3-dipolar reactions, there exists a big interest in understanding the mechanism of these cycloadditions.[222] Most of the actual theoretical studies consider that a concerted $[4\pi_s+2\pi_s]$ mechanism is followed, although large asyncronous transition state can be observed. The two-step process is usually less favorable as it is higher in energy than the concerted pathway for Diels-Alder scheme.[222–226] Regarding 1,3-dipolar reactions, Huisgen proposed a concerted mechanism that can be or not asynchronous, whereas Firestone suggested a two-step biradical reaction mechanism.[216–219,223,227–229] Few years later, after a vivid debate, it was accepted that in general the reaction is concerted according to the *supra-supra* mechanim proposed by Huisgen,[217,218] although in some cases the 1,3-dipolar cycloaddition occurs through a stepwise mechanism. In the latter case, the reaction intermediates are zwitterionic structures and not biradical species,[219,220] as represented in figure 1.17. Later on, Cossío and co-workers demonstrated

that when N-metalated 1,3-dipoles are used, then the dipolar addition can be stepwise.[221,230,231] They showed that the reaction can be concerted or stepwise, depending on the ability of the N-substituents to stabilize zwitterionic intermediates generated (see figure 1.17).

The 1,3-dipolar addition of azomethine ylides on fullerenes was first reported in 1993 by Prof. Prato and co-workers, when they used the C_{60} molecule as a dipolarophile in this type of additions.[232] Consequently, th particular case of 1,3-dipolar addition of azomethine ylides on fullerene compounds to generate fulleropyrrolidines is known as the Prato reaction.

Diels-Alder cycloaddition reactions on endohedral metallofullerenes

Because TNT I_h-C_{80}-based EMFs are those most abundant, their exohedral functionalization have been intensively explored in the quest for new materials of interest for future applications in biomedicine and materials science.[233] The first exohedral functionalization of an EMF was a Diels-Alder cycloaddition of 6,7-methoxyisochrom-3-one on $Sc_3N@I_h$-C_{80}.[234] The icosahedral I_h-C_{80} cage is highly symmetric (see figure 1.18), and only two different regioisomers are possible after functionalization: the adduct on a corannulenic [5,6] bond type (type D) or the adduct on the type B [6,6] bond (see figure 1.18). Based on NMR experiments, it was suggested that the addition must take place on a [5,6] position.[234] The latter was confirmed by the crystal structure of the $Sc_3N@C_{80}$-$C_{10}H_{12}O_2$ monoadduct[212] and rationalized by means of DFT calculations, which showed that the addition over the corannulene [5,6] bond is at least 11 kcal·mol^{-1} more stable than the addition on the [6,6] bond.[235,236] It is important to mention here that the encapsulated Sc_3N moiety can freely rotate inside the fullerene cage, and it has been found that its relative orientation towards a given bond induces large changes on its reactivity.[235–238]

The Diels-Alder functionalization of $Gd_3N@I_h$-C_{80} was reported in 2005 by Stevenson *et al.* obtaining different bisadducts that were not further characterized.[213] The same year, Akasaka and co-workers[211] reported the DA addition of cyclopentadiene (Cp) on $La@C_{2v}$-C_{82}. The authors, based on the shape of the LUMO orbital and few DFT calculations at B3LYP/6-31G*(La:ECP), proposed that the addition of Cp took place on a [6,6] bond, namely (2-3)-bond as labeled in figure 1.19 from the original publication. In a subsequent work, 1,2,3,4,5-pentamethylcyclopentadiene (Cp^*) was used as the diene in the same DA reaction, where the final product could be isolated and characterized by X-ray crystallography.[210] In this case, the addition of Cp^* corresponded to the

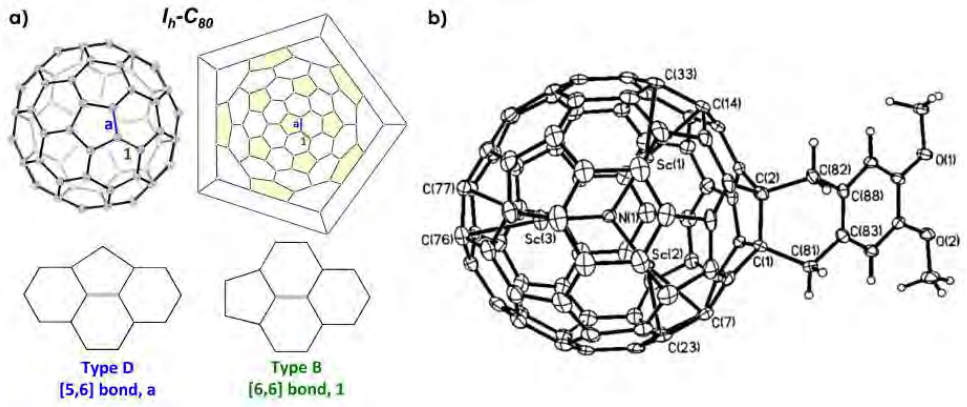

Figure 1.18: a) Schematic representation of the the two different bond types present on I_h-C_{80} fullerene; b) X-ray structure of the Diels-Alder $Sc_3N@C_{80}$-$C_{10}H_{12}O_2$ cycloadduct, the first EMF funcionalized[212,234] (adapted from ref.[212]).

attack on (22-23)-bond. Thus, it was surprising that relatively similar dienes (Cp and Cp*) presented markedly different regioselectivities. In addition to that, the final stabilities of both modoadducts were found to be largely different. At 298K, only 36% of $La@C_{2v}$-$C_{82}Cp^*$ decomposes into $La@C_{2v}$-C_{82} and Cp^* after 12h,[210] while the half-life of $La@C_{2v}$-$C_{82}Cp$ under the same conditions is only τ = 1.8h (for comparison, τ = 1800h for the decomposition of $C_{60}Cp$).[211]

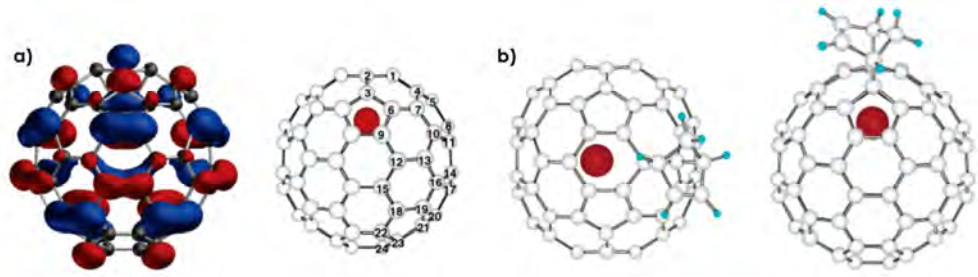

Figure 1.19: a) The LUMO orbital of $La@C_{82}$; b) Two views of the DFT optimized structure of $La@C_{82}Cp$ (adapted from ref.[211]).

Based on the higher reactivity observed for empty fullerenes and classical EMFs compared to the lower reactivity of TNT EMFs towards the Diels-Alder reactions, Dorn and co-workers proposed a method for the purification of metallic

nitrides EMFs from the extracted fullerenes.[239,240]

Several computational studies were reported by Osuna and co-workers about the DA reactivity of $Sc_3N@D_{3h}$-C_{78},[241] $Y_3N@D_{3h}$-C_{78} and $Y_3N@C_2(22010)$-C_{78}[242] non-IPR TNT EMFs. C_{78}-based EMFs represent the perfect scenario for the computational exploration of the regioselectivity towards cycloaddition reactions because the inner metal clusters are fixed and cannot rotate. They showed that critical changes in the regioselectivity of the process are observed when increasing the size of the metallic cluster. This increase changes the regioselective DA addition from a [6,6] addition in Sc_3N EMF towards a [5,6] addition for Y_3N system. This change is induced by the reduction of the fullerene cage strain due to the adduct formationin the case of the larger metallic cluster, Y_3N.[242] They theoretical predictions are in agreement with the experimental regioselectivity observed in the 1,3-dipolar additions on these EMFs (see next section). Moreover, they showed that the DA cycloaddition in non-IPR $Sc_3N@C_2(22010)$-C_{78} is preferred on a [5,5] bond, i.e., a pentagon-pentagon junction. In 2012, the effect of the TNT cluster size on the DA regioselectivity for C_{80} based TNT EMFs was systematically studied by the groups of Poblet and Solà .[236] They studied the DA addition of 1,3-*cis*-butadiene on $M_3N@I_h/D_{5h}$-C_{80} EMFs ($M = Sc, Lu, Gd$) from the kinetic and thermodynamic point of view. They results, at BP86/TZP//BP86/DZP level of theory, indicated that [5,6] bonds are more reactive than [6,6] for both isomers, but when the largest *Gd*-based cluster is considered, the regioselectivity is, however, significantly reduced. Finally, they also showed that the D_{5h} isomer is kinetically more reactive than the I_h one.

From the experimental and theoretical examples seen above, it seems clear that endohedral clusters play a major role in directing the addition sites of the exohedral reactivity of the fullerene cage. This fact has been computationally reinforced by a series of thermodynamic and kinetic studies performed in this thesis (see chapters 5 and 6).

1,3-Dipolar cycloaddition reactions on endohedral metallofullerenes

In 2004, Akasaka and co-workers reported the synthesis of a pyrrolidine adduct of $La@C_{2v}$-C_{82}.[170] They obtained three different bisadducts, and two monoadducts, although only one bisadduct and one monoadduct could be isolated. In the same year, the Prato reaction on $Y@C_{82}$[168] and $Gd@C_{82}$[168,177] using N-methyl-glicine and different aldehydes was achieved. Again, different multiple additions were observed but the isolation of the adducts was not accomplished.

The Prato reaction on the most important $M_3N@I_h$-C_{80} EMFs family was achieved by Echegoyen and co-workers. In 2005, they group reported the first pyrrolidine adduct of the most abundant EMF, $Sc_3N@I_h$-C_{80}, using the now standard synthetic strategy described in figure 1.20.[190] Based on ^{1}H-NMR and ^{13}C-NMR characterizations they showed that the pyrrolidine was selectively formed on a [5,6] bond. The same group reported the first pyrrolidine adduct of $Y_3N@I_h$-C_{80}, but in this case the addition took place on a [6,6] bond.[197] The same year, Dorn, Gibson and co-workers[189] reported the functionalization of $Sc_3N@I_h$-C_{80} and $Er_3N@I_h$-C_{80} with N-methylglycine and ^{1}3C-formaldehyde, observing that the addition took place on a [5,6] bond, in a similar way as the first $Sc_3N@I_h$-C_{80} monoadduct reported by Echegoyen.

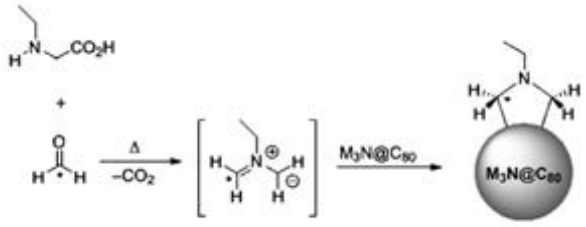

Figure 1.20: General mechanism of the 1,3-dipolar (Prato) cycloaddition of azomethine ylides on TNT-based EMFs (adapted from ref.[94]).

One year later, the Echegoyen lab reported the unexpected quantitative thermal isomerization of the [6,6] adduct to the [5,6] adduct of the N-ethylpyrrolidino $Y_3N@I_h$-C_{80} and $Er_3N@I_h$-C_{80}.[196] They proposed that the [6,6] monoadduct was the kinetic product, being the [5,6] the thermodynamic one. The same behavior was also observed for N-tritylpyrrolidino derivative of $Sc_3N@I_h$-C_{80}.[184] Rodríguez-Fortea *et al.* using computational methods, reported that although the [5,6] pyrrolidino adduct is more stable than the [6,6] adduct in general for $M_3N@I_h$-C_{80}, when the charge transfer increases this difference decreases and both monoadducts are equally stable for $Y_3N@I_h$-C_{80}.[243] They also suggested a *pirouette*-type mechanism for the observed [6,6]-to-[5,6] isomerization under thermal conditions, instead of a retrocycloaddition-cycloaddition process.[243] Finally, the X-ray crystal structure of [5,6] $Y_3N@I_h$-C_{80} monoadduct was reported by Echegoyen *et al.*,[195] showing that the N atom is out of the plain of the three yttrium atoms as represented in figure 1.21, indicating a high tension on the metallic cluster. Due to this strain, the carbon atoms that reside at the junction of two hexagons and one pentagon closest to the yttrium atoms

are extremely pyramidalized in comparison to the rest of carbons of the fullerene structure. Moreover, they observed different fractional occupancies of the cluster in the crystal structure, thus indicating a possible movement of the inner cluster inside the fullerene.[195]

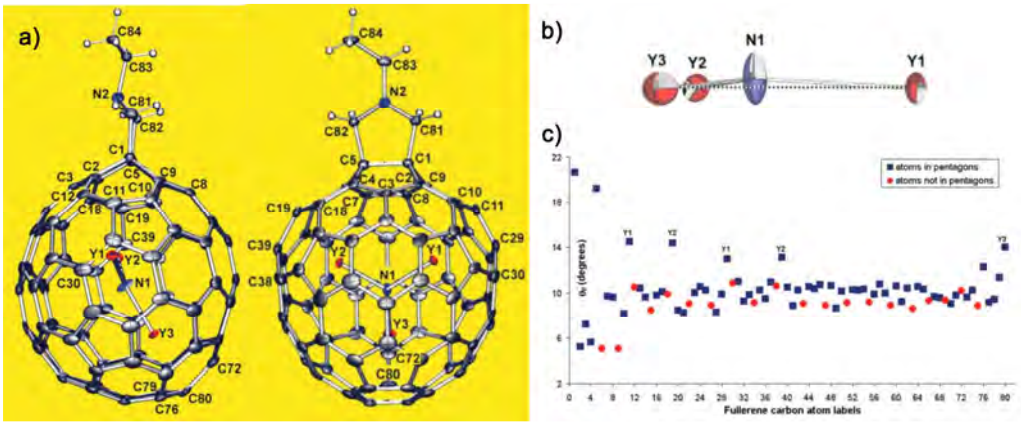

Figure 1.21: a) X-ray crystal structure of the [5,6]-pyrrolidine monoadduct of $Y_3N@I_h$-C_{80}; b) Pyramidalization of the Y_3N unit; c) Plot of the pyramidalization angles (θ_p) for the fullerene carbon atoms in $Y_3N@I_h$-C_{80} X-ray structure. The sixty carbon atoms that reside at the junction of a pentagon and two hexagons are shown as squares while the twenty others that reside at the junction of three hexagons are shown as circles. The carbon atoms that are closest to yttrium atoms are labeled Y1, Y2, or Y3 (adapted from ref.[195]).

The formation of two monoaducts and two bisadducts of N-tritylpyrrolidino-$Sc_3N@D_{5h}$-C_{80} EMF was reported by Dorn and co-workers.[184] They observed a higher reactivity of the the D_{5h}-C_{80} TNT EMF isomer than the I_h-C_{80}, in line with the Diels-Alder behavior. Because of the symmetry for the D_{5h}-C_{80} cage there are nine nonequivalent C-C bonds. Based on the NMR spectroscopic analysis, they suggested that the addition in one monoadduct occurred at a symmetric [6,6] bond of a pyracylene unit, whereas in the other monoadduct the reaction was predicted to be at a nonsymmetric [6,6] bond.[194] Nevertheless, none of the detected bisadducts could not be isolated or characterized. Few years later, Osuna *et al.*[244] reported the DFT relative stabilites and NMR data related to the N-tritylpyrrolidino-$Sc_3N@D_{5h}$-C_{80} monoadducts, and showed that the Prato reaction on $Sc_3N@D_{5h}$-C_{80} takes place preferentially on [5,6] bond and not on a pyracylene [6,6] position as initially reported by Dorn and co-workers.[194] The effective thermal retrocycloaddition of the N-ethylpyrrolidino-$Sc_3N@I_h$-C_{80} derivative was reported in a collabo-

ration between the groups of Echegoyen and N. Martín in 2006.[191]

A regiochemistry study of the Prato reaction on I_h-C_{80}-based EMFs was reported in 2007 by Lu and co-workers.[185] They studied the 1,3-dipolar addition reaction between $Sc_xGd_{3-x}N@C_{80}$ and N-ethylglycine and formaldehyde. They reported that for the smaller cluster of the series (Sc_3N), the [5,6] adduct was favored, whereas the [6,6] adduct was dominant in the case of the largest cluster (Gd_3N). For mixed clusters, both adducts were obtained, but after a thermal treatment at 180°C resulted in the isomerization to the [5,6] adduct. Nevertheless, [5,6] Gd_3N adduct isomerized into the formation of exclusively [6,6] adduct upon heating. These results suggested that the regioselectivity of the Prato reactions on $Sc_xGd_{3-x}N@C_{80}$ systems strongly depends on the size of the inner metal cluster.[185]

More recently, Aroua and Yamakoshi reported the kinetic study of the Prato reaction on $M_3N@C_{80}$ ($M = Sc, Lu, Y, Gd$).[192] In this study, they found that the initial addition ocurred at the [6,6] position and then a thermal rearrangement to a [5,6] adduct took place. Kinetics of the rearrangement were shown also to depend on the metal cluster size, being this isomerization complete for scandium and lutetium EMFs, whereas for yttrium and gadolinium an equilibrium mixture of [5,6] and [6,6] isomers is obtained.

Other non-TNT EMFs based on the I_h-C_{80} cage have also been exohedrally functionalized. The 1,3-dipolar cycloaddition was successfully produced on $La_2@I_h$-C_{80} and $Ce_2@I_h$-C_{80}.[173,174] The Prato cycloaddition between $La_2@I_h$-C_{80} and 3-triphenylmethyl-5-oxazolidinone has been achieved to obtain the corresponding $La_2@I_h$-$C_{80}(CH_2)_2NTrt$ (Trt = triphenylmethyl) [5,6] and [6,6] adducts.[173] Interestingly, the two metal atoms were fixed at the slantwise positions on the mirror plane in the [6,6]-adducts, whereas they were collinear with the pyrrolidino ring in the [5,6]-pyrrolidinodimetallofullerenes.[174] Very recently, another Prato reaction between 11,11,12,12-tetracyano-9,10-anthra-p-quinodimethane and $La_2@I_h$-C_{80} was reported, affording the corresponding [5,6] monoadducts.[176] The Prato addition on a [5,6] position of paramagnetic $Sc_3C_2@I_h$-C_{80} EMF directly modified the spin distribution and paramagnetic properties of this endohedral metallofullerene.[180] Recenty, the same authors reported the formation of several bisadducts (9), although they were not completely characterized.[181]

The Prato reaction on EMFs based on other fullerenes than I_h-C_{80} have been reported. In 2007, Dorn, Balch, and co-workers prepared the [6,6]-N-pyrrolidino derivatives of the ellipsoidal $Sc_3N@D_{3h}(5)$-C_{78}, where the internal Sc_3N was

planar. They obtained two mono- and one bisadduct, although only the two monoadducts were characterized by means of NMR and mass spectroscopy, DFT calculations based on a previous computational prediction from Poblet's group,[235] and one of them by X-ray crystallography.[182] In this case, they observed that the Sc_3N moiety remained in a planar orientation far away from the addition site, indicating a regiocontrol of the reaction by the internal cluster.[182] The regioselective Prato formation of a [5,6]-Sc_2C_2@C_s(6)-$C_{82}N(CH_2)_2Trt$ adduct was reported by Akasaka and co-workers,[178] and was characterized by single-crystal X-ray diffraction. In 2012 the same group reported the Prato addition on Sc_2C_2@C_s(9)-C_{82}, and they observed the formation of three monoadducts, being the major isomer a [5,6] adduct characterized by X-ray crystallography.[245]

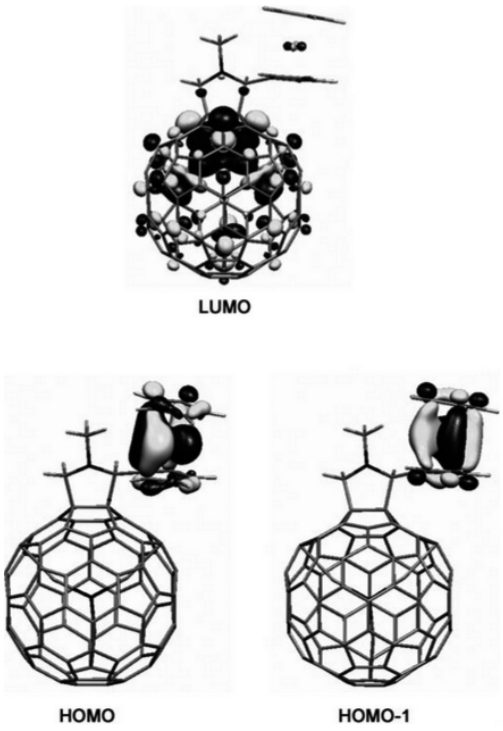

Figure 1.22: Representation of the LUMO (up) and the quasidegenerated HOMO and HOMO-1 (down) of N-methyl-2-ferrocenyl-[5,6]-Sc_3N@I_h-C_{80}-fulleropyrrolidine (Reproduced with permission from ref.[186]).

Finally, the Prato reaction was utilized to couple EMFs with organic donor moieties for the formation of intramolecular electron donor-acceptor dyads. In

2008, Pinzón *et al.*[161] successfully synthesized a ferrocenylpyrrolidine adduct of $Sc_3N@I_h$-C_{80}. In 2009, Echegoyen *et al.*[187] synthesized two isomeric [5,6]-pyrrolidine-$Sc_3N@I_h$-C_{80} conjugates containing triphenylamone (TPA) in different positions as the new donor system, observing that the dyad with the N-connected TPA donor had the largest thermal stability and longer lifetime of the photoinduced charge separated state.[187] The groups of Echegoyen, Martín, Guldi, Torres, and Poblet reported the systematic synthesis of a series of donor-acceptor dyads based on $M_3N@I_h$-C_{80} ($M = Sc, Y$) and different donors, such are tetrathiafulvalene, phtalocyanine or ferrocene (see figure 1.22).[186] More recently, Martín, Echegoyen, and Guldi have reported dyads based on the zinc tetraphenylporphyrine connected to the pyrrolidine moiety of the [5,6]-pyrrolidine-$Sc_3N@I_h$-C_{80} via long linkers.[188]

Very recently, the synthesis of $LaSc_2N@C_s(hept)$-C_{80} was reported by Balch, Popov, and co-workers.[246] This EMF, containing one heptagonal ring surrounded by two pentalene units, corresponds to a new class of endohedral metallofullerenes that not only contain hexagonal and pentagonal rings. The thermodynamically controled Prato addittion on $LaSc_2N@C_s(hept)$-C_{80} EMF has been computationally explored by Deng and Popov.[247] They observed that the most favorable monoadducts are those corresponding to the attack of the pentalene [5,5] bonds, in a similar way to the Diels-Alder addition on non-IPR EMFs, previously described.[242]

1.7.2 Bingel-Hirsch cycloaddition reactions on fullerenes

The Bingel-Hirsch (BH) reaction, a nucleophilic [2+1] cycloaddition reaction,[248] between bromomalonate and EMFs has been shown to be a very powerful and versatile tool for functionalizing endohedral metallofullerenes in a rapid and efficient manner.[15] Through the BH reaction, one can tune and modify the physical (solubility, for example) and (electro)chemical (such as band-gaps) properties of EMFs.

The BH reaction takes place in the presence of a strong base to deprotonate the bromomalonate and to form an enolate, and proceeds following a two-step mechanism as represented in figure 1.23. In the first step, the bromomalonate carbanion attacks the fullerene cage via nucleophilic addition in a barrierless process. During the second step, a cyclopropane ring closure takes place where the newly generated carbanion on the fullerene cage displaces the bromine anion in a SN_2 intramolecular nucleophilic substitution.[15]

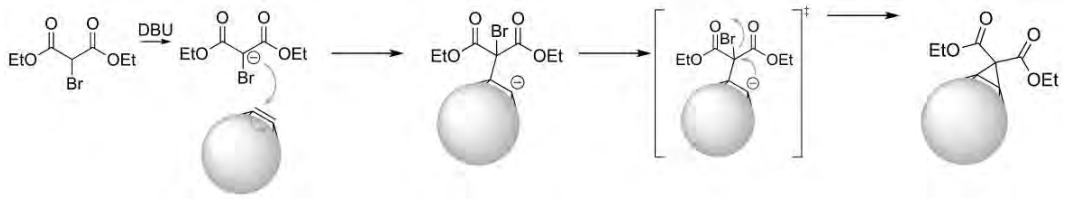

Figure 1.23: General mechanism of the Bingel-Hirsch [2+1] nucleophilic addition of diethylbromomalonate over fullerenes in the presence of 1,8-diazabicycloundec-7-ene (DBU).

Bingel-Hirsch cycloaddition reactions on endohedral metallofullerenes

The first BH cycloaddition on EMFs was reported by Alford and co-workers in 2003.[208] They were looking for a strategy to improve the water solubility of $Gd@C_{60}$ EMF in order to evaluate its application as a magnetic resonance imaging contrast agent. By using the BH reaction, they could synthetize for the first time a highly soluble $Gd@C_{60}$ derivative, $Gd@C_{60}[C(COOH)_2]_{10}$. The latter compound was evaluated in vivo and it was found to be a very promising candidate for its use as an MRI contrast agent, opening the doors for the future design and synthesis of new highly soluble EMF derivatives for biological applications. In this direction, the same strategy was followed by Diener *et al.*[249] for generating water-soluble ester derivatives of $^{212}Pb@C_{60}$ radiofullerene, for their use as an α-emitting radionuclides in radioinmunotherapy.

In 2005, Akasaka, Nagase, and collaborators synthetized and reported the first singly bonded Bingel-Hirsch intermediate. The isolation of the EPR inactive $La@C_{82}CBr(CO_2C_2H_5)_2$ (see figure 1.24) monoadduct demonstrated that the BH reaction takes place through a two-step process, as described previously. The authors could capture the $[La@C_{82}CBr(CO_2C_2H_5)_2]^-$ intermediate formed during the nucleophilic attack at the first step of the reaction by treating it with oxidants in order to get the $La@C_{82}CBr(CO_2C_2H_5)_2$ species.[250]

Echegoyen and co-workers reported the first monomethanofullerene derivative of I_h-C_{80}-based EMFs in 2005.[196,197] They showed that cyclopropanation of $Y_3N@I_hC_{80}$[197] and $Er_3N@I_hC_{80}$[196] with diethyl bromomalonate takes place regioselectively under mild conditions (room temperature in ortho-dichlorobenzene, o-DCB, and in presence of 1,8-diazabicyclo[5.4.0]undec-7-ene, DBU, as a base) on the [6,6] bond. However, the reaction did not take place when $Sc_3N@I_hC_{80}$ nor $Lu_3N@I_hC_{80}$ EMFs were considered.[197] They also showed that in EMFs

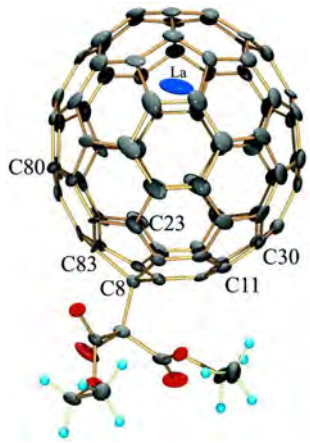

Figure 1.24: X-ray structure of the singly bonded Bingel-Hirsch intermediate $La@C_{82}CBr(CO_2C_2H_5)_2$ (Reprinted with permission from ref.[250]).

the retrocycloaddition induced by multiple electrochemically reductions did not occur, in contrast to the previously reported C_{60} case.[196,251]

In 2007, Dorn, Gibson, and co-workers reported the BH funtionalization of $Sc_3N@D_{3h}$-C_{78}, affording a single monoadduct, and a symmetric bis(ethyl malonate) adduct derivative characterized by means of ^{1}H-NMR and ^{13}H-NMR measures.[209] Nevertheless, no further characterization of the monoadduct or the bisadduct formed has been reported up to date. The same group synthetized the first two examples of open [6,6] methano-bridged derivatives of $Sc_3N@I_hC_{80}$ using a manganese(III)−Catalyzed free radical reaction.[252] This is a completely different reaction and many monoadducts were detected as side products, for example a [6,6]-open monoadduct containing only one ester group and an hydrogen atom on the central bridge carbon atom. Even so, it is interesting to mention that the measured $^1J_{(C,H)} = 147Hz$ of the C-H bridge atoms in the latter side product was in complete agreement with the one corresponding to a π-homoaromatic system.[252,253]

In 2010, the Echegoyen's group showed that $Sc_3N@I_h$-C_{80} and $Lu_3N@I_h$-C_{80} can be functionalized through the BH addition to obtain the corresponding [6,6]-open monoadducts by modifying the typical reaction conditions: *i*) replacing the base from DBU to NaH; and *ii*) modifying the solvent from *o*-DCB to a 4:1 mixture of *o*-DCB/DMF (DMF = N,N-dimethylformamide).[204]

Very recently, Yang *et al.* have found that by replacing one Sc atom by Ti in

the $Sc_3N@I_h$-C_{80}, the Bingel reaction under typical conditions occurs forming two different singly-bonded regioisomers (with relative yield c.a. 6:1).[254] These results are in line with the metal-dependence reactivity of the BH additions on EMFs observed by earlier studies.

In 2007, Echegoyen, Balch and collaborators reported the crystallographic characterization of the $Y_3N@C_{80}C(CO_2CH_2Ph)_2$ BH monoadduct.[206] They confirmed that open fulleroid structures with one of the yttrium atom directly pointing to the attacked bond were obtained rather than closed methanofullerene structures (see figure 1.25). DFT calculations also indicated that $Y_3N@C_{80}$ [6,6] open structures are more stable than closed ones, confirming that, in general, I_h-C_{80} EMFs fulleroid structures are better stabilized, and the formation of an open-cage adduct is in line with the fact of having π-homoaromatic systems. X-ray structures and DFT calculations also indicated that the rotation of the TNT unit inside the functionalized EMF, in contrast to the free rotation of pristine Y_3N EMF, is partially hindered although slighly rotation along the Y-N axis is possible, as shown in figure 1.25 .[206] Moreover, they found that for I_h-C_{80} pristine cage the addition of a methyl-malonate group is more favored to be on a closed [5,6] position.[206]

The fullerene cage size has also a large influence on the BH chemical reactivity. In 2008, Chaur *et al.* studied the BH reactivity of C_{80}, C_{84}, and C_{88} based Gd_3N EMFs using the typical reaction conditions.[207] They observed that when the size of the fullerene cage increases, the BH reactivity tends to decrease. For the C_{80}-based EMF, a monoadduct and a bisadduct are rapidly formed. For the $Gd_3N@C_{84}$ case, the monoadduct formation occurs after 20 minutes, while the reaction on $Gd_3N@C_{88}$ does not take place even if the temperature is increased up to $60°C$. The authors attributed the decrease in the reactivity of the $C_{80} > C_{84} >> C_{88}$ Gd_3N series due to the gradual decrease of the carbon pyramidalizations (higher pyramidalization led to the most reactive species).[207]

More recently, BH additions on non-IPR EMFs ($Gd_3N@C_{82}$, $Gd_3N@C_{84}$) have been reported by Echegoyen and co-workers,[71,207] and theoretically studied by Rodríguez-Fortea, Poblet and collaborators.[71,255] They showed that thermodynamically more stable products usually present open fulleroid structures, in the same line as the previously reported IPR EMFs. In addition to that, the same group has theoretically studied the complete electronic reaction paths for the BH additions on $Sc_3N@I_h$-C_{80} and $Sc_3N@D_3(6140)$-C_{68},[255] and over $Gd_3N@C_S(39663)$-C_{82} and $Gd_3N@C_S(51365)$-C_{84} EMFs.[256] By means of DFT calculations, they observed that BH thermodynamic and kinetic products do not coincide. And, more importantly, they showed that BH reaction under

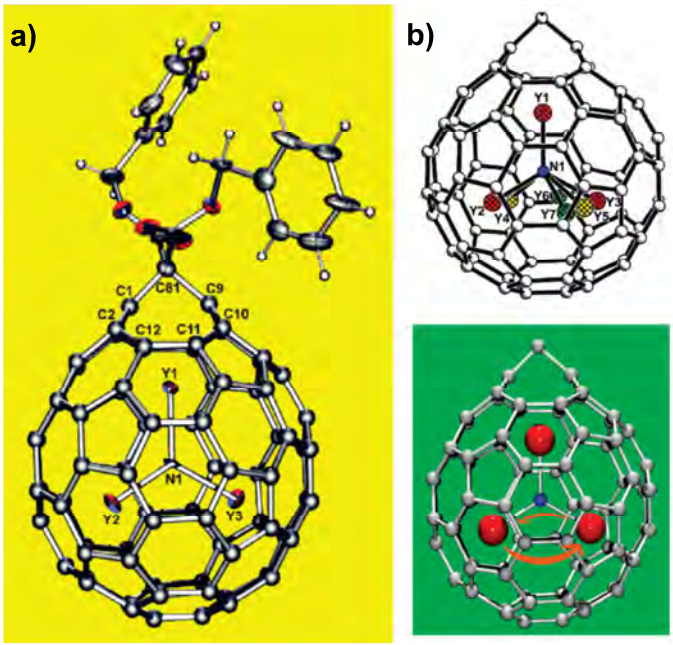

Figure 1.25: a) Bingel-Hirsch $Y_3N@I_h$-C_{80}-$C(CO_2CH_2Ph)_2$ crystallographic structure obtained for the major orientation of the Y_3N group. b) The three orientations of the Y_3N units. Yttrium ions in the major planar site (0.70 occupancy) are colored red, in yellow the second fractional occupancy (0.21 occupancy), and in green the third Y_3N group with 0.09 occupancy (adapted with permission from ref.[206]).

common reaction conditions (*i.e.* room temperature, *o*-DCB as a solvent and in presence of DBU as a base) leads to the kinetically controlled products.[255] The reaction barrier corresponding to the addition on the [6,6] bond in $Sc_3N@I_h$-C_{80} is 5 kcal·mol^{-1} lower in energy that the one corresponding to the [5,6] addition (at M06/6-311G**(TZV for *Sc*)//BP86/TZP level of theory, including *o*-DCB solvent effects through PCM approach). These results were in perfect agreement with the previously reported experimental observations for the BH addition on I_h-C_{80}-based EMFs which take place regioselectively on [6,6] positions.[255,256] For the non-IPR $Sc_3N@D_3(6140)$-C_{68} EMF, DFT computations indicated that the kinetic product corresponds to the addition over a type-B [6,6] bond, placed in an adjacent position to a pentalene unit, coinciding with the ^{13}C-NMR experimental assignment by Dorn and co-workers.[203] A similar situation is found for $Gd_3N@C_S(39663)$-C_{82} and $Gd_3N@C_S(51365)$-C_{84} systems, where kinetic products are predicted to be the ones corresponding to the additions over [6,6] B-type bonds placed near the pentalene unit in both cases.[256]

Finally, the BH functionalizaton of $LaSc_2N@C_s(hept)$-C_{80} new EMF has been computationally studied by Deng Popov.[247] Based on their computations, at PBE-D3BJ/def2-TZVP//PBE/TZ2P level, they found that the kinetic BH addition should proceed on the C-C bonds placed next to the pentalene units that surround the heptagonal ring, similar to that obserbed on non-IPR EMFs by Poblet and co-workers.[247,255,256]

1.8 Reactivity of endohedral H_2 and H_2O fullerenes

Since the synthesis of $H_2@C_{60}$ and $H_2O@C_{60}$ in 2005 and 2011, respectively, they have attracted the attention of researchers due to their particular structures. The $H_2O@C_{60}$ molecule, which has been considered as "wet fullerene" or "polar C_{60}" (see figure 1.26), has been proposed to allow the study of the intrinsic properties of a single molecule of water since the encapsulated H_2O does not have any hydrogen bond and it is completely isolated.[91] This is in the same line of the homologue H_2 endohedral fullerene.[89]

The [2+2] dimerization reaction of $H_2@C_{60}$ was achieved by Murata and co-workers.[89] They could characterize resulting dimer by analyzing its ^{1}H-NMR spectrum. They concluded that no effect of the encapsulated H_2 molecule was observed on the reactivity of the C_{60} cage, as the dumbbell-shaped dimer of

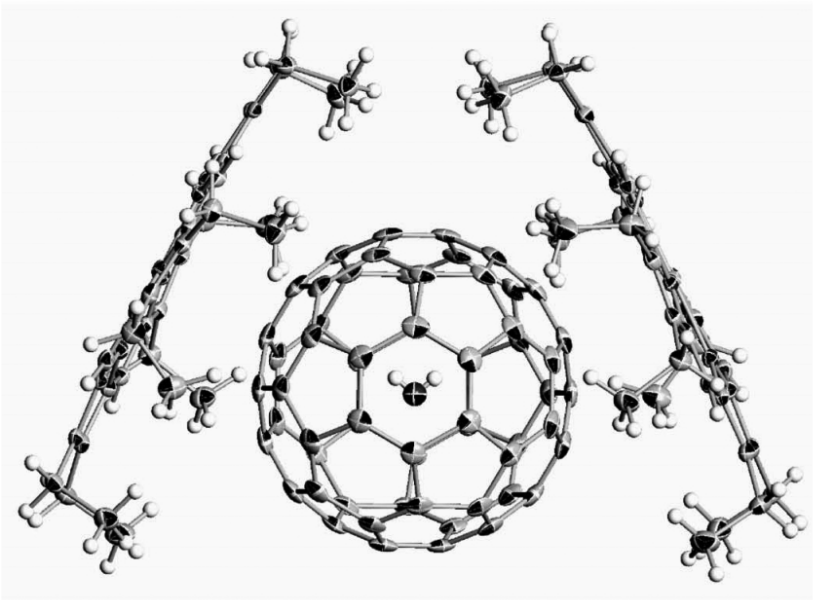

Figure 1.26: X-ray structure of the molecular complex $H_2O@C_{60} \cdot (NiOEP)_2$ at the 50% probability level (Reprinted with permission from ref.[91]).

$H_2@C_{60}$ was formed in the same yield as that for the empy C_{60}.

Following this line, the same group reported the dimerization of $H_2O@C_{60}$ using the same conditions.[257] They observed that the dimerization occurred with almost no difference with respect to the empty C_{60} system. Thus, the authors concluded that the inner water molecule does not affect the exohedral reactivity of the fullerene.

Nevertheless, the interaction between the inner water molecule and the fullerene carbon atoms has been analyzed by means of quantum chemical calculations by Varadwaj *et al.*.[258] Using DFT calculations, together with the quantum theory of atoms in molecules (QTAIM), they analyzed the possible noncovalent interactions between the entrapped water molecule and the fullerene structure. Their results suggested that the H_2O molecule is not chemically isolated, and there exist significant electronic (noncovalent) interactions between the water and the carbon cage. As a consequence, they classified the encaged water molecule as a non innocent guest of the fullerene C_{60} cage.[258]

Enantiospecific formation of chiral fulleropyrrolidines

Very recently, the group of Prof. Nazario Martín has reported the first efficient 1,3-dipolar catalytic synthesis of chiral pyrrolidinofullerenes in high yields under very mild conditions at low temperature.[259–263] They synthetized, for the first time, pyrrolidinofullerenes with controlled stereochemistry in a very high enantiomeric excess (greater than 90%) by combining a particular metal catalyst (Ag(I) or Cu(II)) and a specific chiral ligand as summarized in figure 1.27. Martín and co-workers showed that stereodivergent syntheses of cis/trans pyrrolidinofullerenes depends on the catalyst used, and in addition, in collaboration with the group of Prof. Cossío they suggested that a stepwise mechanism is followed.[260,262,263]

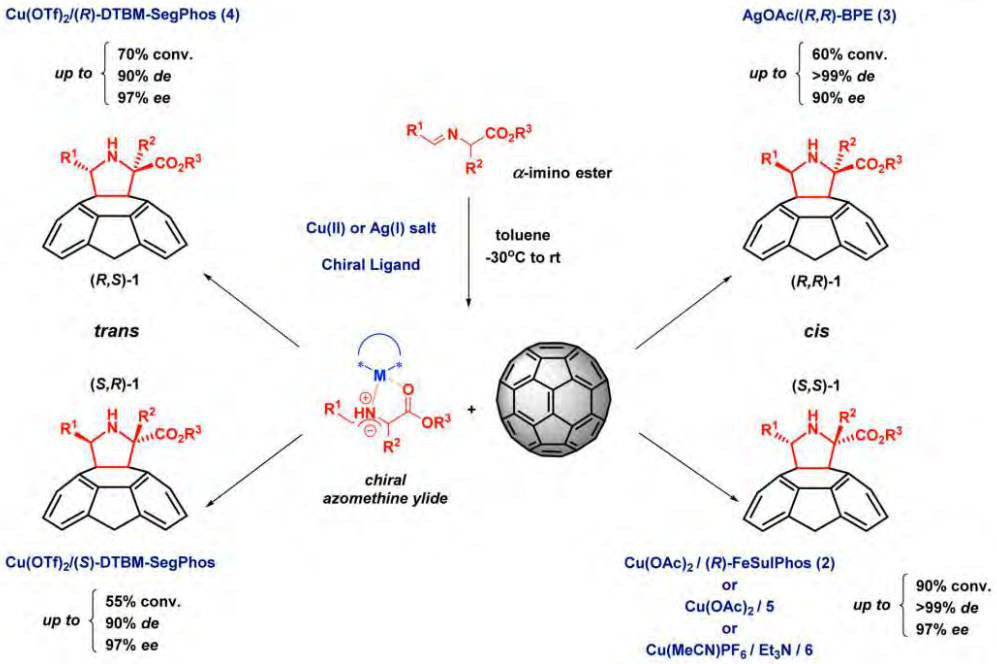

Figure 1.27: Stereodivergent 1,3-dipolar cycloaddition of N-metalated azomethine ylides onto C_{60} (Reprinted with permission from ref.[263]).

In 2014, the scope of these enantioselective 1,3-dipolar cycloadditions of N-metalated azomethine ylides was explored in the $H_2@C_{60}$ endohedral fullerene.[264] The reaction afforded both enantiomers of each *cis* and *trans* diastereoisomer with high enantiomeric excess. The experimental results found by Martín and co-workers revealed that the chemical behavior of this endohedral fullerene is the same as that observed for pristine C_{60}, concluding that

the presence of the H_2 molecule inside the C_{60} structure does not modify its chemical reactivity.[264]

Computational Chemistry

During the last 50 years, the discovery of theoretical and computational principles and algorithms, toghether with the development of fast computers, has resulted in enormous leaps in the accuracy and speed of computational methods. As a consequence, it is now feasible to model, *in silico*, reactions that involve molecules with thousands of atoms.

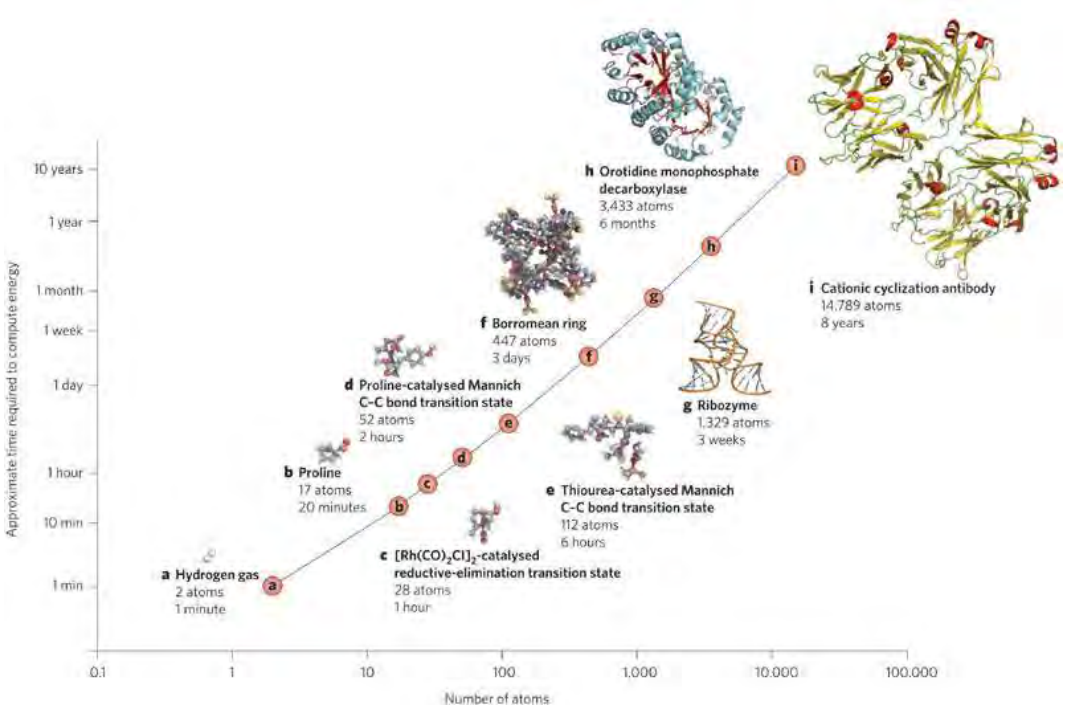

Figure 1.28: Time required to compute the energies of molecular structures of various sizes by using density functional theory and double-zeta basis sets on a modern desktop computer with appropiate memory and storage. The time required (shown on a log scale) increases exponentially with the size of the molecule (reproduced with permission from ref.[265]).

The development of quantum mechanical techniques, and density functional theory (DFT) calculations in particular,[266] proceeded at an ever accelerating pace.[267] Today, there exist computational methods for modelling molecules and reactions that can obtain results at almost any desired accuracy, as long as sufficient computer resources are avaliable (figure 1.28).

In this chapter, the different methodologies and strategies used to carry out the studies included in the present thesis are briefly summarized. Most of the calculations included in this work have been done under the Density Functional Theory approach, although in some cases, in order to reduce the enormous computational cost required, semiempirical methods have been used as a first approach. Density Functional Theory will be described based on the books "Essentials of Computational Chemistry: Theory and Models"[267] by Christopher Cramer and "Introduction to Computational Chemistry"[268] by Frank Jensen. Afterwards, different computational tools, useful to analyze, rationalize and understand the chemical behavior of fullerenes and endohedral metallofullerenes are presented.

1.9 The Density Functional Theory

Density Functional Theory (DFT) is an alternative formalism to the conventional *ab initio* methods (*e. g.*, correlated wave-function methods) to solve the Schrödinger equation and determine the wave functions and energy eigenvalues for a given many-electrons system.

According to the DFT theory, the energy of the ground state of a many-electron system can be expressed through the electron density, and in fact, the use of the electron density in place of the wave function to calculate the energy of the system is the fundament of the DFT. Nevertheless, the exact Hamiltonian which relates the energy eigenvalues with a given density is not known, and different approximations are needed.

During the last two decades, different methods and strategies to calculate the energies of chemical systems using DFT have been proposed, making possible the energy estimation and geometry optimization of systems of medium to large size using DFT at a reasonable computational cost (see figure 1.28).

The basis for Density Functional Theory is the proof by Hohenberg and Kohn[269] that the ground-state electronic energy is determined completely by the electron density ρ. There exist a one-to-one correspondence between the electron density of a system and its energy. A wave function for an N-electron system contains $3N$ coordinates, three for each electron (four if spin is included). The electron density is the square of the wave function, integrated over N-1 electron coordinates, and only depends on three coordinates independently of number of electrons. Although the complexity of a wave function increases with the number of electrons, the electron density has always the same number of variables and not depending of the system size. Nevertheless, the problem in DFT is that although it has been proven that each different density yields a different ground-state energy, the functional that connects these two quantities is not known. Thus, the main goal of DFT development is to design functionals that connect the electron density with the energy.[270–272]

A functional is a prescription for producing a number from a function, which in turn, is a prescription for producing a number from a set of variables, in this case, coordinates. Thus, in DFT the energy depending on the electron density is a functional of the density. The energy functional may be divided into three parts, kinetic energy $T[\rho]$, attraction between the nuclei and electrons $E_{ne}[\rho]$, and electron-electron repulsion $E_{ee}[\rho]$, being the nuclear-nuclear repulsion a

constant since the most common DFT implementations are based on the Born-Oppenheimer approximation. Furthemore, the $E_{ee}[\rho]$ term may be divided into Coulomb and Exchange part, $J[\rho]$ and $K[\rho]$, implicitly including correlation energy in all terms. The $E_{ne}[\rho]$ and $J[\rho]$ functionals are given by their classical expressions, where the factor of $1/2$ in $J[\rho]$ is needed to integrate over all space for both variables

$$E_{ne}[\rho] = \sum \int \frac{Z_a \rho(r)}{|R_a - r|} dr \tag{1.12}$$

$$J[\rho] = \frac{1}{2} \int \int \frac{\rho(r)\rho(r')}{|r - r'|} dr dr' \tag{1.13}$$

The application of DFT methods in computational chemistry was possible due to the introduction of orbitals by Kohn and Sham.[273] Since the exact density matrix is not known, the approximate density is written in terms of a set of auxiliary one-electron functions, the KS orbitals

$$\rho(r) = \sum_{i=1}^{N} |\phi_i(r)|^2 \tag{1.14}$$

The basic idea in the Kohn and Sham (KS) formalism is splitting the kinetic energy functional into two parts, one of which can be calculated exactly by applying the classical kinetic operator on the KS molecular orbitals, and the other corresponds to the kinetic correlation energy part, which is always a positive energy. Thus, the exact part of the kinetic energy functional is given as

$$T_S = \sum_{i=1}^{N} \langle \phi_i | -\frac{1}{2} \nabla^2 | \phi_i \rangle \tag{1.15}$$

where the subscript S denotes that it is the kinetic energy calculated from a Slater determinant. The remaining kinetic energy is absorbed into the exchange-correlation term, and a general DFT energy expression can be written as

$$E_{DFT}[\rho] = T_S[\rho] + E_{ne}[\rho] + J[\rho] + E_{xc}[\rho] \tag{1.16}$$

and it is customary to separate $E_{xc}[\rho]$ into two parts, a pure exchange E_x and a correlation part E_c

$$E_{xc}[\rho] = E_x[\rho] + E_c[\rho] \tag{1.17}$$

although it is not clear that this is a valid assumption.

The strength of DFT is that only the total density needs to be considered. In order to calculate the kinetic energy with sufficient accuracy, however, orbitals have to be reintroduced. Nevertheless, the computational cost that DFT requires is similar to HF theory, with the possibility of providing more accurate results.

The major problem in DFT is to derive accurate formulas to describe the exchange-correlation term. Assuming that such a funtional is available, the problem is then similar to that found in wave function based HF theory: determine a set of orthogonal orbitals wich minimize the energy. Since $J[\rho]$ and $E_{xc}[\rho]$ functionals depend on the total density, a determination of the orbitals involves an iterative sequence. The unknown KS orbitals may be determined by numerical methods, or expanded in a set of basis functions, analogously to the HF method. Typically, all calculations employ an expansion of the KS orbitals in an atomic basis set as described in next subsections.

Although it its clear that there are many similarities between HF theory and DFT, there is an important difference. If the exact $E_{xc}[\rho]$ was known, DFT would be able to provide the exact total energy, including the electron correlation. DFT methods therefore have the potential of including the computationally difficult part in wave-mechanics, the correlation energy, at a similar computational cost that the one needed for determining the uncorrelated HF energy.

It is possible to prove that the exchange-correlation potential is a unique functional and valid for all systems, but an explicit functional form of this potential has been elusive. The difference between DFT methods is the choice of the functional form of the exchange-correlation energy. There is a little guidance from theory how such functionals should be chosen, and consequently many different potentials have been proposed. Functionals are often designed to have a certain limiting behavior, and a number of parameters are fitted to known accurate data.

Local density methods

In the *Local Density Approximation* (LDA) it is assumed that the density locally can be treated as a uniform electron gas, or equivalently that the density is a slowly varying function. In a more general case, where the α and β den-

sities are not equal, LDA has been virtually abandoned and replaced by the *Local Spin Density Approximation* (LSDA).

In the LSDA approximation the exchange energy is in general underestimated by $\sim$ 10%, thus creating errors which could be larger than the whole correlation energy. Electron correlation is furthermore overestimated, often by a factor close to 2, and as a consequence, bond strengths are overestimated.

Despite the simplicity of the fundamental assumptions, LSDA methods are often as accurate as wave function based HF methods.

Gradient corrected methods

Improvements over LSDA approach have to consider a non-uniform electron gas. A step in this direction is to make the exchange and correlation energies dependent not only on the electron density, but also on derivatives of the density. Such methods are known as *Gradient Corrected* or *Generalized Gradient Approximation* (GGA) methods.

Different approximations and corrections to the LSDA exchange expression were reported in 1990s, such are the Perdew and Wang PW86,[274] or Becke's B88.[275] In addition, there have been various gradient corrected functional forms proposed for the correlation energy. One popular functional, not a correction, is due to Lee, Yang and Parr (LYP).[276] Perdew also proposed a gradient correction to the LSDA result, known by the acronym P86.[277,278]

There also exist the so-called *meta* GGA functionals. These functionals are constructed by including a further term in the expansion, and thus, depend on the density, the gradient of the density and its second derivative (Laplacian). In addition, it is common to include the orbital-dependent kinetic energy density as an ingredient to construct nonempirical meta-GGA functionals.[279]

Hybrid methods

Considering the exact wave function a single Slater determinant composed of KS orbitals, the exchange energy is in this case exactly to that given by Hartree-Fock theory. If the KS orbitals are identical to the HF orbitals, then the "exact" exchange is precisely the exchange energy calculated by HF wave function method. Thus, an approximation for the exchange-correlation en-

ergy by the LSDA result defines the *Half-and-Half* (H&H) method,[280] and the exchange-correlation energy can be written as

$$E_{xc}^{H\&H} = \frac{1}{2}E_x^{exact} + \frac{1}{2}(E_x^{LSDA}) + E_c^{LSDA} \tag{1.18}$$

Furthemore, since the GGA methods give a substantial improvement over LDA, a generalized version of the H&H method may be defined by writting the exchange energy as suitable combination of LSDA, exact exchange, and a gradient correction term. The correlation energy may be similarly taken as the LSDA formula plus a gradient correction term. Models than include exact exchange are called *hybrid* methods, and *Becke 3 parameter functional* (B3) is probably the maximum exponent of these methods, whose exchange-correlation energy is given by

$$E_{xc}^{B3} = (1-a)E_x^{LSDA} + aE_x^{exact} + b\Delta E_x^{B88} + E_c^{LSDA} + c\Delta E_c^{GGA} \tag{1.19}$$

where the a, b and c values are determined by fitting to experimental data to be 0.20, 0.72 and 0.81 respectively.[281] When B3 exchange is used in combination with the LYP GGA correlation, and the $\Delta E_c^{LYP} \approx E_c^{LYP} - E_c^{VWN}$ approximation is assumed, the B3LYP hybrid functional is obtained.[282]

$$E_{xc}^{B3LYP} = (1-a)E_x^{LSDA} + aE_x^{exact} + b\Delta E_x^{B88} + (1-c)E_c^{VWN} + cE_c^{LYP} \tag{1.20}$$

Because of the extraordinary performance of B3 procedure, Half-and-Half is rarely used anymore. And, moreover, although the B3 procedure has been generalized to include more fitting parameters, it could not be significantly improved.

Computational considerations

The specification of a DFT method requires the selection of a suitable form for the correlation and exchange energies. Nowadays, the term LSDA has become almost synonymous with the acronym SVWN,which uses the LSDA correlation functional constructed by Vosko, Wilk and Nusair,[283] and the exchange given by the Dirac-Slater expression.

Gradient corrected methods have typically used the B88 exchange or the B3 hybrid, and either the LYP, P86, or PW91 correlation functonals. Associated acronyms for those methods are BLYP, BP86, BPW91, B3LYP, B3P86, and

B3PW91.

Gradient corrected methods usually perform much better than LSDA. In general, it is found that GGA methods often give geometries for stable molecules of the same, or even of better quality than MP2 at a computational cost similar to HF. For systems containing multi-reference character, where MP2 usually fails badly, DFT methods are often found to generate results of a quality comparable to that obtained with coupled cluster methods.[284]

Weak interactions due to dispersion forces, like van der Waals interactions, are poorly described by density funtionals that do not properly include correlation effects.[285] Nevertheless, parameterized meta-GGA functionals where non-locality is included *via* incorporating the kinetic energy density, have been assessed to quantitatively account for dispersion effects.[286]

Wave function methods employ the exact Hamiltonian operator and make approximations for the wave funtion, while DFT makes approximations in the Hamilton operator and uses the exact density. Notwithstanding, it is easier to improve on the wave function description than to add corrections to the operator. Although GGA and hybrid DFT methods give quite accurate results, the lack of a systematic way to improve DFT functionals towards the exact result is a major drawback of DFT. The results converge towards a certain value when the basis set is increased, but theory does not allow an evaluation of the errors inherent in this limit. The final quality of a given DFT result can therefore only be determined by comparing the performance for similar systems where experimental or high *ab initio* wave function results are available.

The acceptable quality of DFT results, that requires a similar computational effort as a HF calculation, made these methods one of the most powerful tools in modern computational chemistry.

1.9.1 Basis functions

The computed KS orbitals are usually expanded in a set of known functions. The one electron atomic orbital expression is given by:

$$\phi_i = \sum_{j=1}^{\infty} C_{ij}\varphi_j \tag{1.21}$$

The expansion of the atomic orbitals can be done in terms of Slater type orbitals STOs or in Gaussian type orbitals GTOs. STOs expression is:

$$\varphi_{nlm_l}^{STO} = N_\xi r^{n-1} e^{-\xi r} Y_{lm_l} \tag{1.22}$$

where N_ξ is the normalization constant, Y_{lm_l} is the spherical harmonics and ξ is a variational parameter which is related to the radial function and indicates the orbital compression. They reproduce accurately electronic behavior round the nucleus. But the Slater functions present the disadvantage that the two-electron integrals cannot be solved analytically, so a numerical procedure is required.

For the GTOs:

$$\varphi_{nlm_l}^{GTO} = N_\xi r^{n-1} e^{-\xi r^2} Y_{lm_l} \tag{1.23}$$

The only difference of the GTOs with respect to STOs is a quadratic dependence on r in the exponential part. That means the analytical form of the two-electron integrals can be analytically solved. GTOs does not have a cusp at the nucleus and decay to zero too rapidly. Thus, a linear combination of GTOs are needed to represent accurately the electronic behavior close to the nucleus and in the tail.

Usually, the charge distribution in a molecule is not uniform as more electronegative atoms might be more negatively charged, and *vice versa*, the more electropositive atoms are more positively charged. This fact has an effect on the shape of the atomic orbitals, which can be described more adequately by introducing *polarization* functions. That is, for example, adding d-type functions to the first row atoms Li-F and p-type functions to H and He.

Finally, *diffuse* functions can also be added to increase the flexibility of the basis set, which is specially needed in the case of anionic species. Including diffuse functions implies the incorporation of an extra set of s- and p- or d-type functions with low ξ value for each atom.

DFT methods are one-dimensional as HF method is. That means that increasing the size of the basis set allows a better description of the KS orbitals.

1.9.2 Treating core electrons

For systems involving elements from the third row or higher in the periodic table, there is a large number of core electrons which in general are chem-

ically unimportant. This is the case of endohedral metallofullerenes, where encapsulated clusters usually contain heavy metal atoms and lanthanides. It is necessary to use a large number of basis functions to expand the corresponding orbitals, otherwise the valence orbitals will not be properly described due to a poor electron-electron repulsion description.

There exists one strategy included in the ADF computational package[287] called *frozen core approximation* to describe the core electrons at low computational cost. In this approximation, deep-core atomic orbitals are kept frozen in the molecular calculation as they practically do not change upon molecule formation. They are previously obtained from very accurate single-atom calculations using large STOs basis sets.[287] The deep-core orbitals are explicitly orthogonalized against the valence orbitals and then, the frozen core density can be included in the calculation.

In a previous work by Osuna *et al.*,[242] it was demonstrated that the effect of using the frozen core approximation versus an all-electron basis set calculation in an EMF geometry optimization is rather small. For the optimization of isolated Sc_3N and Y_3N clusters, differences of 0.001 Å and 0.006 Å were found, showing the validity of this approximation for the computation of EMF structures.

Relativistic effects: ZORA approximation

The zeroth-order regular approximation (ZORA), as implemented in ADF software, is a good option to introduce relativistic effects in routinary DFT calculations.[288–292] The formulation and deduction of the relativistic ZORA approximation can be found in the book "*Introduction to Computational Chemistry*" by Jensen.[268] Relativistic effects are found to be important for the correct description of the more internal orbitals of heavy metal atoms.[268] In this thesis, the ZORA approximation has been used to systematically include relativistic effects in DFT calculations to correctly describe lanthanides and heavy metal based clusters encapsulated inside the endohedral metallofullerenes.

1.9.3 Solvation models

There exist many different methods for evaluating the effect of solvent into quantum chemical calculations. The latter can be mainly divided into two types: those describing the individual solvent molecules, i. e. explicit solvent

methods; and those which treat the solvent as a continuous medium, *i.e.* including it in an implicit way.[268,293] In this thesis, we have included solvation effects using implicit models. For example, for the study of reactions where ions, or charged species participate as the case of the Bingel-Hirsch reaction, we have included the effect of the solvation. The approximations used are the *Polarizable Continuum Model* (PCM) as implemented in Gaussian09[294] software, and the *COnductor-like Screening MOdel* (COSMO) in the ADF[287] package. A brief introduction to these solvation models is given below following the description reported in the book "*Introduction to computational chemistry*" by Jensen.[268]

The effect of solvent may be divided into two major contributions: specific solvation or "short-range" effects, for example hydrogen bonding or preferential orientation of solvent molecules near an ion; an "macroscopic" or "long-range" effects, involving screening of charges (solvent polarization). The long-range part is responsible for generating a (macroscopic) dielectric constant different from 1. The specific solvation effect is mainly concentrated in the first solvation sphere, but the long-range effect requires a large number of solvent molecules. There are several methods for modelling the latter contribution without explicitly considering the individual molecules, usually employing the concept of a "reaction field".

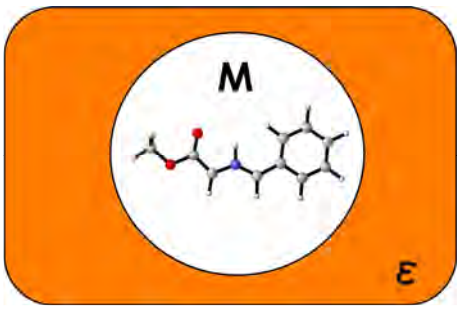

Figure 1.29: Representation of the Self-Consistent Reaction Field Model, where the solute molecule **M** is placed in a generated cavity inside the solvent medium with a dielectric constant of ε (adapted from ref.[268]).

The *Self-Consistent Reaction Field* (SCRF) model considers the solvent as a uniform polarizable medium with a dielectric constant of ε, with the solute M placed in a suitable shaped hole in the medium as represented in figure 1.29.[295] The generation of the cavity in the medium implies an energetic cost, thus being a destabilizing effect, while dispersion interactions between the solvent

and the solute molecule are stabilizing. The electric charge distribution of M polarizes the medium, inducing charge moments, which in turns acts back on the molecule producing and electrostatic stabilization. The solvation energy can be written as follows:

$$\Delta G_{solvation} = \Delta G_{cavity} + \Delta G_{dispersion} + \Delta G_{electrostatic} \tag{1.24}$$

Reaction field models can differ in different aspects on how: *a*) the size and shape of the cavity is defined; *b*) the dispersion contributions are calculated; *c*) how the charge distribution of M is represented; *d*) the solute M is described, using classical force fields or using quantum mechanics semiempirical or *ab initio* methods; and *e*) the dielectric medium is described.

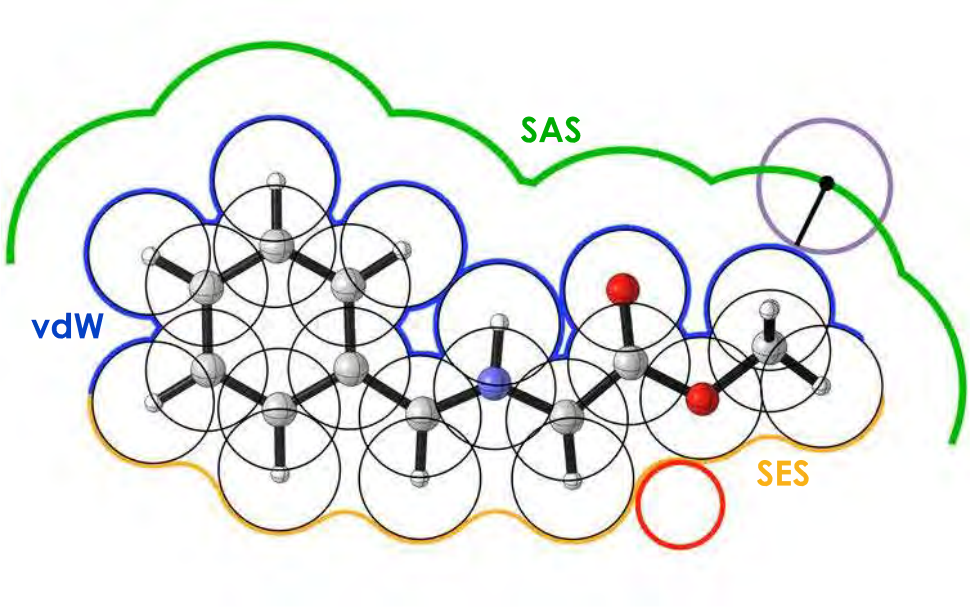

Figure 1.30: Representation of the different solvation cavity definitions based on interlocking spheres. In black, the spheres centred on atoms, in blue the van der Waals surface, in green the solvent acessible surface (SAS), in orange the solvent excluding surface (SES) (adapted from ref.[296]).

The simplest cavity shape representation is a sphere or an ellipsoid. In those cases, the electrostatic interaction can be computed analytically. But more realistic models employ molecular shaped cavities. For example, they can be generated by interlocking spheres located on each nuclei whose radius is defined as the atomic radius of every atom multiplied by a scale factor (typically

1.2) to define a van der Waals surface (see figure 1.30). Nevertheless, these surfaces may have some small areas where no solvent molecules can access. Then, more appropiate descriptors can be employed to avoid this problem, such is the *Solvent Accessible Surface* (SAS), defined as the surface traced out by a spherical particle of a given radius rolling on the van der Waals surface (see figure 1.30). There exists a variant called *Solvent Excluding Surface* (SES) which consists on the path traced by the surface of a spherical solvent molecule rolling about the van der Waals surface. In principle, this consist of the van der Waals surface, but in the regions where the spheres would intersect, the convave part of the solvent sphere replaces the cusp. Alternatively, the cavity can be calculated directly from the wave function, for example by taking a surface corresponding to an electron density of 0.001.[268,297]

It should be emphasized, however, that SCFR models are incapable of modelling specific short-range solvation effects, that is, those occuring in the first solvation sphere for example hydrogen bonding.

The energy required to create the cavity, including the entropy factors and loss of solvent-solvent interactions, and the stabilization due to dispersion interactions between the solute and solvent are usually assumed to be proportional to the surface area. This energy is then calculated to be proportional to the surface area, or parametrized by fitting to experimetal data.[268]

The electrostatic contribution is produced due to the electric field created by the charge distribution of the solute that polarizes the continuum medium, which in turns creates an electrostatic potential inside the cavity. There are different proposed models to characterize this electrostatic contribution.[268,298–301]

The PCM model employs a van der Waals surface type cavity, a detailed description of the electrostatic potential, and parametrizes the cavity/dispersion contributions based on the surface area.[302] The COSMO model employs a SES molecular shaped cavities, and represents the electrostatic potential by partial atomic charges. Initially, COSMO was implemented for semiempirical methods, but later on it has been used in conjunction with *ab initio* methods.[303,304] The actual parametrization of these models appear to be able to give absolute values with an accuracy of a few kcal·mol^{-1}.[305]

1.9.4 Dispersion interactions

London dispersion forces are intermolecular weak forces due to the interaction between temporary induced multipoles in molecules which do not have permanent dipole moment. These interactions can take place also between large distance separated regions of the same molecule.

Dispersion energy is usually not correctly described by DFT functionals as they underestimate its value. Then, the DFT interaction energies between two molecules are quite smaller than the real ones. Nevertheless, some meta-GGA parameterized functionals intrinsically include dispersion corrections, as discussed above, such are the meta-GGA M06 and later Minnesota functionals, for example.[306,307]

For example, in cycloaddition reactions involving fullerene compounds, a reactant adduct is formed. But it can only be well described if dispersion interactions are considered. This fact is quite important because it directly affects the computed energy barrier and reaction energy values. In the present thesis, when the use of hybrid functionals was not possible, dispersion corrections have been included when necessary by using the methodology proposed by Grimme and co-workers.[308–310]

Grimme's correction consists in an add-on term to standard Kohn-Sham density functional energy values to describe the total energy as follows:

$$E_{DFT-D} = E_{KS-DFT} + E_{disp} \tag{1.25}$$

where E_{KS-DFT} is the self consistent Kohn-Sham energy as obtained from the chosen density functional from a rutinary energy calculation, and E_{disp} is the dispersion correction term.

There exist different ways to define the dispersion correction term, but the one proposed by Grimme and co-workers is based on the use of the classical definition of long distance forces.[308–310] The Grimme's dispersion correction terms are directly proportional to the C_n^{AB}/r_{AB}^n relationship, where C_n^{AB} is a parametrized nth-order dispersion coefficient for atom pair AB, r_{AB}^n is the internuclear AB distance, and $n = 6, 8, 10, \ldots$.

The second dispersion correction term reported by Grimme's group, namely D2, uses an empirical interpolation formula to determine the dispersion coefficients C_n^{AB}, while in the following version, namely D3, they used time-dependent DFT calculations to compute the most important parameters, among

other differences.[308–310]

Corminboeuf and co-workers[311–313] proposed an alternative dispersion correction scheme, the density dependent dispersion corrections (dDsC), where the dispersion coefficients are computed depending on the reduced density gradient, and two functional dependent damping parameters. Thus, dDsC correction terms employ electronic structure information to determine dispersion coefficients in addition to empirical parameterizations.

In a previous work, Osuna *et al.*[314] demonstrated that the inclusion of dispersion corrections in the study of the chemical reactivity of fullerenes with standard density functionals is essential to reduce the errors in the computed reaction barriers and reaction energies when compared with the experimental values. Nevertheless, although standard DFT energies overestimates the reaction barriers and energies (higher barriers, and smaller reaction energies), the reactivity trends remains unchanged.

In the present thesis, D2 and D3, and dDsC approaches have been used to include the dispersion corrections to standard DFT energies, when necessary.

1.10 Computational chemistry tools for chemical reactivity studies

In this section, a general overview of the computational chemistry tools that are employed in this thesis for the study of the chemical reactivity and properties of fullerene compounds is presented.

1.10.1 General overview of geometry optimizations

The computational study of reaction mechanisms implies the location and characterization of the different stationary points involved in the corresponding reaction path. The latter is the minimum energy path that connects the reactant and product structures through a transition state structure. Each stationary point is obtained after applying a series of iterations, which include modifications to the initial structure, until the energy of the system has reached a point on the potential energy surface (PES) with gradient equal to zero (in practice, with gradient value below a given threshold). Reactants and products are relative minima on the PES, whereas transition states are first-order

saddle-points as shown in figure 1.31.

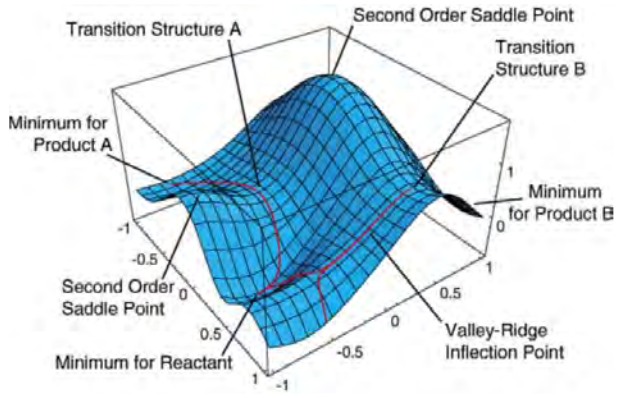

Figure 1.31: Representation of a model potential energy surface (PES) ilustrating minima, transition structures, second-order saddle points, and reaction paths (reproduced with permission from ref.[315]).

To find the reactant and product optimized geometries, one has to find the relative minima in the reaction coordinate path. To know the path, the gradient has to be evaluated, which gradient is the first derivative of the energy with respect to the Cartesian coordinates of all the nuclei. Following the gradient slope downhill, a point where the slope will be equal to zero should be found. That point corresponds to a minimum of the PES.

The procedure that is behind the geometry optimization process can be described as follows. One starts with an initial geometry, computes the potential energy and the gradient, and afterwards the geometry of the molecule is changed by moving downhill. Once a new geometry is obtained, the cycle starts again until the change on the geometry as well as on the energy of the system is below a defined threshold value.

The procedure for the localization of the transition states (TSs) is slightly different, as they correspond to a maximum along the reaction coordinate, but minima in the other directions as they are first-order saddle-points. Although the gradient is used to locate transition state geometries, the second derivatives of the energy (*i.e.* the Hessian Matrix) are also required. Constructing the Hessian in each geometry optimization step is often computationally too high, but there exist different strategies to avoid this problem. One solution consists in computing the Hessian only at the first point of the geometry optimization, and then updating it following a certain scheme, such as the Bofill

updating method.[316] Another strategy is constructing a model Hessian with the correct number of eigenvalues corresponding to the approach of reacting molecules. The latter is the approach mainly used in our calculations as we use the QUILD (QUantum regions Interconnected by Local Descriptions) program, which functions as a wrapper around the ADF program.[317,318] Within the QUILD optimization scheme, ADF is used only for the generation of the energy and gradients.

For the final characterization of the different stationary points, an evaluation of the vibrational normal modes is required. The structures corresponding to a minimum in the PES must have all the frequency values real (positive), *i.e.* all the diagonal Hessian Matrix elements positive. For the transition state geometries, as they are first-order saddle-points, they must have one (and only one) imaginary frequency (negative), which means having one negative Hessian Matrix eigenvalue, and corresponding to the desired bond formation/breaking or rotation.

1.10.2 Computing the reaction energies

A large amount of valuable information can be extracted from the energies computed for the optimized stationary points on the reaction path. For large systems, such as fullerenes or metalloporphyrines, the use of highly accurate methods or large basis sets during the optimization procedure is computationally unaffordable. That is the reason why sometimes single point energy calculations (SP) are performed using higher basis sets or different methods to obtain more accurate energies, as geometries are less sensitive to the method employed than energies.

The energies obtained from reactants, products and transition states can be very useful to extract information about the thermodynamics (reaction energies, in equation 1.26) and kinetics (reaction activation barriers, in equation 1.27) of a certain reaction as represented in figure 1.32. The more negative the reaction energy, and the lower the activation barrier, the more favorable the reaction.

$$\Delta E_{rx} = \Delta E_{products} - \Delta E_{reactants} \tag{1.26}$$

$$\Delta E^{\ddagger} = \Delta E_{transitionstate} - \Delta E_{reactants} \tag{1.27}$$

Activation and reaction energies are better represented in terms of enthalpies

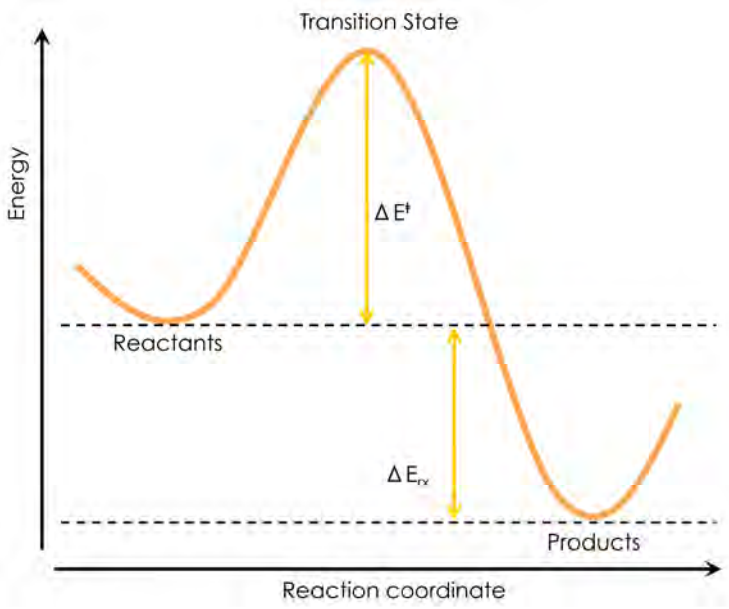

Figure 1.32: Schematic reaction profile where reactants, transition state and products are represented along the reaction coordinate, as well as the activation energy ($\Delta E^{\ddagger}$) and reaction energy (ΔE_{rx}).

or Gibbs energies. They are obtained using the equivalent expressions to equations 1.26 and 1.27. Gibbs energies have significant interest when the number of reacting molecules changes along the reaction coordinate, which implies a modification of the total entropy of the system. To obtain the enthalpies or Gibbs energies using the thermostatistic expressions it is needed a frequency calculation, *i.e.* computing the second derivates of the energy with respect to Cartesian coordinates.

1.10.3 Frontier molecular orbital theory

In 1967, Fukui developed the *Frontier Molecular Orbital* (FMO) Theory.[319–321] This methodology is widely used to understand and predict the reactivity and regioselectivity of cycloaddition reactions, and for Diels-Alder and 1,3-dipolar reactions in particular.

The simplest but representative description of the FMO theory was expressed by Fukui as "*those orbitals will interact most which overlap best and are closest in energy*".[320] If the two orbitals contain two or three electrons, the interaction will result in a stabilization, or a net lowering of electronic energy, while

the presence of four electrons, a destabilization will occure as a result of a closed-shell repulsion. Regarding to the stabilizing terms, those arising from the interaction of the highest energy occupied molecular orbital (HOMO) of one molecule with the lowest unnoccupied molecular orbital (LUMO) of the second, and *vice versa*, will dominate energy changes, since these orbitals are the closest in energy.[319]

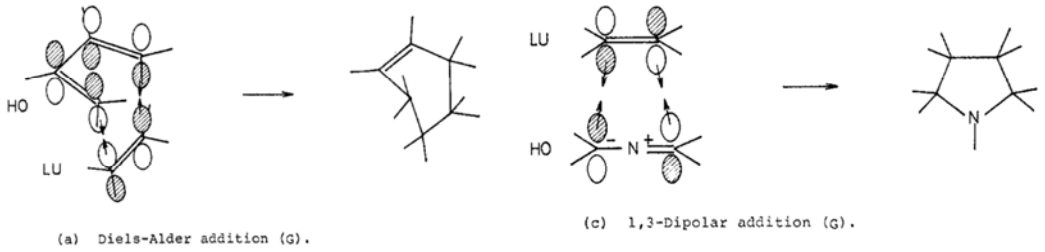

Figure 1.33: Diels-Alder and 1,3-dipolar intermolecular HOMO-LUMO orbital interactions in terms of FMO theory (adapted with permission from ref.[320]).

From the FMO, it is clear that the usual strongest orbital interaction in the Diels-Alder reaction (and 1,3-dipolar) is produced between the HOMO of the diene (dipole) and the LUMO of the dienophile (dipolarophile), as showed in figure 1.33. But different interations can be found, and thus 1,3-dipolar reactions can be classified into different types: *i*) class I, the most significant contribution comes from the interaction between the HOMO of the dipole and the LUMO of the dipolarophile; *ii*) class II, the most important contribution is the one between the LUMO of the dipole and the HOMO of the dipolarophile; and *iii*) class III, where both interactions are approximately equal. Nevertheless, in the case of the Diels-Alder reaction there exists a strong electronic substituent effect. If an electron-poor diene and an electron-rich dienophile react, the strongest orbital interaction which take place is between the HOMO of the dienophile and the LUMO of the diene. That is called inverse electron demand Diels-Alder reaction. Usually Diels-Alder reactions in fullerenes follow a normal electronic demand, that is, fullerene acting as a dienophile and contributing more with its LUMO orbital.

The application of FMO theory on the Diels-Alder and 1,3-dipolar reactions gives a rational explanation of the experimentally observed regioselectivites and reactivity trends. For example, the group of Prof. Houk has extensively studied the cycloaddition reactions in terms of FMO theory.[322,323] They early reported the computation of orbital energies and coefficients of 1,3-dipoles and

dipolarophiles,[322] showing that substituents have a large effect on them, and explained the different reactivity trends experimentally observed. In addition to that, and based on the perturbational molecular orbital theory applied to cycloaddition reactions,[324] they showed that the greater stabilization of the transition state structures and final regioisomeric rates can be explained based on the FMO theory.[323]

Nevertheless, FMO theory fails for example when predicting the reactivity of polyaromatic hydrocarbon (PAH) compounds. For example, FMO predicts that the 1,4-addition to benzene is more favored than to the hexacene, although experimental observations and more accurate computational methods show that is just the opposite.[325]

1.10.4 Distortion-interaction / activation-strain model in cycloaddition reactions

A few years ago, Ess and Houk showed that the reactivity of cycloadditions of 1,3-dipoles with alkenes or alkyls is controlled by the energy required to distort the 1,3-dipole and dipolarophile to the transition state geometry.[326,327] This conclusion was later expanded to the Diels-Alder additions on small alkenes and aromatic molecules.[226,328,329]

The distortion-interaction model[326,327] or activation-strain model[330,331] is a fragment approach to analyze the behavior of chemical reactions, in which the height of reaction barriers is described in terms of the original reactants.[330,332] This model is an extension of the fragment approach initially used by Morokuma to analyze stable molecules.[333] Within the distortion-interaction model, the reaction energy along the reaction coordinate is decomposed into two contributions: the distortion (strain) term ΔE_d; and the interaction term ΔE_i. When this model is applied to the transition state structure, the barrier can be defined as

$$\Delta E^{\ddagger} = \Delta E_d^{\ddagger} + \Delta E_i^{\ddagger} \tag{1.28}$$

The distortion energy (deformation energy) is defined as the energy required to deform the reactant structures from their equilibrium geometry to the geometry they present in the transition state, without allowing the interaction between the fragments, which corresponds to the interaction energy term, as represented in figure 1.34.

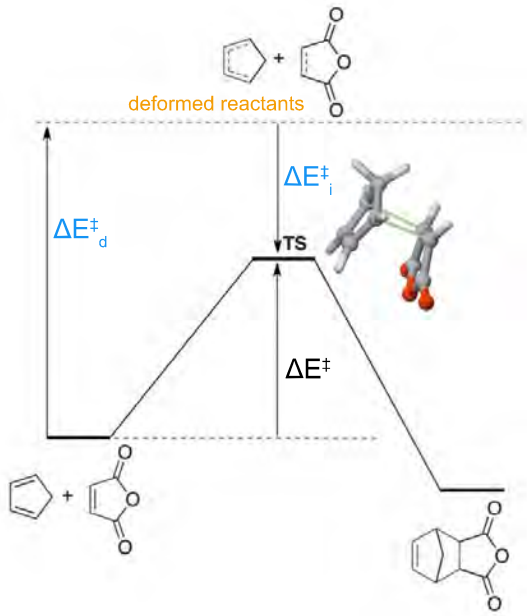

Figure 1.34: Schematic representation of the distortion-interaction / activation-strain model in cycloaddition reactions (adapted from ref.[331]).

In general, deformation energies are positive, which means that they are destabilizing, while interaction energies are negative, counteracting the deformation term and stabilizing the system. For cycloaddition reactions, a good correlation has been found between activation barriers and distortion energies. A high reaction barrier implies a higher deformation of the reactants in the transition state, although this is not always the case.[327,334]

In 2009, Osuna and Houk reported the first analysis of the Diels-Alder cycloadditions and 1,3-dipolar additions of azomethine ylide, fulminic acid, and methylene nitrone to polyacenes, fullerenes and carbon nanotubes.[334] They observed that activation barriers of cycloaddition reactions on these planar and curved systems, including fullerenes, was highly correlated to the energy needed to distort the reactants to the transition state geometry.[334]

In the present thesis, the distortion-interaction model has been applied to analyze the reactivity of endohedral metallofullerenes for the first time (see chapter 3).[237,335] The Diels-Alder reactivity between 1,3-cis-butadiene and D_{3h}-C_{78}-based Sc_3N, Y_3N, and Ti_2C_2 EMFs in comparison to the pristine D_{3h}-C_{78} empty fullerene have been studied and analyzed in detail.

Later on, different studies about the Diels-Alder reactivity on endohedral fullerenes have been reported where the same distortion-interaction (activation-strain) analysis as the ones reported in this thesis[237,335] have been carried out.[336,337]

Deformation energy is an effective tool to understand the chemistry of fullerene compounds. Usually, but not always, the most reactive bonds of an (endo)fullerene cage are those which involve lower deformation energies to reach the TS.[241,242] Moreover, the insertion of a large compound inside the fullerene cavity implies also a deformation energy. An extremely high deformation energy found theoretically for the encapsulation of the moiety inside the fullerene means that the endohedral fullerene will not be experimentally formed.

In this context, we have introduced in this thesis a new energetic parameter, the so-called *non-cluster deformation energy*, which allows us to understand the reactivity differences between the equivalent bonds of free cages and endohedral derivatives.[237,335] The electronic effects due to the encapsulation of the cluster moiety on the reaction barrier can be evaluated as the difference between a single point energy calculation of the TS optimized structure where the metallic cluster is removed, and the SP energy calculation of the reactant structure also without the cluster inside. As it will be extensively discussed in chapter 3, bonds presenting the highest values for this parameter are those exhibiting the largest differences in the reactivity when comparing the free and endohedral fullerenes.[237,335]

1.10.5 Semiempirical methods as a first approach

In this thesis, in order to investigate the relative stability of thousands of fullerene isomeric structures, semiempirical methods have been used as a first approach to compute them. More specifically, the Austin Model 1 (AM1)[338] method has been employed when a large amount of fullerene structures had to be optimized.

In a previous work, Rodríguez-Fortea *et al.*[145] showed that there exists a good correspondence between the relative stabilities of fullerene isomers computed at DFT BP86/TZP level and semiempirical AM1 level (see table 1.3). Thus demonstrating that AM1 optimized structures are good starting points to make a first selection of the most stable structures to be further re-optimized using computationally more expensive DFT methods.

Table 1.3: Relative energies at AM1 and DFT BP86/TZP levels (in kcal·mol^{-1}) for the five most stable C_{104}^{4-} IPR isomers (adapted from ref.[145]).

Isomer	822	821	816	706	553
symmetry	D_{3d}	D_2	C_2	C_2	C_2
ΔE AM1	0.0	8.6	9.6	10.2	10.3
ΔE DFT	0.0	5.6	5.9	8.5	9.3

The AM1 method[338] developed by Dewar and co-workers in the 1980s, is a semiempirical method to compute the electronic structure of chemical systems. The AM1 was based on the previous semiempirical method MNDO, but among other differences it uses a different parametrization. Dewar semiempirical methods are mainly based on the *neglect of differential diatomic overlap* integral approximation (NDDO), introduced by John Pople.[339] The approximations used in the semiempirical AM1 formulation allow to solve the Schrödinger equation in a computationally efficient way, obtaining reasonable energy estimations when the treated system is not very different from those species used during the AM1 parametrization.

An extensive review of these semiempirical methods can be found in "*Essentials of computational chemistry: theory and models*", by Christopher J. Cramer.[267]

1.10.6 Aromaticity indexes

In the next subsections, the aromaticity indicators used in this thesis are described.

Geometric index: HOMA

The HOMA index has been applied as a geometry-based indicator of local aromaticity.[340,341] According to its definition, the HOMA index can be expressed as defined in equation 1.29.

$$HOMA = 1 - \frac{1}{n}\sum_{j=1}^{n} \alpha_i (R_{opt,i} - R_j) \tag{1.29}$$

where n represents the total number of bonds in the molecule or the considered ring and α_i is a normalization constant (for C-C, $R_{opt,C-C} = 1.388$ Å and

$\alpha_{C-C} = 257.7$) fixed to give $HOMA = 0$ for a model non-aromatic system, e.g. the Kekulé structure of benzene, and $HOMA = 1$ for the system in which all bonds are equal to the optimal value $R_{opt,i}$, assumed to be realized for fully aromatic systems.

In this thesis, the HOMA index has been evaluated using the HOMA code by Dr. Eduard Matito.

Magnetic index: NICS

One of the most widely employed indicators of aromaticity is the NICS.[342,343] This is a magnetic indicator of aromaticity defined as the negative value of absolute shielding computed at a ring center (or in the cage center in fullerenes) determined by the non-weighted average of the heavy atoms' coordinates in the ring. NICS(0) values calculated in the center of the five- or six-membered rings may contain important spurious contributions from the in-plane tensor components that are not related to aromaticity.[344] For this reason, NICS(1) measured at 1 Å above the center of the ring or NICS(1)$_{zz}$ (the zz NICS tensor component perpendicular to the ring) are preferred.[36,342,345] Both NICS(1) and NICS(1)$_{zz}$ better reflect aromaticity patterns because at 1 Å the effects of the π-electron ring current are dominant and local σ-bonding contributions are diminished.

The magnetic index NICS has been determined using the GIAO method[346] to compute the *isotropic shielding* of different ghost atoms (Bq) placed in the center of the rings (NICS(0)), and 1 Å above and below the center (NICS(1)$_{zz}$, NICS(-1)$_{zz}$), as implemented in the Gaussian09 software.[294]

Electronic index: MCI

In this thesis, the multicenter index (MCI) has been employed as an electronic-based aromaticity indicator. MCI[347,348] is a particular extension of the I_{ring} index,[349] described as

$$I_{ring}(A) = 2^N \sum_{i_1,i_2,\ldots,i_N}^{OCC} S_{i_1 i_2}(A_1) S_{i_2 i_3}(A_2) \ldots S_{i_N i_1}(A_N) \tag{1.30}$$

being $S_{ij}(A)$ the overlap between MOs i and j within the molecular space assigned to atom A. More recently, Cioslowski, Matito and Solà[350] proposed the normalization of I_{ring} index as follows

$$I_{NG}(A) = \frac{\pi^2}{4NN_\pi} I_{ring}(A)^{1/N} \tag{1.31}$$

where N is the total number of atoms in the ring and N_π the total number of π electrons.

Summing up all the I_{ring} values resulting from the permutations of indices $A_1, A_2, ..., A_n$, the MCI index is obtained as:

$$MCI(A) = \frac{1}{2N} \sum_{P(A)} I_{ring}(A) = \frac{1}{2N} \sum_{P(A)} \sum_{i_1,i_2,...,i_N}^{OCC} S_{i_1 i_2}(A_1) S_{i_2 i_3}(A_2) ... S_{i_N i_1}(A_N) \tag{1.32}$$

where $P(A)$ stands for a permutation operator which interchanges the atomic labels $A_1, A_2, ..., A_N$ to generate up to the $N!$ permutations of the elements in the string A. As a result of the large amount of permutations that needs to be computed, this index has a high computational cost associated that limits its use to rings up to nine members.

Finally, a normalized version of the MCI index, the so-called I_{NB},[350] can be described as

$$I_{NB}(A) = \frac{C}{NN_\pi} [2N \cdot MCI(A)]^{1/N} \tag{1.33}$$

where N is the total number of atoms in the ring, N_π is the total number of π electrons, and C≈1.5155, which is a proportionality constant.

Both MCI and I_{ring}, and their corresponding normalized versions, give an idea of the electron sharing between all atoms in the ring.

The atomic overlap matrices have been obtained using an overlapping atomic definition. In these schemes, at every point r of the space a weight funtion $\omega_A(r)$ is defined for each atom A to measure to which extent the given point belongs to atom A. These atomic weight factors are chosen to be non-negative and satisfy the condition $\sum_A \omega_A(r) = 1$ when summing over all atoms of the system.

$$S_{ij}(A) = \int \psi_i^*(r) \omega_A(r) \psi_j(r) dr \tag{1.34}$$

In this thesis, we have defined the weight functions $\omega(r)$ according to the topological fuzzy Voronoi cells (TFVC)[351] partition scheme. The TFVC represents a fast and simple alternative to Bader's Quantum Theory of Atoms

in Molecules (QTAIM) scheme. TVFC can be routinely applied to large-scale calculations, being computationally more efficient than QTAIM procedures.[351] The results obtained using this integration scheme are quite close to those generated with the QTAIM partition.[351,352] The atomic overlap matrices have been computed using APOST-3D program by Dr. Eloy Ramos-Cordoba and Dr. Pedro Salvador.[353] The program implements a Becke's multicenter integration[354,355] algorithm with Chebyshev radial and Lebedev angular quadratures. The MCI index of aromaticity has been calculated using the ESI-3D program by Dr. Eduard Matito.[356,357]

The unique combination of Becke's multicentered integration as implemented in APOST-3D, and the calculation of the delocalization indices and MCI index as implemented in ESI-3D software has made possible the aromaticity studies reported in this thesis.

For these indices, the higher the HOMA, and MCI values and the lower the NICS (more negative), the more aromatic the ring in question is.

1.10.7 Tools used to predict and understand fullerene reactivity

Bond distances

The regioselectivity of a cycloaddition reaction on a fullerene cage can be described and rationalized in terms of carbon-carbon bond distances. The shortest bond distances indicate a higher π electronic density and π bonding orbital interactions on the highest occupied molecular orbital (HOMO). The [6,6] bonds are usually the shortest bonds in the cage. On the other hand, [5,6] bonds are usually the larger as a consequence of the antibonding π contribution of the orbitals present in the HOMO. Shorter C-C distances are associated with a higher reactivity. This is because shorter C-C bonds have more double bond character that facilitates the interaction with dienes/dipoles in cycloaddition reactions. However, very frequently it is not possible to rationalize the relative stabilities of the final fullerene adducts or the reaction barriers only considering the C-C bond distances. There are reported several studies regarding EMFs where, for example, the Diels-Alder reaction occurs on one of the longest C-C bond of the fullerene structure.[242]

Pyramidalization angles

The relationship between chemical reactivity and the carbon pyramidalization angle (θ_p) was proposed by Haddon.[358,359] The carbon pyramidalization angle is a simple a measure of the local curvature of carbon containing systems, which is defined by equation 1.35.

$$\theta_p = \theta_{\sigma\pi} - 90^\circ \tag{1.35}$$

$\theta_{\sigma\pi}$ is defined as the vector that equalizes the three angles between the vector centred on the atom of interest, and the three attached bonds, as represented in figure 1.35. The pyramidalization angle for sp^2 carbon centers is 0° and for sp^3 is 19.47°.

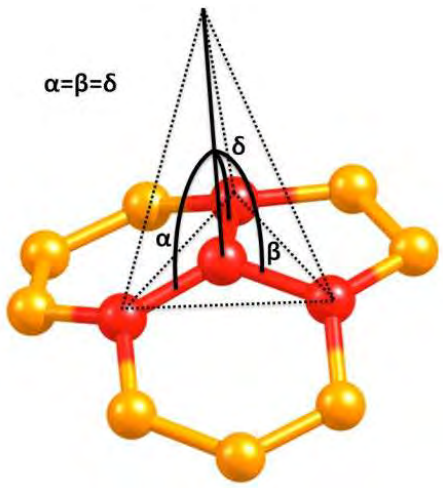

Figure 1.35: Representation of the pyramidalization angle. A vector (black colored in the figure) that equalizes the α, β and δ angles is defined in order to compute the final pyramidalization angle value ($\theta_p = \alpha - 90^\circ$).

The more pyramidalized the carbon atoms are, the closer to the final sp^3 situation and the lower the deformation of the system to achieve the TS that connects reactants with products. Thus in principle, those bonds with higher pyramidalization angles are expected to be more reactive. Although pyramidalization angles are useful to understand the empty fullerenes reactivities, when EMFs are considered there are several cases where the reactivity is not well described.

All pyramidalization angle measures reported in this thesis were evaluated using the π-orbital axis vector approach (POAV1)[20] as implemented in the POAV3 program.[360]

Frontier orbitals

As described prevously, FMO theory is a powerful tool to describe and analyze cycloaddition reactions. When fullerenes or endohedral metallofulleres are considered as dienophiles or dipolarophiles, the interaction that takes place during the Diels-Alder or 1,3-dipolar reaction could be the one between the HOMO of fullerene and the LUMO of *viceversa*. Usually, the most prominent contribution is the one between the HOMO of the diene and the LUMO of the fullerene compound due to the stabilized LUMO orbitals of the fullerenes.

The theoretical analysis of the distribution and shape of the LUMO orbitals of fullerene compounds might give a prediction of the most reactive C-C positions. Only those bonds presenting a suitable shape (an antibonding π contribution) to interact with the HOMO of the diene should be reactive. It is important to notice here that fullerene orbitals are highly delocalized, so a large number of C-C bonds with suitable orbitals for interacting with diene are usually found.

A simple indicator to get an estimation of the relative reactivity between two different species is to directly compare the energy of their LUMO orbital which should interact with the HOMO of the diene. In principle, one expects that the one presenting the lowest energy LUMO, closest in energy to the HOMO of the diene, would be more reactive.

The difference in energy between the HOMO and LUMO (*i.e.* the HOMO-LUMO gap) also gives an idea of how reactive the considered fullerene is.[242] Small gaps are usually found for highly reactive compounds. Introducing moieties inside the fullerene cages to obtain the endohedral fullerene compounds, usually implies an increase of the HOMO-LUMO gap, which usually leads to a reduction of the exohedral chemical reactivity.[242]

Chapter 2

Objectives

Since the discovery of C_{60} in 1985, the interest for understanding the structure, properties and reactivity of fullerene compounds has attracted the broad interest of researchers. This is mainly due to the potential applications of these compounds to obtain new (bio)materials for constructing more efficient solar cells, for its application as magnetic resonance imaging contrast agents, or as biomedical radiotracers, for example. The main goal of this thesis is to apply state-of-the-art computational tools to further understand the chemical structure and reactivity of these fascinating compounds, and the related endohedral (metallo)fullerenes.

This thesis is divided in three main blocks. The first block is devoted to the computational study of the Diels-Alder cycloaddition reaction on endohedral metallofullerenes. The second part is centered on the understanding of the factors that control the thermodynamic stability and isomerization rate of (metallo)fulleropyrrolidines, while in the third block the aromaticity of endohedral metallofullerenes is thoroughly studied and linked to their stability and reactivity.

The first functionalization of a trimetallic nitride template (TNT) endohedral metallofullerene was achieved through a Diels-Alder addition on the most abundant EMF, the $S_3N@I_h$-C_{80}. The Diels-Alder reaction represents a very powerful tool for functionalizing endohedral metallofullerenes, although the complete understanding of its regioselectivity is still not clear. *The first objective of this thesis is to investigate the effect of the encapsulation of metallic clusters of different nature on the Diels-Alder regioselectivity and reaction rate.* Therefore, the Diels-Alder [4+2] cycloaddition reaction on the $Ti_2C_2@C_{78}$ metallic carbide is explored and compared to the previously studied $M_3N@C_{78}$ (M=Sc, Y) systems. In addition, the exohedral Diels-Alder reactivity of I_h-

C_{80} based EMFs is analyzed for a different set of metals and metallic clusters: metallic ions, TNTs, metallic carbides hydrocarbides and carbonitrides, and metallic oxides. To that end, *the second objective of this thesis is to develope new computational tools, indicators and approaches to feasibly and accurately study the Diels-Alder cycloaddition on endohedral metallofullerenes.* The effect of the diene nature on the Diels-Alder addition on EMFs has never been considered up to date. *The third objective is to rationalize the different regioselectivity experimentally observed for the Diels-Alder addition when different dienes are used.* We computationally explore the Diels-Alder addition of cyclopentadiene and (1,2,3,4,5-pentamethyl)-cyclopentadiene on $La@C_{82}$, which have been reported to occur in a different regioselective manner.

The 1,3-dipolar addition of azomethine ylides to fullerenes, *i. e.* the Prato reaction, is a versatile and widely used method for functionalizing EMFs. Depending on the substituents on the azomethine ylide quiral fulleropyrrolidines can be generated. It has been shown that different kinetic and thermodynamic regioselectivities are found depending on the encapsulated metallic cluster. Additionally, the possibility of isomerization from the kinetic products to the thermodynamic ones has been reported. A complete understanding of the factors that control the thermodynamic equilibrium, and the isomerization process have, however, not been assessed. *The fourth objective of this thesis is to study the effect of the endohedral moieties and exohedral substituents on the thermodynamic regioselectivity and kinetic isomerization between different possible regioisomeric or enantiomeric fulleropyrrolidines.* To achieve this objective, the isomerization from kinetic [6,6] to thermodynamic more stable [5,6] fulleropyrrolidines of $M_3N@I_h$-C_{80} (M=Sc, Lu, Y, Gd) EMFs including different exohedral substituents is analyzed. Furthemore, the enantiospecific isomerization of C_{60} and $H_2O@C_{60}$ chiral fulleropyrrolidines is evaluated focusing on the role played by the encapsulated water molecule on the isomerization rate. *The fifth objective is to determine the factors that control the thermodynamic Prato bisadduct addition on EMFs*, focusing on the role played by the metallic cluster, and how the first addition affects the second reaction in $M_3N@I_h$-C_{80} (M=Y, Gd) EMFs.

Aromaticity is a fascinating property that accounts for the molecular and electronic structure, stability and reactivity of many different compounds. Although empty neutral fullerenes have ambiguous aromatic character and its aromaticity has been widely studied from different points of view, the role of aromaticity on endohedral metallofullerene compounds has still not been considered. Encapsulated metallic clusters dictate the electronic structure, stability and reactivity of endohedral metallofullerenes. In that sense, *the sixth*

objective of this thesis is to, for the first time, study the role of the aromaticity on the endohedral metallofullerene compounds stabilities. To this end, the aromaticity of the different negatively charged C_{2n} fullerene isomers, which are used as models to describe the relative stabilities of EMFs, are analyzed. The Bingel-Hirsch reaction is one of the most employed strategies for functionalizing fullerene compounds. It takes place through a two-step mechanism which includes nucleophilic S_N2 substitution. In that sense, it is expected that the electronic structure of EMFs plays a major role in determining the regioselectivity of these reactions. Since aromaticity is an indicator of the electronic structure distribution, *the seventh objective of this thesis is to identify a Bingel-Hirsch reactivity pattern for the additions on EMFs based on aromaticity criteria to predict the regioselectivity of these reactions.* To achieve this goal, the Bingel-Hirsch reaction involving endohedral metallofullerenes is explored, analyzed and rationalized using aromaticity measures.

Chapter 3

Diels-Alder additions on Endohedral MetalloFullerenes

3.1 The Exohedral Diels-Alder Reactivity of the Titanium Carbide Endohedral Metallofullerene $Ti_2C_2@D_{3h}$-C_{78}: Comparison with D_{3h}-C_{78} and $M_3N@D_{3h}$-C_{78} ($M = Sc, Y$) Reactivity

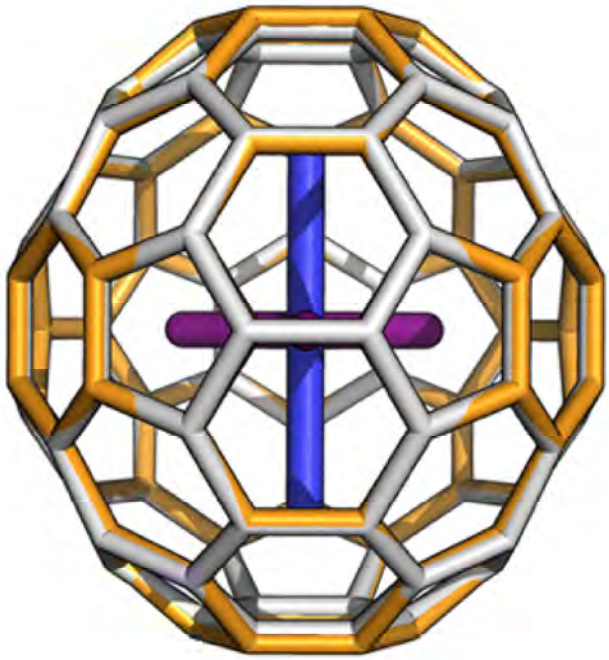

Garcia-Borràs, M.; Osuna, S.; Luis, J.M.; Swart, M.; Solà, M., **The Exohedral Diels-Alder Reactivity of the Titanium Carbide Endohedral Metallofullerene $Ti_2C_2@D_{3h}$-C_{78}: Comparison with D_{3h}-C_{78} and $M_3N@D_{3h}$-C_{78} (M=Sc and Y) Reactivity**, *Chem. Eur. J.*, **2012**, 18, 7141-7154.

M.G.-B. participated in the design of the project, performed all the calculations, analyzed the results, and co-wrote the manuscript.

Garcia-Borràs, M., Osuna, S., Luis, J. M., Swart, M. and Solà, M. "The Exohedral Diels–Alder Reactivity of the Titanium Carbide Endohedral Metallofullerene Ti2C2@D3h-C78: Comparison with D3h-C78 and M3N@D3h-C78 (M=Sc and Y) Reactivity". *Chem. Eur. J.* Vol. 18 (2012) : 7141–7154

http://dx.doi.org/10.1002/chem.201103701

http://onlinelibrary.wiley.com/doi/10.1002/chem.201103701/full

Article first published online: 19 APR 2012

Abstract

The chemical functionalization of endohedral (metallo)fullerenes has become a main focus of research in the last few years. It has been found that the reactivity of endohedral (metallo)fullerenes may be quite different from that of the empty fullerenes. Encapsulated species have an enormous influence on the thermodynamics, kinetics, and regiochemistry of the exohedral addition reactions undergone by these species. A detailed understanding of the changes in chemical reactivity due to incarceration of atoms or clusters of atoms is essential to assist the synthesis of new functionalized endohedral fullerenes with specific properties. Herein, we report the study of the Diels–Alder cycloaddition between 1,3-butadiene and all nonequivalent bonds of the Ti_2C_2@D_3h-C_{78} metallic carbide endohedral metallofullerene (EMF) at the BP86/TZP//BP86/DZP level of theory. The results obtained are compared with those found by some of us at the same level of theory for the D_3h-C_{78} free cage and the M_3N@D_3h-C_{78} (M=Sc and Y) metallic nitride EMFs. It is found that the free cage is more reactive than the Ti_2C_2@D_3h-C_{78} EMF and this, in turn, has a higher reactivity than M_3N@D_3h-C_{78}. The results indicate that, for Ti_2C_2@D_3h-C_{78}, the corannulene-type [5, 6] bonds **c** and **f**, and the type B [6, 6] bond **3** are those thermodynamically and kinetically preferred. In contrast, the D_3h-C_{78} free cage has a preference for addition to the [6, 6] **1** and **6** bonds and the [5, 6] **b** bond, whereas M_3N@D_3h-C_{78} favors additions to the [6, 6] **6** (M=Sc) and [5, 6] **d** (M=Y) bonds. The reasons for the regioselectivity found in Ti_2C_2@D_3h-C_{78} are discussed.

Keywords

bond theory; cage compounds; cycloaddition; fullerenes; regioselectivity

3.2 The Frozen Cage Model: A Computationally Low-Cost Tool for Predicting the Exohedral Regioselectivity of Cycloaddition Reactions Involving Endohedral Metallofullerenes

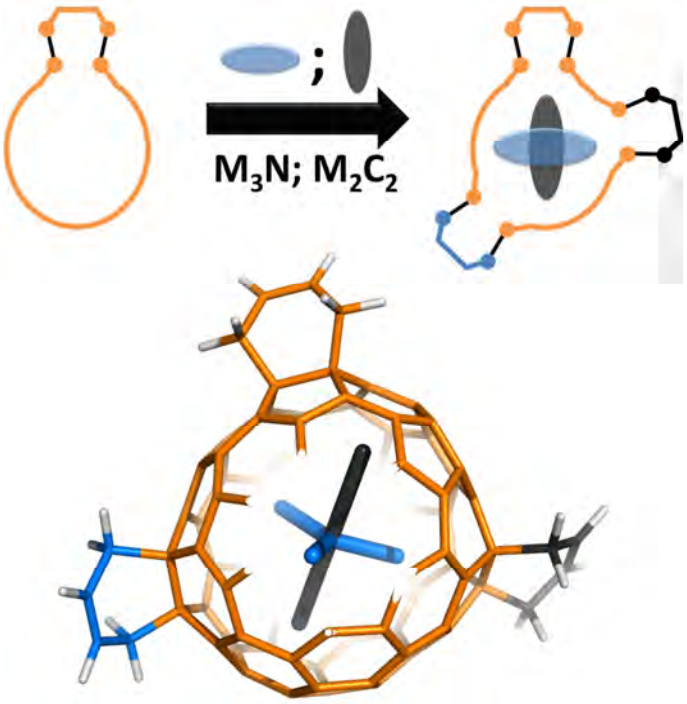

Garcia-Borràs, M.; Romero-Rivera, A., Osuna, S.; Luis, J.M.; Swart, M.; Solà, M., **The Frozen Cage Model: A Computationally Low-Cost Tool for Predicting the Exohedral Regioselectivity of Cycloaddition Reactions Involving Endohedral Metallofullerenes**, *J. Chem. Theory Comput.*, **2012**, 8, 1671-1683.

M.G.-B. participated in the design of the project, performed the calculations, analyzed the results, and co-wrote the manuscript. He also co-supervised the undergraduate student A.R.-R.

Marc Garcia-Borràs, Adrian Romero-Rivera, Sílvia Osuna, Josep M. Luis, Marcel Swart, and Miquel Solà. "The Frozen Cage Model: A Computationally Low-Cost Tool for Predicting the Exohedral Regioselectivity of Cycloaddition Reactions Involving Endohedral Metallofullerenes". *Journal of Chemical Theory and Computation*. Vol 8, Issue 5 (2012) : 1671-1683

http://dx.doi.org/10.1021/ct300044x

http://pubs.acs.org/doi/abs/10.1021/ct300044x

Publication Date (Web): March 15, 2012

Abstract

Functionalization of endohedral metallofullerenes (EMFs) is an active line of research that is important for obtaining nanomaterials with unique properties that might be used in a variety of fields, ranging from molecular electronics to biomedical applications. Such functionalization is commonly achieved by means of cycloaddition reactions. The scarcity of both experimental and theoretical studies analyzing the exohedral regioselectivity of cycloaddition reactions involving EMFs translates into a poor understanding of the EMF reactivity. From a theoretical point of view, the main obstacle is the high computational cost associated with this kind of studies. To alleviate the situation, we propose an approach named the frozen cage model (FCM) based on single point energy calculations at the optimized geometries of the empty cage products. The FCM represents a fast and computationally inexpensive way to perform accurate qualitative predictions of the exohedral regioselectivity of cycloaddition reactions in EMFs. Analysis of the Dimroth approximation, the activation strain or distortion/interaction model, and the noncluster energies in the Diels–Alder cycloaddition of *s-cis*-1,3-butadiene to X@D_{3h}-C_{78} (X = Ti_2C_2, Sc_3N, and Y_3N) EMFs provides a justification of the method.

Keywords

bond theory; cage compounds; cycloaddition; fullerenes; regioselectivity

3.3 A Complete Guide on the Influence of Metal Clusters in the Diels-Alder Regioselectivity of I_h-C_{80} Endohedral Metallofullerenes

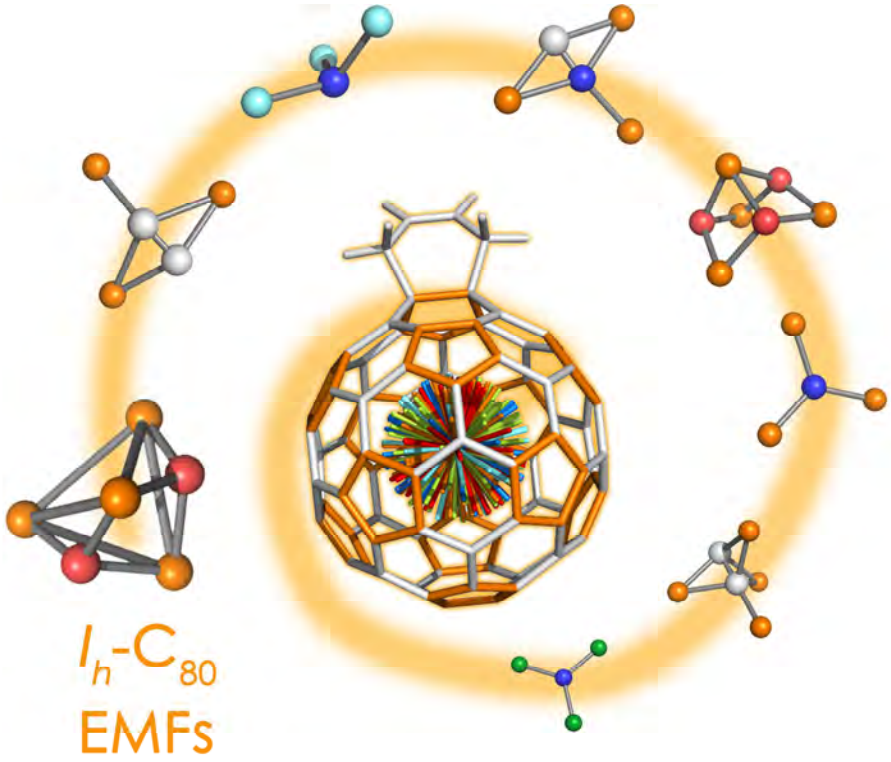

Garcia-Borràs, M.; Osuna, S.; Luis, J.M.; Swart, M.; Solà, M., **A Complete Guide on the Influence of Metal Clusters in the Diels-Alder Regioselectivity of Ih-C80 Endohedral Metallofullerenes**, *Chem. Eur. J.*, **2013**, 19, 14931-14940.

M.G.-B. conceived the initial project, developed the different scripts used to manage the data, performed all the calculations, analyzed the results, and co-wrote the manuscript.

Garcia-Borràs, M., Osuna, S., Luis, J. M., Swart, M. and Solà, M. "A Complete Guide on the Influence of Metal Clusters in the Diels–Alder Regioselectivity of Ih-C80 Endohedral Metallofullerenes" . *Chem. Eur. J.* Vol. 19 (2013) : 14931–14940

http://dx.doi.org/10.1002/chem.201302202

http://onlinelibrary.wiley.com/doi/10.1002/chem.201302202/full

Article first published online: 13 SEP 2013

Abstract

The chemical functionalization of endohedral metallofullerenes (EMFs) has aroused considerable interest due to the possibility of synthesizing new species with potential applications in materials science and medicine. Experimental and theoretical studies on the reactivity of endohedral metallofullerenes are scarce. To improve our understanding of the endohedral metallofullerene reactivity, we have systematically studied with DFT methods the Diels–Alder cycloaddition between s-*cis*-1,3-butadiene and practically all X@I_h-C_{80}EMFs synthesized to date: X=Sc_3N, Lu_3N, Y_3N, La_2, Y_3, Sc_3C_2, Sc_4C_2, Sc_3CH, Sc_3NC, Sc_4O_2 and Sc_4O_3. We have studied both the thermodynamic and kinetic regioselectivity, taking into account the free rotation of the metallic cluster inside the fullerene. This systematic study has been made possible through the use of the frozen cage model (FCM), a computationally cheap approach to accurately predicting the exohedral regioselectivity of cycloaddition reactions in EMFs. Our results show that the EMFs are less reactive than the hollow I_h-C_{80} cage. Except for the Y_3 cluster, the additions occur predominantly at the [5,6] bond. In many cases, however, a mixture of the two possible regioisomers is predicted. In general, [6,6] addition is favored in EMFs that have a larger charge transfer from the metal cluster to the cage or a voluminous metal cluster inside. The present guide represents the first complete and exhaustive investigation of the reactivity of I_h-C_{80}-based EMFs.

Keywords

metal clusters; cycloaddition; density functional calculations; Diels-Alder reactions; fullerenes; regioselectivity

3.4 Diels-Alder and Retro-Diels-Alder Cycloadditions of (1,2,3,4,5-Pentamethyl)cyclopentadiene to $La@C_{2v}$-C_{82}: Regioselectivity and Product Stability

Garcia-Borràs, M.; Luis, J.M.; Swart, M.; Solà, M., **Diels-Alder and Retro-Diels-Alder Cycloadditions of (1,2,3,4,5-Pentamethyl)cyclopentadiene to $La@C_{2v}$-C_{82}: Regioselectivity and Product Stability**, *Chem. Eur. J.*, **2013**, 19, 4468-4479. Corrigendum: *Chem. Eur. J.*, **2013**, 19, 9739-9739.

M.G.-B. participated in the design of the project, performed the calculations, analyzed the results, and co-wrote the manuscript.

Garcia-Borràs, M., Luis, J. M., Swart, M. and Solà, M. "Diels–Alder and Retro-Diels–Alder Cycloadditions of (1,2,3,4,5-Pentamethyl)cyclopentadiene to La@C2v-C82: Regioselectivity and Product Stability". *Chem. Eur. J.* Vol. 19 (2013) : 4468–4479

http://dx.doi.org/10.1002/chem.201203517

http://onlinelibrary.wiley.com/doi/10.1002/chem.201203517/full

Article first published online: 10 FEB 2013

Abstract

One of the most important reactions in fullerene chemistry is the Diels–Alder (DA) reaction. In two previous experimental studies, the DA cycloaddition reactions of cyclopentadiene (Cp) and 1,2,3,4,5-pentamethylcyclopentadiene (Cp*) with La@C_2v-C_{82} were investigated. The attack of Cp was proposed to occur on bond **19**, whereas that of Cp* was confirmed by X-ray analysis to be over bond **o**. Moreover, the stabilities of the Cp and Cp* adducts were found to be significantly different, that is, the decomposition of La@C_2v-C_{82}Cp was one order of magnitude faster than that of La@C_2v-C_{82}Cp*. Herein, we computationally analyze these DA cycloadditions with two main goals: First, to compute the thermodynamics and kinetics of the cycloadditions of Cp and Cp* to different bonds of La@C_2v-C_{82} to assess and compare the regioselectivity of these two reactions. Second, to understand the origin of the different thermal stabilities of the La@C_{82}Cp and La@C_{82}Cp* adducts. Our results show that the regioselectivity of the two DA cycloadditions is the same, with preferred attack on bond **o**. This result corrects the previous assumption of the regioselectivity of the Cp attack that was made based only on the shape of the La@C_{82} singly occupied molecular orbital. In addition, we show that the higher stability of the La@C_{82}Cp* adduct is not due to the electronic effects of the methyl groups on the Cp ring, as previously suggested, but to higher long-range dispersion interactions in the Cp* case, which enhance the stabilization of the reactant complex, transition state, and products with respect to the separated reactants. This stabilization for the La@C_{82}Cp* case decreases the Gibbs reaction energy, thus allowing competition between the direct and retro reactions and making dissociation more difficult.

Keywords

cycloaddition; Diels–Alder reaction; fullerenes; lanthanum; regioselectivity

Chapter 4

1,3-Dipolar additions on Endohedral MetalloFullerenes

4.1 Essential Factors for Controlling the Equilibrium in Reversible Rearrangement of $M_3N@I_h$-C_{80} Fulleropyrrolidines: Exohedral Functional Groups versus Endohedral Metal Clusters

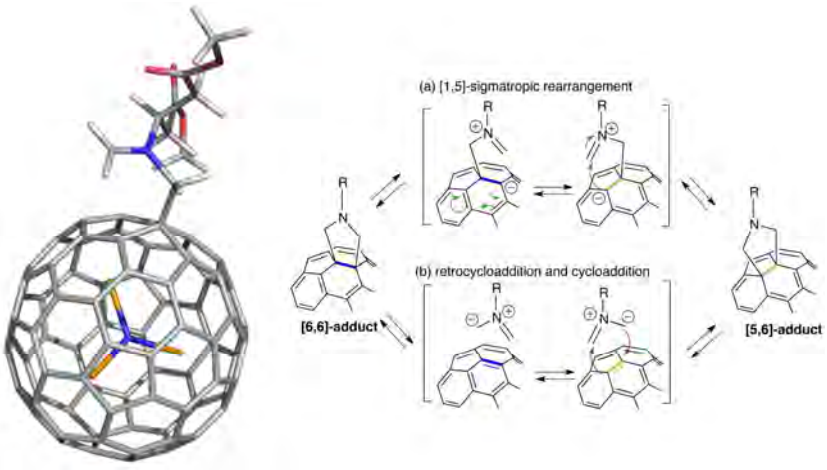

Aroua, S.;† Garcia-Borràs, M.;† Osuna, S.; Yamakoshi, Y., **Essential factors for controlling the equilibrium in reversible rearrangement of $M_3N@I_h$-C_{80} fulleropyrrolidines: exohedral functional groups versus endohedral metal clusters**, *Chem. Eur. J.*, **2014**, 20, 14032-14039. (†: The authors have equally contributed to the work)

M.G.-B. performed the DFT calculations, analyzed the computational results, and co-wrote the manuscript.

Aroua, S., Garcia-Borràs, M., Osuna, S. and Yamakoshi, Y. "Essential Factors for Control of the Equilibrium in the Reversible Rearrangement of M3N@Ih-C80 Fulleropyrrolidines: Exohedral Functional Groups versus Endohedral Metal Clusters". *Chem. Eur. J.* Vol. 20 (2014) : 14032–14039

http://dx.doi.org/10.1002/chem.201403743

http://onlinelibrary.wiley.com/doi/10.1002/chem.201403743/full

Article first published online: 5 SEP 2014

Abstract

The effects of exohedral moieties and endohedral metal clusters on the isomerization of $M_3N@I_h$-C_{80} products from the Prato reaction through [1,5]-sigmatropic rearrangement were systematically investigated by using three types of fulleropyrrolidine derivatives and four different endohedral metal clusters. As a result, all types of derivatives provided the same ratios of the isomers for a given trimetallic nitride template (TNT) as the thermodynamic products, thus indicating that the size of the endohedral metal clusters inside C_{80} was the single essential factor in determining the equilibrium between the [6,6]-isomer (kinetic product) and the [5,6]-isomer. In all the derivatives, the [6,6]- and [5,6]-Prato adducts with larger metal clusters, such as Y_3N and Gd_3N, were equally stable, which is in good agreement with DFT calculations. The reaction rate of the rearrangement was dependent on both the substituent of exohedral functional groups and the endohedral metal-cluster size. Further DFT calculations and ^{13}C NMR spectroscopic studies were employed to rationalize the equilibrium in the rearrangement between the [6,6]- and [5,6]-fulleropyrrolidines.

Keywords

DFT calculations; fullerenes; isomerization; nitrogen heterocycles; Prato reaction

4.2 Enantiospecific cis-trans Isomerization in Chiral Fulleropyrrolidines: H-Bonding assistance in the carbanion stabilization in $H_2O@C_{60}$

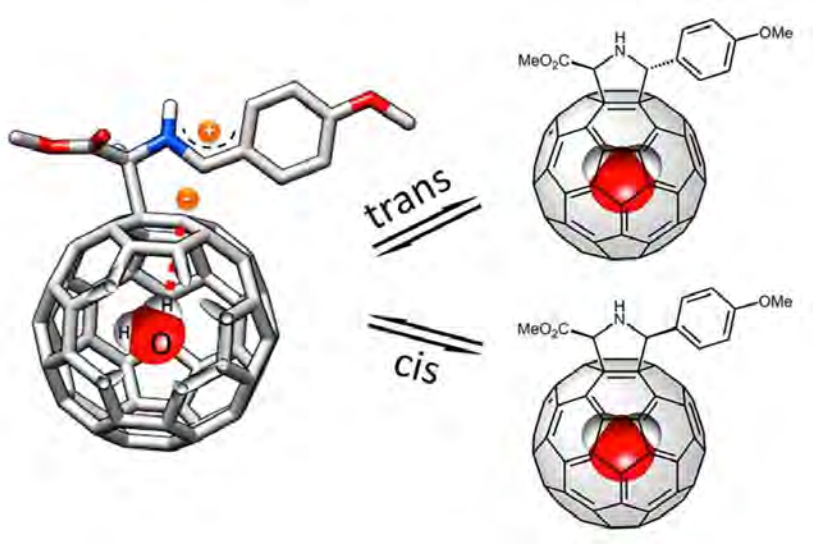

Maroto, E.E.; Mateos, J.; Garcia-Borràs, M.; Osuna, S.; Filippone, S.; Herranz, M. A.; Murata, Y.; Solà, M.; Martín, N., **Enantiospecific cis-trans Isomerization in Chiral Fulleropyrrolidines: H-Bonding assistance in the carbanion stabilization in $H_2O@C_{60}$**, *J. Am. Chem. Soc.*, **2015**, 137, 1190-1197.

M.G.-B. performed the DFT calculations, analyzed the computational results, and co-wrote the manuscript.

Enrique E. Maroto, Jaime Mateos, Marc Garcia-Borràs, Sílvia Osuna, Salvatore Filippone, María Ángeles Herranz, Yasujiro Murata, Miquel Solà, and Nazario Martín. “Enantiospecific cis–trans Isomerization in Chiral Fulleropyrrolidines: Hydrogen-Bonding Assistance in the Carbanion Stabilization in H2O@C60”. *Journal of the American Chemical Society*. Vol. 137, Issue 3 (2015) : 1190-1197

http://dx.doi.org/10.1021/ja5108854

http://pubs.acs.org/doi/abs/10.1021/ja5108854

Publication Date (Web): January 5, 2015

Abstract

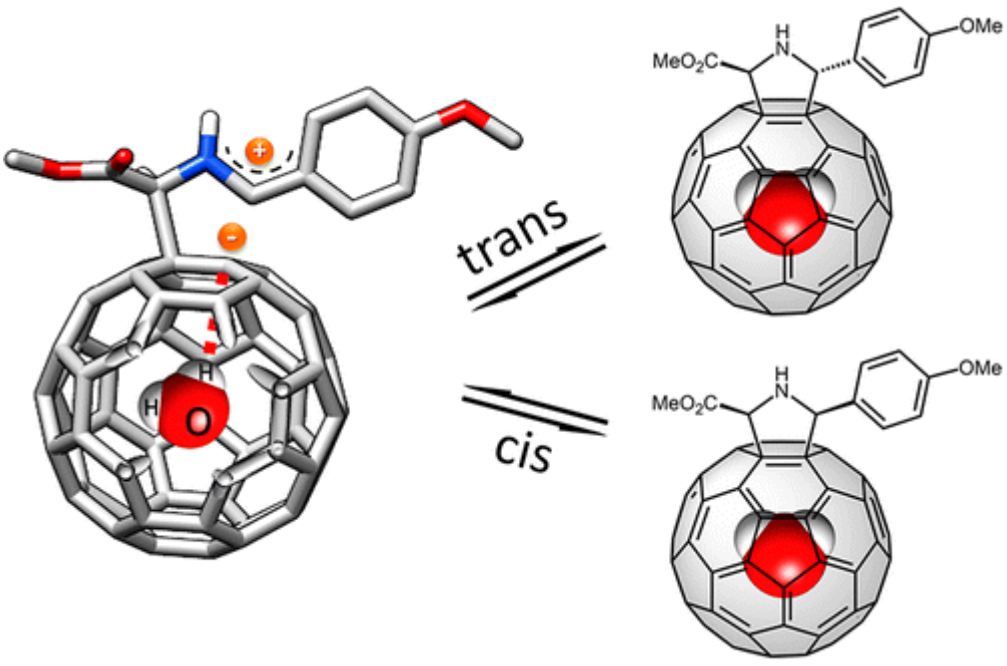

The stereochemical outcome of *cis–trans* isomerization of optically pure [60], [70], and endohedral $H_2O@C_{60}$ fulleropyrrolidines reveals that the electronic nature of substituents, fullerene size, and surprisingly the incarcerated water molecule plays a crucial role in this rearrangement process. Theoretical DFT calculations are in very good agreement with the experimental findings. On the basis of the experimental results and computational calculations, a plausible reaction mechanism

involving the hydrogen-bonding assistance of the inner water molecule in the carbanion stabilization of endofullerene is proposed.

4.3 Endohedral Metal-induced Regioselective Formation of Bis-Prato Adduct of $Y_3N@I_h$-C_{80} and $Gd_3N@I_h$-C_{80}

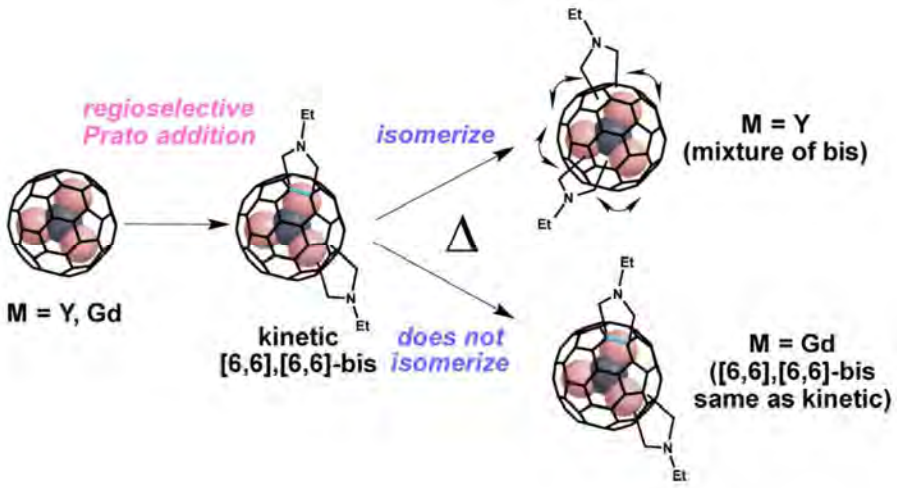

Aroua, S.; Garcia-Borràs, M.; Bölter, M. F.; Osuna, S.; Yamakoshi, Y., **Endohedral Metal-induced Regioselective Formation of Bis-Prato Adduct of $Y_3N@I_h$-C_{80} and $Gd_3N@I_h$-C_{80}**, *J. Am. Chem. Soc.*, **2015**, 137, 58-61.

M.G.-B. performed the DFT calculations, analyzed the computational results, and co-wrote the manuscript.

Safwan Aroua, Marc Garcia-Borràs, Marc Florian Bölter, Sílvia Osuna, and Yoko Yamakoshi. "Endohedral Metal-Induced Regioselective Formation of Bis-Prato Adduct of Y3N@Ih-C80 and Gd3N@Ih-C80". *Journal of the American Chemical Society*. Vol. 137, Issue 1 (2015) : 58-61

http://dx.doi.org/10.1021/ja511008z

http://pubs.acs.org/doi/abs/10.1021/ja511008z

Publication Date (Web): December 24, 2014

Abstract

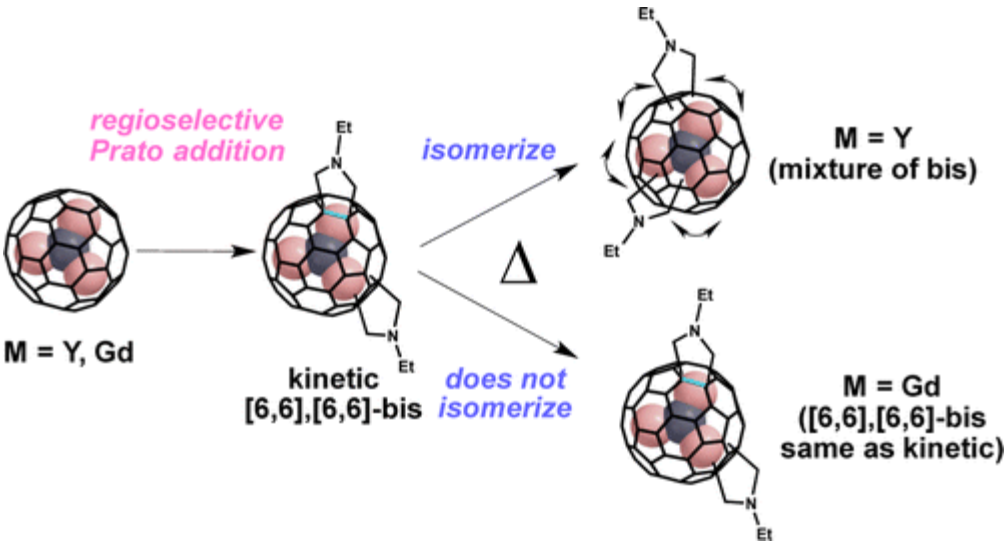

Regioselective bisaddition of $M_3N@I_h$-C_{80} (M = Y, Gd) was observed for the first time in the Prato reaction with *N*-ethylglycine and formaldehyde. The main kinetic bisadduct of $Y_3N@C_{80}$was determined to be a [6,6],[6,6] adduct by ^1H and ^{13}C NMR and vis/NIR spectroscopy, and it converted to a mixture of regioisomers upon heating via a sigmatropic rearrangement. The main kinetic bisadduct of $Gd_3N@C_{80}$ (the [6,6],[6,6] adduct on the basis of vis/NIR data) existed stably under thermal conditions without isomerization. The likely position of the second addition of the $Gd_3N@C_{80}$ bisadduct was predicted by DFT calculations.

Chapter 5

Understanding the structure and reactivity of endohedral metallofullerenes and derivatives from aromaticity analysis

5.1 Electrochemical control of the regioselectivity in the exohedral functionalization of C_{60}: the role of aromaticity

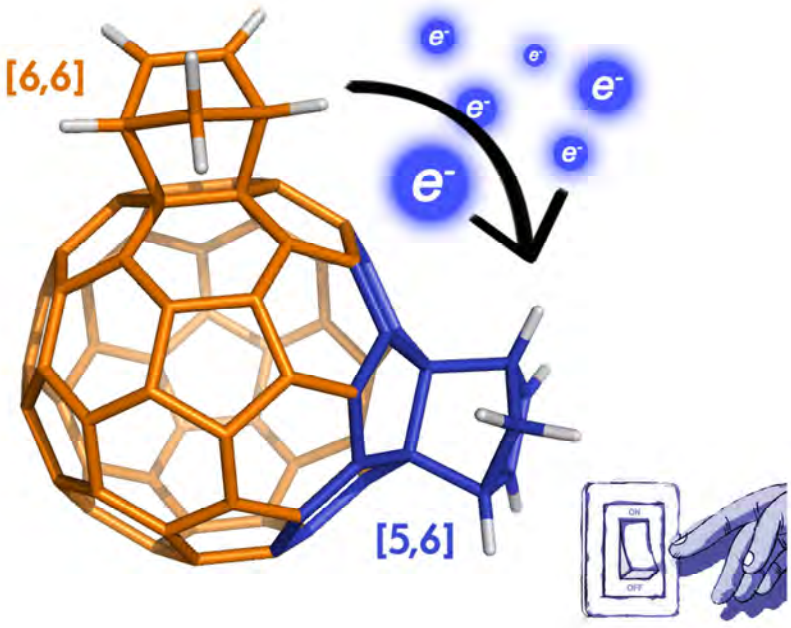

Garcia-Borràs, M.; Osuna, S.; Swart, M.; Luis, J.M.; Solà, M., **Electrochemical control of the regioselectivity in the exohedral functionalization of C_{60}: the role of aromaticity**, *Chem. Commun.*, **2013**, 49, 1220-1222.

M.G.-B. participated in the design of the project, performed all the calculations, analyzed the results, and co-wrote the manuscript.

Marc Garcia-Borràs, Sílvia Osuna, Marcel Swart, Josep M. Luisa and Miquel Solà. "Electrochemical control of the regioselectivity in the exohedral functionalization of C_{60}: the role of aromaticity". *Chem. Commun*. Vol. 49, Issue 12 (2013) : 1220-1222

http://dx.doi.org/10.1039/C2CC38390J

http://pubs.rsc.org/en/content/articlepdf/2013/cc/c2cc38390j

First published online 17 Dec 2012

Abstract

In this work we show that the regioselectivity of the Diels–Alder, 1,3-dipolar, and carbenecycloadditions to C_{60} changes from the usual [6,6] addition in neutral species to the [5,6] attack when the number of electrons added to the fullerenic cage increases. Changes in the aromaticity of the five- and six-membered rings of C_{60} during the reduction process provide a rationale to understand this regioselectivity change.

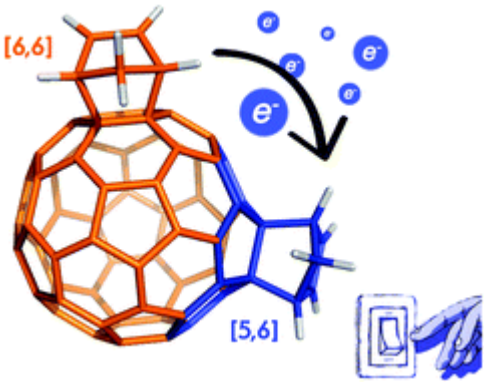

5.2 Maximum aromaticity as a guiding principle for the most suitable hosting cages in endohedral metallofullerenes

Garcia-Borràs, M.; Osuna, S.; Swart, M.; Luis, J.M.; Solà, M., **Maximum Aromaticity as a Guiding Principle for the Most Suitable Hosting Cages in Endohedral Metallofullerenes**, *Angew. Chem. Int. Ed.*, 2013, 52, 9275-9278. Back Cover: *Angew. Chem. Int. Ed.*, **2013**, 52, 9332-9332.

M.G.-B. participated in the design of the project, performed all the calculations, developed the different scripts used to manage the data, analyzed the results, and co-wrote the manuscript.

Garcia-Borràs, M., Osuna, S., Swart, M., Luis, J. M. and Solà, M. “Maximum Aromaticity as a Guiding Principle for the Most Suitable Hosting Cages in Endohedral Metallofullerenes”. Angew. Chem. Int. Ed. Vol. 52 (2013) : 9275–9278

http://dx.doi.org/10.1002/anie.201303636

http://onlinelibrary.wiley.com/doi/10.1002/anie.201303636/abstract

Article first published online: 10 JUL 2013

Abstract

Encapsulating! The encapsulation of metal clusters in endohedral metallofullerenes takes place in cages that, in most cases, are far from being the most stable isomer in the corresponding hollow fullerenes. In contrast to previous proposals, new results indicate that it is the maximum aromaticity criterion that determines the most suitable hosting cages.

Keywords

aromaticity; computational chemistry; endohedral metallofullerenes; fullerenes; maximum aromaticity criterion

5.3 Understanding the relative abundances of TNT-based endohedral metallofullerenes from aromaticity measures

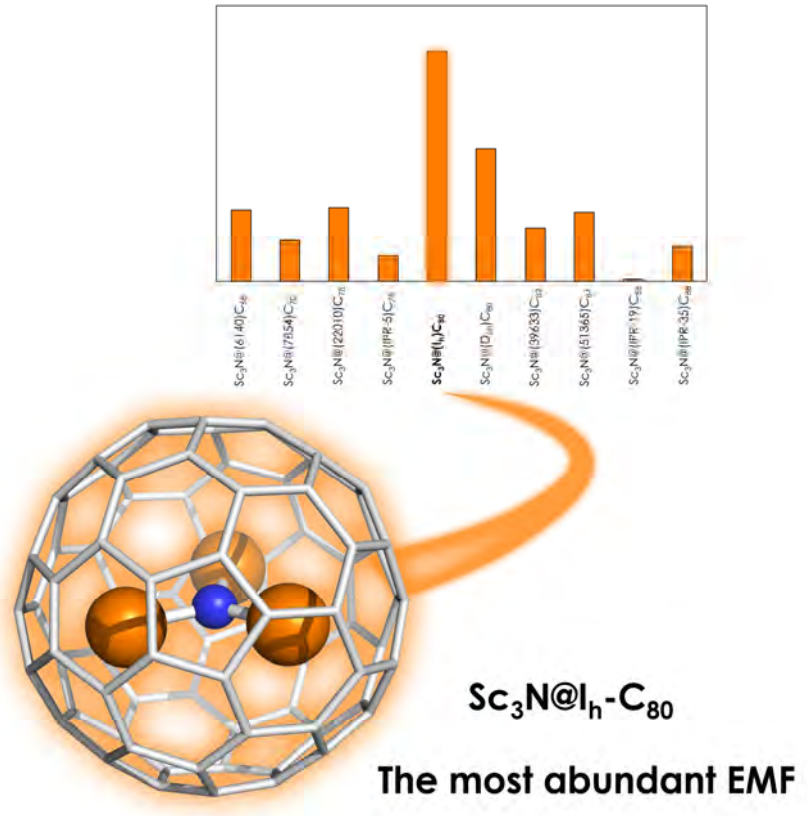

Garcia-Borràs, M.; Osuna, S.; Luis, J.M.; Solà, M., **Understanding the relative abundances of TNT-based endohedral metallofullerenes from aromaticity measures**, *submitted for publication*, **2015**.

M.G.-B. designed the project, developed the different scripts used to manage the data, performed all the calculations, analyzed the results, and co-wrote the manuscript.

Understanding the Relative Abundances of TNT-based Endohedral Metallofullerenes from Aromaticity Measures

Marc Garcia-Borràs, Sílvia Osuna, Josep M. Luis, Miquel Solà

Institut de Química Computacional i Catàlisi (IQCC) and Departament de Química, Universitat de Girona, Campus Montilivi, 17071 Girona, Catalonia, Spain

Supporting Information Placeholder

ABSTRACT: The synthesis of endohedral metallofullerenes (EMFs) from a carbon soot sample of an arc discharge leads to a variety of EMFs that are obtained in different relative abundances. In the present work, we use electronic-based aromaticity measures to show that relative abundances of Sc_3N-based EMFs correlate with the normalized Additive Local Aromaticity (ALA_N) measures. Our results show that, for the Sc_3N-based EMFs, the most abundant EMFs are the most aromatic. This result reinforces the idea that aromaticity plays a key role in determining the stability of EMFs.

Endohedral metallofullerenes (EMFs) have attracted much attention since their discovery because of their extraordinary properties and potential applications.[1-3] The first endohedral metallofullerene obtained in macroscopic quantities was the $Sc_3N@I_h$-C_{80} trimetallic nitride template (TNT), which is the third most abundant fullerene only after C_{60} and C_{70}.[4] The electronic structure of endohedral metallofullerenes can be described by the *ionic model*, proposed by Poblet's group.[5,6] When a metallic cluster is encapsulated inside a fullerene cage, a formal charge transfer takes place from the inner moiety to the carbon structure. In the case of TNT moieties, a formal transfer of six electrons takes place, thus its electronic structure can be described as $M_3N^{6+}@C_{2n}^{6-}$. In 2007, Popov and Dunsch showed that hexaanionic empty fullerene isomers are good models for describing TNT EMFs relative stabilities.[7] Rodríguez-Fortea *et al.* demonstrated that the negative charge is mainly accumulated on the pentagonal rings of the carbon structure, and that their distribution along the fullerene surface is crucial for stabilizing the final EMF.[8,9] Two years later, we reported an extensive study showing that, for a given C_{2n}^{-m} cage, the most stable isomers are the ones whose total aromaticity is maximized, independently of the number of pentagon adjacencies they have.[10,11] The maximum aromaticity criterion (MARC) gives an explanation for the IPR rule violation in EMFs. In this study aromaticity measurements were done in terms of Additive Local Aromaticity (ALA) index.[10,11] Herein, we have generalized the ALA index to expand its scope and allow the direct comparison of C_{2n}^{m-} cages of different size. To achieve this goal, we propose the normalization of the ALA index per number of rings present in the fullerene structure (ALA_N). Using ALA_N one can compare the aromaticity of different fullerene cages regardless the number of carbons of the fullerene structure (see equation 1).

$$ALA_N = \frac{1}{n}\sum_{i=1}^{n} A_i \qquad (1)$$

where A_i is the local aromaticity of ring *i*, and *n* is the number of rings of the fullerene structure, including both 5- and 6-membered rings.

In our previous work, we showed that both geometric HOMA and electronic multicenter (MCI) aromaticity indexes can be employed to compute A_i local aromaticities in ALA index. Both indices provide similar aromaticity trends for fullerene isomers with the same number of carbon atoms.[10] Nevertheless, the massive application of the electronic MCI index was unaffordable because of its large computational cost and the elevated number of structures to study. In the present work, we want to compare and distinguish structures with different number of rings and relatively similar values of ALA_N. And then, the A_i local aromaticities in the ALA_N index were computed using the accurate normalized multicenter index proposed by Cioslowski, Matito and Solà, the so-called I_{NB} electronic index.[12]

In a previous study,[10] we determined the C_{2n} hexaanionic isomers that exhibit the highest aromaticities in terms of ALA, which include all the TNT-based EMF synthesized up to date. Here, we have computed the normalized ALA_N index using the computationally more expensive and accurate I_{NB} electronic index[12-14] with ESI-3D program[15] for selected C_{2n}^{6-} isomers (see Figure 1 caption) at B3LYP/6-31G//BP86/DZP level of theory, using the Becke's multicenter integration scheme and the topological fuzzy Voronoi (TFVC)[16] atomic partition scheme as implemented in

Article in preparation

Garcia-Borras, M.; Osuna, S.; Luis, J.M.; Sola, M., "Understanding the relative abundances of TNT-based endohedral metallofullerenes from aromaticity measures"

5.4 Aromaticity as the driving force for the stability of non-IPR endohedral metallofullerene Bingel-Hirsch adducts

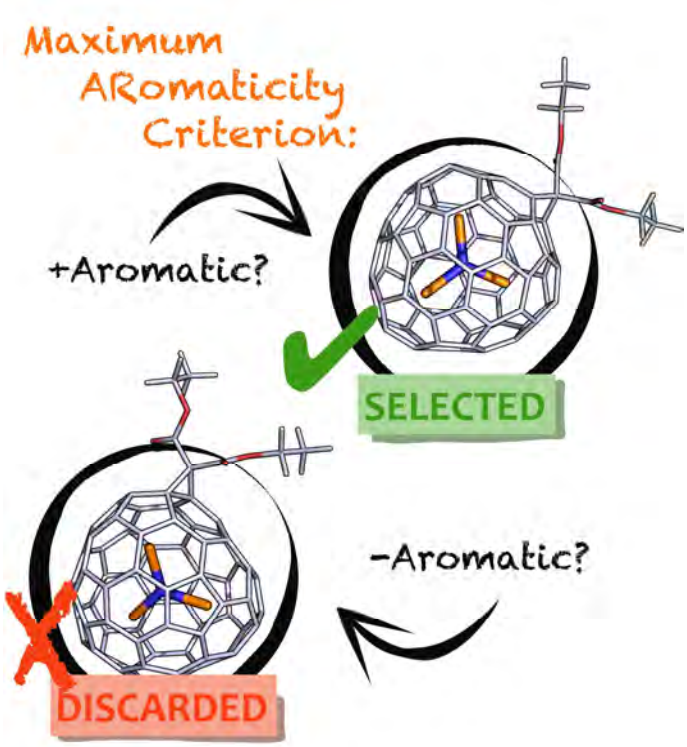

Garcia-Borràs, M.; Osuna, S.; Swart, M.; Luis, J.M.; Echegoyen, L., Solà, M., **Aromaticity as the driving force for the stability of non-IPR endohedral metallofullerene Bingel-Hirsch adducts**, *Chem. Commun.*, **2013**, 49, 8767-8769.

M.G.-B. participated in the design of the project, performed all the calculations, analyzed the results, and co-wrote the manuscript.

Marc Garcia-Borràs, Sílvia Osuna, Marcel Swart, Josep M. Luis, Luis Echegoyenc and Miquel Solà. "Aromaticity as the driving force for the stability of non-IPR endohedral metallofullerene Bingel–Hirsch adducts". *Chem. Commun*. Vol. 49, Issue 78 (2013) : 8767-8769

http://dx.doi.org/10.1039/C3CC44505D

http://pubs.rsc.org/en/content/articlepdf/2013/cc/c3cc44505d

Received 16 Jun 2013, Accepted 10 Jul 2013

First published online 12 Jul 2013

Abstract

We have studied the relative stabilities of Bingel–Hirsch non-IPR endohedral metallofullerene monoadducts having one, two, or three adjacent pentagon pairs. The most stable addition always leads to an open adduct and never occurs on [5,5] bonds. Our results show that the thermodynamics of the addition is governed by the additive local aromaticity of the rings of the final adducts.

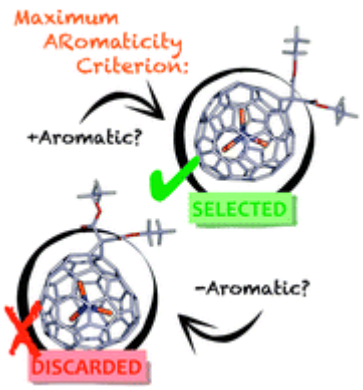

5.5 Bingel-Hirsch derivatization of TNT endohedral metallofullerenes predicted from simple aromaticity measures. The $Sc_3N@D_{3h}C_{78}$ and $Sc_3N@D_{5h}$-C_{80} as model systems.

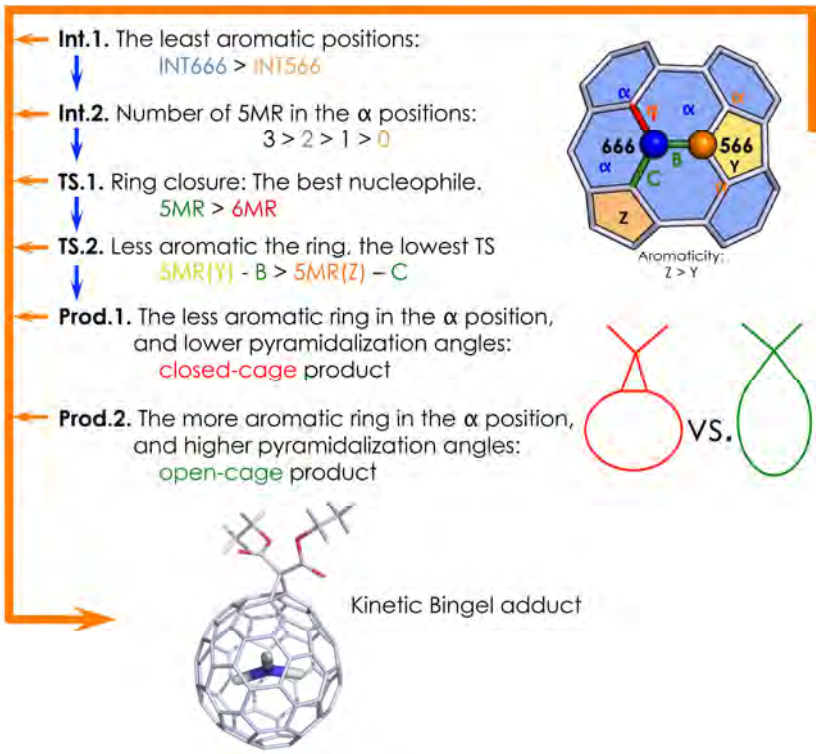

Garcia-Borràs, M.; Cerón, M.; Osuna, S.; Izquierdo-Barroso, M.; Luis, J.M.; Echegoyen, L., Solà, M., **Bingel-Hirsch derivatization of TNT endohedral metallofullerenes predicted from simple aromaticity measures. The $Sc_3N@D_{3h}$-C_{78} and $Sc_3N@D_{5h}$-C_{80}**, *submitted for publication*, **2015**.

M.G.-B. participated in the design of the project, performed all the calculations, analyzed the results, and co-wrote the manuscript.

The regioselectivity of Bingel-Hirsch cycloadditions on IPR Endohedral Metallofullerenes predicted from simple Aromaticity Criteria. The $Sc_3N@C_{78}$ and $Sc_3N@D_{5h}$-C_{80} as model systems

Marc Garcia-Borràs,[a] Maira Cerón,[b] Sílvia Osuna,[a*] Marta Izquierdo,[b] Josep M. Luis,[a*] Luis Echegoyen,[b*] and Miquel Solà[a*]

[a] Institut de Química Computacional i Catàlisi (IQCC) and Departament de Química, Universitat de Girona, Campus Montilivi, 17071 Girona, Catalonia, Spain

[b] Department of Chemistry, University of Texas at El Paso, El Paso, Texas 79968, United States

Supporting Information Placeholder

ABSTRACT: Functionalization of endohedral metallofullerenes (EMFs) is mainly achieved via cycloaddition reactions, principally through Diels-Alder (DA), 1,3-dipolar, and nucleophilic [2+1] Bingel-Hirsch (BH) additions. In many cases, the regioselectivities observed in BH additions differ from those found in DA and 1,3-dipolar cycloadditions. In this work, we analyze with density functional theory calculations the BH addition of diethylbromomalonate over all non-equivalent bonds of $Sc_3N@D_{3h}$-C_{78}. The regioselectivities observed computationally lead us to propose a set of rules, the so-called Predictive Aromaticity Criteria (PAC), to *a priori* identify the most reactive bonds of a given EMFs in BH additions. Application of these rules to BH additions to $Sc_3N@D_{5h}$-C_{80} shows perfect agreement between the PAC predictions and the experiments.

The possibility of encapsulating atoms or clusters inside the fullerene inner cavity to form the so-called endohedral metallofullerenes (EMFs) was considered soon after the C_{60} discovery.[1] Since then, many EMFs have been reported in the literature that range from single atoms to clusters of up to 7-8 atoms.[2] Computations have been crucial for the correct study and characterization of these compounds as they are usually obtained in low yields.[3,4] In EMFs, a formal charge transfer up to six electrons from the metal cluster to the fullerene cage takes place.[5] The charge transfer is mainly responsible for their special properties and reactivity. In 2007, Dunsch and Popov demonstrated that negatively charged fullerene isomers are good models for describing the relative stabilities of EMFs.[6] More recently, Poblet and co-workers showed that the negative charge in EMFs is mainly accumulated on five-membered rings (5-MRs) of the carbon structure and that its distribution along the fullerene structure is of utmost importance for their final stabilization.[7]

In the last years, many EMFs have been synthesized presenting adjacent 5-MRs, and therefore not obeying the so-called isolated pentagon rule (IPR) proposed by Kroto right after the C_{60} discovery.[8] The IPR rule is, however, strictly obeyed only for neutral non-functionalized fullerene cages. It has been recently demonstrated that the main reason behind the noncompliance of the IPR rule in EMFs is the aromaticity of the system. The more aromatic are the negatively charged fullerene cages, the more stable. Therefore, the maximum aromaticity criterion[9,10] determines which fullerene cages are the most suitable to host a certain cluster in a given EMF. In addition, this also indicates that aromaticity could play a key role in the EMFs chemical reactivity.

The exohedral functionalization of EMFs has been extensively studied to expand their range of potential applications. It is generally achieved *via* cycloaddition reactions, in particular through Diels-Alder (DA), 1,3-dipolar, and nucleophilic [2+1] Bingel-Hirsch (BH) additions.[11,12] Computational and experimental studies, investigating mainly DA and 1,3-dipolar cycloaddition reactions on a wide range of EMFs, have determined that the strain of the cage induced by the inner metal cluster is one of the key factors to determine the regioselectivity of the Diels-Alder and Prato additions. Electronic effects due to the formal charge transfer also play a major role in (de)activating certain fullerene regions.[3,4,13-20] The preferred additions sites are usually analyzed in terms of: (a) short C-C bond lengths, (b) relatively high pyramidalization angles, and (c) appropriate shape of some of the LUMOs.[16,19] For a given fullerene cage, and depending on the metal cluster encapsulated, the addition is preferred to be far from the metal cluster influence (i.e. Sc_3N-based C_{80} EMFs) or close to one of the metals (i.e. Y_3N-based C_{80}).[14,16] How-

Article in preparation

Garcia-Borras, M.; Cerón, M.; Osuna, S.; Izquierdo-Barroso, M.; Luis, J.M.; Echegoyen, L., Sola, M., "The regioselectivity of Bingel-Hirsch cycloadditions on IPR endohedral metallofullerenes predicted from simple aromaticity measures. The $Sc_3N©D_3h\text{-}C_{78}$ and $Sc_3N©D_5h\text{-}C_{80}$ as model systems"

5.6 The role of aromaticity in determining the molecular structure and reactivity of (endohedral metallo)fullerenes

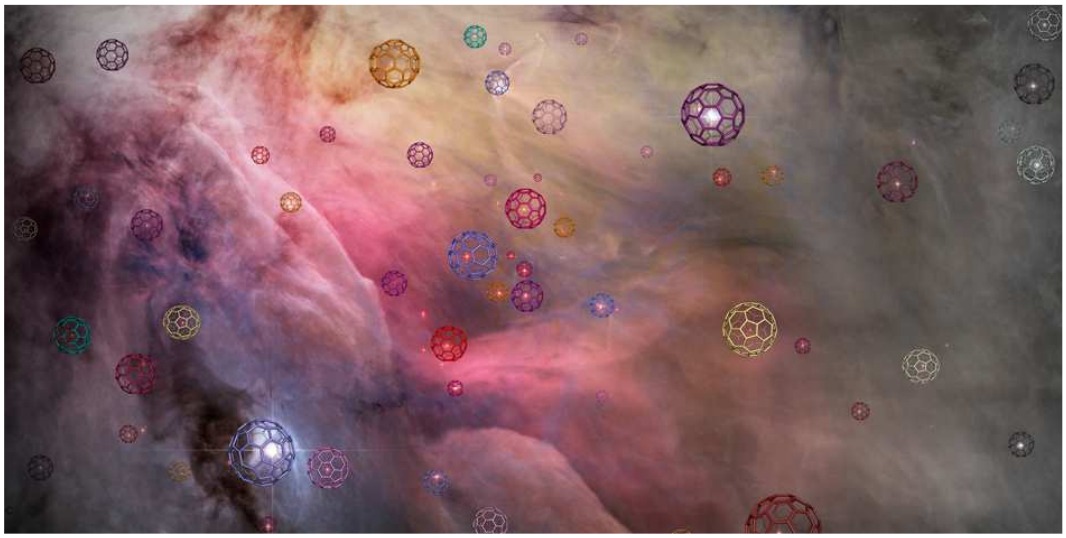

Garcia-Borràs, M.; Osuna, S.; Luis, J.M.; Swart, M.; Solà, M., **The role of aromaticity in determining the molecular structure and reactivity of (endohedral metallo)fullerenes**, *Chem. Soc. Rev.*, **2014**, 43, 5089-5105.

M.G.-B. participated in the design of the outline and contents of the review article, and co-wrote the manuscript.

Marc Garcia-Borràs, Sílvia Osuna, Josep M. Luis, Marcel Swart and Miquel Solà. "The role of aromaticity in determining the molecular structure and reactivity of (endohedral metallo)fullerenes". *Chem. Soc. Rev*. Vol. 43, Issue 14 (2014) : 5089-5105

http://dx.doi.org/10.1039/C4CS00040D

http://pubs.rsc.org/en/content/articlepdf/2014/cs/c4cs00040d

Received 22 Jan 2014

First published online 16 May 2014

Abstract

The encapsulation of metal clusters in endohedral metallofullerenes (EMFs) takes place in cages that in most cases are far from being the most stable isomer in the corresponding hollow fullerenes. There exist several possible explanations for the choice of the hosting cages in EMFs, although the final reasons are actually not totally well understood. Moreover, the reactivity and regioselectivity of (endohedral metallo)fullerenes have in the past decade been shown to be generally dependent on a number of factors, such as the size of the fullerene cage, the type of cluster that is being encapsulated, and the number of electrons that are transferred formally from the cluster to the fullerene cage. Different rationalizations of the observed trends had been proposed, based on bond lengths, pyramidalization angles, shape and energies of (un)occupied orbitals, deformation energies of the cages, or separation distances between the pentagon rings. Recently, in our group we proposed that the quest for the maximum aromaticity (maximum aromaticity criterion) determines the most suitable hosting carbon cage for a given metallic cluster (*i.e.* EMF stabilization), including those cases where the IPR rule is not fulfilled. Moreover, we suggested that local aromaticity plays a determining role in the reactivity of EMFs, which can be used as a criterion for understanding and predicting the regioselectivity of different reactions such as Diels–Alder cycloadditions or Bingel–Hirsch reactions. This review highlights different aspects of the aromaticity of fullerenes and EMFs, starting from how this can be measured and ending by how it can be used to rationalize and predict their molecular structure and reactivity.

Chapter 6

Results and Discussion

In this chapter, the main goals achieved in this thesis will be briefly summarized. In order to simplify the discussion, this section is divided into three main blocks: The Diels-Alder reaction on endohedral metallofullerenes (chapter 5), the Prato addition on endohedral fullerenes (chapter 6), and the study and analysis of structure and reactivity of endohedral metallofullerenes from aromaticity measures (chapter 7).

6.1 Diels-Alder additions on endohedral metallofullerenes

The Diels-Alder regioselectivity on fullerene compounds is usually predicted based on the C-C bond distances, pyramidalization angles and LUMOs shape and energy. In general, for fullerenes and EMFs it is considered that the more pyramidalized the C-C bond being attacked, the closer to the sp^3 bonding situation of the final adduct, and the lower the deformation energy needed for the Diels-Alder adducts formation. Thus, when the strain of the C-C bond due to the presence of large inner metal cluster increases (a more pyramidalized bond), the more reactive the considered bond should be. Moreover, in EMFs, the electronic charge transfer from the metal cluster to the carbon cage should lead to a reduction of the reactivity of the fullerene because of the destabilization of the EMF LUMOs disfavoring their interaction with the HOMO of the diene, as in Diels-Alder reaction fullerene compounds have a dienophile role. It is usually said that for fullerenes and EMFs cycloadditions occur preferentially on short C-C bonds with lobes of opposite sign on each carbon atom in some of the accessible in energy LUMOs of the fullerene cage. The double bond character and appropriate shape of the LUMO of these C-C bonds should

facilitate the interaction with the HOMO of the diene. Because of the small energy differences between LUMO and LUMO+1/LUMO+2/LUMO+3 orbitals in EMFs, it is considered that all of them must be taken into account when the interaction with the HOMO of the diene is analyzed. Thus, bonds with high pyramidalized angles, short C-C distances and properly shaped LUMO+n should correspond to those more reactive in cycloaddition reactions involving EMFs. Nevertheless, as we have found, these criteria do not allow the correct explanation of the EMF behavior. Thus, it is required to develop new tools to predict and understand the Diels-Alder reactivity of endohedral metallofullerenes.

In this section, we present the most important results related to the computational exploration of the Diels-Alder (DA) functionalization of endohedral metallofullerenes extensively described in chapter 3. Different newly proposed tools effectively applied for the analysis and prediction of the DA reactivity of EMFs, such are the Frozen Cage Model or the noncluster energy barriers, are described.

6.1.1 Comparison of $Ti_2C_2@D_{3h}$-C_{78}, D_{3h}-C_{78} and $M_3N@D_{3h}$-C_{78} ($M = Sc, Y$) Diels-Alder reactivity

In different experimental studies, it has been observed that the exohedral reactivity of EMFs is highly affected by the nature of the encapsulated cluster.[197] In order to evaluate the effect of the inner metallic cluster on the exohedral reactivity of the fullerene cages, in 2008 our group studied the Diels-Alder reaction on the pristine D_{3h}-C_{78} fullerene and its related Sc_3N and Y_3N EMFs.[241,242] D_{3h}-C_{78} based TNT EMFs represent the perfect scenario for the study of the reactivity of EMFs because the metallic cluster encapsulated inside is in a fixed position, in contrast to what happens in larger cages such as I_h-C_{80}. In addition, although scandium and yttrium TNTs occupy the same positions inside the D_{3h}-C_{78}, the Ti_2C_2 carbide adopts a completely opposed position inside the cage (see figure 6.1a). Because of the different orientations and nature of these metal clusters, we expected to find significant differences in the exohedral reactivity towards DA reaction. In this context, the Diels-Alder cycloaddition between 1,3-cis-butadiene and $Ti_2C_2@D_{3h}$-C_{78} EMF was studied in detail at BP86/TZP//BP86/DZP level of theory. All 13 non-equivalent addition sites of D_{3h}-C_{78} were explored and compared with the previously studied D_{3h}-C_{78},[241] $Sc_3N@D_{3h}$-C_{78}[241] and $Y_3N@D_{3h}$-C_{78} systems.[242]

In figure 6.1c we report the activation barriers and reaction energies for each

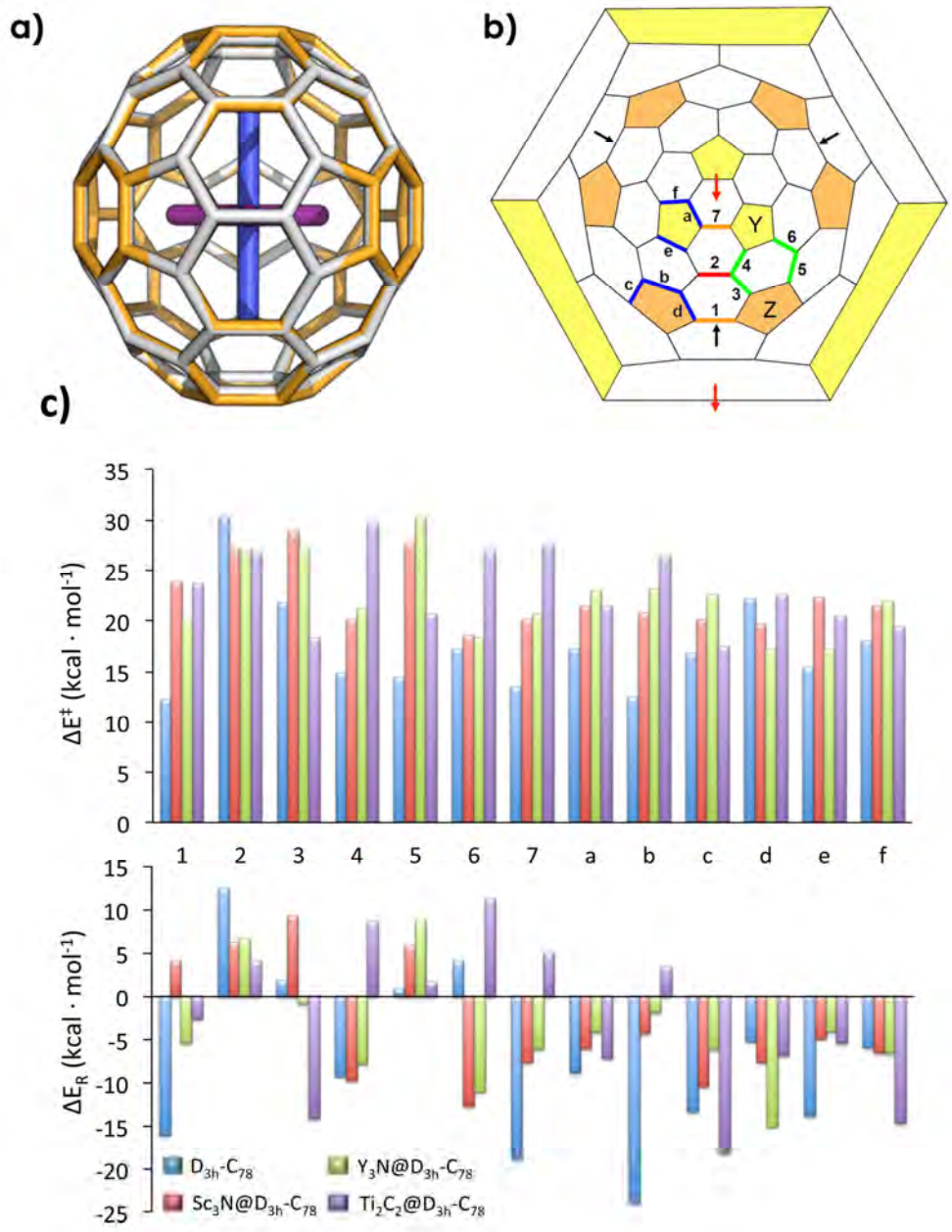

Figure 6.1: a) Representation of superimposed $Ti_2C_2@D_{3h}C_{78}$ (orange cage and blue cluster) and $Sc_3N@D_{3h}$-C_{78} (light gray cage and purple cluster) EMFs; b) Schlegel diagram of $D_{3h}C_{78}$ and its 13 nonequivalent bonds. Black arrows indicate the position of scandium atoms facing the different bonds, while red arrows refer to titanium atoms; c) Reaction energies and reaction barriers for the Diels-Alder reaction over all nonequivalent bonds of D_{3h}-C_{78} and $X@D_{3h}$-C_{78} (X = Sc_3N, Y_3N, and Ti_2C_2) EMFs. For $Y_3N@D_{3h}$-C_{78} only energies for the down region are reported here (see ref.[242]).

addition site of D_{3h}-C_{78}, $Sc_3N@D_{3h}$-C_{78}, $Y_3N@D_{3h}$-C_{78}, and $Ti_2C_2@D_{3h}$-C_{78} obtained at BP86/TZP//BP86/DZP level. Our results indicate that, as a general trend, reaction energies become less exothermic (*i. e.* less favorable) and reaction barrier heights increase when a metallic cluster is encapsulated. For the three EMFs, the formal charge transferred from the metal cluster to the fullerene cage is 6 electrons, inducing a reduction of the electron affinity of the carbon cage.

The most reactive bonds for the titanium carbide D_{3h}-C_{78} based EMF correspond to the cycloaddition over type D [5,6] **c** bond (ΔE_R= -18.1 kcal·mol^{-1}, $\Delta E^{\ddagger}$= 17.4 kcal·mol^{-1}), type B [6,6] **3** bond (ΔE_R = -14.1 kcal·mol^{-1}, $\Delta E^{\ddagger}$= 18.2 kcal·mol^{-1}) and type D [5,6] **f** bond (ΔE_R= -14.6 kcal·mol^{-1}, $\Delta E^{\ddagger}$= 19.3 kcal·mol^{-1}). We observed a good correspondence between reaction barriers and reaction energies computed, thus indicating that kinetic and thermodynamic products coincide. The most favorable additions for the D_{3h}-C_{78} pristine cage are the pyracylenic (type A) [6,6] bonds **1** and **7** and the corannulene (type D) [5,6] bond **b** (for bond **1**: ΔE_R= -16.0 kcal·mol^{-1}, $\Delta E^{\ddagger}$= 12.2 kcal·mol^{-1}; for bond **7**: ΔE_R= -18.8 kcal·mol^{-1}, $\Delta E^{\ddagger}$= 13.5 kcal·mol^{-1}; and for bond **b**: ΔE_R= -23.9 kcal·mol^{-1}, $\Delta E^{\ddagger}$= 12.5 kcal·mol^{-1}). $Ti_2C_2@D_{3h}$-C_{78} is found to be more reactive than scandium and yttrium TNTs, whose more favored additions are on type B [6,6] bond **6** (ΔE_R= -12.7 kcal·mol^{-1}, $\Delta E^{\ddagger}$= 18.5 kcal·mol^{-1}) for Sc_3N,[241] and type D [5,6] bond **d** (ΔE_R= -15.0 kcal·mol^{-1}, $\Delta E^{\ddagger}$= 17.1 kcal·mol^{-1}) for Y_3N[242] EMF.

The reactivity trend observed can be rationalized in terms of the FMO theory. In the Diels-Alder reaction, the main orbital interaction occurs between the HOMO of the diene (cis-1,3-butadiene, -5.77eV at BP86/TZP//BP86/DZP level), and the LUMO of the fullerene, which acts as dienophile. For the $Ti_2C_2@D_{3h}$-C_{78} system, the LUMO - LUMO+3 energies are found between -4.49 and -4.0 eV, while LUMO energy for the free C_{78} is -5.13 eV. The computed energy for the LUMO of $Sc_3N@D_{3h}$-C_{78} species is -3.87 eV. As a consequence, the HOMO(diene)-LUMO(fullerene) gap increases from 0.68 eV for the free fullerene, to 1.28 eV for titanium carbide EMF, and becomes 1.57 eV for the scandium-based TNT EMF. Thus, there exists a perfect agreement between the trend in the computed HOMO(diene)-LUMO(fullerene) gaps and the decrease in the reactivity (higher reaction barriers) of the fullerene compounds: the lower the HOMO-LUMO gap, the higher the reactivity: $C_{78} > Ti_2C_2@D_{3h}$-$C_{78} > Sc_3N@D_{3h}$-C_{78}.

The predictions made from bond lenghts and pyramidalization angles show many inconsistencies. Moreover, because of the delocalized nature of the

molecular orbitals in fullerene compounds, it is very difficult to determine which bond has the correct LUMO lobe shape and sign centered on its carbon atoms to effectively interact with the HOMO of the diene.

The computed distortion (or strain) and interaction energies for all possible additions indicated that, in general, the larger the fullerene deformation energy the least reactive the bond. In this line, we introduced a new concept, the *noncluster energy barrier*. The latter is defined as the energy difference between the single-point energy calculation of TS and reactants when the Ti_2C_2 cluster is removed from the optimized EMF geometry, while keeping the carbon structure of the TS and reactants frozen. The noncluster energy barrier gives an idea of the geometric effect induced by the cluster on the energy barrier as compared to the pristine fullerene. The difference between the actual energy barrier and the noncluster energy barrier is an indicator of the purely electronic effect of the metallic cluster on the energy barrier. When this difference is negative, it means that the electronic charge transferred from the Ti_2C_2 cluster favors the addition.

The computed differences between the actual energy barriers and the noncluster reaction barriers show that for all bonds, except for bond **f**, the electronic interaction between the carbon cage and the metallic cluster reduces their reactivity. For bond **f**, the difference between these two barriers is negative, which means that the reactivity of this bond is enhanced due to the charge transfer and orbital interaction between the metallic cluster and the carbon cage. This conclusion is supported by the fact that C_{78} LUMOs do not have any lobe centred on bond **f** carbon atoms exhibiting the required shape and sign for interacting with the HOMO of the diene. When titanium carbide cluster is encapsulated, the LUMO and LUMO+3 of $Ti_2C_2@D_{3h}$-C_{78} have contributions centred on bond **f** with lobes having the required shape and sign to interact with the HOMO of butadiene.

The most reactive bonds in $Ti_2C_2@D_{3h}$-C_{78} EMF, *i.e.* those having the lowest reaction barriers, bonds **c**, **f**, and **3** are the only ones that present low fullerene deformation energies and low differences between reaction barriers and noncluster energies. On the other hand, bonds **4**, **7** and **b** that have the largest reaction barriers are those disfavored by these two parameters.

We found that the negative charge transferred to the studied EMFs is mainly centred on 5-MRs, and it is not uniformly distributed, depending on the metal cluster position. The 5-MRs closest to the metals are those more negatively charged. In the $Ti_2C_2@D_{3h}$-C_{78} case, **Y** 5-MRs are those closest to the tita-

nium atoms and the ones more negatively charged. This is in contrast to Sc_3N and Y_3N systems, which most negatively charged rings are **Z** 5-MRs (see figure 6.1b). We observed that [6,6] bonds placed next to the most charged 5-MR, bonds **4**, **6**, and **7** in $Ti_2C_2@D_{3h}$-C_{78}, are those with the lowest reactivity. Those [6,6] bonds placed next to the more negatively charged 5-MRs are more electron rich and, therefore, deactivated to act as electron-poor dienophiles towards rich dienes in Diels-Alder reaction. These observations indicate that the electronic charge distribution along 5-MRs is extremely important to understand the [6,6] bond reactivity in metallofullerenes.

In a previous work from our group, it was found that dispersion corrections are essential to correctly reproduce the experimental barriers.[314] We have analyzed the effect of including dispersion corrections at BP86-D3/TZP//BP86/DZP level of theory when EMF reactivity is studied. Our results showed that although the changes in the reaction barriers and reaction energies are relevant, and the location of a reactant-complex structure is only is possible when including dispersion corrections, the reactivity trends remain the same. Hence, the conclusions drawn from non-dispersion corrected calculations are totally valid although the reaction barrier height and reaction energies are not accurately reproduced when compared to experiments.

6.1.2 The Frozen Cage Model: predicting the exohedral regioselectivity in endohedral metallofullerenes

In our previous study, we observed that there exists a good correspondence between reaction energies and activation barriers for the Diels-Alder addition to all nonequivalent bonds in $Ti_2C_2@D_{3h}$-C_{78}. Following this observation, we also analyzed in detail this relationship for the 13 different bonds in D_{3h}-C_{78} and $X@D_{3h}$-C_{78} (X = Sc_3N, Y_3N) compounds. Based on the Marcus thermodynamic model, we demonstrated that a linear correlation between reaction barriers and energies is found when DA on EMFs is considered. The linear Dimroth approximation, which relates the activation barriers and reaction energies following equation 6.1, is followed by EMFs (see figure 6.2a). On the contrary, for the empty D_{3h}-C_{78} cage, in line with what was found previously for C_{60}, the linear relationship is not valid.[334] As a consequence, Diels-Alder additions on EMFs lead to the same regioselectivity trend from both kinetic and thermodynamic points of view.

$$\Delta E^{\ddagger} = \Delta E_0^{\ddagger} + \frac{1}{2}\Delta E_{rxn} \tag{6.1}$$

We analyzed the reactivity trends of all nonequivalent bonds in D_{3h}-C_{78} and related EMFs (Sc_3N, Y_3N, and Ti_2C_2) using the distortion/interaction (activation/strain) model. Our calculations showed that there exists a good correlation between the energy barriers and total distortion energies for EMFs (see for instance the titanium carbide results in figure 6.2b), although no correlations were found for the empty C_{78} fullerene. The interaction terms are always negative, and the most reactive bonds have the smaller interaction energies (in absolute values).

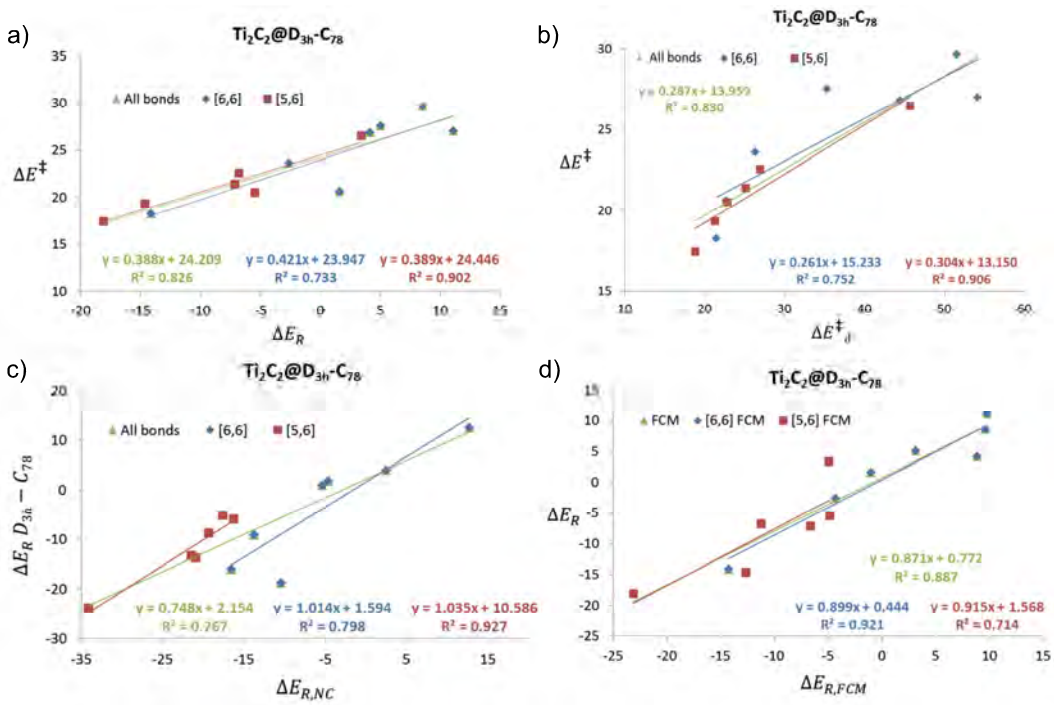

Figure 6.2: Plot of the B3LYP/TZP//BP86/DZP a) energy barriers versus reaction energies; b) reaction barriers versus distortion energies; c) reaction energies of free D_{3h}-C_{78} versus noncluster reaction energies; and d) reaction energies versus frozen cage model reaction energies; for the Diels-Alder reaction between Ti_2C_2@D_{3h}-C_{78} and 1,3-cis-butadiene. All energies are given in kcal·mol^{-1}.

At this point, we analyzed the reactivity trends for all the studied EMFs using the early proposed noncluster reaction barriers. As expected from the previous titanium carbide results, no correlation between these noncluster barriers and the actual reaction barriers was found. We also computed the noncluster barriers but including 6 extra electrons to the system in order to simulate

the EMF molecular orbital occupations. However, correlations were not improved. We applied the noncluster model for the analysis of the different EMF products, and found that there does not exists a direct relationship between reaction energies of the different nonequivalent bonds and their corresponding noncluster energies. Nevertheless, an important observation arose from these analysis: noncluster reaction energies correlate with the reaction energies of the free C_{78} fullerene (see figure 6.2c). Although the fullerene structure is distorted (optimized geometries for the EMF), the reactivity trend of the empty fullerene remains constant when the electronic contributions from the metal cluster are not considered. The latter leads us to propose the inverse road. We tried to reproduce the EMF reactivity trend using the optimized empty fullerene product structures but including explicitly the given metal cluster inside and just performing single-point (SP) energy calculations on these structures, *i.e.* the Frozen Cage Model (FCM) structures. As showed in figure 6.2d for the titanium carbide EMF, the FCM reaction energies correctly reproduce the EMF reaction energies of the Diels-Alder cycloaddition.

Thus, using this FCM approach, which only requires to fully optimize the product structures for the pristine fullerene cage, we can predict the most favorable Diels-Alder additions on any desired related EMF by including the metallic cluster and performing computational less expensive single-point energy calculations. Because of the existing relationship between the kinetic and the thermodynamic products for the Diels-Alder reaction on EMFs, we can also estimate those additions whose barriers will be lower in energy.

6.1.3 A complete guide on the Diels-Alder regioselectivity of I_h-C_{80} based endohedral metallofullerenes

The exohedral functionalization of $X@I_h$-C_{80} EMFs has been extensively explored experimentally because I_h-C_{80} based EMFs are those more abundant and easy to obtain. Nevertheless, the computational exploration of the reactivity of I_h-C_{80} based EMFs has been hindered because of the free rotation of the encapsulated clusters inside the cage. Thus, one has to consider many different orientations of the inner metal with respect a given bond to ensure that the estimated reaction energies and barriers are correct.[236] This requires a large amount of geometry optimizations for both products and transition states of a system of a hundred atoms including different heavy metals, which implies a extremely high computational cost. In this context, our Frozen Cage Model has been applied for the study of a large set of I_h-C_{80} EMFs. We have selected a representative number of existing I_h-C_{80} EMFs of different nature

(classical metal ions, metallic oxides, TNTs, metallic carbides, hydrocarbide and carbonitride) to study and compare their Diels-Alder reactivity and regioselectivity trends, for the addition of *s-cis*-1,3-butadiene.

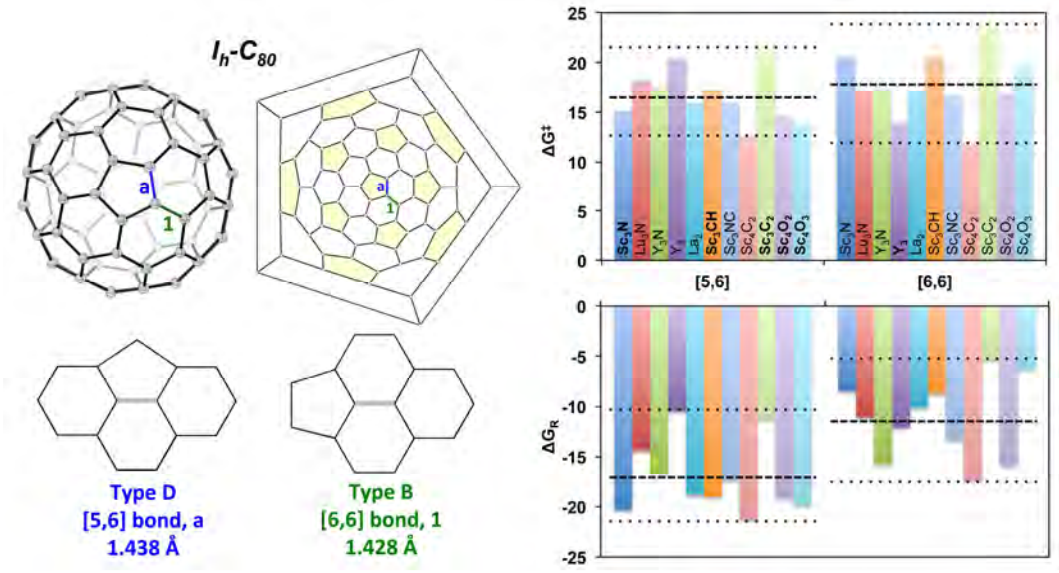

Figure 6.3: Gibbs reaction energies and reaction barriers for the DA reaction on 5,6 and 6,6 positions of different $X@I_h$-C_{80} EMFs. Only energies for the lowest energy metallic cluster orientations are considered. Dotted (stripped) lines indicate the lowest and the highest (average) Gibbs reaction barriers and reaction energies for each case. All energies are given in kcal·mol^{-1}.

I_h-C_{80} fullerene cage has only two different nonequivalent bonds, a type B [6,6] bond and a corannulene type D [5,6] bond (see figure 6.3). We used the FCM approach to first locate the most favorable orientations (about 100 different orientations considered) for each of the two possible additions at a low computational level (SP energy calculations at BP86/DZ level). Afterwards, full optimizations were performed on these more favored products and transition states were located to accurately estimate the Gibbs reaction energy and Gibbs reaction barrier for each addition at a more accurate level (BP86/dDsC/TZP//BP86-D2/DZP). The results obtained are summarized in figure 6.3. For the pristine hollow I_h-C_{80} fullerene, the Gibbs reaction enery for the most favorable addition is -37.7 kcal·mol^{-1} and corresponds to the [5,6] position. The Gibbs reaction barriers are 3.4 and 2.4 kcal·mol^{-1} for the [5,6] and [6,6] additions at this level of theory. Thus, the empty cage is very reactive, much more than its related EMFs, and the kinetic and thermodynamic

Table 6.1: Metallic cluster volumes, charge transferred to the fullerene cage, EMFs HOMO-LUMO gaps, and deformation energies in $X@I_h$-C_{80} species. Data from ref.[238]

X	V (Å^3)	Charge (a.u.)	HOMO-LUMO gap (eV)	$\Delta E_{def.}$ (kcal·mol^{-1})
Sc_3N	453.1	1.279	2.294	6.9
Lu_3N	473.1	1.425	2.516	20.5
Y_3N	496.4	1.362	2.540	20.1
Y_3	491.4	1.570	1.236	13.9
La_2	369.5	1.542	1.287	5.5
Sc_3CH	471.3	1.253	2.520	8.5
Sc_3NC	473.9	1.189	2.294	14.9
Sc_3C_2	484.1	1.100	2.264	16.3
Sc_4C_2	571.2	1.044	2.021	13.8
Sc_4O_2	550.3	1.196	1.709	8.5
Sc_4O_3	562.1	1.126	2.294	9.4

products do not coincide. Based on our calculations, we have found different reactivity trends depending on the metallic cluster family:

TNT clusters (Sc_3N, Lu_3N, Y_3N): those systems that present a large HOMO-LUMO gap and a high charge transfer between the metallic cluster and the cage (see table 6.1) exhibit a low reactivity (*i.e.* high activation barriers). The regioselectivity of the cycloaddition reaction depends strongly on the volume of the inner TNT and the related fullerene deformation energy. The larger the TNT (or the more deformed the fullerene cage), the smaller the energy difference between [6,6] and [5,6] additions, and the less regioselective the reaction. The preference for the [6,6] addition increases for those systems that present a larger volume of the metal cluster and fullerene distortion energy. In addition, it is found that, for the lowest-energy regioisomer of the Sc_3N EMF, none of the metal atoms point towards the attacked bond, in contrast to what is found for lutetium and yttrium based EMFs, where the most stable final products have a metal atom directly facing the functionalized bond.

Classical clusters (La_2, Y_3): the charge transfer and HOMO-LUMO gaps are practically the same in the two considered cases as presented in table 6.1. Therefore, the main factors that differentiate their reactivity are the volume of the cluster and the fullerene deformation energy. A larger volume of the

inner cluster (and so a higher fullerene deformation energy) leads to an increase of the exohedral reactivity of the classical EMF. As observed in the TNT cases, the preference for the [6,6] addition increases for those systems that have a larger cluster volume and fullerene deformation energy, which is the case for Y_3.

Metallic carbide (Sc_3C_2, Sc_4C_2), hydrocarbide (Sc_3CH), and carbonitride (Sc_3NC): for these types of I_h-C_{80} EMFs in general the reaction barriers decrease when the charge transferred to the cage decreases and the volume of the metallic cluster increases (see table 6.1). This implies that also for these EMFs larger fullerene deformation energies decrease reaction barriers. The only exception for the latter observation is the $Sc_4C_2@I_h$-C_{80} EMF. Also for this type of EMFs the [6,6] addition is preferred from a kinetic point of view for the EMF that has the larger metallic cluster encapsulated (*i.e.* Sc_4C_2), while [5,6] addition is the one preferred for the other cases. However under thermodynamic control, the most favored addition is the one corresponding to the [5,6] position for all the present studied cases.

Metallic oxide (Sc_4O_2, Sc_4O_3): the spherical shape of the metallic oxide clusters makes this class of EMFs significantly different from the rest of the considered cases. The [5,6] addition is preferred in all cases, from both thermodynamic and kinetic points of view. Moreover, by increasing the cluster size the reaction becomes more regioselective, and the EMF more reactive (lower reaction barriers and more negative reaction energies).

As a whole, our results showed that the exothermicity of the reactions in EMFs tends to decrease when the charge transfer to the cage increases because the cage has less electron affinity. In general, the [6,6] addition becomes more favored as compared to the [5,6] one when the size of the metallic cluster increases and the deformation of the fullerene cage is higher, and when the charge transferred to the cage is larger.

Our study is the first reported investigation that provides an extended guideline for experimental and computational chemists to understand and predict the reactivity and regioselectivity of the Diels-Alder cycloaddition on the I_h-C_{80} based EMFs. The systematic computation of the large amount of different metallic clusters considered in the study, which can freely rotate inside the fullerenic cage, has only been possible due to the application of the previously developed Frozen Cage Model approximation.

6.1.4 The Diels-Alder regioselectivity and product stability of $La@C_{2v}$-C_{82}(1,2,3,4,5-penta)cyclopentadiene

In 2005, the Diels-Alder addition between cyclopentadiene (Cp) and $La@C_{2v}$-C_{82} was achieved.[211] The attack of Cp on [6,6] bond **19** (as labeled in figure 6.4) was proposed to be the major product of the reaction.[211] This suggestion was made by the simply inspection of the shape of the singly occupied molecular orbital (SOMO) orbital because the final $La@C_{2v}$-C_{82}Cp product could not be isolated. In a subsequent related work, 1,2,3,4,5-pentamethylcyclopentadiene (Cp*) was used as the diene in the DA reaction on $La@C_{2v}$-C_{82} EMF.[210] In this case, the final product could be isolated and characterized by X-ray crystallography, and it was found that the addition corresponded to the attack to [5,6] bond **o**.[210] It was surprising that relatively similar dienes (Cp and Cp*) presented markedly different regioselectivities. Moreover, the final stabilities of both products were found to be largely different. At 298K, only 36% of $La@C_{2v}$-$C_{82}Cp^*$ decomposes into $La@C_{2v}$-C_{82} and Cp* after 12h,[210] while the half-life of $La@C_{2v}$-$C_{82}Cp$ under the same conditions is only τ=1.8h (for comparison, τ=1800h for the decomposition of $C_{60}Cp$).[211]

In order to rationalize these observations, we performed a complete study on the regioselectivity of the process. We studied the thermodynamics of the DA addition between Cp and $La@C_{2v}$-C_{82} for all 35 nonequivalent bonds, and for the 10 most favored cases, we also studied the kinetics of the reaction. For the Cp* case, we considered 4 different additions based on the previously reported experimental X-ray data.[210] In table 6.2, there are reported the electronic and Gibbs reaction energies and activation (retro)-barriers for the selected DA addition of Cp and Cp* on $La@C_{2v}$-C_{82} at BLYP-D2/TZP//BLYP-D2/DZP level. Our results indicate that both cycloadditions present similar reactivities, with the thermodynamic most stable product being the one corresponding to the attack to [5,6] bond **o** in the Cp* case, but also when the Cp is considered. In this case, we did not find good correlations between the shape of the LUMO $La@C_{2v}$-C_{82} EMF orbitals and the final reactivity of the bonds (see figure 6.4 and table 6.2), or even with the C-C bond distances or pyramidalization angles as expected from our previous studies (see previous subsections). It is important to mention that from the kinetic point of view, the reaction barriers found for additions to bond **o** and bond **11** are very close in energy (Cp: $\Delta G^{\ddagger}$=20.2 kcal·mol^{-1} and $\Delta G^{\ddagger}$=19.5 kcal·mol^{-1} for bond **o** and **11**, respectively; Cp*: $\Delta G^{\ddagger}$=9.8 kcal·mol^{-1} and $\Delta G^{\ddagger}$=10.1 kcal·mol^{-1} for bond **o** and **11**, respectively), presenting the addition to bond **11** the lowest reaction barrier for the Cp case. However, the attack over bond **11** is very endergonic and, consequently, once product **11** is formed rapidly reverts back to original

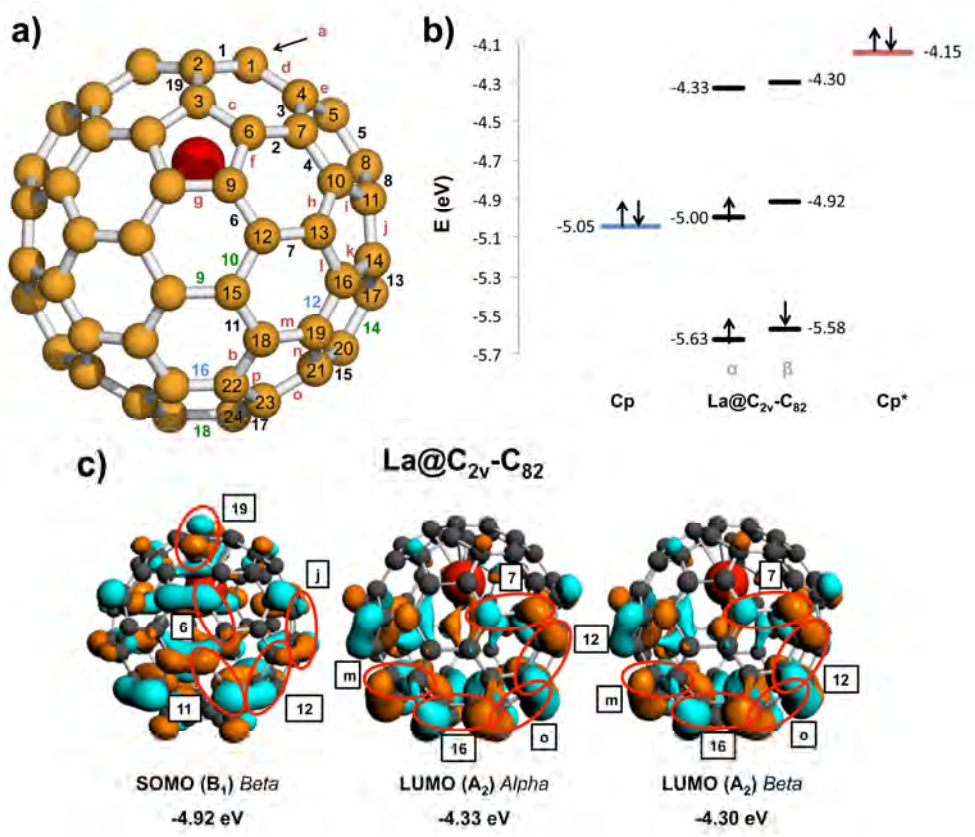

Figure 6.4: Representation of: a) all different nonequivalent bonds in $La@C_{2v}$-C_{82}; b) Molecular orbital levels of the frontier orbitals of $La@C_{2v}$-C_{82}, cyclopentadiene (Cp) and 1,2,3,4,5-pentamethylcyclopentadiene (Cp*); c) SOMO (unoccupied beta) and LUMO MOs (alpha and beta) of $La@C_{2v}$-C_{82} (isosurface 0.02 a.u.). Those bonds with favorable lobes for interacting with the HOMO of the diene are marked with ellipses. Energies are given in eV.

Table 6.2: BLYP-D2/TZP//BLYP-D2/DZP reaction energies (ΔE_R) and Gibbs reaction energies (ΔG_R), reaction barriers ($\Delta E^{\ddagger}$) and Gibbs reaction barriers ($\Delta G^{\ddagger}$), and values for the retro-reaction barriers ($\Delta E^{\ddagger}$ - retro) and Gibbs retro-barriers ($\Delta G^{\ddagger}$ - retro) for the Diels-Alder cycloaddition reactions of Cp and Cp* at the most favorable addition sites of the $La@C_{2v}$-C_{82} EMF at 298.15 K. Values in italics were obtained relative to the first reactant complex that was formed. Values given in kcal·mol^{-1}.

				$La@C_{2v}$-C_{82}Cp			
Bond	**Type**	ΔE_R	ΔG_R	$\Delta E^{\ddagger}$	$\Delta G^{\ddagger}$	$\Delta E^{\ddagger}$-retro	$\Delta G^{\ddagger}$-retro
11	B [6,6]	-4.6	13.5	4.8	19.5	9.4	6.1
		1.6	*5.7*	*11.0*	*11.8*		
12	A [6,6]	-5.5	12.6	6.9	22.1	12.4	10.8
		0.5	*3.1*	*12.9*	*12.6*		
16	A [6,6]	-6.4	11.8	7.5	22.6	13.9	11.0
		-0.5	*2.5*	*13.4*	*13.3*		
19	B [6,6]	-5.1	12.7	8.7	23.7	13.8	12.4
		1.9	*7.1*	*15.7*	*18.2*		
d	C [5,6]	-6.2	11.7	10.2	24.1	16.4	10.3
		0.3	*4.1*	*16.7*	*16.5*		
e	C [5,6]	-4.9	13.2	9.6	23.5	14.5	10.7
		1.3	*7.3*	*16.1*	*17.6*		
f	C [5,6]	-5.3	12.9	8.8	23.6	14.1	10.8
		0.2	*3.4*	*14.4*	*14.1*		
h	C [5,6]	-4.0	13.7	9.9	24.5	13.9	11.8
		2.0	*4.9*	*16.0*	*15.7*		
j	C [5,6]	-7.1	10.9	8.6	22.7	15.7	12.4
		-1.7	*1.7*	*14.0*	*13.5*		
o	C [5,6]	-10.5	7.8	5.6	20.2	16.0	12.4
		-4.7	*-1.5*	*11.3*	*10.9*		
				$La@C_{2v}$-C_{82}Cp*			
Bond	**Type**	ΔE_R	ΔG_R	$\Delta E^{\ddagger}$	$\Delta G^{\ddagger}$	$\Delta E^{\ddagger}$-retro	$\Delta G^{\ddagger}$-retro
11	B [6,6]	-13.1	5.6	-5.3	10.1	7.8	10.2
		1.8	*7.3*	*9.6*	*11.8*		
16	A [6,6]	-14.8	4.0	-3.7	10.3	11.1	6.3
		-0.8	*5.1*	*10.3*	*11.4*		
j	C [5,6]	-15.5	2.9	-1.9	13.1	13.6	10.2
		-1.7	*3.6*	*12.0*	*13.9*		
o	C [5,6]	-19.4	-0.7	-5.4	9.5	14.0	10.2
		-5.1	*0.5*	*8.9*	*10.8*		

reactants. Thus, the reaction presents a clearly regioselective formation of the **o** products in both Cp and Cp* cases. Our results correct the previous wrong assignment for the $La@C_{2v}$-C_{82}Cp adduct, indicating that there exist no regioselective differences between the DA cycloaddition of both Cp and Cp* over $La@C_{2v}$-C_{82} EMF.

Finally, we investigated the different product stabilities. As mentioned previously, it was found experimentally that the stabilities of the Cp and Cp* adducts were significantly different, with the decomposition of $La@C_{2v}$-C_{82}Cp being one order of magnitude faster than that of $La@C_{2v}$-C_{82}Cp*. We demostrated that electronic effects of the methyl substituents do not play a major role in the different Cp and Cp* product stabilities. It is known that BLYP underestimates the DA barriers, whilst B3LYP-D2 provides very good estimations for the DA barriers in fullerenes.[314] As a consequence, for the most favorable addition to bond **o** we computed the reaction Gibbs energy profile at B3LYP-D2/TZP//BLYP-D2/DZP level (see figure 6.5). Comparing the retro reaction barriers obtained ($\Delta G^{\ddagger}$-retro=19.0 kcal·mol^{-1} for Cp* and $\Delta G^{\ddagger}$-retro=20.5 kcal·mol^{-1} for Cp, see figure 6.5a), we can conclude that electronic effects of the methyl groups slightly decrease the retro-barrier favoring the dissociation of $La@C_{2v}$-C_{82}Cp*, which goes against experimental observations. In fact, we found that the higher stability of the Cp* adduct arises from the long-range stabilizing dispersion interactions. If we analyze the effect of the dispersion energy contribution on both reactions pathways (see figure 6.5b), we can see that a lack of dispersion corrections completely changes the reaction energy profile. The reaction pathways for Cp and Cp* additions are quite similar once the initial reactant complex is formed. Thus, the electronic effects due to the methyl groups on Cp* diene do not play a determinant role on the different half-life decomposition times of Cp and Cp*. Hence, without considering dispersion corrections, the Cp monoadduct would be more stable than the Cp* one. Nevertheless, when dispersion interactions are considered, this situation is inverted, with the Cp* adduct being the one largely more stabilized. The reason is the highest stability of the Cp* reactant complex due to dispersion interactions. This result confirms that dispersion corrections are essential for analyzing the experimentally observed behavior of fullerenes and related compounds towards cycloaddition reactions.

A few weeks after the publication of our results, a work by Nagase, Akasaka and co-workers was published in *J. Am. Chem. Soc.* journal.[361] In their work, a combined experimental and computational study of the DA addition of Cp* on $La@C_{2v}$-C_{82} was reported. They concluded that the mechanism followed is a concerted DA path, as we found previously, and more important, they

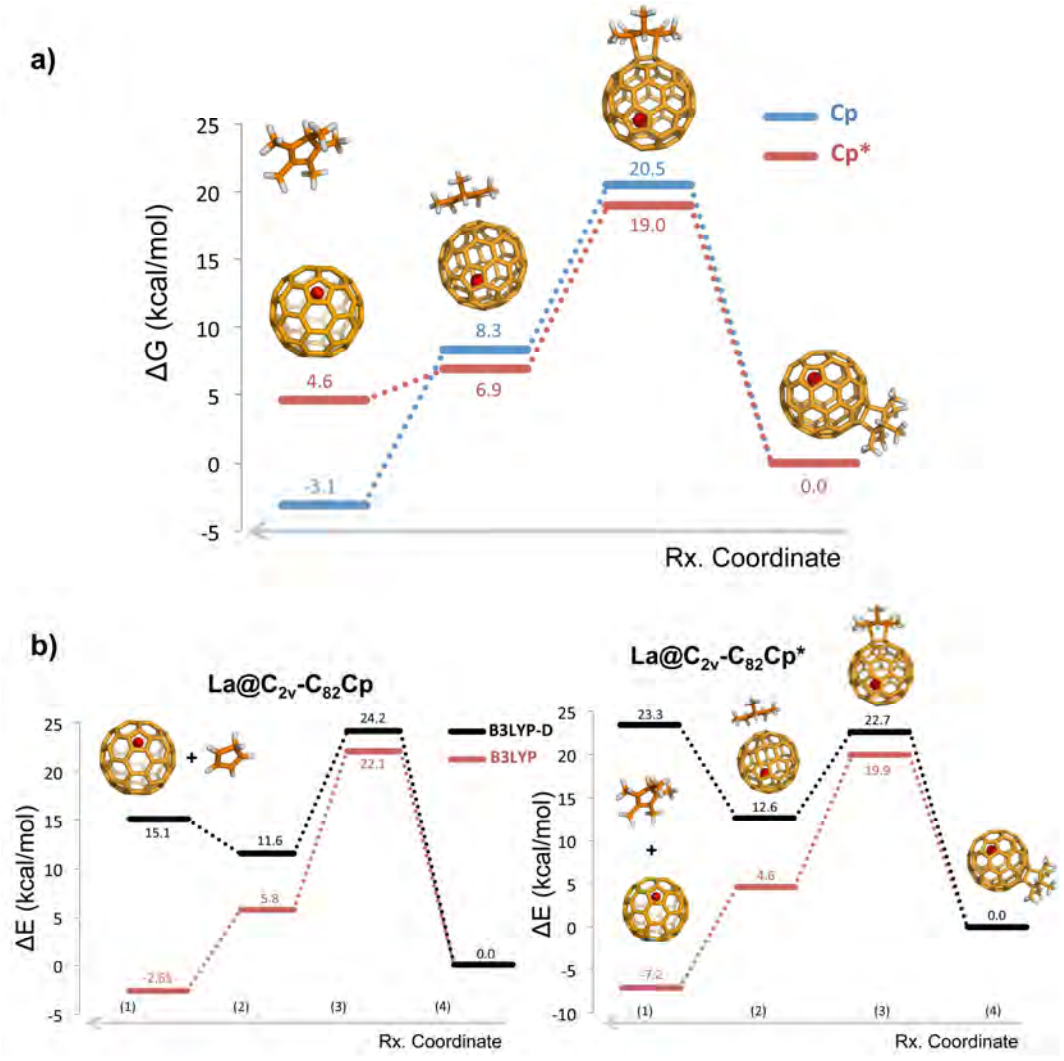

Figure 6.5: a) Gibbs energy profiles and b) reaction energy profiles including dispersion corrections (black) and without them (red), computed at B3LYP-D2/TZP//BLYP-D2/DZP level of theory for the Diels-Alder cycloaddition between $La@C_{2v}$-C_{82} and Cp and Cp* for the attack over the most reactive bond (bond **o**). The stationary points represented are: (1) reactants, (2) reactant intermediate structure, (3) transition state, and (4) product. Relative energy values are given in kcal·mol^{-1}.

reported the Gibbs retro-reaction barriers for Cp and Cp* DA monoadducts. Their experimental values, obtained from kinetic measures of the rate constant of the retro-DA at different temperatures, were $\Delta G^{\ddagger}$-retro=22.9 kcal·mol^{-1} for Cp and $\Delta G^{\ddagger}$-retro=22.5 kcal·mol^{-1} for Cp*, which are in perfect agreement with our computational predictions $\Delta G^{\ddagger}$-retro=20.5 kcal·mol^{-1} for Cp and $\Delta G^{\ddagger}$-retro=19.0 kcal·mol^{-1} for Cp* at B3LYP-D2/TZP//BLYP-D2/DZP level. These new results confirmed the accuracy of our calculations and fully validated our conclusions.

6.2 1,3-dipolar additions on endohedral fullerenes

The Prato reaction has been widely used as a useful method to covalently functionalize fullerenes and endohedral metallofullerenes in high yields. The application of this 1,3-dipolar cycloaddition reaction to $M_3N@C_{80}$ has been intensively studied in the last years.[94] Although the Prato addition to C_{60} fullerene takes place exclusively on the [6,6] position, when the reaction takes place on a TNT C_{80}-based EMF, both [5,6] and [6,6] adducts are obtained depending on the TNT unit considered.[197] In addition, the isomerization from the kinetic [6,6] product to the [5,6] thermodynamic more stable in $Y_3N@C_{80}$ system was reported by Echegoyen, Poblet, Rodríguez-Fortea and co-workers,[243] showing that the isomerization takes place through a concerted rearrangement mecanism and not by retrocycloadition-cycloaddition. Even so, the effect of the endohedral moiety or the exohedral pyrrolidine substituents on the isomerization process was not assessed and clarified. We reported a systematic and thorough study in collaboration with the experimental group of Dr. Yamakoshi (see chapter 4.1), investigating the role of the metal and the dipole substituent on the isomerization process.

As described, monofunctionalization of TNT EMFs has been well-studied, although there are only few reports on the bisfuntionalization of EMFs. Bisadditions on EMFs have only been achieved for the Bingel-Hirsch addition to $Sc_3N@C_{78}$,[209] the carbene addition to $La@C_{80}$,[362] and metal-catalyzed dipolar addition to $La@C_{72}(C_6H_3Cl_2)$.[169] The simple Prato bisaddition on EMFs had not been achieved till now (see section section 4.3).

Very recently, the possibility of controlling the chiral 1,3-dipolar formation of fulleropyrrolidines using metal catalysts was reported and extensivelty studied by the group of Prof. Martín.[263] The chiral derivatization of endoherdal fu-

llerenes has been previously achieved only for the $H_2@C_{60}$, showing the same behavior as the one observed for the C_{60} molecule.[264] In a collaborative effort between the experimental group of Prof. Martín and our group, we have extensively studied the chiral Prato funtionalization of $H_2O@C_{60}$ endohedral fullerene, and the *cis*-to-*trans* isomerization in the fulleropyrrolidino adducts(see chapter 4.2).

In this section, we summarize the most important results for the Prato isomerization of fulleropyrrolidines, as well as for the Prato bisfunctionalization of EMFs, obtained from fruitful experimental and computational collaborations.

6.2.1 Essential factors controlling the equilibrium of $M_3N@I_h$-C_{80} fulleropyrrolidines: exohedral functional groups versus endohedral metal clusters.

Experimentally, the isomerization rates for the [6,6]-to-[5,6] Prato adducts in $M_3N@I_h$-C_{80} (M=Sc, Lu, Y, and Gd) using three different glycine derivatives (see figure 6.6a) were determined by HPLC analysis. Moreover, the final [6,6]/[5,6] ratios corresponding to the thermodynamic equilibrium were found to be equivalent for the three different derivatives and they only differed when the inner TNT cluster was modified.

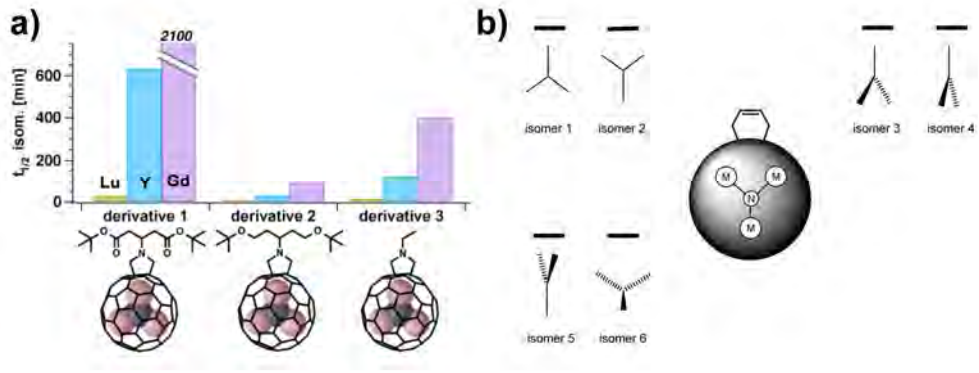

Figure 6.6: a) The $t_{1/2}$ values (half time to reach to the equilibrium) of $[6,6]$ and $[5,6]$ Prato adducts. Derivative **2** was used as an analogue compound of **1** without carbonyl group and derivative **3** was as a representative of fulleropyrrolidine. b) Representations of the relative positions of the metal nitride (shown as a Y-shaped figure) with respect to the C-C bond of the fullerene where the adduct is formed (indicated by a bar).

Using the **3'** computational model of derivative **3**, which includes a N-methyl group instead a N-ethyl substituent, we explored the relative stabilities of [5, 6] and [6, 6] Prato adducts of $M_3N@I_h$-C_{80} (M=Sc, Lu, Y, and Gd). As reported in table 6.3 and in figure 6.6b, we considered 6 different orientations of the TNT unit with respect to the attacked [5, 6] or [6, 6] bond because the encapsulated metal cluster is not fixed and then it can freely rotate. The computed relative thermodynamic stabilities for the most favorable orientations show that for the smaller clusters, *i.e.* Sc_3N, the [5,6] monoadduct is regioselectively obtained. On the contrary, for the larger TNT units, *i.e.* Gd_3N, an equilibrium of [5, 6] and [6, 6] Prato adducts is expected. These results correctly reproduce the experimental observed thermodynamic [6, 6]:[5, 6] ratios (see table 6.3).

Table 6.3: Relative stabilities of [5, 6] and [6, 6] Prato adducts 3' (N-methyl group has been used as a computational model) considering different metal cluster orientations (see figure 6.6b) for $M_3N@I_h$-C_{80} (M=Sc, Lu, Y, and Gd) at BP86-D2/TZP//BP86-D2/DZP-COSMO(o-DCB). Relative energies given in kcal·mol^{-1}.

Relative [5,6]/[6,6] stabilities					
Product	**Bond type**	$\boldsymbol{Sc_3N}$	$\boldsymbol{Lu_3N}$	$\boldsymbol{Y_3N}$	$\boldsymbol{Gd_3N}$
1_1	B[6,6]	**8.3**	4.6	**0.0**	0.7
1_2	B[6,6]	9.8	9.8	10.7	12.8
1_3	B[6,6]	11.4	**1.7**	0.1	**0.0**
1_4	B[6,6]	12.1	3.3	2.1	1.6
1_5	B[6,6]	10.4	10.5	10.9	-
1_6	B[6,6]	10.6	11.1	10.5	-
a_1	D[5,6]	8.0	1.0	**0.1**	**0.0**
a_2	D[5,6]	**0.0**	**0.0**	1.3	2.2
a_3	D[5,6]	7.4	0.0	**0.1**	0.6
a_4	D[5,6]	9.0	1.3	0.6	1.4
a_5	D[5,6]	-	-	-	-
a_6	D[5,6]	0.3	0.7	1.1	2.9
$\boldsymbol{\Delta E}([6,6]-[5,6])$		8.3	1.7	-0.1	0.0
Exp. ratio derivative 3		0:100	0:100	13:87	52:48

Our computations indicate that the stability of the different monoadducts is highly affected by the orientation of the inner metal cluster. For the most stable [5, 6] additions, different orientations are found for the smaller clusters (Sc and Lu, with no metal pointing to the attacked bond), and for the larger

ones (Lu, Y, and Gd, with a metal atom pointing to the attacked bond). For [6, 6] additions, the most stable monoadducts have a metal is directly facing the functionalized bond. When the size of the metal TNT atoms increase (when going from Sc to Gd), the TNT unit is more strained, and is no longer planar for Y_3N and Gd_3N clusters. When the fullerene functionalization occurs, the inner cavity of the cage is enlarged due to the pyramizalization of the functionalized sp^3 carbon atoms,which by facing one of the metal atoms to the attacked bond these large strained TNT clusters are better accomodated. These results are in agreement with our previous results for the Diels-Alder reaction on I_h-C_{80}-based TNT EMFs.

The [6, 6]-to-[5, 6] isomerization process for bis-ester **1'** (methyl ester) and **2'** (bis-methyl ether) for $Sc_3N@C_{80}$ and $Y_3N@C_{80}$ EMFs has been computationally explored as presented in figure 6.7. This process takes place through a sigmatropic rearrangement instead of a retrocycloaddition-cycloaddition pathway, in the line with the previously reported mechanism for N-ethylpyrrolidino-$Y_3N@C_{80}$.[243] Thus, confirming that the exohedral substituents do not affect the mechanism of the [6, 6]-to-[5, 6] isomerization. Nevertheless, the experimental assays indicated that the isomerization rate is highly affected by the nature of the TNT cluster and the exohedral group.

As showed in figure 6.7a, the relative stability of yttrium bis-ester **1'** monoadduct with respect to isolated reactants (-50.6 kcal·mol^{-1}) is 7.5 kcal·mol^{-1} larger than the one corresponding to Sc_3N (-43.1 kcal·mol^{-1}). In addition, the relative stability of the yttrium bis-ester **1'**-I$_{[6,6]}$ intermediate with respect to isolated reactants (-21.2 kcal·mol^{-1}) is exactly the same as the one computed for the Sc_3N bis-ester **1'**-I$_{[6,6]}$ intermediate (-21.0 kcal·mol^{-1}). Consequently, the Y_3N-I$_{[6,6]}$ intermediate is 7.3 kcal·mol^{-1} higher in energy with respect to the [6,6] monoadduct than the scandium intermediate (29.4 versus 22.1 kcal·mol^{-1} for Y and Sc, respectively), because of the higher stability of the yttrium based monoadducts. The latter is due to the metallic cluster strain release, as discussed before, being the isomerization process hindered (slowed) when the size of the TNT unit increases, as it is experimentally observed (figure 6.6a)

We computationally analyzed the effect of the exohedral groups on the isomerization rate, as reported in figure 6.7b. Our results, based on the comparison of ester and ether substituent groups, demonstrate that exohedral groups play a determinant role on the stabilization of the formed zwitterionic intermediates. We found that electron-withdrawing groups (ester groups) concentrate more negative charge on the dipole region when the zwitterionic intermediate is formed. A higher accumulation of positive charge on the dipole region leads

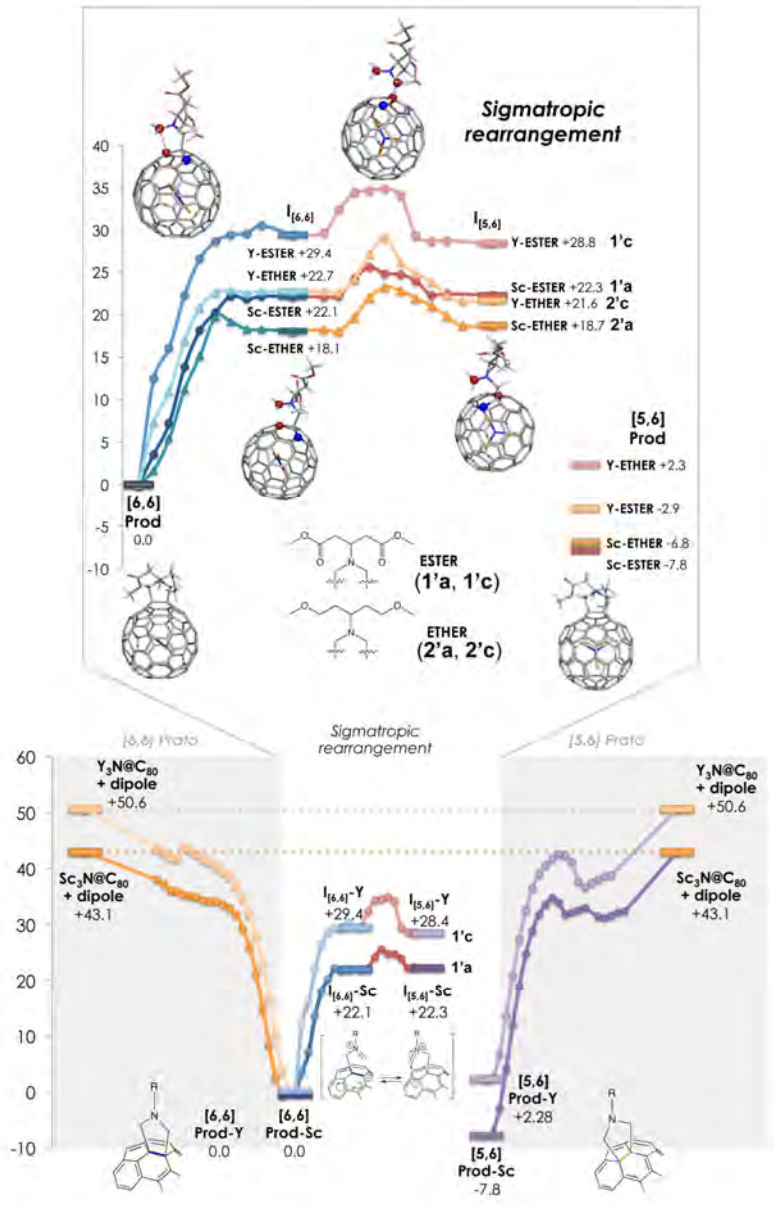

Figure 6.7: Bottom: The [6, 6]-to-[5, 6] isomerization process of bis-ester **1'** (methyl ester) of $Sc_3N@C_{80}$ (**1'a**, dark colors) and $Y_3N@C_{80}$ (**1'c**, light colors). Top: Diagram of the sigmatropic [6, 6]-to-[5, 6] rearrangement in Prato adducts of $Sc_3N@C_{80}$ and $Y_3N@C_{80}$ for **1'** (bis-methyl ester, in circles) and **2'** (bis-methyl ether, in triangles). Optimized stationary points are represented by horizontal lines and restrained optimizations performed along the reaction coordinate (Linear Transit optimizations, LT) in triangles and circles. Energies calculated at BP86-D2/TZP//BP86-D2/DZP-COSMO(o-DCB) level of theory are given in kcal·mol^{-1}.

to a more stabilized zwitterionic intermediate with the negative charge centred on the fullerene structure and the positive charge centred on the dipole, as schematically represented in figure 6.7b. Thus, the isomerization in the case of electron-withdrawing carbonyl-based derivative **1'** is hampered due to the disruption of the charge distribution on both the dipole and the fullerene in the zwitterionic intermediate required for the sigmatropic rearrangement. Good correlations between the positive charge centred on the dipole region in the ester-ether Y_3N and Sc_3N intermediates and their relative stabilities are found (see figure 6.8).

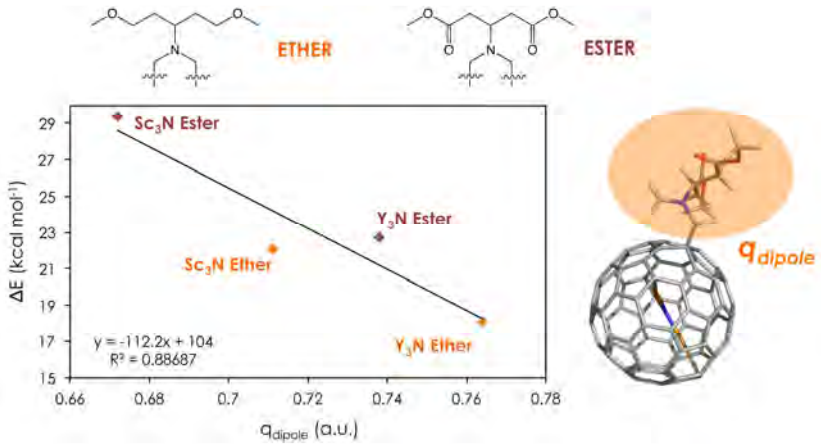

Figure 6.8: Correlation between the computed Bader charges centered on the dipole obtained for the [6, 6]-intermediates and their relative stabilities with respect to the corresponding adducts at BP86-D2/TZP//BP86-D2/DZP-COSMO(o-DCB) level. q_{dipole} is defined as the sum of the atomic charges of all atoms in the dipole region, as indicated in the figure.

6.2.2 Enantiospecific isomerization in chiral fulleropyrrolidines: H-bond assistance in the carbanion stabilization in $H_2O@C_{60}$.

Experimentally, the stereospecific metal-catalyzed formation of $H_2O@C_{60}$ chiral fulleropyrrolidino derivatives was achieved using the same procedure as for C_{60} and $H_2@C_{60}$ systems. It was observed that, for C_{60}, C_{70}, and $H_2O@C_{60}$ systems (see figure 6.9) takes place a *cis-trans* isomerization to achieve a final thermodynamic equilibrium. In this line, we computationally explored the *cis-trans* isomerization mechanism and the role played by the exohedral groups,

the endohedral moiety, and the nature of the fullerene cage.

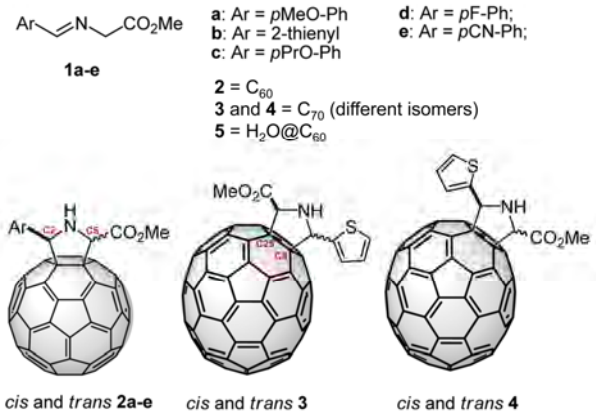

Figure 6.9: Studied fulleropyrrolidines.

First we analyzed the thermodynamic equilibrium between the *cis-trans* fulleropyrrolidines. Our calculations, reported in table 6.4, indicated that in all studied cases, *cis*-fulleropyrrolidines are more stable by ca. 1.5 kcal·mol^{-1}. Neither the exohedral groups or the encapsulated water molecule affect the final *cis-trans* thermodynamic equilibrium. These results are in agreement with the experimental observations, which indicate that in all cases, a final ratio of 70:30 *cis-trans* equilibrium is reached, being the *cis* isomer the one most stable. The large stability of the *cis*-product can be attributed to the higher repulsion of the lone pairs of the nitrogen atom of the pyrrolidine ring and the carbonyl groups of the ester substituent when *trans* isomer is formed.

Based on our previous studies about the Prato adducts isomerization on EMFs, we unraveled the *cis-trans* isomerization mechanism. Starting from the C_{60} *cis*-**2a** species, first we analyzed the C-C dissociation to generate the **INT**-*cis*-**2a**. As presented in figure 6.10a, the lowest energy dissociation path is the one corresponding to the C_{full}-C5 bond, the benzyl substituted one (see figure 6.9 for labeling). This is in line with our previous results, where we found that zwitterionic Prato intermediates are more stabilized when electron donating (electron rich) substituents are present in order to stabilize the positive charge generated on the dipole. Moreover, our computational predictions coincide with the fact that the C2 stereocenter is always preserved along the isomerization process. We analyzed the two possible rotations from **INT**-*cis*-**2a** to **INT**-*trans*-**2a**. As expected, the rotation along the N-C5 bond is much higher in energy because when the zwitterion is generated, this bond has a double

bond character due to the sigmatropic rearrangement, as shown in figure 6.10b. Thus, the *cis-trans* isomerization mechanism takes place through rotation of the **INT**-*cis*-**2a** N-C2 single bond.

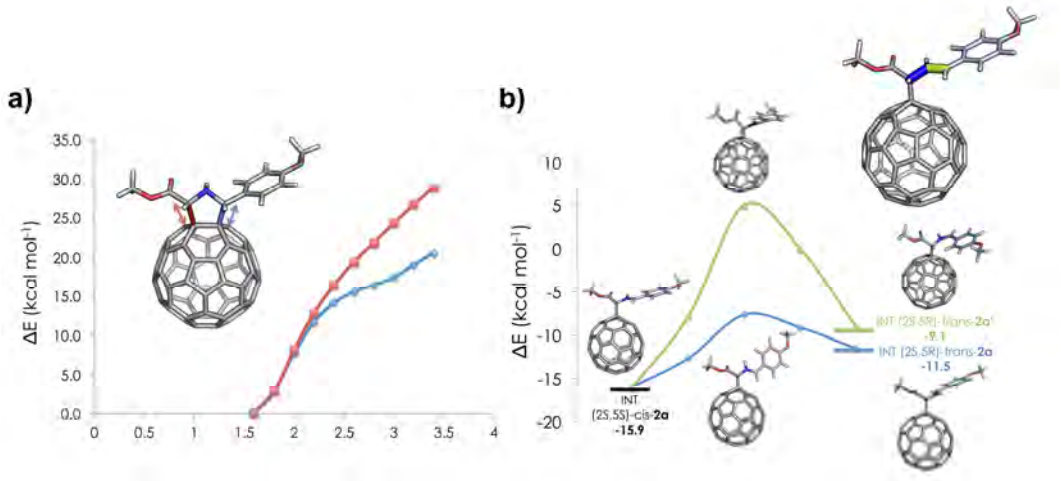

Figure 6.10: a) Representation of the Linear Transit (LT) (optimization at each point) performed for the C-C bond dissociation process along the C_{full}-C2 bond (in red) and C_{full}-C5 bond (in blue) in C_{60} **2a**; b) Linear Transit calculations for the two possible isomerization processes: in green the rotation along the double bond N-C5, and in blue along the single N-C2 bond in C_{60} **2a**. Energies are given in kcal·mol^{-1}

By considering all these features, the complete *cis-trans* isomerization was computed as presented in figure 6.11a. It is important to mention that we found that the retro-Prato barrier, once the **INT**-*cis*-**2a** is formed, is only 2.3 kcal·mol^{-1} higher in energy than the isomerization rotation TS (see table 6.4). Thus, when the *cis*-**2a** fulleropyrrolidine is heated the retro-Prato pathway becomes accessible, resulting in a decay of the asymmetric performance as observed experimentally. The exploration of the substituent effect on the aromatic position (see figure 6.9 and table 6.4) indicated that the presence of electron-withdrawing groups on the C5 position (**2d** and **2e** entries in table 6.4), destabilize the intermediates and the isomerization becomes less favored, in line with what we found for the N-substituted endohedral fulleropyrrolidines.

The effect of the fullerene surface curvature, was found to be also important for the isomerization rate. The comparison of the two different isomers **3**/**4**-C_{70} with the equivalent **2b**-C_{60} showed that there exists a relationship between the

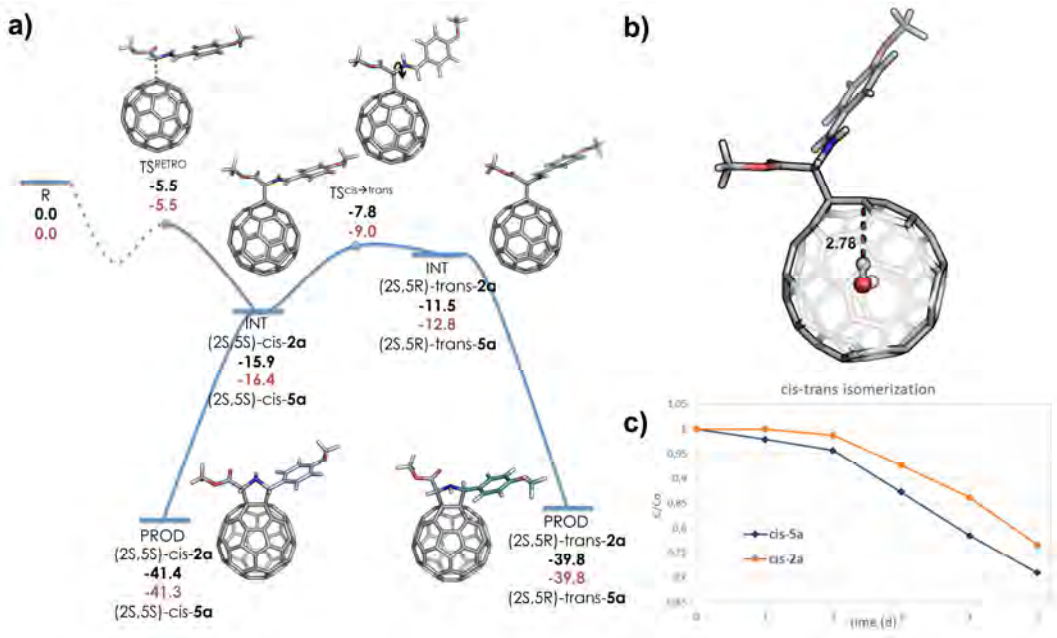

Figure 6.11: a) Computed isomerization mechanism for the *cis-tras* isomerism versus the retro-Prato reaction at the M06-2X/6-311+G(d,p)//OLYP/TZP level of theory for C_{60} **2a** and $H_2O@C_{60}$ **5a** endohedral derivative. Energies given in kcal·mol^{-1}; b) Optimized INT(2S,5R)-*trans*-**5a**; c) Representation of the experimental observed reaction rates for the *cis-trans* isomerism for C_{60} **2a** and $H_2O@C_{60}$ **5a**.

Table 6.4: Relative stabilities of *cis-trans* products and intermediates with respect to the isolated reactants for C_{60}, $H_2@C_{60}$ and C_{70}. Relative energies given in kcal·mol^{-1}.

	C_{60}				$H_2O@C_{60}$	C_{70}	
	2a	**2d**	**2e**	**2b**	**5a**	**3**	**4**
PROD-cis	-41.4	-42	-41.1	-41.9	-41.3	-42.3	-42.1
INT-cis	-15.9	-13.3	-11.4	-14.8	-16.4	-19	-13.3
TS int. cis-trans	-7.8	-	-	-	-9.0	-	-
INT-trans	-11.5	-7.6	-3	-10.4	-12.8	-14.8	-8.6
PROD-trans	-39.8	-40.2	-39.4	-40.6	-39.8	-40.9	-40.8
RETRO	-5.5	-	-	-	-5.5	-	-
ΔE_{PROD}**(trans-cis)**	1.6	1.8	1.7	1.3	1.5	1.4	1.3
ΔE_{INT}**(trans-cis)**	4.4	5.7	8.4	4.4	3.6	4.2	4.7

average pyramidalization angle of the fullerene pentagonal ring where the new C-C bond is formed (10.0°, 10.4°, and 10.8° for **3**, **2b**, and **4**, respectively) and the stability of the **INT**-*cis* species (-19, -14.8, and -13.3 kcal·mol^{-1} for **3**, **2b** and **4**, respectively), being the more planar region, the one which better stabilizes the zwitterionic negative charge centred on the fullerene.

Finally, we investigated the effect of the encapsulated water molecule on the *cis-trans* isomerization process. We showed that the inner water molecule does not affect the thermodynamic *cis-trans* equilibrium, although it has a major role on the isomerization kinetics: *cis*-**5a** is 0.5 kcal·mol^{-1} more stable than the equivalent empty cage, and INT-*trans*-**5a** and TS$^{cis-trans}$ are *ca.* 1.3 kcal·mol^{-1} lower in energy, while the retro-Prato barrier is exactly the same (see figure 6.11a). Analyzing the optimized **INT**-*trans*-**5a** structure, presented in figure 6.11b, we observe that the extra stabilization of the zwitterion intermediates arises from the interaction of the negatively charged carbon atom on the fullerene surface and the hydrogen atom of the water molecule. We explored different possible orientations of the water molecule, being the one with the hydrogen atom directly pointing to the negatively charged carbon atom the one preferred. The $C_{full} \cdots$H-OH distance is ca. 2.7 Å in both *cis* and *trans* intermediates, corresponding to the usual H-bond distances. Our computational results indicate that the acceleration of the *cis-trans* isomerization process is due to the H-bond stabilization of the zwitterionic intermediate species. The inner water molecule does not affect the final *cis-trans* ratio, and

does not promote the loss of stereochemical control through the retro reaction pathway, as summarized in figure 6.11a.

6.2.3 Endohedral metal-induced regioselective formation of bis-Prato adducts of $Y_3N@I_h$-C_{80} and $Gd_3N@I_h$-C_{80}

The regioselective formation of Prato bisadducts of I_h-C_{80} TNT EMFs has been observed for the first time. Experimentally, significant amounts of bisadducts corresponding to the additions to $Y_3N@I_h$-C_{80} and $Gd_3N@I_h$-C_{80} were isolated, and although bisadduct formation for the reactions of $Sc_3N@I_h$-C_{80} and $Lu_3N@I_h$-C_{80} were observed, they could not be isolated. From vis/NIR (visible - near infrared) spectra, ^{1}H-NMR and ^{13}C-NMR experiments, it could be concluded that: 1) for the $Gd_3N@I_h$-C_{80} system, only one bisadduct is isolated which does not isomerize under thermal treatment, and corresponds to an unsymmetric [6,6]-[6,6] addition. 2) for the $Y_3N@I_h$-C_{80} case, one unsymmetric [6,6]-[6,6] bisadduct is kinetically formed and isolated. After heating, the kinetic bisadduct isomerizes to give a mixture of various bisadducts.

Based on the experimental observations from the NMR measures, we have computationally characterized the thermodynamic $Gd_3N@I_h$-C_{80} bisadduct. We selected 23 different possible second addition sites, including both [6,6] and [5,6] positions, and starting from the [6,6] monoadduct as presented in figure 6.12. They were selected based on the relative position of the metal atoms. From our previous studies related with the Prato monoadducts stabilities, we know that the most stable [6,6] products are those closer to the metals. Thus, it would be expected that the second addition takes place in a similar way.

Our calculations show that the thermodynamic $Gd_3N@I_h$-C_{80} bisadduct is the one corresponding to the second [6,6] addition on 57-58 positions (see figures 6.12 and 6.14). It is an unsymmetric [6,6],[6,6] bisadduct, which is *ca.* 0.6 kcal·mol^{-1} more stable than the second most stable bisadduct, the 16-20 [6,6],[5,6] product. In our work on EMF Prato monoadduct, we observed that [6,6] additions are kinetically favored. In this manner, and based on our calculations and in available experimental data, we characterize the isolated $Gd_3N@I_h$-C_{80} bisadduct to be the 57-58 [6,6],[6,6] product. It is important to mention that the most stable bisadducts are found in the closest regions where the metal atoms are pointing (see figure 6.12). This is due to the high strain that fullerene cage has in these regions, with higher pyramidalized carbons, in contrast to the smaller TNTs (see figure 6.13 and table 6.5). As a consequence,

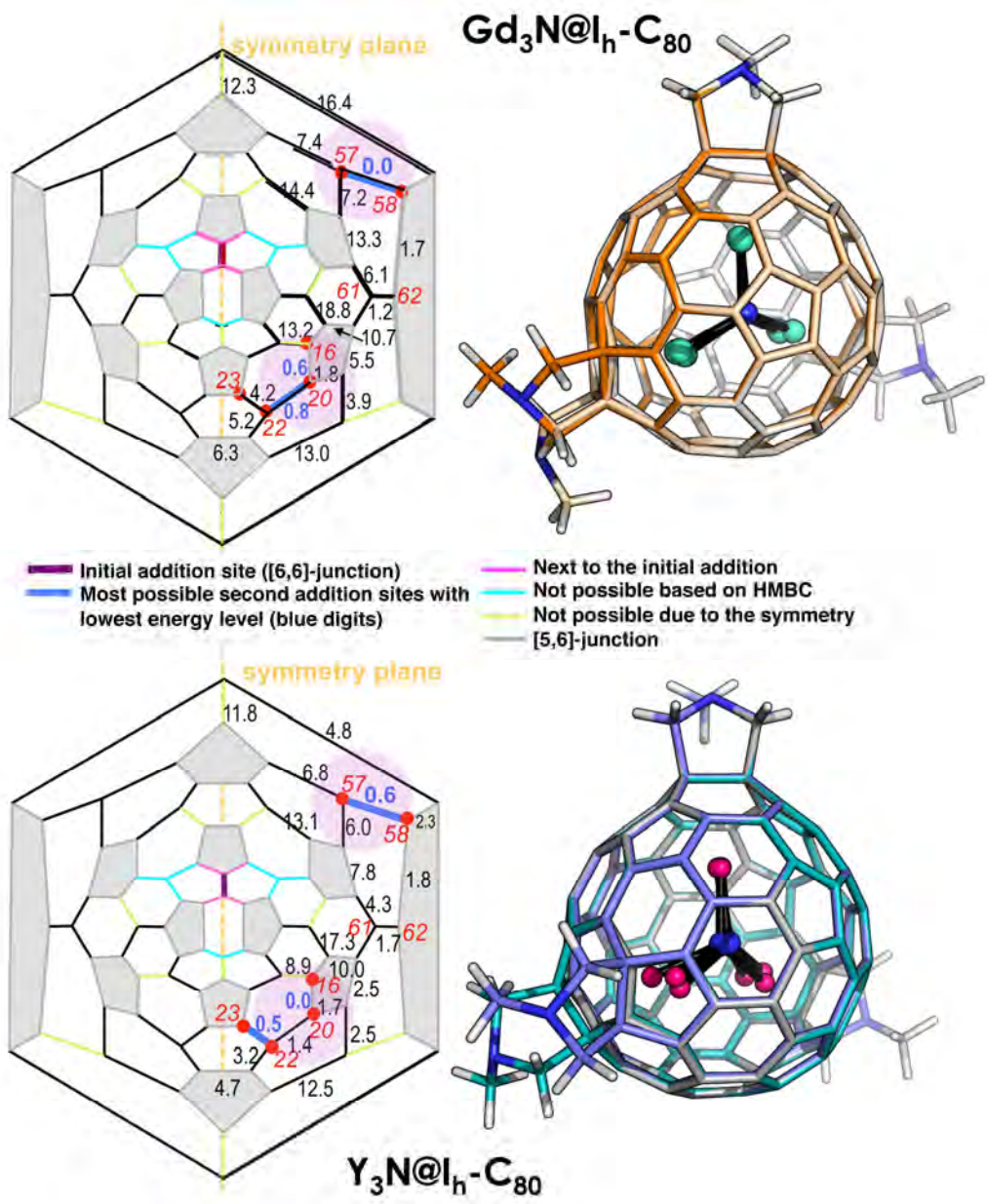

Figure 6.12: Left: Schlegel structure of $Gd_3N@C_{80}$ $Y_3N@C_{80}$ with relative stabilities for 23 different bisadducts calculated at BP86-D2/TZP//BP86-D2/DZP level of theory. Blue thick bonds represent the most stable second addition sites of bisadducts (non-italic numbers are energies in kcal·mol^{-1}, red italic numbers correspond to the positions), and bonds situated close to the metal cluster are highlighted in pink; Right: Overlay of the lowest energy thermodynamic [6,6],[6,6]-bisadducts: for $Gd_3N@C_{80}$, 16-20 in orange, 20-22 in light orange, and 57-58 in gray; and for $Y_3N@C_{80}$, 22-23 in teal, 16-20 in blue, and 57-58 in gray.

the first addition fixes the position of the metal cluster and directs the second Prato addition toward those bonds situated in close contact to the other metallic atoms (see figure 6.13). These regions of the fullerene are highly distorted, and those bonds are highly pyramidalized. The functionalization of these areas releases the fullerene and metal cluster strain, stabilizing the most the bisadduct formed, as the optimized most stable bisadduct structures showed (figure 6.12).

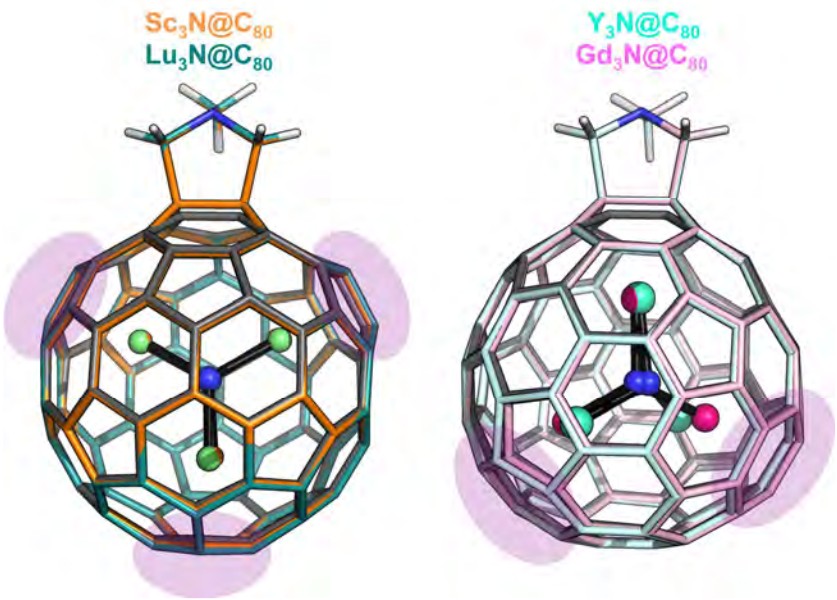

Figure 6.13: Superposition of the most stable monoadducts of (left) C_{80}, $Sc_3N@C_{80}$, $Lu_3N@C_{80}$ and (right) C_{80}, $Y_3N@C_{80}$, $Gd_3N@C_{80}$.

For the $Y_3N@C_{80}$ case, we also characterized the thermodynamic most stable products. As presented in figure 6.12, the thermodynamic second most stable Prato addition on $Y_3N@C_{80}$ starting from [6,6] monoadduct are those occurring on the [5,6] bond (16-20, with the lowest energy), and on two [6,6] bonds (22-23 and 57-58, 0.5 and 0.6 kcal·mol^{-1} higher in energy). Thus, computational results point to a [6,6]-[5,6] bisadduct to be one of the thermodynamically most stable, in agreement with experiments. As previously mentioned, the thermodynamic and kinetic products in the yttrium based bisadditions do not coincide. Because of the impossibility of locating the transition states for the bisadditions due to the flatness of the potential energy surface, we could only suggest that the kinetic additions might be favored at the [6,6] bond 20-22, which could subsequently isomerize under thermal conditions to the most sta-

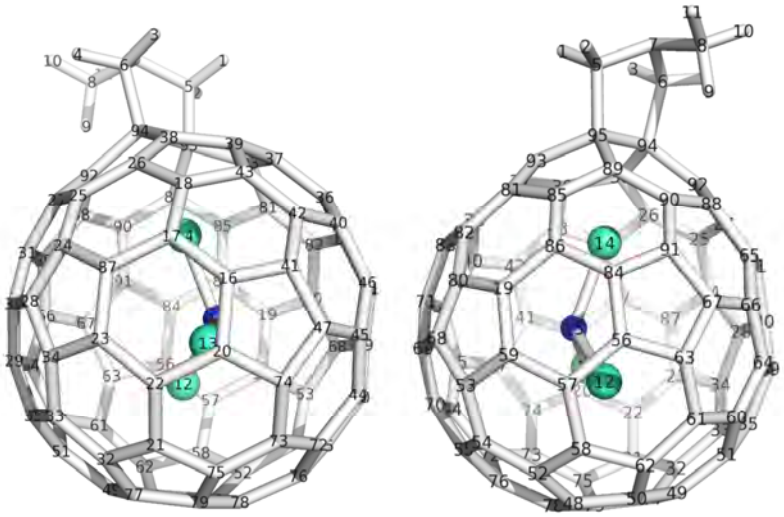

Figure 6.14: $Gd_3N@C_{80}$ monoadduct atomic labels.

Table 6.5: Average pyramidalization angles (in degrees) for some selected bonds of the [6,6] $Lu_3N@C_{80}$ and $Gd_3N@C_{80}$ monoadducts.

Bond	**type**	**Lu Pyr.**	**Gd Pyr.**	**ΔPyr.(Gd-Lu)**
16-20	[5,6]	12.22	12.31	0.09
20-22	[6,6]	12.29	12.59	**0.30**
20-74	[5,6]	13.29	13.16	-0.13
16-41	[5,6]	9.71	10.01	**0.30**
47-74	[5,6]	11.04	11.02	-0.02
57-58	[6,6]	11.89	12.02	0.13
58-62	[5,6]	13.48	13.40	-0.07
61-62	[6,6]	11.67	11.83	0.17
21-22	[6,6]	12.29	12.59	**0.30**
22-23	[6,6]	10.67	11.32	**0.65**
56-57	[6,6]	10.06	10.22	0.16

ble 16-20 [5,6] and 22-23 [6,6] positions. The initial kinetic bisadduct would be mostly isomerized as experimentally observed (figure 6.12). The formation of 57-58 bisadduct where the second addition takes place in a remote position from the kinetic 20-22 one, can be explained by the fact that after 24h under heating conditions, retro-Prato reactions on the pristine $Y_3N@C_{80}$ bisadduct are observed.

Our computational analysis based on what we learned from the monoadduct TNT EMFs formation showed that the final thermodynamic bis-Prato additions are metal-directed: the orientation of the inner metal cluster fixed by the first Prato addition directs the position where the second addition will take place.

6.3 Understanding the structure and reactivity of endohedral metallofullerenes and derivatives from aromaticity analysis

The presence of a metal atom or metal cluster inside a fullerene cage has large consequences and effects on their electronic structure, stability and reactivity. Whereas the aromaticity of free fullerenes has been widely studied from different points of view, the role of aromaticity on endohedral metallofullerene compounds had not been considered yet. In this thesis, we have introduced for the first time the study of the aromaticity in EMFs as an indicator of their stability and reactivity.

In section 5.6, we report an extensive summary of the aromaticity related studies involving fullerenes, endohedral metallofullerenes and related compound that we have recently published as a review article, which also includes the recent advances in the field reported in this thesis. This review highlights different aspects of the aromaticity of fullerenes and EMFs, from how it can be measured to how it can be used to rationalize and predict their molecular structure and reactivity. Our contributions in the field, are briefly summarized in the following lines.

6.3.1 Electrochemical control of the regioselectivity in the exohedral functionalization of C_{60}: the role of aromaticity.

The Diels-Alder cycloaddition involving C_{60} has been extensively studied, and it is well known that both the kinetic and thermodynamic addition takes place regioselectively on the pyracylenic [6,6] bond. We computed the complete reaction path for the DA reaction between cyclopentadiene (Cp) and C_{60} on [6,6] and [5,6] positions, as showed in figure 6.15, finding that the [6,6] reaction barrier and reaction energy are *ca.* 12 and 16 kcal·mol^{-1} more favorable than those for the [5,6] addition. Nevertheless, our calculations revealed that when C_{60} fullerene is reduced with up to 6 electrons, the tendency is inverted becoming the addition on [5,6] position the most favored from kinetic and thermodinamic points of view. The differences in the reaction energies and reaction barriers for the additions on [6,6] and [5,6] bonds when adding n=0-6 electrons to the fullerene are represented in figure 6.15. Negative differences indicate that the addition on [6,6] bond is favored while positive differences indicate a more favorable addition on [5,6] position. Thermodynamic and kinetic behaviour are found to follow the same trend. Thus, the regioselectivity of the Diels-Alder addition on C_{60} can be controlled by electrochemical reduction of the fullerene molecule.

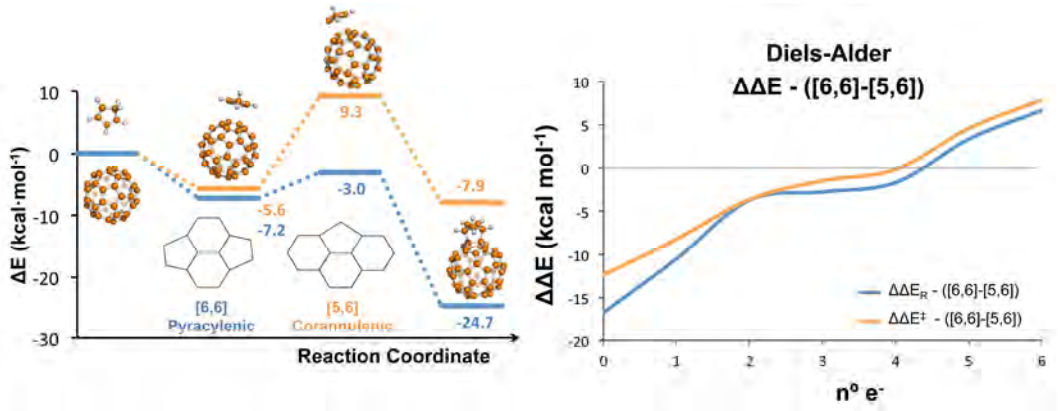

Figure 6.15: Energy profiles obtained at BP86-D2-TZP//BP86-D2/DZP level of the Diels-Alder addition of cyclopentadiene to the [5,6] and [6,6] bonds of C_{60} (left); and energy differences in reaction energies and reaction barriers for the additions on [6,6] and [5,6] bonds when the C_{60} is reduced by n electrons (n=0-6).

In order to analyze this change on the DA regioselectivity, we studied the changes in the aromaticity of the five and six- membered rings (5-MRs and 6-MRs). As showed in figure 6.16, we found that aromaticity of 5-MRs increases while the 6-MRs decreases when electrons are added to the C_{60} molecule. It has been shown that charge distribution in negatively charged fullerenes is not uniform, and the negative charge is mainly localized on 5-MRs.[145] As a consequence, when a 5-MR is negatively charged, it becomes more cyclopentadienyl anion-like, which fulfills the Hückel 4N+2 rule, and thus becomes more aromatic. On the contrary, the negative charge induces a decrease of the 6-MR aromaticity because they lose the ideal 4N+2 electronic structure.

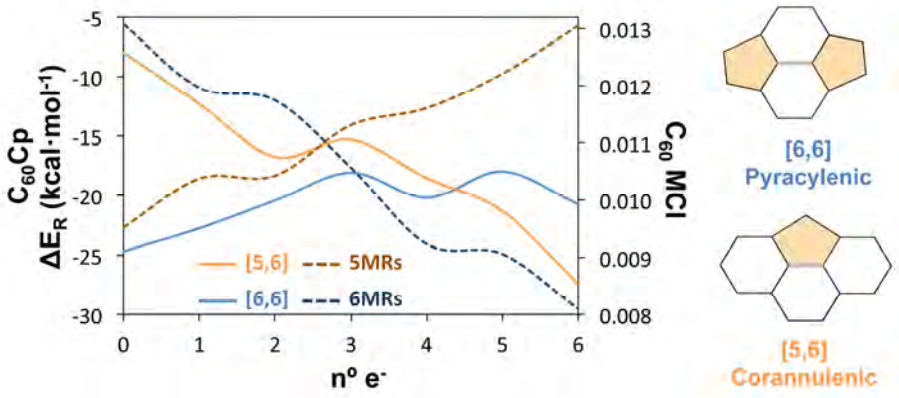

Figure 6.16: Representation of the reaction energies for the Diels-Alder reaction of cyclopentadiene to [6,6] and [5,6] bonds of C_{60} and aromaticity MCI values (dashed lines) of the 5-MRs and 6-MRs in C_{60} when the fullerene is reduced by n electrons.

When the reaction takes place on a pyracylenic [6,6] bond type, the π conjugation of two 5-MRs and two 6-MRs is lost. On the other hand, when the addition is on a corannulenic [5,6] bond, the conjugation banishes in three 6-MRs and one 5-MR. From this observation, we can rationalize the changes induced in the regioselectivity of the reaction. A higher aromaticity of a given ring implies more resistance towards an attack over one of its bonds, and vice versa for lower aromativity. Consequently, when 6 electrons are transferred to the C_{60}, the [5,6] addition barrier is lower in energy because it only destroys the conjugation of only one more aromatic 5-MR.

We have shown that it is possible to electrochemically control the regioselectivity in the DA reaction on fullerenes, and it can be rationalized in terms

of 5-MR and 6-MR local aromaticity. Negatively charged fullerenes are used as a models for describing the structure of endohedral metallofullerenes. In that sense, our results could help in explaining why in EMFs the DA on [6,6] position is not regioselective preferred and [5,6] adducts are often obtained, in contrast to what happens for empty and neutral fullerenes.

6.3.2 Maximum aromaticity as a guiding principle to determine most suitable hosting cages in endohedral metallofullerenes

In our previuos work, we found that when negative charged is transferred to a fullerene cage the aromaticity of its 5-MRs and 6-MRs is modified. In addition, it was previously reported that there exists a correlation between the negative charge centred on 5-MRs and the relative stability of C_{2n} anionic fullerenes with the same number of carbons and adjacent pentagon pairs (APPs).[95,145] Negatively charged fullerene isomeric structures are good models for describing EMF stabilities,[143] as their electronic structure can be described using the ionic model (for example, $M_3N^{6+}@C_{2n}^{6-}$ for TNTs, or $M_2C_2^{4+}@C_{2n}^{4-}$ for metallic carbides).

Based on the mentioned precedents, we proposed that the aromaticity of the fullerene rings could have also a key role on the stability of endohedral metallofullerenes. In this line, we proposed the additive local aromaticity (ALA) index as an aromaticity indicator for the study of the stability of negatively charged fullerene isomers. ALA index is defined as the sum of the local aromaticities of all rings in the cage:

$$ALA = \sum_{i=1}^{n} A_i \tag{6.2}$$

where A_i is the local aromaticity of ring i, and n is the number of rings in the fullerene, including both 5- and 6-MRs. This index aims to be a representative indicator for comparing the local aromaticities of the rings in different fullerene cages with the same number of carbon atoms.

We have computed the ALA index using the geometric HOMA aromaticity indicator for all the possible C_{72} isomers with 0, 1, 2, and 3 APPs and we have compared them with their relative stabilities computed at AM1 level. As showed in figure 6.17, no correlation between the relative stability and aromaticity is found when the neutral fullerene is considered. The most stable isomer

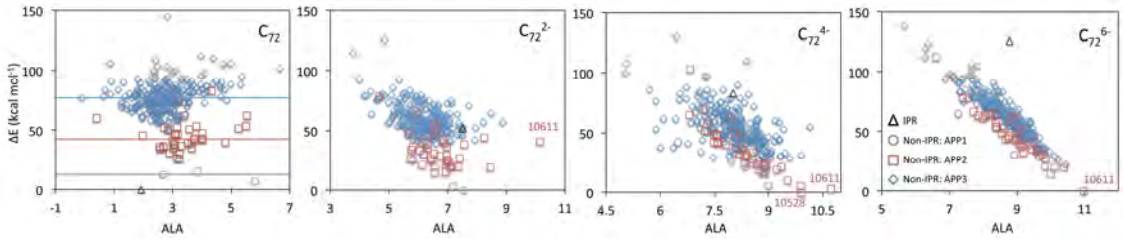

Figure 6.17: Relative stabilities (at AM1 level) of C_{72}^{m-} isomers with 1-3 APPs with respect to the ALA index. The lines in C_{72} neutral case indicate the relative average energies with respect to the IPR case for each isomeric type. Isomers experimentally observed in EMFs are indicated with their corresponding label.

is the IPR one, and when the number of APPs increases, the relative stability of the fullerene isomers decreases. The latter was expected from the isolated pentagon rule (IPR) and the pentagon adjacency penalty rule (PAPR). Nevertheless, when the negative charge of the fullerene isomers increases up to six electrons, we found a very good correlation between the relative stabilities of the fullerene isomers and their local aromaticities in terms of ALA index, regardless of the number of APPs they have. Here it is important to remark that C_{2n} hexaanions are very good models for describing endohedral metallofullerene relative stabilities. The most stable isomer, the non-IPR (10611)−C_{72} cage which experimentally forms $La_2^{6+}@C_{72}^{6-}$ EMF, is the one that exhibits the largest ALA index value. Thus, our results indicate that the most stable isomers are those which maximize their local aromaticity (Maximum ARomaticity Criterion, MARC). In addition to that, our results can explain why the IPR rule is no longer fulfilled when EMFs are considered. The isomer which can better stabilize the negative charge transferred by the encapsulated metal cluster is the most aromatic one due to its electronic structure, regardless the number of pentagon adjacent pairs it has.

We have systematically computed the ΔE vs. ALA for all the most common C_{2n} ($2n$= 66-104) EMFs reported to date, including IPR and non-IPR cages in their anionic form. The considered negative charge depends on the formal electron transfer from the metallic cluster to the fullerene. Our results, summarized in figure 6.18, indicate that fullerene isomers that are experimentally detected forming EMFs, are those which have the largest local aromaticities in terms of the ALA index.

The proposed maximum aromaticity criterion can predict the formation of a

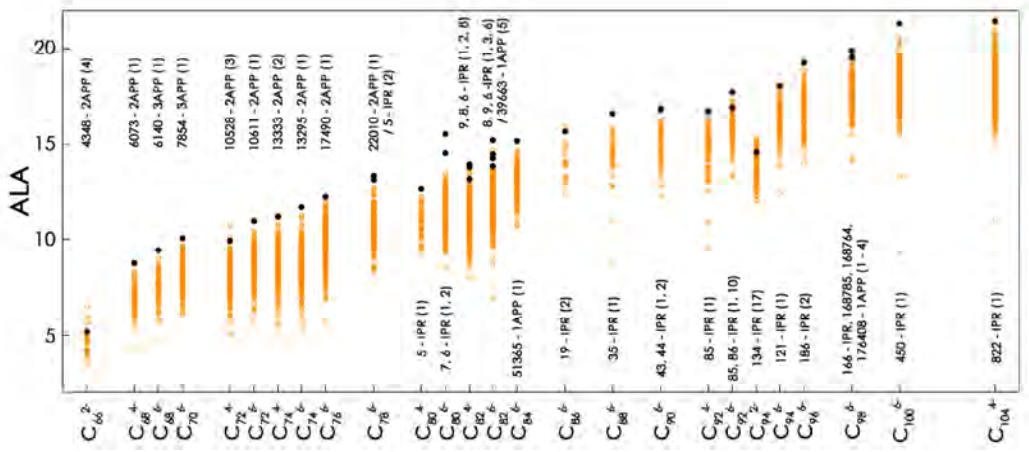

Figure 6.18: Classification in terms of the ALA index of the anionic IPR and non-IPR fullerene isomers with 1-3 APPs for the most common C_{2n} ($2n$=66-104) EMFs reported to date. Isomers experimentally observed are marked using black dots, and their corresponding isomer labels are indicated. The ALA prediction ordering for the experimentally observed isomers are given in parentheses.

non-IPR EMF, as for instance the case of C_{72}^{6-}, but it can also predict the IPR EMF stabilization. For example, C_{80}-based TNT EMFs can be synthetized in two different isomeric forms: the I_h-C_{80} ($Sc_3N@I_h$-C_{80}, the most abundant EMF), and D_{5h}-C_{80} ($Sc_3N@D_{5h}$-C_{80}, less abundant). These two isomers are the C_{80}^{6-} isomers whith the largest ALA values, as showed in figures 6.18 and 6.19a. The same good performance of the aromaticity criterion and ALA index is found to describe mixed IPR and non-IPR EMFs formation, as for example in C_{78}^{6-} systems (see figure 6.19b). Depending on the nature of the metallic cluster encapsulated, different number of electrons are formally transferred from the cluster to the fullerene. Our results also showed that using the ALA index one can rationalize the different isomer stabilization when six (figure 6.21c) or four electrons (figure 6.21d) are transferred, for example, to the C_{68} fullerene.

Finally, we have also shown that the maximum aromaticity criterion does not depend on the method used for computing the local aromaticities of the fullerene rings. The same trends and correlations are found when using the electronic multicenter index MCI and DFT optimized structures (see figure 6.19e) instead of HOMA aromaticity measures and the AM1 optimized structures

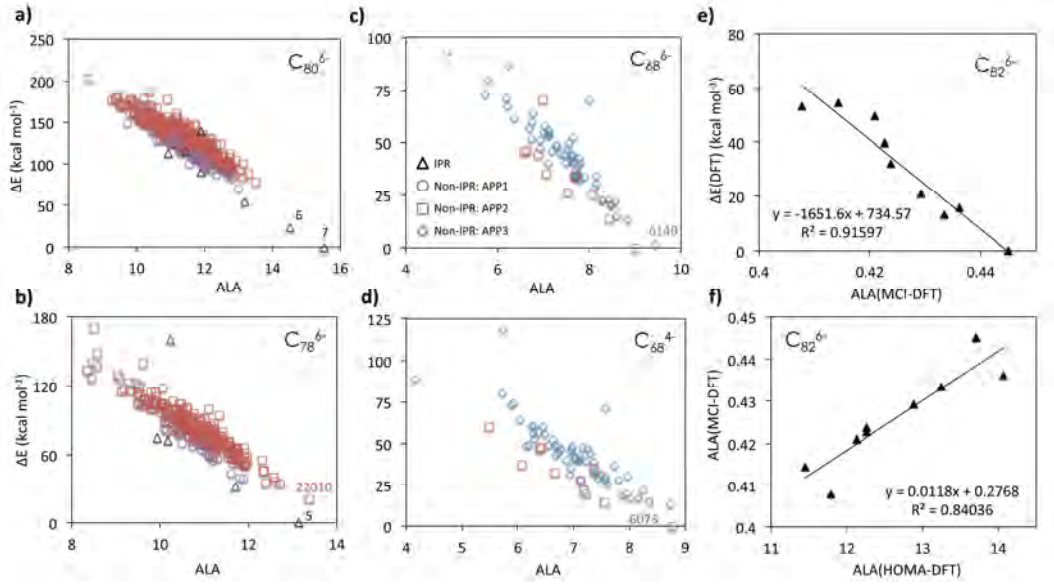

Figure 6.19: Relative stabilities (at AM1 level) of a) C_{80}^{6-}, b) C_{78}^{6-}, c) C_{68}^{6-}, and d) C_{68}^{4-} isomers with 1-3 APPs with respect to the ALA index. Isomers experimentally observed in EMFs are indicated with their corresponding label. e) Relative stabilities (at BP86/DZP level) of C_{82}^{6-} IPR isomers versus the computed ALA index using MCI measures. f) Computed ALA index using MCI index for C_{82}^{6-} IPR isomers versus computed ALA index using HOMA index.

(see figure 6.19f).

6.3.3 Understanding the relative abundances of TNT-based endohedral metallofullerenes from aromaticity measures

Following the line started with our previous study, we have generalized the ALA index to expand its scope. In this work, we proposed the normalization of the ALA index per number of rings present in the fullerene structure to allow the comparison between fullerenes with different number of carbon atoms, as follows:

$$ALA_N = \frac{1}{n}\sum_{i=1}^{n} A_i \tag{6.3}$$

where A_i is the local aromaticity of ring i, and n is the number of rings in the fullerene, including both 5- and 6-MRs. In order to compare ALA_N measures which include different number of rings, we needed to use an accurate aromaticity index which equally treats both ring types. In that sense, we proposed to use the normalized version of the MCI multicenter index, the so-called I_{NB} electronic index.

In figure 6.20 we summarize the ALA_N values for selected C_{2n} ($2n$=68-88) isomers, sorted by their ALA_N values. As a general trend, fullerene isomers experimentally observed containing TNT moieties have the largest ALA_N values, which indicates that they are more aromatic in terms of ALA_N. The rest of thousands less stable C_{2n} isomers exhibit lower ALA_N values (lower ALA values, from our previous work). Thus, our computations indicate that the most aromatic C_{2n} ($2n$=68-88) fullerene cages, independently of their size or their number of APPs, are those most suitable for stabilizing a TNT-based EMF.

Finally, we have applied the ALA_N index for the analysis of the relative abundances of $Sc_3N@C_{2n}$ ($2n$=68-88) EMFs. We have computed the aromaticity in terms of ALA_N using the electronic delocalization I_{NB} index for the optimized EMFs structures explicitly containing scandium TNT metallic cluster inside. The results, included in figure 6.21, demonstrate that the most abundant EMF, $Sc_3N@I_h$-C_{80}, is also the most aromatic scandium-based TNT EMF. The second most aromatic EMF is D_{5h}-C_{80}, followed by the $Sc_3N@C_{68}$ and $Sc_3N@C_{78}$ TNTs, which are the following most abundant scandium based TNT EMFs obtained from an arc discharge synthesis. Consequently, our re-

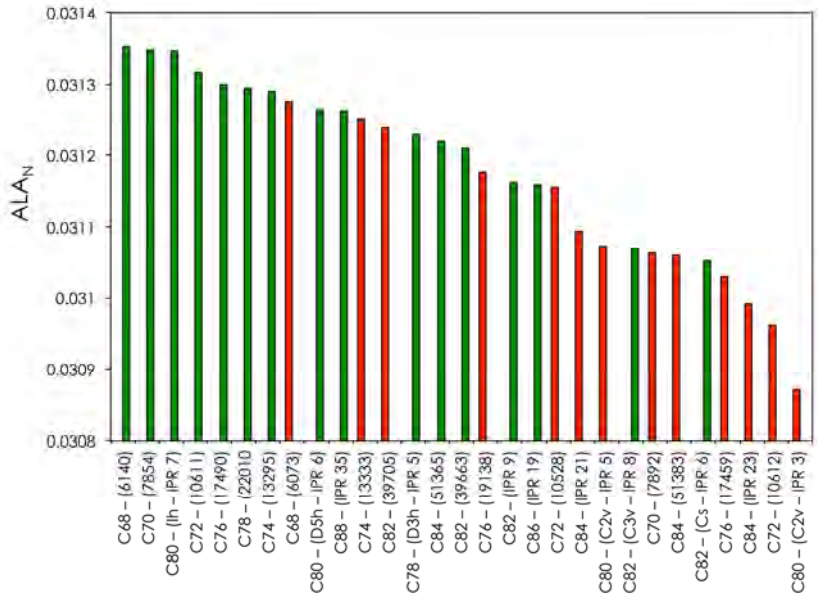

Figure 6.20: Classification in terms of the ALA_N index (calculated at B3LYP/6-31G//BP86/DZP level) of the hexaanionic most stable C_{2n} isomers, which also exhibit the largest ALA values for each C_{2n} ($2n$=68-88) fullerene family, obtained from our previous work.[363] Isomers experimentally observed containing TNT units are displayed in greeen, while isomers experimentally not formed are colored in red.

sults indicate that the ALA_N index obtained for Sc_3N based EMFs can be used to predict the relative stabilities of endohedral metallofullerenes regardless the fullerene cage size or the number of adjacent pentagon pairs, being the experimentally detected most abundant EMFs formed the most aromatic ones.

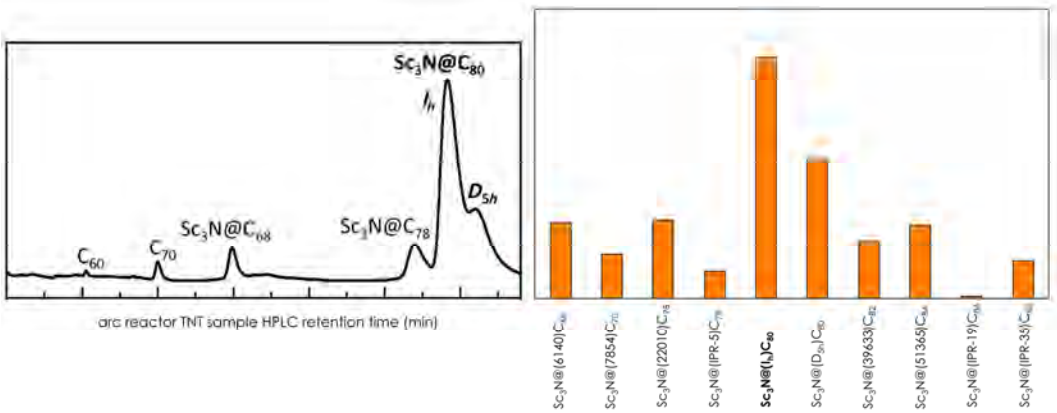

Figure 6.21: Right: Relative ALA_N values (calculated at B3LYP/6-31g//BP86/DZP level) for $Sc_3N@C_{2n}$ fullerenes, sorted by increasing cage size; Left: Quantitative HPLC chromatograms of the arc reactor carbon sample of a typical scandium based TNT EMFs synthesis (from Prof. Echegoyen's lab).

It is important to mention that our calculations indicate that the most aromatic C_{78} isomer is the non-IPR-(22010) isomer, and the second the IPR-(5) D_{3h} isomer when scandium TNT unit is encapsulated (see figure 6.21). These results are consistent with the ones obtained for the hexaanionic empty isomers (see figure 6.20). For scandium TNT, the IPR isomer is the one formed instead of the non-IPR, being the latter the one that encapsulates larger metallic TNTs such are Y_3N, Gd_3N or Dy_3N. These results indicate that both cages are equally suitable for hosting the TNT units, but due to the different size of the TNT moieties and the strain suffered by the metallic cluster and the fullerene structure due to incarceration, they are differently stabilized when the metallic cluster is encapsulated inside.

6.3.4 Aromaticity as the driving force for the stability of non-IPR endohedral metallofullerene Bingel-Hirsch adducts

Bingel-Hirsch (BH) reaction is one of the most employed strategies for functionalizing fullerenes and endohedral metallofullerenes. In general, the thermodynamically most stable EMF products obtained are those corresponding to open-cage adducts (termed fulleroids). None of the traditional parameters used to understand the regioselectivity in EMFs, that is C-C bond distances and pyramidalization angles, are able to describe the stability tendencies found. Based on our previous findings where we relate the endohedral metallofullerenes stabilities with the local aromaticity of their rings, we have studied the relationship between the aromaticity of the BH EMF monoadducts and their relative stabilities.

We have computed the relative stabilities of selected monoadducts, at BP86-D2/TZP//BP86-D2/DZP level, for $Gd_3N@C_s(51365)$-C_{84}, $Y_3N@C_2(22010)$-C_{78}, and $Sc_3N@D_3(6140)$-C_{68} EMFs , as showed in figure 6.22. In addition, we calculated the ALA index at HOMA level for each optimized BH monoadduct structure. The correlations found between the relative stabilities of the different monoadducts and their corresponding ALA values indicate that the lowest in energy products are those that are more aromatic in terms of local ALA index, independently of the number of APP units on the structure (1 for C_{84}, 2 for C_{78}, and 3 for C_{68} based EMFs).

We found that, in general, closed-cage adducts are the least aromatic and the least stable. In these adducts, there is an hybridization change of the attacked carbon atoms from sp^2 to sp^3, disrupting the π electron delocalization of the rings. In the case of the open-cage structures, all fullerene carbon atoms keep their sp^2 hybridization (large π electron delocalization) resulting in the so-called homofullerenes.

Those products with similar ALA values have similar stabilities, regardless of their bond type. For example, we found that product **C**, a [6,6] monoadduct in $Sc_3N@D_3(6140)$-C_{68} and product **D**, a [5,6] addition, have relative stabilities of 0.0 and 0.2 kcal·mol^{-1}, and exhibit equivalent ALA index measures. In addition, aromaticity measures rationalize the different stabilities found for analogous bonds which have similar C-C bond distances and pyramidalization angles. This is the case, for example, of products **F1** (2.4 kcal·mol^{-1}) and **F2** (ca. 11 kcal·mol^{-1}) in $Sc_3N@D_3(6140)$-C_{68} EMF that have equivalent bond distances and pyramidalization angles.

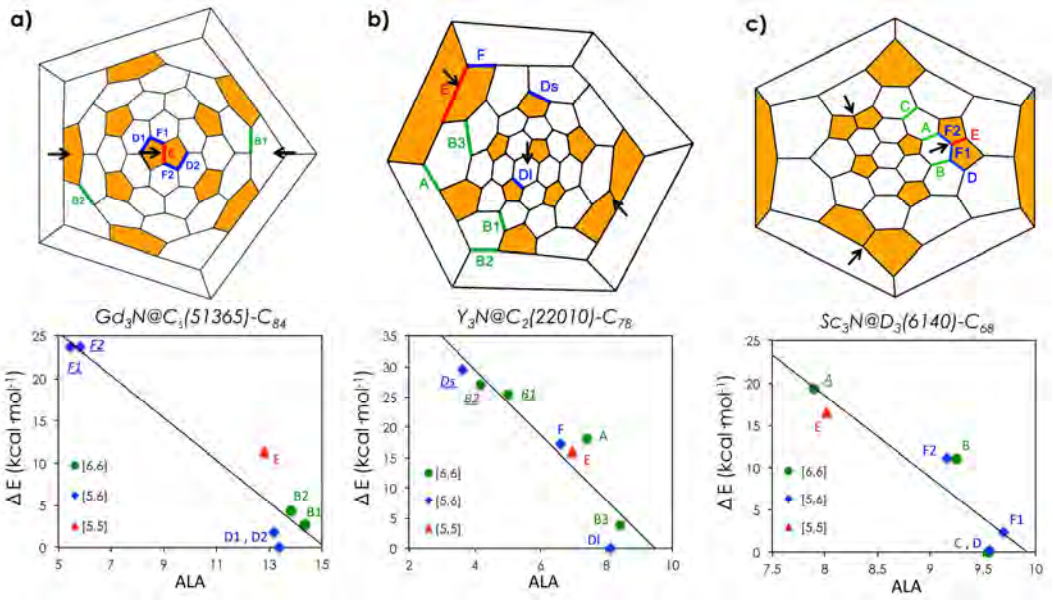

Figure 6.22: Schlegel diagram representations with the considered bonds and the relative stability of Bingel-Hirsch monoadducts at BP86-D2/TZP//BP86-D2/DZP level with respect to the ALA index of: a) $Gd_3N@C_s$(51365)-C_{84}; b) $Y_3N@C_2$(22010)-C_{78}; and c) $Sc_3N@D_3$(6140)-C_{68} EMFs. Green circles, blue diamonds, and red triangles represent [6,6], [5,6] and [5,5] bonds, respectively. Closed-cage products are labeled in italics and underlined. The positions of metallic atoms are symbolized by black arrows and 5-MRs are highlighted in orange.

An important observation is that in none of the three studied systems, the thermodynamic addition to the [5,5] bond is favored, as opposite to what is found for the Diels-Alder addition on $Y_3N@C_2(22010)$-C_{78} EMF.[242] The presence of a metallic atom facing the attacked C-C bond, as experimentally observed in the $Y_3N@I_h$-C_{80} X-ray monoadduct structures, is also found in most of the the optimized most stable products of the studied systems. For example, the latter is observed for the **Dl** product of $Y_3N@C_2(22010)$-C_{78} EMF, as showed in figure 6.23. The occupancy of this position by the metal atom, also improves the *p*-*p* overlap between the functionalized carbon atom orbitals enhancing the ring π-homoaromaticity.

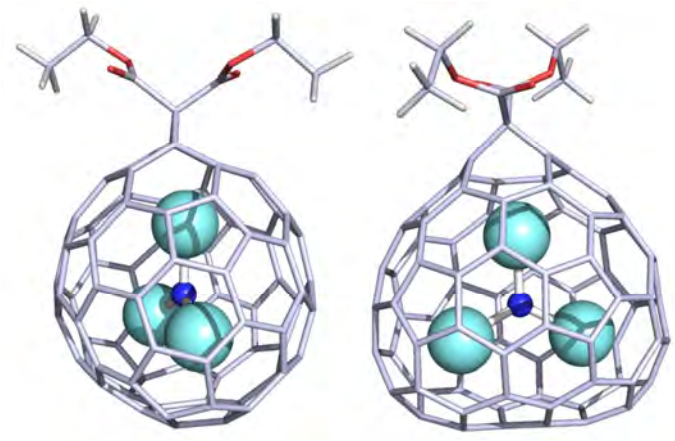

Figure 6.23: Optimized structure at BP86-D2/DZP of the most stable Bingel-Hirsch $Y_3N@C_2(22010)$-C_{78} **Dl** monoadduct, with an yttrium atom directly facind the functionalized open-cage C-C bond.

Our computational exploration showed that there exists a relationship between the relative stabilities of BH monoadducts of non-IPR EMFs and their aromaticities measured in terms of ALA index. This fact, confirms that the maximum aromaticity criterion is a powerful tool for analyzing and rationalizing the stability of EMF thermodynamic BH products.

6.3.5 Bingel-Hirsch derivatization of TNT endohedral metallofullerenes predicted from simple aromaticity measures. The $Sc_3N@D_{3h}$-C_{78} and $Sc_3N@D_{5h}$-C_{80}

As observed in our previous work, we found a relationship between the stability of Bingel-Hirsch EMF monoadducts and their ALA aromaticity. Nevertheless, the group of Prof. Poblet has demonstrated that the BH reaction under typical conditions is kinetically controlled.[255,256] As a consequence, we decided to try to find some parameters and/or rules for predicting the regioselectivity of BH additions on IPR EMFs under kinetic control.

To that end, we computationally studied the Bingel-Hirsch addition of diethylbromomalonate over all 13 nonequivalent bonds of $Sc_3N@D_{3h}$-C_{78} EMF at BP86-D2/TZP//BP86-D2/DZP level. In figure 6.24 we summarize the results obtained. Our computations revealed that the addition to bond **6** has the lowest activation energy among all possible additions ($\Delta G^{\ddagger} = 7.3$ kcal·mol^{-1}). This result is in agreement with the experimental monoadduct detected and characterized by means of NMR measures by Dorn and co-workers.[209] In addition, we found that those bonds presenting the most exothermic reaction energies do not coincide with those having the lowest reaction barriers, as previously reported for BH additions on non-IPR EMFs.[255,256]

The lowest energy intermediate **int56**, which leads to the kinetic product **6** formation, and **int234** are substantially lower in energy that the other possible intermediates (see figure 6.24). We have found thatthe aaromaticity can be used to understand why those intermediates corresponding to the attack on a carbon atom situated in a three hexagonal rings junction (denoted as *int666* in figure 6.24) are the most stable ones. First, 5-MRs in EMFs are those that concentrate the negative charge transferred from the metal to the fullerene structure, thus become more aromatic. Then, the *int666* intermediates are more stable than *int566* because in the former no 5-MRs aromaticity is lost in the attack of the C atom. And second, the formed intermediate is negatively charged, with the negative charge delocalized on the vicinity of the attacked carbon atom. Therefore, those intermediates having 5-MRs on neighbor positions, as **int56** and **int234**, will be able to better stabilize the extra negative charge.

The difference in the reaction activation barrier for the formation of products **5** and **6** (ca. 10 kcal·mol^{-1}), which come from the same intermediate (see figure 6.24), has also been rationalized in terms of aromaticity measures. Be-

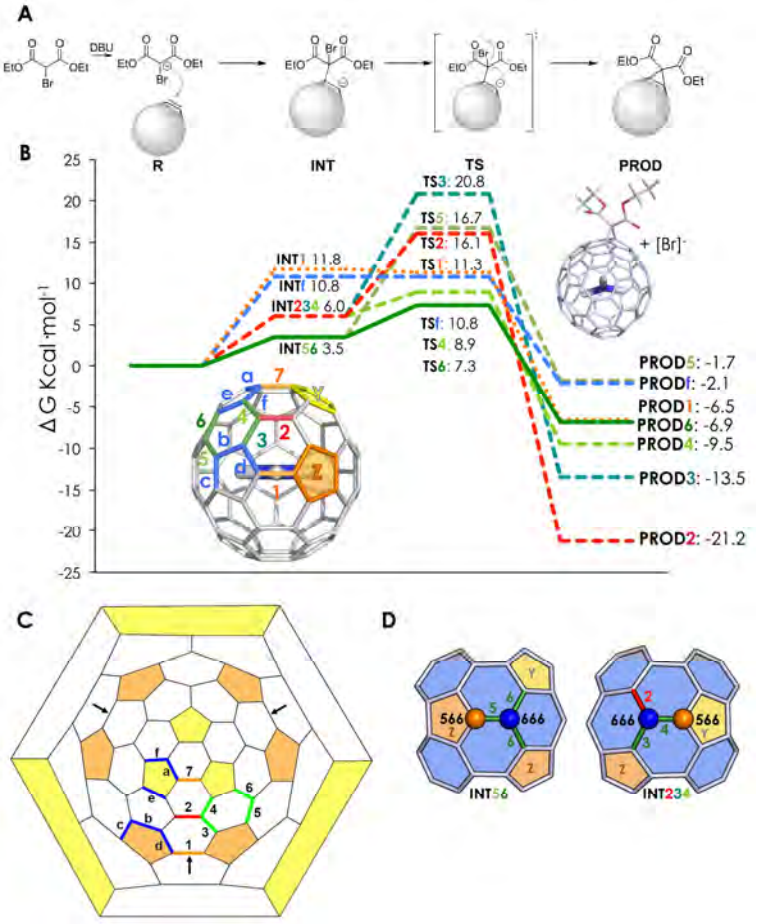

Figure 6.24: A) The Bingel-Hirsch mechanism. B) Gibbs free energy profile for the BH cycloaddition to selected non-equivalent bonds of $Sc_3N@D_{3h}$-C_{78} (in kcal·mol^{-1}). C) Representation of the seven non-equivalent [6,6] bonds: pyracylene bonds **1** and **7**, pyrene or type C bond **2**, and type B bonds **3**, **4**, **5**, and **6**; and the six types of [5,6] D corannulene bonds, **a**-**f**. D) Schematic representation of intermediates **int56** and **int234**. Blue carbon atoms (in spheres) represent the initial addition site corresponding to *int666*; orange carbon atoms denote *int566*. For clarity, 6-MRs are colored in blue, Z-5-MRs in orange and Y-5-MRs in light yellow.

cause of the proximity of the metal atoms, 5-MRs **Z** in $Sc_3N@D_{3h}$-C_{78} are more aromatic than **Y** 5-MRs. It is energetically more favored to attack the less aromatic **Y** 5-MR than **Z** 5-MRs during the BH nucleophilic second step. In general, our calculations indicate that the cyclopropane ring closure is preferred to be on 5-MRs than 6-MRs because 5-MRs are better nucleophiles. In addition to that, we observed that closed-cage products are usually obtained when the cyclopropane ring closure takes place on a carbon atom having a lower pyramidalization angle and located in a ring with low aromatic character. On the other hand, open-cage products usually present a high pyramidalization angle of the attacked carbon atom located in a ring with large aromatic character.

The understanding of the BH reactivity patterns observed in the case of $Sc_3N@D_{3h}$-C_{78} in terms of aromaticity led us to proprose an aromaticity-based criteria (Predictive Aromaticity Criteria, PAC) to predict the regioselectivity of Bingel-Hirsch additions on IPR EMFs (figure 6.25a).

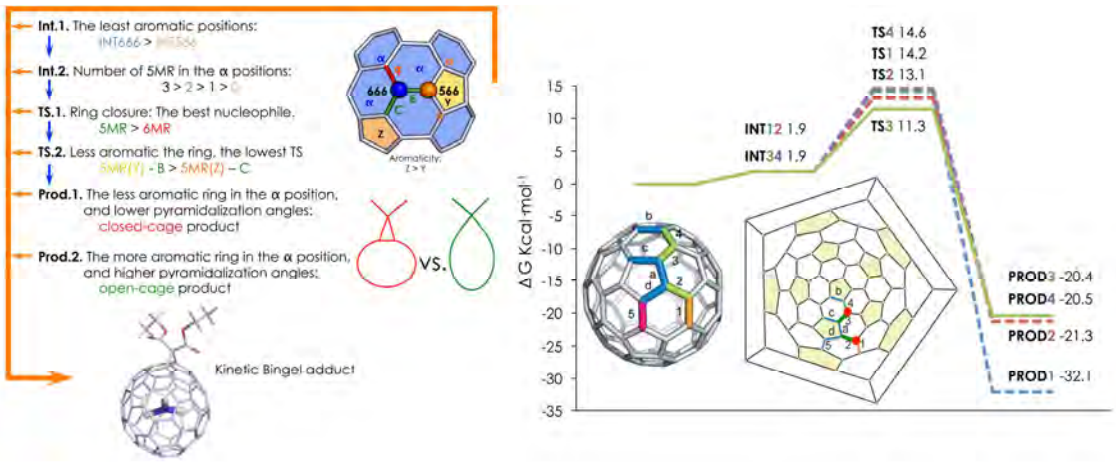

Figure 6.25: Left: Predictive Aromaticity-based rules for the Bingel-Hirsch addition on IPR EMFs; Right: Gibbs free energy profile for the BH cycloaddition to selected non-equivalent bonds of $Sc_3N@D_{5h}$-C_{80} (in kcal·mol^{-1}) and the representation of the five non-equivalent [6,6] bonds: pyrene bond type bond **1**, pyracylene bond **5**, and type B bonds **2**, **3**, **4**, and **5**; and the four type D corannulene bonds **a-d**.

We subsequently applied the PAC criteria to predict the regioselectivity of BH addition on the challenging $Sc_3N@D_{5h}$-C_{80} system. The D_{5h}-C_{80} cage has 9 different possible addition sites (see figure 6.25), and the TNT cluster can

freely rotate inside. Applying our proposed aromaticity criteria, we identified two possible *int666* on the $Sc_3N@D_{5h}$-C_{80} EMF, **int12** and **int34** as shown in figure 6.25, and predicted **int34** to be slightly more stable because of having 3 pentagons on vicinity positions. According to PAC, and our aromaticity calculations which indicate that 5-MR rings containing bonds **a-c-d** are less aromatic than 5-MR rings containing bond **b**, we concluded that the formation of product **3** should be more favored.

The computational exploration of the BH reaction on all 9 different addition sites, considering 7 different orientations of the inner cluster, are in complete agreement with the PAC prediction. The Gibbs energy profiles for some selected additions are shown in figure 6.25. As predicted, intermediates **int12** and **int34** are those more stable, and the transition state for the formation of product **3** is the one lowest in energy, thus being the proposed kinetic product for the BH addition on $Sc_3N@D_{5h}$-C_{80} EMF.

The PAC predictions for the BH addition on $Sc_3N@D_{5h}$-C_{80} EMF were also experimentally tested. Three different monoadducts were obtained, the major isomer being the one corresponding to product **3** as predicted initially by the PAC criteria, and our subsequent computational exploration. The good agreement between our proposed PAC predictions and the experiments, indicates that these rules are rather general and could be extensible to other IPR EMFs.

Chapter 7

Conclusions

The main conclusions drawn from this thesis are collected in this chapter, and organized in three main groups.

Diels-Alder Additions on Endohedral Metallofullerenes

First:
The Diels-Alder (DA) reaction on all nonequivalent bonds of the titanium-based metallic carbide endohedral metallofullerene $Ti_2C_2@C_{78}$ has been explored. The results show that the regioselectivity of the addition is dictated by the encapsulated metal cluster, and it is completely changed as compared to the previously studied Sc_3N and Y_3N EMFs. The most favored addition for $Ti_2C_2@C_{78}$ takes place on [5,6] bond called **c**, while additions on Sc_3N and Y_3N EMFs correspond to the attack over the [5,6] bond **d** and [6,6] bond **6**, respectively. $Ti_2C_2@C_{78}$ is found to be less reactive than empty fullerene but more reactive than TNT C_{78} EMFs, which is explained by the HOMO(diene)-LUMO(dienophile) gap increase along the series: $C_{78} < Ti_2C_2@C_{78} < Sc_3N@C_{78}$. The computed distortion (or strain) energy indicate that, the larger the fullerene deformation energy the least reactive the bond. In that sense, the noncluster energy barrier has been introduced as an indicator of the geometric effect induced by the metallic cluster on the reaction barrier as compared to the pristine fullerene. The difference between noncluster reaction barriers and reaction barriers indicates the electronic effect of the metallic cluster on the barrier. The most reactive bonds in $Ti_2C_2@C_{78}$ EMF, bonds **c**, **f**, and **3** are the only ones that present low fullerene deformation energies and favorable differences between reaction barriers and noncluster barriers. This is indicating that the presence of the titanium cluster activates the bond from an electronic point of view. The orientation of the metallic cluster directs the negative charge distribution on the fullerene structure, mainly centered on 5-MRs. Those 5-MRs situated closer to the metallic cluster are more negatively

charged. It is observed that [6,6] bonds placed next to the most charged 5-MRs, are those with the lowest reactivity.

Second:
The Diels-Alder reaction on Ti_2C_2, Sc_3N, and Y_3N C_{78} EMFs has been assessed using the activation/strain (distortion/interaction) model, and the early proposed noncluster model. First, it is shown that activation barriers and reaction energies of DA additions on EMFs are linearly correlated, on the contrary to what is observed for the pristine C_{78}. There exists a good correlation between the reaction energy barriers and the total distortion energies for the DA addition to EMFs. From the noncluster analysis on product structures, it was found that distorted geometries corresponding to the optimized EMF monoadduct structures correctly reproduce the empty fullerene reactivity trends. The inverse road is also fulfilled: the optimized empty fullerene structures where the metallic cluster is included in a SP calculation reproduce the reactivity pattern of the fully optimized EMFs. Based on the latter observations, a new computational approach called the *Frozen Cage Model* (FCM) has been proposed to reduce the computational cost associated with a complete regioselectivity study of Diels-Alder reaction involving EMFs.

Third:
Using the early proposed Frozen Cage Model strategy, the Diels-Alder reactivity of a large variety of I_h-C_{80} based EMFs has been explored. A selected representative number of existing I_h-C_{80} EMFs of different nature, which include classical metal ions, metallic oxides, TNTs, metallic carbides, hydrocarbides and carbonitrides, a total of 11 different metallic clusters, have been considered. The systematic application of the FCM allowed the correct description of the metallic clusters rotation inside the C_{80} cage. Once the best orientation for each [5,6] and [6,6] additions were located, full optimizations of the products and TSs were performed in order to accurately estimate the Gibbs reaction energies and barriers. It is found that the empty cage is much more reactive than its related EMFs. The reactivity trend of each metallo cluster family has been assessed and analyzed in terms of metal cluster size, charge transferred to the fullerene structure, the HOMO-LUMO gap, and the deformation energy of the fullerene structure required to accomodate the metallic cluster inside. As a general trend, the [6,6] addition becomes more favored as compared to the [5,6] one when the size of the metallic cluster increases, the deformation of the fullerene cage is higher, and the charge transfer to the cage is larger. The computation of the large amount of different metallic clusters considered, which can freely rotate inside the fullerene cage, has only been possible due to the application of the previously developed Frozen Cage Model strategy.

Fourth:
The Diels-Alder reaction between $La@C_{2v}$-C_{82} EMF and cyclopentadienyl (Cp) and pentamethyl-substituted Cp (Cp*) has been computationally explored considering all 35 possible addition sites. It is found that the regioselectivity of both Cp and Cp* additions are equivalent, taking place on the [5,6] bond called **o**, as opposite to what was previously reported. The electronic effects due to the presence of methyl substituents on Cp* do not change the regioselectivity of the Diels-Alder reaction initially proposed. In addition to that, the large difference in the Cp and Cp* product stabilities experimentally observed has been analyzed. Experimentally, it was found that the $La@C_{82}$Cp monoadduct decomposition is one order of magnitude faster than that of $La@C_{82}$Cp*. The reaction pathways for Cp and Cp* adducts are similar once the initial reactant complex is formed. Nevertheless, when isolated reactants are considered, the retro-reaction for Cp adduct is slightly exergonic while it is endergonic for Cp* . Electronic effects due to methyl substituents are not important. On the contrary, the dispersion interactions between Cp* and the EMF structure are of the utmost importance to stabilize the final product with respect to the isolated reactants, and they explain the different stability observed experimentally.

1,3-Dipolar Additions on Endohedral (Metallo)Fullerenes

Fifth:
The computational exploration of $M_3N@I_h$-C_{80} (M=Sc, Lu, Y, Gd) [6,6]-to-[5,6] isomerization path has revealed that larger inner metallic clusters favor the stabilization of [6,6]-fulleropyrrolidine mainly due to strain effects. The thermodynamic ratio of [6,6]:[5,6] adducts does not depend on the exohedral substituent of the pyrrolidine ring. For the Sc_3N case, the [5,6] monoadduct is by far the most stable. The large energy difference between both [6,6] and [5,6] adducts coincides with the experimental selective formation of the scandium [5,6] Prato adduct. However, a thermodynamic equilibrium is reached for yttrium and gadolinium based EMFs. The kinetic product always corresponds to the [6,6] addition on the TNT EMF, independently of the metallic cluster or the exohedral substituient. The isomerization from the kinetic [6,6] product to the thermodynamic [5,6] product takes place through a sigmatropic rearrangement instead of a retrocycloaddition-cycloaddition pathway, regardless of the exohedral substituent or TNT metallic cluster. The isomerization process is faster for the smaller TNT clusters because monoadducts containing large clusters are more stabilized due to strain release. The corresponding

zwitterionic intermediates are also higher in energy for large TNT EMFs with respect to the Prato adducts. In addition, the formed zwitterionic intermediates are better stabilized (*i. e.* increasing the isomerization rates) when electron-rich N-substituents on the fulleropyrrolidine ring are considered instead of electron-withdrawing groups. The latter cannot stabilize the positive charge generated on the dipole thus hampering the sigmatropic rearrangement.

Sixth:
The enantiospecific *cis/tras* isomerization in chiral C_{60}, C_{70} and $H_2O@C_{60}$ fulleropyrrolidines has been unraveled. The process occurs via a zwitterionic intermediate in a similar way to the isomerization process found in EMFs, and it is found that the *cis*-to-*trans* isomerization takes place through the rotation of the N-C2 single bond at the zwitterionic intermediate. The isomerization process is thermodynamically driven. It is found that the *cis/trans* relative stabilities do not depend on the exohedral group, the fullerene cage, nor the encapsulated water molecule. Nevertheless, the isomerization rate is highly affected by all these factors: 1) electron-rich C-substituents on the pyrrolidine ring stabilize the zwitterionic intermediate, lowering the isomerization barriers in a similar manner that what is found for EMFs; 2) the encapsulated water molecule stabilizes the zwiterionic intermediate by forming a H-bond with the negatively charged fullerene carbon atom, and thus increasing the isomerization rate; and 3) the more curved the fullerene surface, the less stable the zwitterionic intermediate and the higher the isomerization barriers are.

Seventh:
The Prato bisadduct formation of $M_3N@I_h$-C_{80} (M=Y, Gd) TNT EMFs has been explored in detail. It is found that the most stable bisadditions on Y_3N and Gd_3N EMFs take place in the regions located close to the TNT metal atoms. The thermodynamic addition to the [6,6] 57-58 position is the most stable in Gd_3N case, in agreement with the experimental observations, while two different thermodynamic bisadducts are predicted for the Y_3N system (at [5,6]16-20 and [6,6] 22-23 and 57-58 positions). The bisadduct formation toward these positions located close to the metal atoms is favored due to the partial release of the fullerene and metallic cluster strain after reaction. THese areas are highly distorted (as shown by the high pyramidalization angles), which after reaction provide additional space to the TNT unit to adopt a more planar disposition. As a consequence, the first addition that takes place on a [6,6] bond fixes the position of the metal cluster, and regioselectively directs the second Prato addition towards those bonds situated in close contact to the other metallic atoms.

Structure and Reactivity of Endohedral Metallofullerenes from Aromaticity Analysis

Eighth:
The effect of successive reductions of the C_{60} molecule on the Diels-Alder regioselectivity towards cyclopentadiene addition has been explored. It is found that both from thermodynamic and kinetic point of view, the regioselective formation of [6,6] monoadduct for the neutral C_{60} case changes towards the [5,6] formation when the C_{60}^{6-} anion is considered. This result is indicating that it is possible to electrochemically control the Diels-Alder cycloaddition on fullerenes. Additionally, the aromaticity of the different 5-MRs and 6-MRs dramatically changes when the C_{60} molecule is reduced. The computed MCI and NICS aromaticities indicate that when electrons are added to the fullerene molecule, the aromaticity of 5-MRs increases, whereas for the 6-MRs it decreases. When the reaction takes place on the pyracylene [6,6] bond, the π conjugation of two 5-MRs is lost, whereas in the case of corannulene [5,6] bond the conjugation is lost for only one aromatic 5-MR. Therefore, the addition to the [5,6] position when 6 electrons are transferred to C_{60} becomes more favored.

Ninth:
The relative stabilities of C_{2n}^{m-} anionic fullerene isomers, which were found to properly describe the stability of EMFs, have been studied in terms of their aromaticities. To that end, the Additive Local Aromaticity index (ALA) is proposed as a measure of the fullerene aromaticites. It is found that the aromaticity of C_{2n}^{m-} ($2n$=66-104, m=4/6) anionic fullerene isomers correlates with their relative stabilities, regardless the number of adjacent pentagon pairs (APPs) they have. This is indicating that the most stable C_{2n}^{m-} isomers are those most aromatic (*i. e.* the maximum aromaticity criterion). The most aromatic tetra- and hexa-anionic C_{2n} fullerene isomers are those experimentally detected forming the corresponding $X^{m+}@C_{2n}^{m-}$ EMFs. In this manner, it can be explained why the IPR rule is not always fulfilled when EMFs are considered and non-IPR structures can be stabilized: the most aromatic anionic isomer leads to the most stable EMF regarless the number of APPs they have. It is important to note that these results are not dependent on the aromaticity indicator used to compute the ALA index, since HOMA and MCI measures give the same trends. A normalized version of the ALA index, the ALA_N computed using the normalized version of the aromatic multicenter index I_{NB}, has also been proposed. ALA_N allows the comparison between fullerene isomers with different number of carbon atoms. The most aromatic C_{2n} hexaanionic fullerene isomers in terms of ALA_N, in the $2n$=68-88 range, are those experimentally observed forming TNTs EMFs. The computed ALA_N aromaticities

of $Sc_3N@C_{2n}$ EMFs demostrate that $Sc_3N@I_h$-C_{80} EMF, the most abundant EMF, is indeed the most aromatic scandium-based TNT EMF. Interestingly the relative aromaticities of $Sc_3N@C_{2n}$ EMFs, according to this index, describe their experimental relative abundances, independently to the fullerene cage size or the number of APPs. Therefore, the experimentally detected most abundant EMFs actually correspond to the most aromatic ones. Consequently, the ALA_N index can be used to predict the stability of TNT EMFs.

Tenth:
The thermodynamic stabilities of $Gd_3N@C_s(51365)$-C_{84}, $Y_3N@C_2(22010)$-C_{78}, and $Sc_3N@D_3(6140)$-C_{68} Bingel-Hirsch monoaddutcs have been analyzed in terms of ALA aromaticities. Good correlations between these two factors are found, indicating that those BH most aromatic adducts, in terms of ALA, are those most stable. This confirms that the maximum aromaticity criterion is a powerful tool for analyzing the stability of EMFs thermodynamic BH monoadducts. It is found that, in general, closed-cage adducts are the least aromatic and the least stable. Instead, open-cage structures allow all fullerene carbon atoms to keep their sp^2 hybridization (large π delocalization) resulting in the so-called homofullerenes. The presence of metallic atoms facing the open-cage monoadduct attacked bond, found for the most stable adducts, also improves the *p*-*p* overlap between the functionalized carbon atom orbitals enhancing the ring π-homoaromaticity. The complete exploration of the Bingel-Hirsch addition to all nonequivalent bonds of $Sc_3N@C_{78}$ system, allow us to propose a set of aromaticity based rules to predict the kinetic regioselectivity of BH additions on IPR TNT EMFs: the Predictive Aromaticity-based criteria (PAC). The PAC rules have been applied to predict the kinetically most favored additions on the challenging $Sc_3N@D_{5h}$-C_{80} system, which pointed to the addition to unsymmetric bond **3**. The computational exploration of the addition to all 9 nonequivalent bonds of the structure (considering the rotation of the scandium TNT) indicated that the addition to bond **3** actually presents the lowest activation barrier, in fully agreement with the PAC predicitions. Finally, the experimental functionalization of $Sc_3N@D_{5h}$-C_{80} revealed that the major regioisomer obtained, according to ^{1}H-NMR measures, corresponds to a [6,6] unsymmetric addition. Again, this is in agreement with the addition to **3** as anticipated by the PAC rules. The good agreement between the proposed PAC predictions, the full computational exploration, and the experiments indicates that these rules are rather general and could be extensible to other IPR EMFs.

Bibliography

1 Kroto, H. W.; Heath, J. R.; O'Brien, S. C.; Curl, R. F.; Smalley, R. E. *Nature* **1985**, *318*, 162–163, 10.1038/318162a0.

2 Jones, D. *New Sci* **1966**, *32*, 245.

3 Jones, D. E.; Jones, D. E. *The inventions of Daedalus: A compendium of plausible schemes*; Freeman, 1982.

4 Osawa, E. *Kagaku* **1970**, *25*, 854–863.

5 Bochvar, D.; Gal'pern, E. *Proc. Acad. Sci. USSR* **1973**, *209*, 239–244.

6 Krätschmer, W.; Lamb, L. D.; Fostiropoulos, K.; Huffman, D. R. *Nature* **1990**, *347*, 354–358.

7 Taylor, R.; Hare, J. P.; Abdul-Sada, A. K.; Kroto, H. W. *J. Chem. Soc., Chem. Commun.* **1990**, 1423–1425.

8 Schmalz, T.; Seitz, W. A.; Klein, D. J.; Hite, G. *J. Am. Chem. Soc.* **1988**, *110*, 1113–1127.

9 Fowler, P.; Manolopoulos, D. *An atlas of fullerenes*; International series of monographs on chemistry; Clarendon Press, 1995.

10 Kroto, H. *Nature* **1987**, *329*, 529–531.

11 Campbell, E.; Fowler, P.; Mitchell, D.; Zerbetto, F. *Chem. Phys. Lett.* **1996**, *250*, 544–548.

12 Albertazzi, E.; Domene, C.; Fowler, P. W.; Heine, T.; Seifert, G.; Van Alsenoy, C.; Zerbetto, F. *Phys. Chem. Chem. Phys.* **1999**, *1*, 2913–2918.

13 Zettergren, H.; Alcamí, M.; Martín, F. *ChemPhysChem* **2008**, *9*, 861–866.

14 Klein, D. J.; Schmalz, T. G.; Hite, G.; Seitz, W. *J. Am. Chem. Soc.* **1986**, *108*, 1301–1302.

15 Hirsch, A.; Brettreich, M. *Fullerenes: chemistry and reactions*; John Wiley & Sons, 2006.

16 Pasquarello, A.; Schlüter, M.; Haddon, R. *Science* **1992**, *257*, 1660–1661.

17 Haddon, R. *Nature* **1995**, *378*, 249–255.

18 Steiner, E.; Fowler, P. W.; Jenneskens, L. W. *Angew. Chem. Int. Ed.* **2001**, *40*, 362–366.

19 Fowler, P. *Nature* **1991**, *350*, 20–21.

20 Haddon, R. *Science* **1993**, *261*, 1545–1550.

21 Bühl, M.; Hirsch, A. *Chem. Rev.* **2001**, *101*, 1153–1184.

22 Cyranski, M. K.; Krygowski, T. M.; Katritzky, A. R.; Schleyer, P. v. R. *J. Org. Chem.* **2002**, *67*, 1333–1338.

23 Saunders, M.; Jiménez-Vázquez, H. A.; Cross, R. J.; Mroczkowski, S.; Freedberg, D. I.; Anet, F. A. *Nature* **1994**, *367*, 256–258.

24 Saunders, M.; Jimenez-Vazquez, H. A.; Bangerter, B. W.; Cross, R. J.; Mroczkowski, S.; Freedberg, D. I.; Anet, F. A. *J. Am. Chem. Soc.* **1994**, *116*, 3621–3622.

25 Saunders, M.; Cross, R. J.; Jiménez-Vázquez, H. A.; Shimshi, R.; Khong, A. *Science* **1996**, *271*, 1693–1697.

26 Sternfeld, T.; Hoffman, R. E.; Saunders, M.; Cross, R. J.; Syamala, M.; Rabinovitz, M. *J. Am. Chem. Soc.* **2002**, *124*, 8786–8787.

27 Syamala, M.; Cross, R. J.; Saunders, M. *J. Am. Chem. Soc.* **2002**, *124*, 6216–6219.

28 Frunzi, M.; Cross, R. J.; Saunders, M. *J. Am. Chem. Soc.* **2007**, *129*, 13343–13346.

29 Murata, M.; Murata, Y.; Komatsu, K. *Chem. Commun.* **2008**, 6083–6094.

30 Murata, M.; Ochi, Y.; Tanabe, F.; Komatsu, K.; Murata, Y. *Angew. Chem. Int. Ed.* **2008**, *47*, 2039–2041.

31 Sternfeld, T.; Thilgen, C.; Hoffman, R. E.; del Rosario Colorado Heras, M.; Diederich, F.; Wudl, F.; Scott, L. T.; Mack, J.; Rabinovitz, M. *J. Am. Chem. Soc.* **2002**, *124*, 5734–5738.

32 Elser, V.; Haddon, R. *Nature* **1987**, *325*, 792–794.

33 Haddon, R. C. et al. *Nature* **1991**, *350*, 46–47.

34 Ruoff, R.; Beach, D.; Cuomo, J.; McGuire, T.; Whetten, R.; Diederich, F. *J. Phys. Chem.* **1991**, *95*, 3457–3459.

35 von Ragué Schleyer, P.; Manoharan, M.; Wang, Z.-X.; Kiran, B.; Jiao, H.; Puchta, R.; van Eikema Hommes, N. J. *Org. Lett.* **2001**, *3*, 2465–2468.

36 Corminboeuf, C.; Heine, T.; Seifert, G.; von Ragué Schleyer, P.; Weber, J. *Phys. Chem. Chem. Phys.* **2004**, *6*, 273–276.

37 Bühl, M.; Patchkovskii, S.; Thiel, W. *Chem. Phys. Lett.* **1997**, *275*, 14–18.

38 Chen, Z.; Cioslowski, J.; Rao, N.; Moncrieff, D.; Bühl, M.; Hirsch, A.; Thiel, W. *Theoretical Chemistry Accounts* **2001**, *106*, 364–368.

39 Cyrański, M. K.; Howard, S. T.; Chodkiewicz, M. L. *Chem. Commun.* **2004**, 2458–2459.

40 Straka, M.; Lantto, P.; Vaara, J. *J. Phys. Chem. A* **2008**, *112*, 2658–2668.

41 Pasquarello, A.; Schlüter, M.; Haddon, R. *Phys. Rev. A* **1993**, *47*, 1783–1789.

42 Zanasi, R.; Fowler, P. *Chem. Phys. Lett.* **1995**, *238*, 270–280.

43 Zanasi, R.; Lazzeretti, P.; Fowler, P. *Chem. Phys. Lett.* **1997**, *278*, 251–255.

44 Baker, J.; Fowler, P.; Lazzeretti, P.; Malagoli, M.; Zanasi, R. *Chem. Phys. Lett.* **1991**, *184*, 182–186.

45 Van Lier, G.; De Proft, F.; Geerlings, P. *Phys. Solid State* **2002**, *44*, 588–592.

46 Krygowski, T. M.; Ciesielski, A. *J. Chem. Inf. Comput. Sci.* **1995**, *35*, 1001–1003.

47 Poater, J.; Fradera, X.; Duran, M.; Solà, M. *Chem. Eur. J.* **2003**, *9*, 1113–1122.

48 Slayden, S. W.; Liebman, J. F. *Chem. Rev.* **2001**, *101*, 1541–1566.

49 Aihara, J.-i. *J. Mol. Struct.* **1994**, *311*, 1–8.

50 Aihara, J.-i. *Internet Electron. J. Mol. Des* **2002**, *1*, 236–241.

51 Poater, J.; Solà, M. *Chem. Commun.* **2011**, *47*, 11647–11649.

52 Poater, J.; Duran, M.; Solà, M. *Int. J. Quantum Chem.* **2004**, *98*, 361–366.

53 Matito, E.; Salvador, P.; Duran, M.; Solà, M. *J. Phys. Chem. A* **2006**, *110*, 5108–5113.

54 Hückel, E. *Z. Physik* **1931**, *70*, 204–286.

55 Hückel, E. *Z. Physik* **1931**, *72*, 310–337.

56 Hückel, E. *Z. Physik* **1932**, *76*, 628–648.

57 Hückel, E. *Z. Elektrochem. Angew. P.* **1937**, *43*, 752–788.

58 Ottosson, H. *Nature Chem.* **2012**, *4*, 969–971.

59 Baird, N. C.; West, R. M. *J. Am. Chem. Soc.* **1971**, *93*, 4427–4432.

60 Baird, N. C. *J. Am. Chem. Soc.* **1972**, *94*, 4941–4948.

61 Hirsch, A.; Chen, Z.; Jiao, H. *Angew. Chem. Int. Ed.* **2000**, *39*, 3915–3917.

62 Chen, Z.; Jiao, H.; Hirsch, A.; Thiel, W. *Mol. Model. Annu.* **2001**, *7*, 161–163.

63 Chen, Z.; King, R. B. *Chem. Rev.* **2005**, *105*, 3613–3642.

64 Johansson, M. P.; Jusélius, J.; Sundholm, D. *Angew. Chem. Int. Ed.* **2005**, *44*, 1843–1846.

65 Chen, Z.; Wu, J. I.; Corminboeuf, C.; Bohmann, J.; Lu, X.; Hirsch, A.; von Ragué Schleyer, P. *Phys. Chem. Chem. Phys.* **2012**, *14*, 14886–14891.

66 Bühl, M. *Chem. Eur. J.* **1998**, *4*, 734–739.

67 Fallah-Bagher-Shaidaei, H.; Wannere, C. S.; Corminboeuf, C.; Puchta, R.; Schleyer, P. v. R. *Org. Lett.* **2006**, *8*, 863–866.

68 Van Lier, G.; Fowler, P.; De Proft, F.; Geerlings, P. *J. Phys. Chem. A* **2002**, *106*, 5128–5135.

69 Winstein, S. *J. Am. Chem. Soc.* **1959**, *81*, 6524–6525.

70 Kiely, A. F.; Haddon, R. C.; Meier, M. S.; Selegue, J. P.; Brock, C. P.; Patrick, B. O.; Wang, G.-W.; Chen, Y. *J. Am. Chem. Soc.* **1999**, *121*, 7971–7972.

71 Alegret, N.; Chaur, M. N.; Santos, E.; Rodríguez-Fortea, A.; Echegoyen, L.; Poblet, J. M. *J. Org. Chem.* **2010**, *75*, 8299–8302.

72 Garcia-Borràs, M.; Osuna, S.; Swart, M.; Luis, J. M.; Echegoyen, L.; Solà, M. *Chem. Commun.* **2013**, *49*, 8767–8769.

73 Williams, R. V. *Chem. Rev.* **2001**, *101*, 1185–1204.

74 Garcia-Borràs, M.; Osuna, S.; Luis, J. M.; Swart, M.; Solà, M. *Chem. Soc. Rev.* **2014**, *43*, 5089–5105.

75 Prato, M.; Lucchini, V.; Maggini, M.; Stimpfl, E.; Scorrano, G.; Eiermann, M.; Suzuki, T.; Wudl, F. *J. Am. Chem. Soc.* **1993**, *115*, 8479–8480.

76 Smith III, A. B.; Strongin, R. M.; Brard, L.; Furst, G. T.; Romanow, W. J.; Owens, K. G.; King, R. C. *J. Am. Chem. Soc.* **1993**, *115*, 5829–5830.

77 Suzuki, T.; Li, Q.; Khemani, K.; Wudl, F. *J. Am. Chem. Soc.* **1992**, *114*, 7301–7302.

78 Poater, J.; Fradera, X.; Duran, M.; Solà, M. *The Electrochemical Society Inc., Pennington* **2002**, *12*, 707–719.

79 Cioslowski, J.; Fleischmann, E. D. *J. Chem. Phys.* **1991**, *94*, 3730–3734.

80 Weiske, T.; Böhme, D. K.; Hrušák, J.; Krätschmer, W.; Schwarz, H. *Angew. Chem. Int. Ed.* **1991**, *30*, 884–886.

81 Heath, J.; O'brien, S.; Zhang, Q.; Liu, Y.; Curl, R.; Tittel, F.; Smalley, R. *J. Am. Chem. Soc.* **1985**, *107*, 7779–7780.

82 Yamamoto, K.; Saunders, M.; Khong, A.; Cross, R. J.; Grayson, M.; Gross, M. L.; Benedetto, A. F.; Weisman, R. B. *J. Am. Chem. Soc.* **1999**, *121*, 1591–1596.

83 Almeida Murphy, T.; Pawlik, T.; Weidinger, A.; Höhne, M.; Alcala, R.; Spaeth, J.-M. *Phys. Rev. Lett.* **1996**, *77*, 1075–1078.

84 Mauser, H.; Hirsch, A.; van Eikema Hommes, N. J.; Clark, T.; Pietzak, B.; Weidinger, A.; Dunsch, L. *Angew. Chem. Int. Ed.* **1997**, *36*, 2835–2838.

85 Weidinger, A.; Waiblinger, M.; Pietzak, B.; Murphy, T. A. *Appl. Phys. A* **1998**, *66*, 287–292.

86 Waiblinger, M.; Lips, K.; Harneit, W.; Weidinger, A.; Dietel, E.; Hirsch, A. *Phys. Rev. B* **2001**, *64*, 159901.

87 Aoyagi, S. et al. *Nature Chem.* **2010**, *2*, 678–683.

88 Stevenson, S.; Rice, G.; Glass, T.; Harich, K.; Cromer, F.; Jordan, M. R.; Craft, J.; Hadju, E.; Bible, R.; Olmstead, M. M.; Maitra, K.; Fisher, A. J.; Balch, A. L.; Dorn, H. C. *Nature* **1999**, *401*, 55–57.

89 Komatsu, K.; Murata, M.; Murata, Y. *Science* **2005**, *307*, 238–240.

90 Suetsuna, T.; Dragoe, N.; Harneit, W.; Weidinger, A.; Shimotani, H.; Ito, S.; Takagi, H.; Kitazawa, K. *Chem. Eur. J.* **2002**, *8*, 5079–5083.

91 Kurotobi, K.; Murata, Y. *Science* **2011**, *333*, 613–616.

92 Lu, X.; Feng, L.; Akasaka, T.; Nagase, S. *Chem. Soc. Rev.* **2012**, *41*, 7723–7760.

93 Chai, Y.; Guo, T.; Jin, C.; Haufler, R. E.; Chibante, L. F.; Fure, J.; Wang, L.; Alford, J. M.; Smalley, R. E. *J. Phys. Chem.* **1991**, *95*, 7564–7568.

94 Chaur, M. N.; Melin, F.; Ortiz, A. L.; Echegoyen, L. *Angew. Chem. Int. Ed.* **2009**, *48*, 7514–7538.

95 Rodríguez-Fortea, A.; Balch, A. L.; Poblet, J. M. *Chem. Soc. Rev.* **2011**, *40*, 3551–3563.

96 Akasaka, T.; Nagase, S. *Endofullerenes: a new family of carbon clusters*; Springer Science & Business Media, 2002; Vol. 3.

97 Shinohara, H. *Reports on Progress in Physics* **2000**, *63*, 843.

98 Dunsch, L.; Yang, S. *Phys. Chem. Chem. Phys.* **2007**, *9*, 3067–3081.

99 Chaur, M. N.; Athans, A. J.; Echegoyen, L. *Tetrahedron* **2008**, *64*, 11387–11393.

100 Dunsch, L.; Krause, M.; Noack, J.; Georgi, P. *J. Phys. Chem. Solids* **2004**, *65*, 309–315.

101 Stevenson, S.; Mackey, M. A.; Stuart, M. A.; Phillips, J. P.; Easterling, M. L.; Chancellor, C. J.; Olmstead, M. M.; Balch, A. L. *J. Am. Chem. Soc.* **2008**, *130*, 11844–11845.

102 Mercado, B. Q.; Stuart, M. A.; Mackey, M. A.; Pickens, J. E.; Confait, B. S.; Stevenson, S.; Easterling, M. L.; Valencia, R.; RodrÃŋguez-Fortea, A.; Poblet, J. M.; Olmstead, M. M.; Balch, A. L. *J. Am. Chem. Soc.* **2010**, *132*, 12098–12105.

103 Mercado, B. Q.; Olmstead, M. M.; Beavers, C. M.; Easterling, M. L.; Stevenson, S.; Mackey, M. A.; Coumbe, C. E.; Phillips, J. D.; Phillips, J. P.; Poblet, J. M.; Balch, A. L. *Chem. Commun.* **2010**, *46*, 279–281.

104 Chen, N.; Chaur, M. N.; Moore, C.; Pinzón, J. R.; Valencia, R.; Rodríguez-Fortea, A.; Poblet, J. M.; Echegoyen, L. *Chem. Commun.* **2010**, *46*, 4818–4820.

105 Chen, N.; Beavers, C. M.; Mulet-Gas, M.; Rodríguez-Fortea, A.; Munoz, E. J.; Li, Y.-Y.; Olmstead, M. M.; Balch, A. L.; Poblet, J. M.; Echegoyen, L. *J. Am. Chem. Soc.* **2012**, *134*, 7851–7860.

106 Chen, N.; Mulet-Gas, M.; Li, Y.-Y.; Stene, R. E.; Atherton, C. W.; Rodríguez-Fortea, A.; Poblet, J. M.; Echegoyen, L. *Chem. Sci.* **2013**, *4*, 180–186.

107 Popov, A. A.; Yang, S.; Dunsch, L. *Chem. Rev.* **2013**, *113*, 5989–6113.

108 Takata, M.; Nishibori, E.; Sakata, M.; Shinohara, H. *Struct. Chem.* **2003**, *14*, 23–38.

109 Takata, M.; Nishibori, E.; Sakata, M.; Shinohara, H. *Fullerene-Based Materials*; Springer, 2004; pp 59–84.

110 Olmstead, M. M.; Costa, D. A.; Maitra, K.; Noll, B. C.; Phillips, S. L.; Van Calcar, P. M.; Balch, A. L. *J. Am. Chem. Soc.* **1999**, *121*, 7090–7097.

111 Lu, X.; Akasaka, T.; Nagase, S. *Chem. Commun.* **2011**, *47*, 5942–5957.

112 Wakahara, T.; Kobayashi, J.-i.; Yamada, M.; Maeda, Y.; Tsuchiya, T.; Okamura, M.; Akasaka, T.; Waelchli, M.; Kobayashi, K.; Nagase, S.; Kato, T.; Kako, M.; Yamamoto, K.; Kadish, K. M. *J. Am. Chem. Soc.* **2004**, *126*, 4883–4887.

113 Li, F.-F.; Chen, N.; Mulet-Gas, M.; Triana, V.; Murillo, J.; Rodríguez-Fortea, A.; Poblet, J. M.; Echegoyen, L. *Chem. Sci.* **2013**, *4*, 3404–3410.

114 Shinohara, H.; Sato, H.; Ohkohchi, M.; Ando, Y.; Kodama, T.; Shida, T.; Kato, T.; Saito, Y. *Nature* **1992**, *357*, 52–54.

115 Yannoni, C. S.; Hoinkis, M.; de Vries, M. S.; Bethune, D. S.; Salem, J. R.; Crowder, M. S.; Johnson, R. D. *Science* **1992**, *256*, 1191–1192.

116 Iiduka, Y.; Wakahara, T.; Nakahodo, T.; Tsuchiya, T.; Sakuraba, A.; Maeda, Y.; Akasaka, T.; Yoza, K.; Horn, E.; Kato, T.; Liu, M. T. H.; Mizorogi, N.; Kobayashi, K.; Nagase, S. *J. Am. Chem. Soc.* **2005**, *127*, 12500–12501.

117 Nishibori, E.; Terauchi, I.; Sakata, M.; Takata, M.; Ito, Y.; Sugai, T.; Shinohara, H. *J. Phys. Chem. B* **2006**, *110*, 19215–19219.

118 Rubin, Y. *Chem. Eur. J.* **1997**, *3*, 1009–1016.

119 Vougioukalakis, G. C.; Roubelakis, M. M.; Orfanopoulos, M. *Chem. Soc. Rev.* **2010**, *39*, 817–844.

120 Stanisky, C. M.; Cross, R. J.; Saunders, M.; Murata, M.; Murata, Y.; Komatsu, K. *J. Am. Chem. Soc.* **2005**, *127*, 299–302.

121 Murata, Y.; Murata, M.; Komatsu, K. *J. Am. Chem. Soc.* **2003**, *125*, 7152–7153.

122 Murata, M.; Murata, Y.; Komatsu, K. *J. Am. Chem. Soc.* **2006**, *128*, 8024–8033.

123 Murata, M.; Maeda, S.; Morinaka, Y.; Murata, Y.; Komatsu, K. *J. Am. Chem. Soc.* **2008**, *130*, 15800–15801.

124 Iwamatsu, S.-i.; Uozaki, T.; Kobayashi, K.; Re, S.; Nagase, S.; Murata, S. *J. Am. Chem. Soc.* **2004**, *126*, 2668–2669.

125 Whitener Jr, K. E.; Frunzi, M.; Iwamatsu, S.-i.; Murata, S.; Cross, R. J.; Saunders, M. *J. Am. Chem. Soc.* **2008**, *130*, 13996–13999.

126 Iwamatsu, S.-i.; Stanisky, C. M.; Cross, R. J.; Saunders, M.; Mizorogi, N.; Nagase, S.; Murata, S. *Angew. Chem. Int. Ed.* **2006**, *45*, 5337–5340.

127 Duchamp, J. C.; Demortier, A.; Fletcher, K. R.; Dorn, D.; Iezzi, E. B.; Glass, T.; Dorn, H. C. *Chem. Phys. Lett.* **2003**, *375*, 655–659.

128 Khamatgalimov, A. R.; Kovalenko, V. I. *Fullerenes, Nanotubes and Carbon Nanostruct.* **2011**, *19*, 599–604.

129 Osuna, S.; Swart, M.; Solà, M. *Phys. Chem. Chem. Phys.* **2011**, *13*, 3585–3603.

130 Yang, S.; Popov, A. A.; Dunsch, L. *Angew. Chem. Int. Ed.* **2007**, *46*, 1256–1259.

131 Stevenson, S.; Fowler, P.; Heine, T.; Duchamp, J.; Rice, G.; Glass, T.; Harich, K.; Hajdu, E.; Bible, R.; Dorn, H. *Nature* **2000**, *408*, 427–428.

132 Olmstead, M. M.; Lee, H. M.; Duchamp, J. C.; Stevenson, S.; Marciu, D.; Dorn, H. C.; Balch, A. L. *Angew. Chem.* **2003**, *115*, 928–931.

133 Stevenson, S.; Burbank, P.; Harich, K.; Sun, Z.; Dorn, H. C.; van Loosdrecht, P. H. M.; deVries, M. S.; Salem, J. R.; Kiang, C.-H.; Johnson, R. D.; Bethune, D. S. *J. Phys. Chem. A* **1998**, *102*, 2833–2837.

134 Kato, H.; Taninaka, A.; Sugai, T.; Shinohara, H. *J. Am. Chem. Soc.* **2003**, *125*, 7782–7783.

135 Mercado, B. Q.; Beavers, C. M.; Olmstead, M. M.; Chaur, M. N.; Walker, K.; Holloway, B. C.; Echegoyen, L.; Balch, A. L. *J. Am. Chem. Soc.* **2008**, *130*, 7854–7855.

136 Beavers, C. M.; Zuo, T.; Duchamp, J. C.; Harich, K.; Dorn, H. C.; Olmstead, M. M.; Balch, A. L. *J. Am. Chem. Soc.* **2006**, *128*, 11352–11353.

137 Zuo, T.; Walker, K.; Olmstead, M. M.; Melin, F.; Holloway, B. C.; Echegoyen, L.; Dorn, H. C.; Chaur, M. N.; Chancellor, C. J.; Beavers, C. M.; Balch, A. L.; Athans, A. J. *Chem. Commun.* **2008**, 1067–1069.

138 Campanera, J. M.; Bo, C.; Olmstead, M. M.; Balch, A. L.; Poblet, J. M. *J. Phys. Chem. A* **2002**, *106*, 12356–12364.

139 Jakes, P.; Dinse, K.-P. *J. Am. Chem. Soc.* **2001**, *123*, 8854–8855.

140 Alvarez, L.; Pichler, T.; Georgi, P.; Schwieger, T.; Peisert, H.; Dunsch, L.; Hu, Z.; Knupfer, M.; Fink, J.; Bressler, P.; Mast, M.; Golden, M. S. *Phys. Rev. B* **2002**, *66*, 035107.

141 Campanera, J. M.; Bo, C.; Poblet, J. M. *Angew. Chem. Int. Ed.* **2005**, *44*, 7230–7233.

142 Chaur, M. N.; Valencia, R.; Rodríguez-Fortea, A.; Poblet, J. M.; Echegoyen, L. *Angew. Chem. Int. Ed.* **2009**, *48*, 1425–1428.

143 Popov, A. A.; Dunsch, L. *J. Am. Chem. Soc.* **2007**, *129*, 11835–11849.

144 Valencia, R.; Rodríguez-Fortea, A.; Poblet, J. M. *J. Phys. Chem. A* **2008**, *112*, 4550–4555.

145 Rodríguez-Fortea, A.; Alegret, N.; Balch, A. L.; Poblet, J. M. *Nature Chem.* **2010**, *2*, 955–961.

146 Zuo, T.; Beavers, C. M.; Duchamp, J. C.; Campbell, A.; Dorn, H. C.; Olmstead, M. M.; Balch, A. L. *J. Am. Chem. Soc.* **2007**, *129*, 2035–2043.

147 Wilson, L. J.; Cagle, D. W.; Thrash, T. P.; Kennel, S. J.; Mirzadeh, S.; Alford, J. M.; Ehrhardt, G. J. *Coord. Chem. Rev* **1999**, *190*, 199–207.

148 Wilson, L. J. *The Electrochemical Society Interface* **1999**, *8*, 24–28.

149 Da Ros, T. In *Medicinal Chemistry and Pharmacological Potential of Fullerenes and Carbon Nanotubes*; Cataldo, F., Da Ros, T., Eds.; Carbon Materials: Chemistry and Physics; Springer Netherlands, 2008; Vol. 1; pp 1–21.

150 Fortner, J.; Lyon, D.; Sayes, C.; Boyd, A.; Falkner, J.; Hotze, E.; Alemany, L.; Tao, Y.; Guo, W.; Ausman, K.; Colvin, V.; Hughes, J. *Environ. Sci. Technol.* **2005**, *39*, 4307–4316.

151 Lovern, S. B.; Klaper, R. *Environ. Toxicol. Chem.* **2006**, *25*, 1132–1137.

152 Sayes, C. M.; Gobin, A. M.; Ausman, K. D.; Mendez, J.; West, J. L.; Colvin, V. L. *Biomaterials* **2005**, *26*, 7587–7595.

153 Isakovic, A.; Markovic, Z.; Nikolic, N.; Todorovic-Markovic, B.; Vranjes-Djuric, S.; Harhaji, L.; Raicevic, N.; Romcevic, N.; Vasiljevic-Radovic, D.; Dramicanin, M.; Trajkovic, V. *Biomaterials* **2006**, *27*, 5049–5058.

154 Mikawa, M.; Kato, H.; Okumura, M.; Narazaki, M.; Kanazawa, Y.; Miwa, N.; Shinohara, H. *Bioconjugate Chem.* **2001**, *12*, 510–514.

155 Iezzi, E. B.; Duchamp, J. C.; Fletcher, K. R.; Glass, T. E.; Dorn, H. C. *Nano Lett.* **2002**, *2*, 1187–1190.

156 Cagle, D. W.; Kennel, S. J.; Mirzadeh, S.; Alford, J. M.; Wilson, L. J. *Proc. Natl. Acad. Sci. U. S. A.* **1999**, *96*, 5182–5187.

157 Kobayashi, K.; Kuwano, M.; Sueki, K.; Kikuchi, K.; Achiba, Y.; Nakahara, H.; Kananishi, N.; Watanabe, M.; Tomura, K. *J. Radioanal. Nucl. Chem.* **1995**, *192*, 81–89.

158 Chen, C. et al. *Nano Lett.* **2005**, *5*, 2050–2057.

159 Günes, S.; Neugebauer, H.; Sariciftci, N. S. *Chem. Rev.* **2007**, *107*, 1324–1338.

160 Thompson, B. C.; Fréchet, J. M. *Angew. Chem. Int. Ed.* **2008**, *47*, 58–77.

161 Pinzon, J. R.; Plonska-Brzezinska, M. E.; Cardona, C. M.; Athans, A. J.; Gayathri, S. S.; Guldi, D. M.; Herranz, M.; Martin, N.; Torres, T.; Echegoyen, L. *Angew. Chem. Int. Ed.* **2008**, *47*, 4173–4176.

162 Ariens, E. *Trends in pharmacological sciences* **1993**, *14*, 68–75.

163 Friedman, S. H.; Ganapathi, P. S.; Rubin, Y.; Kenyon, G. L. *J. Med. Chem.* **1998**, *41*, 2424–2429.

164 Nishimura, T.; Tsuchiya, K.; Ohsawa, S.; Maeda, K.; Yashima, E.; Nakamura, Y.; Nishimura, J. *J. Am. Chem. Soc.* **2004**, *126*, 11711–11717.

165 Bianco, A.; Maggini, M.; Scorrano, G.; Toniolo, C.; Marconi, G.; Villani, C.; Prato, M. *J. Am. Chem. Soc.* **1996**, *118*, 4072–4080.

166 Crivillers, N.; Takano, Y.; Matsumoto, Y.; Casado-Montenegro, J.; Mas-Torrent, M.; Rovira, C.; Akasaka, T.; Veciana, J. *Chem. Commun.* **2013**, *49*, 8145–8147.

167 López, A. M.; Mateo-Alonso, A.; Prato, M. *J. Mater. Chem.* **2011**, *21*, 1305–1318.

168 Feng, L.; Lu, X.; He, X.; Shi, Z.; Gu, Z. *Inorg. Chem. Commun.* **2004**, *7*, 1010–1013.

169 Sawai, K.; Takano, Y.; Izquierdo, M.; Filippone, S.; MartÃŋn, N.; Slanina, Z.; Mizorogi, N.; Waelchli, M.; Tsuchiya, T.; Akasaka, T.; Nagase, S. *J. Am. Chem. Soc.* **2011**, *133*, 17746–17752.

170 Cao, B.; Wakahara, T.; Maeda, Y.; Han, A.; Akasaka, T.; Kato, T.; Kobayashi, K.; Nagase, S. *Chem. Eur. J.* **2004**, *10*, 716–720.

171 Takano, Y.; Obuchi, S.; Mizorogi, N.; GarcÃŋa, R.; Herranz, M. Ã.; Rudolf, M.; Wolfrum, S.; Guldi, D. M.; MartÃŋn, N.; Nagase, S.; Akasaka, T. *J. Am. Chem. Soc.* **2012**, *134*, 16103–16106.

172 Tsuchiya, T.; Rudolf, M.; Wolfrum, S.; Radhakrishnan, S. G.; Aoyama, R.; Yokosawa, Y.; Oshima, A.; Akasaka, T.; Nagase, S.; Guldi, D. M. *Chem. Eur. J.* **2013**, *19*, 558–565.

173 Yamada, M.; Wakahara, T.; Nakahodo, T.; Tsuchiya, T.; Maeda, Y.; Akasaka, T.; Yoza, K.; Horn, E.; Mizorogi, N.; Nagase, S. *J. Am. Chem. Soc.* **2006**, *128*, 1402–1403.

174 Yamada, M.; Okamura, M.; Sato, S.; Someya, C. I.; Mizorogi, N.; Tsuchiya, T.; Akasaka, T.; Kato, T.; Nagase, S. *Chem. Eur. J.* **2009**, *15*, 10533–10542.

175 Takano, Y.; Herranz, M. A.; Martín, N.; Radhakrishnan, S. G.; Guldi, D. M.; Tsuchiya, T.; Nagase, S.; Akasaka, T. *J. Am. Chem. Soc.* **2010**, *132*, 8048–8055.

176 Takano, Y.; Obuchi, S.; Mizorogi, N.; GarciÌĄa, R.; Herranz, M. A.; Rudolf, M.; Guldi, D. M.; Martín, N.; Nagase, S.; Akasaka, T. *J. Am. Chem. Soc.* **2012**, *134*, 19401–19408.

177 Lu, X.; He, X.; Feng, L.; Shi, Z.; Gu, Z. *Tetrahedron* **2004**, *60*, 3713–3716.

178 Lu, X.; Nakajima, K.; Iiduka, Y.; Nikawa, H.; Mizorogi, N.; Slanina, Z.; Tsuchiya, T.; Nagase, S.; Akasaka, T. *J. Am. Chem. Soc.* **2011**, *133*, 19553–19558.

179 Lu, X.; Akasaka, T.; Nagase, S. *Acc. Chem. Res.* **2013**, *46*, 1627–1635.

180 Wang, T.; Wu, J.; Xu, W.; Xiang, J.; Lu, X.; Li, B.; Jiang, L.; Shu, C.; Wang, C. *Angew. Chem. Int. Ed.* **2010**, *49*, 1786–1789.

181 Wang, T.; Wu, J.; Feng, Y.; Ma, Y.; Jiang, L.; Shu, C.; Wang, C. *Dalton Trans.* **2012**, *41*, 2567–2570.

182 Cai, T.; Xu, L.; Gibson, H. W.; Dorn, H. C.; Chancellor, C. J.; Olmstead, M. M.; Balch, A. L. *J. Am. Chem. Soc.* **2007**, *129*, 10795–10800.

183 Chen, N.; Fan, L.-Z.; Tan, K.; Wu, Y.-Q.; Shu, C.-Y.; Lu, X.; Wang, C.-R. *J. Phys. Chem. C* **2007**, *111*, 11823–11828.

184 Cai, T.; Slebodnick, C.; Xu, L.; Harich, K.; Glass, T. E.; Chancellor, C.; Fettinger, J. C.; Olmstead, M. M.; Balch, A. L.; Gibson, H. W.; Dorn, H. C. *J. Am. Chem. Soc.* **2006**, *128*, 6486–6492.

185 Chen, N.; Zhang, E.-Y.; Tan, K.; Wang, C.-R.; Lu, X. *Org. Lett.* **2007**, *9*, 2011–2013.

186 Pinzón, J.; Cardona, C.; Herranz, M.; Plonska-Brzezinska, M.; Palkar, A.; Athans, A.; Martín, N.; Rodríguez-Fortea, A.; Poblet, J.; Bottari, G.; Torres, T.; Gayathri, S.; Guldi, D.; Echegoyen, L. *Chem. Eur. J.* **2009**, *15*, 864–877.

187 Pinzón, J. R.; Gasca, D. C.; Sankaranarayanan, S. G.; Bottari, G.; Torres, T.; Guldi, D. M.; Echegoyen, L. *J. Am. Chem. Soc.* **2009**, *131*, 7727–7734.

188 Wolfrum, S.; Pinzón, J. R.; Molina-Ontoria, A.; Gouloumis, A.; Martín, N.; Echegoyen, L.; Guldi, D. M. *Chem. Commun.* **2011**, *47*, 2270–2272.

189 Cai, T.; Ge, Z.; Iezzi, E. B.; Glass, T. E.; Harich, K.; Gibson, H. W.; Dorn, H. C. *Chem. Commun.* **2005**, 3594–3596.

190 Cardona, C. M.; Kitaygorodskiy, A.; Ortiz, A.; Herranz, M. Á.; Echegoyen, L. *J. Org. Chem.* **2005**, *70*, 5092–5097.

191 Martín, N.; Altable, M.; Filippone, S.; Martín-Domenech, A.; Echegoyen, L.; Cardona, C. M. *Angew. Chem.* **2006**, *118*, 116–120.

192 Aroua, S.; Yamakoshi, Y. *J. Am. Chem. Soc.* **2012**, *134*, 20242–20245.

193 Aroua, S.; Garcia-Borràs, M.; Osuna, S.; Yamakoshi, Y. *Chem. Eur. J.* **2014**, *20*, 14032–14039.

194 Cai, T.; Xu, L.; Anderson, M. R.; Ge, Z.; Zuo, T.; Wang, X.; Olmstead, M. M.; Balch, A. L.; Gibson, H. W.; Dorn, H. C. *J. Am. Chem. Soc.* **2006**, *128*, 8581–8589.

195 Echegoyen, L.; Chancellor, C. J.; Cardona, C. M.; Elliott, B.; Rivera, J.; Olmstead, M. M.; Balch, A. L. *Chem. Commun.* **2006**, 2653–2655.

196 Cardona, C. M.; Elliott, B.; Echegoyen, L. *J. Am. Chem. Soc.* **2006**, *128*, 6480–6485.

197 Cardona, C. M.; Kitaygorodskiy, A.; Echegoyen, L. *J. Am. Chem. Soc.* **2005**, *127*, 10448–10453.

198 Aroua, S.; Garcia-Borràs, M.; Bölter, M.; Osuna, S.; Yamakoshi, Y. *J. Am. Chem. Soc.* **2015**, *137*, 58.

199 Braun, K.; Dunsch, L.; Pipkorn, R.; Bock, M.; Baeuerle, T.; Yang, S.; Waldeck, W.; Wiessler, M. *Int. J. Med. Sci.* **2010**, *7*, 136.

200 Gimenez-Lopez, M. d. C.; Gardener, J. A.; Shaw, A. Q.; Iwasiewicz-Wabnig, A.; Porfyrakis, K.; Balmer, C.; Dantelle, G.; Hadjipanayi, M.; Crossley, A.; Champness, N. R.; Castell, M. R.; Briggs, G. A. D.; Khlobystov, A. N. *Phys. Chem. Chem. Phys.* **2010**, *12*, 123–131.

201 Chen, N.; Pinzón, J. R.; Echegoyen, L. *ChemPhysChem* **2011**, *12*, 1422–1425.

202 Feng, L.; Wakahara, T.; Nakahodo, T.; Tsuchiya, T.; Piao, Q.; Maeda, Y.; Lian, Y.; Akasaka, T.; Horn, E.; Yoza, K.; Kato, T.; Mizorogi, N.; Nagase, S. *Chem. Eur. J.* **2006**, *12*, 5578–5586.

203 Cai, T.; Xu, L.; Shu, C.; Reid, J. E.; Gibson, H. W.; Dorn, H. C. *J. Phys. Chem. C* **2008**, *112*, 19203–19208.

204 Pinzón, J. R.; Zuo, T.; Echegoyen, L. *Chem. Eur. J.* **2010**, *16*, 4864–4869.

205 Shustova, N. B.; Peryshkov, D. V.; Kuvychko, I. V.; Chen, Y.-S.; Mackey, M. A.; Coumbe, C. E.; Heaps, D. T.; Confait, B. S.; Heine, T.; Phillips, J. P.; Stevenson, S.; Dunsch, L.; Popov, A. A.; Strauss, S. H.; Boltalina, O. V. *J. Am. Chem. Soc.* **2011**, *133*, 2672–2690.

206 Lukoyanova, O.; Cardona, C. M.; Rivera, J.; Lugo-Morales, L. Z.; Chancellor, C. J.; Olmstead, M. M.; Rodríguez-Fortea, A.; Poblet, J. M.; Balch, A. L.; Echegoyen, L. *J. Am. Chem. Soc.* **2007**, *129*, 10423–10430.

207 Chaur, M. N.; Melin, F.; Athans, A. J.; Elliott, B.; Walker, K.; Holloway, B. C.; Echegoyen, L. *Chem. Commun.* **2008**, 2665–2667.

208 Bolskar, R. D.; Benedetto, A. F.; Husebo, L. O.; Price, R. E.; Jackson, E. F.; Wallace, S.; Wilson, L. J.; Alford, J. M. *J. Am. Chem. Soc.* **2003**, *125*, 5471–5478.

209 Cai, T.; Xu, L.; Shu, C.; Champion, H. A.; Reid, J. E.; Anklin, C.; Anderson, M. R.; Gibson, H. W.; Dorn, H. C. *J. Am. Chem. Soc.* **2008**, *130*, 2136–2137.

210 Maeda, Y.; Sato, S.; Inada, K.; Nikawa, H.; Yamada, M.; Mizorogi, N.; Hasegawa, T.; Tsuchiya, T.; Akasaka, T.; Kato, T.; Slanina, Z.; Nagase, S. *Chem. Eur. J.* **2010**, *16*, 2193–2197.

211 Maeda, Y.; Miyashita, J.; Hasegawa, T.; Wakahara, T.; Tsuchiya, T.; Nakahodo, T.; Akasaka, T.; Mizorogi, N.; Kobayashi, K.; Nagase, S.; Kato, T.; Ban, N.; Nakajima, H.; Watanabe, Y. *J. Am. Chem. Soc.* **2005**, *127*, 12190–12191.

212 Lee, H. M.; Olmstead, M. M.; Iezzi, E.; Duchamp, J. C.; Dorn, H. C.; Balch, A. L. *J. Am. Chem. Soc.* **2002**, *124*, 3494–3495.

213 Stevenson, S.; Stephen, R. R.; Amos, T. M.; Cadorette, V. R.; Reid, J. E.; Phillips, J. P. *J. Am. Chem. Soc.* **2005**, *127*, 12776–12777.

214 Diels, O.; Alder, K. *Liebigs Ann.* **1928**, *460*, 98–122.

215 Smith, L. I. *Chem. Rev.* **1938**, *23*, 193–285.

216 Huisgen, R. *Angew. Chem. Int. Ed.* **1963**, *2*, 565–598.

217 Huisgen, R. *Angew. Chem. Int. Ed.* **1963**, *2*, 633–645.

218 Huisgen, R. *J. Org. Chem.* **1976**, *41*, 403–419.

219 Huisgen, R.; Mloston, G.; Langhals, E. *J. Org. Chem.* **1986**, *51*, 4085–4087.

220 Mloston, G.; Huisgen, R. *Tetrahedron Lett.* **1989**, *30*, 7045–7048.

221 Vivanco, S.; Lecea, B.; Arrieta, A.; Prieto, P.; Morao, I.; Linden, A.; Cossío, F. P. *J. Am. Chem. Soc.* **2000**, *122*, 6078–6092.

222 Houk, K. N.; Gonzalez, J.; Li, Y. *Acc. Chem. Res.* **1995**, *28*, 81–90.

223 Houk, K.; Lin, Y. T.; Brown, F. K. *J. Am. Chem. Soc.* **1986**, *108*, 554–556.

224 Houk, K.; Firestone, R. A.; Munchausen, L. L.; Mueller, P. H.; Arison, B. H.; Garcia, L. A. *J. Am. Chem. Soc.* **1985**, *107*, 7227–7228.

225 Hiberty, P. C.; Ohanessian, G.; Schlegel, H. B. *J. Am. Chem. Soc.* **1983**, *105*, 719–723.

226 Liu, F.; Paton, R. S.; Kim, S.; Liang, Y.; Houk, K. *J. Am. Chem. Soc.* **2013**, *135*, 15642–15649.

227 Huisgen, R. *Angew. Chem. Int. Ed.* **1968**, *7*, 321–328.

228 Firestone, R. A. *J. Org. Chem.* **1968**, *33*, 2285–2290.

229 Firestone, R. A. *Tetrahedron* **1977**, *33*, 3009–3039.

230 Zubia, A.; Mendoza, L.; Vivanco, S.; Aldaba, E.; Carrascal, T.; Lecea, B.; Arrieta, A.; Zimmerman, T.; Vidal-Vanaclocha, F.; Cossío, F. P. *Angew. Chem.* **2005**, *117*, 2963–2967.

231 Adrio, J.; Carretero, J. C. *Chem. Commun.* **2011**, *47*, 6784–6794.

232 Maggini, M.; Scorrano, G.; Prato, M. *J. Am. Chem. Soc.* **1993**, *115*, 9798–9799.

233 Rivera-Nazario, D. M.; Pinzón, J. R.; Stevenson, S.; Echegoyen, L. A. *J. Phys. Org. Chem.* **2013**, *26*, 194–205.

234 Iezzi, E. B.; Duchamp, J. C.; Harich, K.; Glass, T. E.; Lee, H. M.; Olmstead, M. M.; Balch, A. L.; Dorn, H. C. *J. Am. Chem. Soc.* **2002**, *124*, 524–525.

235 Campanera, J. M.; Bo, C.; Poblet, J. M. *J. Org. Chem.* **2006**, *71*, 46–54.

236 Osuna, S.; Valencia, R.; Rodríguez-Fortea, A.; Swart, M.; Solà, M.; Poblet, J. M. *Chem. Eur. J.* **2012**, *18*, 8944–8956.

237 Garcia-Borràs, M.; Osuna, S.; Luis, J. M.; Swart, M.; Solà, M. *Chem. Eur. J.* **2012**, *18*, 7141–7154.

238 Garcia-Borràs, M.; Osuna, S.; Luis, J. M.; Swart, M.; Solà, M. *Chem. Eur. J.* **2013**, *19*, 14931–14940.

239 Ge, Z.; Duchamp, J. C.; Cai, T.; Gibson, H. W.; Dorn, H. C. *J. Am. Chem. Soc.* **2005**, *127*, 16292–16298.

240 Angeli, C. D.; Cai, T.; Duchamp, J. C.; Reid, J. E.; Singer, E. S.; Gibson, H. W.; Dorn, H. C. *CHem. Mater.* **2008**, *20*, 4993–4997.

241 Osuna, S.; Swart, M.; Campanera, J. M.; Poblet, J. M.; Solà, M. *J. Am. Chem. Soc.* **2008**, *130*, 6206–6214.

242 Osuna, S.; Swart, M.; Solà, M. *J. Am. Chem. Soc.* **2009**, *131*, 129–139.

243 Rodríguez-Fortea, A.; Campanera, J. M.; Cardona, C. M.; Echegoyen, L.; Poblet, J. M. *Angew. Chem. Int. Ed.* **2006**, *45*, 8176–8180.

244 Osuna, S.; Rodríguez-Fortea, A.; Poblet, J. M.; Solà, M.; Swart, M. *Chem. Commun.* **2012**, *48*, 2486–2488.

245 Lu, X.; Nakajima, K.; Iiduka, Y.; Nikawa, H.; Tsuchiya, T.; Mizorogi, N.; Slanina, Z.; Nagase, S.; Akasaka, T. *Angew. Chem. Int. Ed.* **2012**, *51*, 5889–5892.

246 Zhang, Y.; Ghiassi, K. B.; Deng, Q.; Samoylova, N. A.; Olmstead, M. M.; Balch, A. L.; Popov, A. A. *Angew. Chem. Int. Ed.* **2015**, *54*, 495–499.

247 Deng, Q.; Popov, A. A. *Chem. Commun.* **2015**, *51*, 5637–5640.

248 Bingel, C. *Chem. Ber.* **1993**, *126*, 1957–1959.

249 Diener, M. D.; Alford, J. M.; Kennel, S. J.; Mirzadeh, S. *J. Am. Chem. Soc.* **2007**, *129*, 5131–5138.

250 Feng, L.; Nakahodo, T.; Wakahara, T.; Tsuchiya, T.; Maeda, Y.; Akasaka, T.; Kato, T.; Horn, E.; Yoza, K.; Mizorogi, N.; Nagase, S. *J. Am. Chem. Soc.* **2005**, *127*, 17136–17137.

251 Herranz, M.; Diederich, F.; Echegoyen, L.

252 Shu, C.; Cai, T.; Xu, L.; Zuo, T.; Reid, J.; Harich, K.; Dorn, H. C.; Gibson, H. W. *J. Am. Chem. Soc.* **2007**, *129*, 15710–15717.

253 Isaacs, L.; Wehrsig, A.; Diederich, F. *Helv. Chem. Acta* **1993**, *76*, 1231–1250.

254 Yang, S.; Chen, C.; Li, X.; Wei, T.; Liu, F.; Wang, S. *Chem. Commun.* **2013**, *49*, 10844–10846.

255 Alegret, N.; Rodríguez-Fortea, A.; Poblet, J. M. *Chem. Eur. J.* **2013**, *19*, 5061–5069.

256 Alegret, N.; Salvadǿ, P.; Rodríguez-Fortea, A.; Poblet, J. M. *J. Org. Chem.* **2013**, *78*, 9986–9990.

257 Zhang, R.; Murata, M.; Wakamiya, A.; Murata, Y. *Chemistry Letters* **2013**, *42*, 879–881.

258 Varadwaj, A.; Varadwaj, P. R. *Chem. Eur. J.* **2012**, *18*, 15345–15360.

259 Filippone, S.; Maroto, E. E.; Martín-Domenech, Á.; Suarez, M.; Martín, N. *Nature Chem.* **2009**, *1*, 578–582.

260 Maroto, E. E.; de Cózar, A.; Filippone, S.; Martín-Domenech, Á.; Suarez, M.; Cossío, F. P.; Martín, N. *Angew. Chem.* **2011**, *123*, 6184–6188.

261 Maroto, E. E.; Filippone, S.; Martín-Domenech, A.; Suarez, M.; Martín, N. *J. Am. Chem. Soc.* **2012**, *134*, 12936–12938.

262 Maroto, E. E.; Filippone, S.; Suarez, M.; Martínez-Alvarez, R.; de Cǿzar, A.; Cossío, F. P.; Martín, N. *J. Am. Chem. Soc.* **2014**, *136*, 705–712.

263 Maroto, E. E.; Izquierdo, M.; Reboredo, S.; Marco-Martínez, J.; Filippone, S.; Martín, N. *Acc. Chem. Res.* **2014**, *47*, 2660–2670.

264 Maroto, E. E.; Izquierdo, M.; Murata, M.; Filippone, S.; Komatsu, K.; Murata, Y.; Martín, N. *Chem. Commun.* **2014**, *50*, 740–742.

265 Houk, K.; Cheong, P. H.-Y. *Nature* **2008**, *455*, 309–313.

266 Zhao, Y.; Truhlar, D. G. *Acc. Chem. Res.* **2008**, *41*, 157–167.

267 Cramer, C. J. *Essentials of computational chemistry: theories and models*; John Wiley & Sons, 2013.

268 Jensen, F. *Introduction to computational chemistry*; John Wiley & Sons, 2013.

269 Hohenberg, P.; Kohn, W. *Phys. Rev.* **1964**, *136*, B864.

270 Ziegler, T. *Chem. Rev.* **1991**, *91*, 651–667.

271 Baerends, E. J.; Gritsenko, O. V. *J. Phys. Chem. A* **1997**, *101*, 5383–5403.

272 Parr, R. G.; Yang, R. G. P. W. *Density-functional theory of atoms and molecules*; Oxford university press, 1989.

273 Kohn, W.; Sham, L. J. *Phys. Rev.* **1965**, *140*, A1133.

274 Perdew, J. P.; Yue, W. *Phys. Rev. B* **1986**, *33*, 8800.

275 Becke, A. D. *Phys. Rev. A* **1988**, *38*, 3098.

276 Lee, C.; Yang, W.; Parr, R. G. *Phys. Rev. B* **1988**, *37*, 785.

277 Perdew, J. P. *Phys. Rev. B* **1986**, *33*, 8822.

278 Perdew, J. P. *Phys. Rev. B* **1986**, *34*, 7406.

279 Tao, J.; Perdew, J. P.; Staroverov, V. N.; Scuseria, G. E. *Phys. Rev. Lett.* **2003**, *91*, 146401.

280 Becke, A. D. *J. Chem. Phys.* **1993**, *98*, 1372–1377.

281 Becke, A. D. *J. Chem. Phys.* **1993**, *98*, 5648–5652.

282 Stephens, P.; Devlin, F.; Chabalowski, C.; Frisch, M. J. *J. Phys. Chem.* **1994**, *98*, 11623–11627.

283 Vosko, S.; Wilk, L.; Nusair, M. *Can. J. Phys.* **1980**, *58*, 1200–1211.

284 Oliphant, N.; Bartlett, R. J. *J. Chem. Phys.* **1994**, *100*, 6550–6561.

285 Meijer, E. J.; Sprik, M. *J. Chem. Phys.* **1996**, *105*, 8684–8689.

286 Grimme, S. *WIREs Comput. Mol. Sci.* **2011**, *1*, 211–228.

287 Te Velde, G.; Bickelhaupt, F. M.; Baerends, E. J.; Fonseca Guerra, C.; van Gisbergen, S. J.; Snijders, J. G.; Ziegler, T. *J. Comput. Chem.* **2001**, *22*, 931–967.

288 van Lenthe, E.; Baerends, E.-J.; Snijders, J. G. *J. Chem. Phys.* **1993**, *99*, 4597–4610.

289 van Lenthe, E.; Baerends, E.-J.; Snijders, J. G. *J. Chem. Phys.* **1994**, *101*, 9783–9792.

290 Van Lenthe, E.; Snijders, J.; Baerends, E. *J. Chem. Phys.* **1996**, *105*, 6505–6516.

291 Van Lenthe, E.; Van Leeuwen, R.; Baerends, E. *Int. J. Quant. Chem.* **1996**, *57*, 281–293.

292 van Lenthe, E.; Ehlers, A.; Baerends, E.-J. *J. Chem. Phys.* **1999**, *110*, 8943–8953.

293 Ågren, H.; Mikkelsen, K. V. *J. Mol. Struct.: THEOCHEM* **1991**, *234*, 425–467.

294 Frisch, M. J. et al. Gaussian09 Revision D.01. Gaussian Inc. Wallingford CT 2009.

295 Tomasi, J.; Persico, M. *Chem. Rev.* **1994**, *94*, 2027–2094.

296 Mennucci, B.; Cammi, R.; Interscience, W. *Continuum solvation models in chemical physics: from theory to applications*; Wiley Online Library, 2007.

297 Foresman, J. B.; Keith, T. A.; Wiberg, K. B.; Snoonian, J.; Frisch, M. J. *J. Phys. Chem.* **1996**, *100*, 16098–16104.

298 Born, M. *Z. Physik* **1920**, *1*, 45–48.

299 Onsager, L. *J. Am. Chem. Soc.* **1936**, *58*, 1486–1493.

300 Kirkwood, J. G. *J. Chem. Phys.* **1934**, *2*, 351–361.

301 Kirkwood, J.; Westheimer, F. *J. Chem. Phys.* **1938**, *6*, 506–512.

302 Cossi, M.; Barone, V.; Cammi, R.; Tomasi, J. *Chem. Phys. Lett.* **1996**, *255*, 327–335.

303 Klamt, A. *J. Phys. Chem.* **1995**, *99*, 2224–2235.

304 Truong, T. N.; Stefanovich, E. V. *Chem. Phys. Lett.* **1995**, *240*, 253–260.

305 Barone, V.; Cossi, M.; Tomasi, J. *J. Chem. Phys.* **1997**, *107*, 3210–3221.

306 Zhao, Y.; Truhlar, D. G. *J. Chem. Phys.* **2006**, *125*, 194101.

307 Zhao, Y.; Truhlar, D. G. *Theoretical Chemistry Accounts* **2008**, *120*, 215–241.

308 Grimme, S. *J. Comput. Chem.* **2006**, *27*, 1787–1799.

309 Antony, J.; Grimme, S. *Phys. Chem. Chem. Phys.* **2006**, *8*, 5287–5293.

310 Grimme, S.; Antony, J.; Ehrlich, S.; Krieg, H. *J. Chem. Phys.* **2010**, *132*, 154104.

311 Steinmann, S. N.; Corminboeuf, C. *J. Chem. Phys.* **2011**, *134*, 044117.

312 Steinmann, S. N.; Corminboeuf, C. *J. Chem. Theory Comput.* **2010**, *6*, 1990–2001.

313 Steinmann, S. N.; Corminboeuf, C. *J. Chem. Theory Comput.* **2011**, *7*, 3567–3577.

314 Osuna, S.; Swart, M.; Solà, M. *J. Phys. Chem. A* **2011**, *115*, 3491–3496.

315 Weinhold, F.; Schleyer, P. *Schleyer, PvR* **1998**, 1792–1811.

316 Bofill, J. M. *J. Comput. Chem.* **1994**, *15*, 1–11.

317 Swart, M.; Bickelhaupt, F. M. *J. Comput. Chem.* **2008**, *29*, 724–734.

318 Swart, M.; Matthias Bickelhaupt, F. *Int. J. Quantum Chem.* **2006**, *106*, 2536–2544.

319 Houk, K. N. *Acc. Chem. Res.* **1975**, *8*, 361–369.

320 Fukui, K. *Acc. Chem. Res.* **1971**, *4*, 57–64.

321 Fukui, K. *Angew. Chem. Int. Ed.* **1982**, *21*, 801–809.

322 Houk, K.; Sims, J.; Duke, R.; Strozier, R.; George, J. K. *J. Am. Chem. Soc.* **1973**, *95*, 7287–7301.

323 Houk, K.; Sims, J.; Watts, C. R.; Luskus, L. *J. Am. Chem. Soc.* **1973**, *95*, 7301–7315.

324 Herndon, W. *Chem. Rev.* **1972**, *72*, 157–179.

325 Biermann, D.; Schmidt, W. *J. Am. Chem. Soc.* **1980**, *102*, 3163–3173.

326 Ess, D. H.; Houk, K. *J. Am. Chem. Soc.* **2007**, *129*, 10646–10647.

327 Ess, D. H.; Houk, K. *J. Am. Chem. Soc.* **2008**, *130*, 10187–10198.

328 Hayden, A. E.; Houk, K. *J. Am. Chem. Soc.* **2009**, *131*, 4084–4089.

329 Paton, R. S.; Kim, S.; Ross, A. G.; Danishefsky, S. J.; Houk, K. *Angew. Chem. Int. Ed.* **2011**, *50*, 10366–10368.

330 Bickelhaupt, F. M. *J. Comput. Chem.* **1999**, *20*, 114–128.

331 Fernández, I.; Bickelhaupt, F. M. *Chem. Soc. Rev.* **2014**, *43*, 4953–4967.

332 Houk, K.; Gandour, R. W.; Strozier, R. W.; Rondan, N. G.; Paquette, L. A. *J. Am. Chem. Soc.* **1979**, *101*, 6797–6802.

333 Morokuma, K. *J. Chem. Phys.* **1971**, *55*, 1236–1244.

334 Osuna, S.; Houk, K. N. *Chem. Eur. J.* **2009**, *15*, 13219–13231.

335 Garcia-Borràs, M.; Romero-Rivera, A.; Osuna, S.; Luis, J. M.; Swart, M.; Solà, M. *J. Chem. Theory Comput.* **2012**, *8*, 1671–1683.

336 Fernández, I.; Solà, M.; Bickelhaupt, F. M. *J. Chem. Theory Comput.* **2014**, *10*, 3863–3870.

337 Bickelhaupt, F. M.; Solà, M.; Fernández, I. *Chem. Eur. J.* **2015**, n/a–n/a.

338 Dewar, M. J.; Zoebisch, E. G.; Healy, E. F.; Stewart, J. J. *J. Am. Chem. Soc.* **1985**, *107*, 3902–3909.

339 Pople, J. A.; Beveridge, D. L. *Approximate molecular orbital theory*; McGraw-Hill New York, 1970; Vol. 30.

340 Kruszewski, J.; Krygowski, T. *Tetrahedron Lett.* **1972**, *13*, 3839–3842.

341 Krygowski, T. M. *J. Chem. Inf. Comput. Sci.* **1993**, *33*, 70–78.

342 Chen, Z.; Wannere, C. S.; Corminboeuf, C.; Puchta, R.; Schleyer, P. v. R. *Chem. Rev.* **2005**, *105*, 3842–3888.

343 Schleyer, P. v. R.; Maerker, C.; Dransfeld, A.; Jiao, H.; Hommes, N. J. v. E. *J. Am. Chem. Soc.* **1996**, *118*, 6317–6318.

344 Lazzeretti, P. *Phys. Chem. Chem. Phys.* **2004**, *6*, 217–223.

345 Schleyer, P. v. R.; Manoharan, M.; Jiao, H.; Stahl, F. *Org. Lett.* **2001**, *3*, 3643–3646.

346 Wolinski, K.; Hinton, J. F.; Pulay, P. *J. Am. Chem. Soc.* **1990**, *112*, 8251–8260.

347 Bultinck, P.; Ponec, R.; Van Damme, S. *J. Phys. Org. Chem.* **2005**, *18*, 706–718.

348 Bultinck, P.; Rafat, M.; Ponec, R.; Van Gheluwe, B.; Carbó-Dorca, R.; Popelier, P. *J. Phys. Chem. A* **2006**, *110*, 7642–7648.

349 Giambiagi, M.; de Giambiagi, M. S.; dos Santos Silva, C. D.; de Figueiredo, A. P. *Phys. Chem. Chem. Phys.* **2000**, *2*, 3381–3392.

350 Cioslowski, J.; Matito, E.; Solà, M. *J. Phys. Chem. A* **2007**, *111*, 6521–6525.

351 Salvador, P.; Ramos-Cordoba, E. *J. Chem. Phys.* **2013**, *139*, 071103.

352 Matito, E.; Solà, M.; Salvador, P.; Duran, M. *Faraday Discuss.* **2007**, *135*, 325–345.

353 Salvador, P.; Ramos-Cordoba, E. *APOST-3D, Institute of Computational Chemistry and Catalysis, University of Girona, Girona, Catalonia, Spain* **2012**,

354 Mayer, I.; Salvador, P. *Chem. Phys. Lett.* **2004**, *383*, 368–375.

355 Salvador, P.; Mayer, I. *J. Chem. Phys.* **2004**, *120*, 5046–5052.

356 Matito, E. *ESI-3D: Electron sharing indexes program for 3D molecular space partitioning, Institute of Computational Chemistry and Catalysis, University of Girona, Girona, Catalonia, Spain* **2006**,

357 Matito, E.; Duran, M.; Solà, M. *J. Chem. Phys.* **2005**, *122*, 014109.

358 Haddon, R.; Chow, S.-Y. *J. Am. Chem. Soc.* **1998**, *120*, 10494–10496.

359 Haddon, R. *J. Phys. Chem. A* **2001**, *105*, 4164–4165.

360 Haddon, R. *QCPE Bull.* **1995**, *15*, 81.

361 Sato, S.; Maeda, Y.; Guo, J.-D.; Yamada, M.; Mizorogi, N.; Nagase, S.; Akasaka, T. *J. Am. Chem. Soc.* **2013**, *135*, 5582–5587.

362 Ishitsuka, M. O.; Sano, S.; Enoki, H.; Sato, S.; Nikawa, H.; Tsuchiya, T.; Slanina, Z.; Mizorogi, N.; Liu, M. T. H.; Akasaka, T.; Nagase, S. *J. Am. Chem. Soc.* **2011**, *133*, 7128–7134.

363 Garcia-Borràs, M.; Osuna, S.; Swart, M.; Luis, J. M.; Solà, M. *Angew. Chem. Int. Ed.* **2013**, *52*, 9275–9278.